Semiconductors, Vol. 37, No. 4, 2003, pp. 367–369. Translated from Fizika i Tekhnika Poluprovodnikov, Vol. 37, No. 4, 2003, pp. 385–387.

ATOMIC STRUCTURE AND NONELECTRONIC PROPERTIES OF SEMICONDUCTORS

Structural Disordering and Viedemann–Franz Relation in Melts of Some II–IV–V_2 Semiconductors

Ya. B. Magomedov and M. A. Aĭdamirov

Institute of Physics, Dagestan Scientific Center, Russian Academy of Sciences, ul. 26 Bakinskikh Komissarov 94, Makhachkala, 367003 Russia

e-mail: kamilov@datacom.ru

Submitted July 9, 2002; accepted for publication October 10, 2002

Abstract—The thermal and electrical conductivities, as well as the thermoelectric power of the $CdSnAs_2$, $CdGeAs_2$, $ZnSnAs_2$, and $ZnGeAs_2$ ternary semiconductor compounds, were studied in both solid and liquid states. It was shown that the thermal and electrical conductivities of these compounds increase, while the thermoelectric power decreases in the course of melting to the values characteristic of liquid metals. In contrast to metal melts, the electrical conductivity and the Lorentz numbers calculated from the Viedemann–Franz relation increase with temperature in II–IV–V_2 semiconductor melts. According to the Mott classification, the melts of these compounds are related to group *B*. Melting of II–IV–V_2 semiconductors causes their metallization. © *2003 MAIK "Nauka/Interperiodica".*

In physicochemical parameters, ternary II–IV–V_2 semiconductor compounds are analogues of III–V semiconductors widely used in science and engineering. The kinetic properties of III–V semiconductors have been studied in a wide temperature range in solid and molten states. Melting of III–V compounds is accompanied by radical changes in their structure and short-range order, which is accompanied by drastic changes in the thermal and electrical conductivities, thermoelectric power, Hall coefficient, density, and other parameters [1–3] to values characteristic of metal melts. According to the Mott and Allgaier classification [4, 5], III–V compound melts are related to group *A* and their properties can be explained within the models of almost free electrons.

The kinetic parameters of II–IV–V_2 semiconductor compounds at high temperatures have received little attention in solid and molten states. Nikol'skaya *et al.* [6] studied the $CdSnAs_2$ conductivity in solid and liquid states and believed that this compound retained its short-range order after melting, thus making the $CdSnAs_2$ melt a liquid semiconductor. The thermal conductivity of some compounds of this group in the solid state was studied up to 700 K [7] (see also review [8]); however, the data of these publications are not consistent with each other.

To reveal the influence of the restructuring caused by melting on the electronic structure, as well as on the heat and charge transport mechanisms, we studied the thermal and electrical conductivities and the thermoelectric power of $CdSnAs_2$, $CdGeAs_2$, $ZnSnAs_2$, and $ZnGeAs_2$ compounds in a wide temperature range (300–1200 K) in solid and liquid states.

The thermal conductivity was studied by the absolute spherical method in a steady thermal mode [9]; the electrical conductivity and thermoelectric power were studied by the four-probe compensation method [10].

The relative measurement error did not exceed 4–5% for the thermal conductivity and 3–4% for the electrical conductivity and thermoelectric power. The measurements were carried out in inert gas in the heating–cooling mode with 3–4 samples of each composition. The average thermal and electrical conductivities at temperatures close to the melting point T_m and above are shown in Figs. 1 and 2.

At temperatures close to T_m, the electrical conductivity of all the studied solid-state compounds exponentially increases, while the thermoelectric power decreases, which is characteristic of the intrinsic-conductivity region of semiconductors.

The band gaps calculated by the temperature dependence of the conductivity for all the compounds are consistent with the literature data [8], which indicates reliability of the experimental data under consideration.

The thermal conductivity data we obtained at room temperature are also consistent with published [7].

The basic mechanism of heat conduction in the solid state is the phonon one. The phonon conductivity λ_{ph} decreases with temperature by the law T^{-1}. In the intrinsic-conductivity region, a small increase in the thermal conductivity before melting is observed for all the compounds under study. The electron (λ_e) and bipolar (λ_{bi}) components of the thermal conductivity, calculated from the electrical conductivity and thermoelectric power data (see [11]), adequately explain the thermal conductivity increase observed at high temperatures if

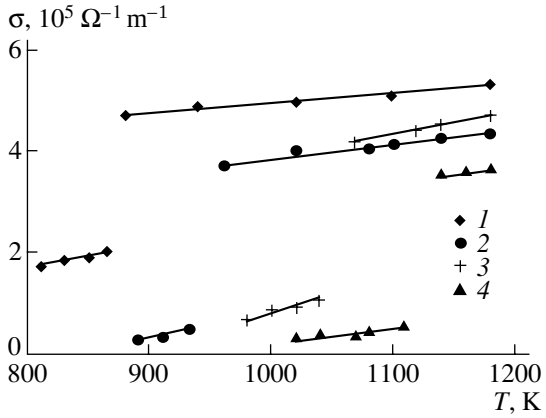

Fig. 1. Temperature dependences of the electrical conductivity of (*1*) $CdSnAs_2$, (*2*) $CdGeAs_2$, (*3*) $ZnSnAs_2$, and (*4*) $ZnGeAs_2$ compounds and their melts.

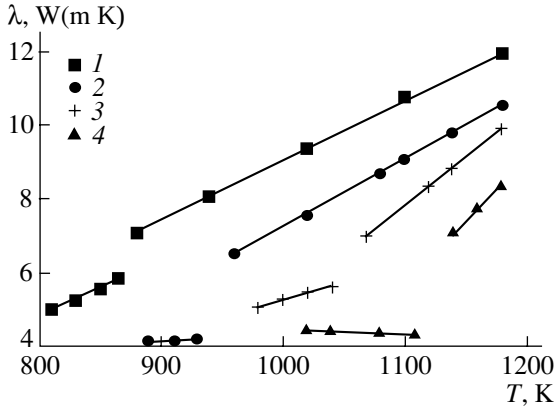

Fig. 2. Temperature dependences of the thermal conductivity of (*1*) $CdSnAs_2$, (*2*) $CdGeAs_2$, (*3*) $ZnSnAs_2$, and (*4*) $ZnGeAs_2$ compounds and their melts.

the Lorentz number L is taken as a value corresponding to the case of nondegenerate electron gas.

The electrical and thermal conductivities of all the compounds under study increase jumpwise at the melting point, while the thermoelectric power decreases.

The electrical conductivity ($\sigma > 3 \times 10^5\ \Omega^{-1}\ m^{-1}$) and the small thermoelectric power (10–30 μV/K) of II–IV–V_2 melts are characteristic of liquid metals [12]. However, the increase in the electrical conductivity with temperature, characteristic of compounds in the liquid state, is anomalous for metal melts.

Since an important feature of the metal state is the electronic character of the heat and charge transport mechanisms, the temperature dependence of the electron thermal conductivity of melts was calculated from the electrical conductivity data obtained using the Viedemann–Franz relation.

The values of λ_e, calculated for the case of partial degeneracy of electron gas taking into account the molecular thermal conductivity (λ_m), satisfactorily conform with the experimental data. The bipolar mechanism of the thermal conductivity characteristic of the semiconductor state is not observed in II–IV–V_2 compound melts. The molecular component of the thermal conductivity, calculated by the Rao formula [13], does not exceed 0.4–0.5 $W\ m^{-1}\ K^{-1}$ in the entire temperature range for all the melts studied.

In metal melts, the Viedemann–Franz law is also valid near the melting point and the Lorentz number is found to be close to L_0 for totally degenerate electron gas. However, the value of L gradually decreases with temperature in metal melts, which is attributed to the influence of inelastic electron scattering by solitary ions [12].

The experimental data on the electrical and thermal conductivity of melts were used to calculate the Lorentz numbers L for various temperatures by the Viedemann–Franz relation, taking into account λ_m. In contrast to metal melts, the values of L calculated for II–IV–V_2 melts are smaller than L_0 in the temperature range studied and increase with temperature (from 1.6×10^{-8} to $1.9 \times 10^{-8}\ V^2\ K^{-2}$).

The values of the electrical conductivity and thermoelectric power, as well as the electronic mechanism of the thermal conductivity, point to the metal character of these melts. According to the Mott and Allgaier classification [4, 5], $GdSnAs_2$, $CdGeAs_2$, $ZnSnAs_2$, and $ZnGeAs_2$ compounds belong to group *B* of elements which melt in conformity with the semiconductor–metal (with weak metal properties) scheme.

The melting of these semiconductors is accompanied by a significant change in the structure and the short-range order; the rigid system of covalent bonds between structural units is damaged, and the energy spectrum significantly changes (the band gap characteristic of the semiconductor state disappears, and the conduction band becomes partially overlapped with the valence band). In contrast to group-*A* semiconductor melts totally metallized on melting, a certain minimum is retained in the energy dependence of the density of states of group-*B* semiconductor melts in the energy range corresponding to the band gap. This indicates a partial retention of the hereditary features of the solid-state short-range order in melts of this group.

The increase of the electrical and thermal conductivity, as well as the Lorentz number, with temperature is caused by further destruction of these structural elements of the short-range order of the solid state; the covalent bonds that remained after melting continue to rupture, the overlap of the valence and conduction bands increases, and the minimum of the energy dependence of the density of states is smoothed out. The melts are gradually transferred to the pure metal state with temperature [14].

REFERENCES

1. A. F. Ioffe and A. R. Regel, Prog. Semicond. **4**, 237 (1960).
2. V. M. Glazov, S. N. Chizhevskaya, and N. N. Glagoleva, *Liquid Semiconductors* (Nauka, Moscow, 1967; Plenum, New York, 1969).
3. Ya. B. Magomedov and A. R. Bilalov, Fiz. Tekh. Poluprovodn. (St. Petersburg) **35**, 521 (2001) [Semiconductors **35**, 499 (2001)].
4. N. F. Mott and E. A. Davis, *Electronic Processes in Non-Crystalline Materials* (Clarendon, Oxford, 1971; Mir, Moscow, 1974).
5. R. S. Allgaier, Phys. Rev. **185**, 227 (1969).
6. G. F. Nikol'skaya, L. N. Berger, I. V. Efimovskiĭ, *et al.*, Neorg. Mater. **2**, 1876 (1966).
7. P. Leroux-Hugan, C. R. Acad. Sci. **73**, 35 (1963).
8. N. A. Goryunova and Yu. A. Valov, *II–IV–V_2 Semiconductors* (Sovetskoe Radio, Moscow, 1974).
9. Ya. B. Magomedov, Teplofiz. Vys. Temp. **28**, 396 (1990).
10. Kh. I. Amirkhanov, Ya. B. Magomedov, S. A. Aliev, *et al.*, in *Physical Properties of Tellurium* (Daguchpedgiz, Makhachkala, 1969).
11. B. M. Mogilevskiĭ and A. F. Chudnovskiĭ, *Thermal Conductivity of Semiconductors* (Nauka, Moscow, 1972).
12. L. P. Filippov, *Measurement of Thermal Properties of Solid and Liquid Metals at High Temperatures* (Mosk. Gos. Univ., Moscow, 1967).
13. M. R. Rao, Phys. Rev. **59**, 212 (1971).
14. A. R. Regel' and V. M. Glazov, *Mechanisms of Formation of the Electron Melt Structures* (Nauka, Moscow, 1982).

Translated by A. Kazantsev

Semiconductors, Vol. 37, No. 4, 2003, pp. 370–374. Translated from Fizika i Tekhnika Poluprovodnikov, Vol. 37, No. 4, 2003, pp. 388–392.

ELECTRONIC AND OPTICAL PROPERTIES OF SEMICONDUCTORS

Effect of Crystallization of Amorphous Vanadium Dioxide Films on the Parameters of a Semiconductor–Metal Phase Transition

V. A. Klimov*, I. O. Timofeeva*, S. D. Khanin*, E. B. Shadrin*, A. V. Il'inskiĭ, and F. Silva-Andrade****

** Ioffe Physicotechnical Institute, Russian Academy of Sciences, Politekhnicheskaya ul. 26, St. Petersburg, 194021 Russia*

e-mail: shadr.solid@mail.ioffe.ru

*** Autonomous University of Puebla, Mexico*

Submitted July 22, 2002; accepted for publication October 4, 2002

Abstract—The hysteresis loops of reflectivity and capacitance of amorphous and polycrystalline vanadium dioxide films in the range of a semiconductor–metal phase transition were studied. The morphology of these films was studied by an atomic-force microscope. It is established that the small number (2–3) of temperature cycles suppress the phase transition due to possible diffusion of oxygen from VO_2 clusters into adjacent clusters consisting of the lowest oxides of the Magnelli series. It is shown that the annealing of an amorphous film of vanadium dioxide in oxygen leads to an additional oxidation of low oxides and the formation of VO_2, the formation of a polycrystalline film, and the recovery of the phase transition. The above results and the data obtained by atomic-force microscopy are indicative of the high optical quality of the polycrystalline vanadium dioxide films produced by the annealing of amorphous VO_2 films. The results also show that these films can be used in interferometers and optical limiters. © *2003 MAIK "Nauka/Interperiodica".*

The study of the physical properties of vanadium dioxide is a pressing task because of the possible application of this compound in various devices, e.g., in thin-film Fabry–Perot interferometers [1].

Crystalline vanadium dioxide (VO_2) undergoes a first-order phase transition at a critical temperature of $T_c \approx 67$°C [1, 2] (T_c is the temperature of equilibrium between semiconducting and metallic phases). Dimensional effects cause the transition to the metallic phase to occur at a temperature slightly above T_c by the difference ΔT, which depends on the size of the crystal in which this transition takes place [3]. This effect is determined by the considerable contribution of the surface tension energy of the outer boundary of a crystallite to the energy state of the phase transition. The surface tension energy depends on the curvature of the crystallite surface, which, in turn, is directly related to the size and shape of the crystallite. In bulk single crystals of VO_2, the difference ΔT is about 1–2°C, whereas in grained polycrystalline films it can be as large as 20–30°C. The reverse phase transition occurs at a temperature $T_c - \Delta T$. Thus, we are dealing with the thermal hysteresis of physical properties in a material with a loop width $2\Delta T$ and a large variety of loop shapes. [4].

The application of vanadium dioxide is mostly associated with its use as thin films, e.g., thin-film VO_2 is used for hologram recording in a Fabry–Perot interferometer. The latter consist of a substrate with a successively deposited aluminum mirror and homogeneous VO_2 film. In a simple device, the outer surface of the VO_2 film serves as the second mirror. The reflectivity of such an interferometer abruptly changes at the point on the surface which is affected by the heat pulse inducing the phase transition. The configuration of the thermal field is stored due to the existence of thermal hysteresis.

From the above follows the urgency of growing VO_2 films with as large an area as possible with a high homogeneity of optical characteristics both across the width and the surface. Many studies have been aimed at solving this problem [5–7]. This study is also devoted to solving such a problem, i.e., to the investigation of the optical and electrical properties of amorphous VO_2 films obtained by anodic oxidation of a metallic vanadium film. Polycrystalline VO_2 films prepared by successive thermocrystallization of amorphous films [8] are also studied.

Thermocrystallization, according to [8], consists in the annealing of amorphous VO_2 film in air at a temperature of 450°C for 2 minutes. As a result of this treatment, polycrystalline VO_2 film was formed. As the starting material for anodic oxidation, we used vanadium foil 0.15 mm in thickness, or thin (about 500 Å) vanadium films deposited by a resistive method on high-resistivity germanium substrate. In the former case, the foil was electrochemically polished with a 40% solution of sulfuric acid in ethanol at a current density of 0.5 A/cm^2. Acetic acid, CH_3COOH, with the addition of an aqueous solution of borax, $Na_2B_4O_7 \cdot 10H_2O$, was used as an electrolyte for anodic oxidation. Anodization was performed in the constant-voltage

mode [8]. The electrochemical oxidation method used at this stage in the synthesis of metallic vanadium [8] has the advantage that it allows obtaining homogeneous amorphous VO_2 films of large area without using a high-vacuum technique. However, as will be shown below, these films were found to be unstable during thermal cycling. To eliminate this problem, such films were annealed in oxygen atmosphere. At each stage, the morphology of the films was controlled by an atomic-force microscope, and their electrical and optical parameters were determined by measuring the thermal hysteresis loops of physical properties in the region of phase transition.

The temperature dependence of reflectivity of the samples was measured at several fixed wavelengths in the range of 0.6–1.7 μm at temperatures from 23 to 90°C using a conventional spectrophotometer based on an MDR-2 monochromator. The electrical resistance of the VO_2 samples was measured in the direct-current mode, and the complex impedance was measured at a frequency of 3 MHz.

An image of the surface of an amorphous VO_2 film, which was obtained using an atomic-force microscope, is shown in Fig. 1. This film was synthesized by anodic oxidation of metallic vanadium film preliminarily deposited on germanium substrate. The most striking distinction between this image and the image of the polycrystalline VO_2 films published in [9] is the absence in Fig. 1 of a grain structure typical of polycrystalline films, despite the fact that the grain structure is inherent in metallic vanadium. The atomic-force image of the area of the amorphous VO_2 film shows structureless formation with a surface reproducing the surface of the substrate. The thickness of this film is about 1100 ± 20 Å and remains almost constant over the entire film surface.

Figure 2 shows the hysteresis loops of (a) reflectivity at 1.3 μm and (b) the capacitance of an amorphous film measured in the region of 67°C. The loops are nonclosed and asymmetrical with a width of about 20°C, with their branches covering the temperature range of about 80°C.

The absence of a pronounced grain structure in amorphous VO_2 film makes it impossible to analyze the loop shapes on the basis of the notion that each grain-crystallite in the film possesses a single, unique elementary thermal hysteresis loop; these elementary loops are "vertical" with respect to temperature; i.e., when reaching the transition temperature, the nucleus of a new phase grows with the sound velocity through the entire grain which had just been in the preceding phase [1, 9]. At the same time, it is beyond question that the change in reflectivity of amorphous VO_2 film at heating near the semiconductor–metal phase transition is related to the occurrence of a metal phase within the semiconductor bulk. It would appear reasonable to assume that there are certain grainlike regions of VO_2 in the amorphous film; these regions restrict the growth of

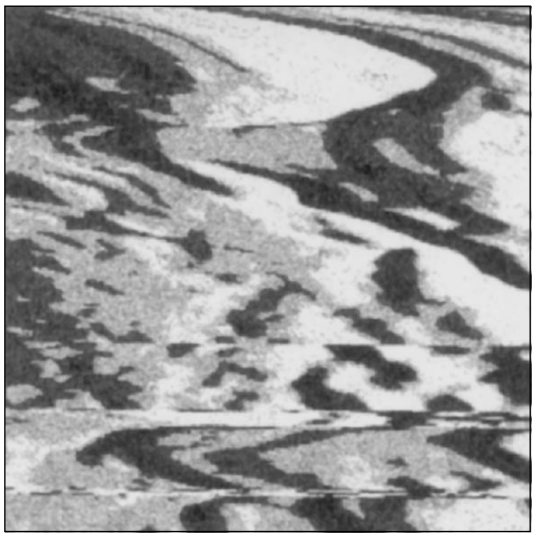

Fig. 1. Atomic-force micrograph of amorphous vanadium dioxide film synthesized by electrochemical oxidation.

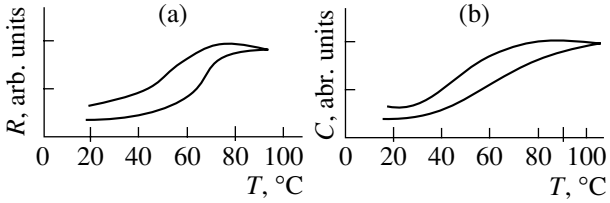

Fig. 2. Hysteresis loops of amorphous vanadium dioxide film: (a) reflectivity, and (b) capacitance measured at a frequency of 3 MHz.

nuclei of the new phase and determine, according to the elastic properties of the boundaries of such regions, the width of elementary loops [3]. Among possible sources of such regions, we could point to the regions of short-range order in an amorphous material with the cross section of these regions on the order of several lattice parameters (20–50 Å), or to the random network of clusters with a cross section of several hundreds of lattice parameters and with a stoichiometry corresponding to various oxides in Magnelli series [1] with differing oxygen content. These clusters most likely arise from the initial metallic vanadium film containing grains that transformed into the amorphous state in the course of anodic oxidation.

In our opinion, regions with short-range order and with a cross section of several lattice parameters in amorphous film can hardly play the part of the regions under consideration because the experimentally obtained width of the total loop (20°C) is relatively small for VO_2 films. Indeed, the total loop consisting of elementary loops inherent in the regions with a cross section of 20–50 Å should have a width on the order of 100–200°C, since the width of an elementary hysteresis

loop is inversely proportional to the square root of the cross section of the region restricting the growth of a nucleus [10]. As was mentioned above, we do not observe this in the experiment.

Thus, it is most reasonable to assume that the random network of cluster regions with a cross section of several hundred (not tens) lattice parameters arising during synthesis plays an important role in this process. These VO_2 regions are surrounded by regions with a stoichiometry that differs from the VO_2 oxides of the Magnelli series and with dissimilar phase-transition temperatures. The existence of such oxides can be related to the polyvalence of the vanadium atom [5]. This concept suggestion seems quite reasonable because the synthesis of an oxide film by the oxidation of an initial metallic film in an electrolyte solution under an electric current results in the spread of electric-field strengths and current densities in the process of oxidation, i.e., in the spread of the degree of local oxidation of vanadium, because the cross sections of grains have a Gaussian distribution. This idea is supported by the strong dependence of the observed properties of amorphous VO_2 film, synthesized by anodic oxidation, on the method of preparation of initial metallic vanadium [8].

In the context of the suggested concept, one can estimate, according to [9], the size of VO_2 clusters and their degree of imperfection. Indeed, a small (for films) width of hysteresis loops (20°C) is indicative of large sizes of VO_2 regions (the estimation, according to [9], yields 60–100 nm), where the phase transition occurs. At the same time, a comparatively large temperature extent of the branches of the loops (about 80°C) points to a large temperature spread in the position of the elementary loops determining the total loop in amorphous VO_2. This, in turn, points to a large spread in the concentration of free charge carriers (electrons) in the regions corresponding to elementary hysteresis loops, because the carrier concentration strongly affects the temperature position of elementary loops. The spread of the electron concentration in VO_2, in turn, is caused by the spread of the concentration of defects, which act as donors [11]. This spread can be estimated using the data obtained in [12, 13], where a shift of T_c per 1 at. % of donor-type defects in the VO_2 lattice is reported. The estimation of spread yields a value of about 6 at. % for the extent of total loop branches equal to 80°C. This estimate of the degree of imperfection of clusters in amorphous film, despite the large value, seems quite reasonable because the bond energy of oxygen in the compounds corresponding to the Magnelli series varies only slightly. Therefore, even a slight variation in the synthesis conditions results in considerable structural imperfection for each member of the Magnelli series within its range of homogeneity, as well as in the simultaneous synthesis of several neighboring members of this series.

The suggested concept based on the important role of a VO_2 cluster network surrounded by regions of low vanadium oxides is supported by the rapid aging of an amorphous film. The aging manifests itself in a drastic decrease in the jump of the physical parameters of the material during the phase transition after each heating–cooling cycle. After several cycles, the phase transition is no longer observed at 67°C. For the film, whose loop is shown in Fig. 2, it is sufficient to perform only two heating–cooling cycles, after which the optical (Fig. 2a) and electrical (Fig. 2b) hysteresis loops can be detected. The decrease in the jumps of parameters at the phase transition after the first temperature cycle was compensated by a high sensitivity of the impedance measurement. It should be mentioned that the presence of nonclosed hysteresis loops suggests that the process of aging is effective even during a single heating–cooling cycle, which begins after reaching a temperature of 90°C. This can be explained by the increase in the portion of the metallic phase across the thickness of the film in the course of detection of the hysteresis loop which results in the irreversible increase in the reflection coefficient and the capacitance of the film at 20°C; this increase is responsible for the nonclosed shape of the loop (Fig. 2).

In the context of the suggested concept, the observed change in the form of the hysteresis loop after each temperature cycle is caused by the fact that, at temperatures above the phase transition, oxygen diffuses from the VO_2 clusters as a result of heating (up to 90°C) with the subsequent capture of this oxygen by low oxides belonging to the Magnelli series and surrounding the VO_2 clusters. This process gives rise to the chemical reduction of VO_2 to lower vanadium oxides and reduces the relative VO_2 content in a film. The increased (in comparison with polycrystalline films) diffusion rate of oxygen in films at 90°C (the upper temperature boundary of the total hysteresis loop) is related to the fact that amorphous film contains a large number of dangling valence bonds characteristic of the amorphous state [8]. The final result of oxygen diffusion under thermocycling is the formation of an amorphous film containing no vanadium dioxide and consisting entirely of lower vanadium oxides which undergo phase transition at much lower temperatures than vanadium dioxide; as a result, these lower oxides exhibit metallic properties at 20°C [1]. This is the reason why the hysteresis loops become nonclosed even during the first temperature cycle and the phase transition at 67°C disappears after several cycles. Upon heating to 90°C, the process of disappearance of VO_2 regions becomes more intense due to the equalization of the oxygen content over the film volume as a result of diffusion. The coefficients of chemical diffusion of oxygen through the interface between two members of the Magnelli series adjacent to VO_2 for the crystalline state at the temperatures of 20 and 90°C, according to estimates [14], are close to 2×10^{-6} and 10^{-5} m^2/s, respectively. For an amorphous film, these values

should be at least an order of magnitude larger. Moreover, the estimations based on the experimental values of oxidation current, anodic oxidation time, and the sample sizes show that the average oxygen content in a synthesized amorphous film is 5–7 times lower than the content necessary for the stoichiometric composition of VO_2.

The assumed importance of oxygen diffusion accompanied by the leveling of its content and disappearance of clusters filled with vanadium dioxide quite naturally necessitates an additional oxidation of films in order to restore the experimental manifestation of the semiconductor–metal phase transition at 67°C. For this purpose, amorphous films were annealed at a temperature of 450°C in an oxygen-containing atmosphere (at atmospheric pressure for 2 minutes), which resulted in the formation of fully oxidated VO_2 regions.

The atomic-force image of such fully oxidized film is shown in Fig. 3. It can be seen that during the second stage of synthesis, apart from the additional oxidation, the crystallization of the initial amorphous film occurs. Oriented crystalline VO_2 grains of triangular shape with a cross section of 250–300 nm can be distinctly seen in this image. The spread in grain size is not too large, and the half-width of the histogram of size distribution is 70 nm. It is worth noting that amorphous VO_2 films are thermodynamically unstable and can begin to crystallize even at 90°C [8].

High-temperature annealing, apart from restoring a phase transition at 67°C, allows the attainment of a large jump of physical parameters inherent in polycrystalline VO_2 film (three orders of magnitude for capacitance) with the retention of (typical of amorphous film) a large temperature extent of branches in loops (Fig. 4). It is also worth noting that, when annealing oxide amorphous films aged by the thermocycling, the duration required for reaching the phase transition parameters typical of polycrystalline VO_2 is 5–10 times shorter than the time necessary for the synthesis of polycrystalline VO_2 film by the direct thermal oxidation of the initial film in the same atmosphere and at the same temperature. The difference in annealing times is additional evidence for the formation of low vanadium oxides inside amorphous VO_2 film during its electrolytic oxidation.

Figure 4 (to be compared with Fig. 2) clearly illustrated the transformation of semiconductor–metal phase transition parameters as a result of the crystallization of amorphous VO_2 film. Indeed, the hysteresis loops become narrower and more symmetrical after annealing, but retain an appreciable extent of branches inherent in amorphous film. For anodic-oxidized VO_2 films annealed in air, neither the magnitude of the jump of parameters at the semiconductor–metal phase transition nor the shape of the hysteresis loop depend on the number of heating–cooling cycles.

The narrowing of the total hysteresis loop of the annealed sample (from 20 to 12°C for the reflectivity loop, Figs. 2a and 4a, and from 15 to 10°C for the capacitance loop, Figs. 2b and 4b) is caused by the enlargement of VO_2 regions in the course of thermal oxidation. This process prevents the growth of nuclei of a new phase and, according to the martensite model of a phase transition in VO_2 [3], narrows the elementary loops inherent in these regions.

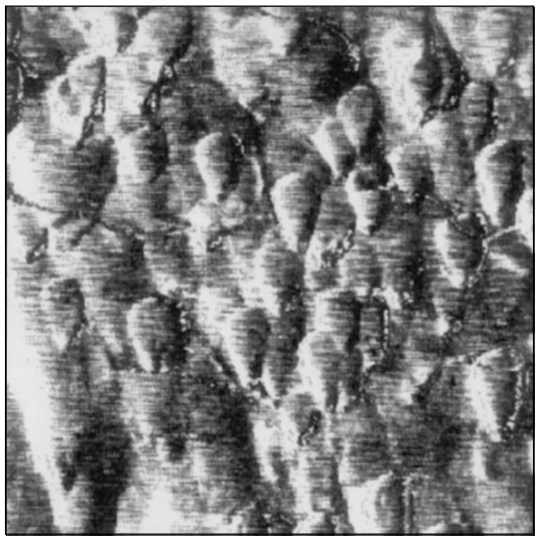

Fig. 3. Atomic-force micrograph of polycrystalline vanadium dioxide film obtained by high-temperature annealing of amorphous VO_2 film in oxygen-containing atmosphere at 450°C for 2 min.

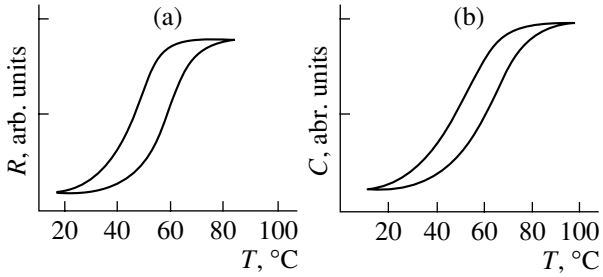

Fig. 4. Hysteresis loops of polycrystalline vanadium dioxide film obtained by high-temperature annealing of amorphous VO_2 film in oxygen-containing atmosphere at 450°C for 2 minutes: (a) reflectivity, and (b) capacitance measured at a frequency of 3 MHz.

In the context of the suggested concept, the symmetrization of the total loop can be explained in the following way. It is known [9] that the asymmetry of the total hysteresis loop at the semiconductor–metal phase transition in VO_2 is related to the correlation between the sizes of regions which restrict the growth of nuclei of a new phase (and determine the width of the elementary loop), as well as to the oxygen nonstoichiometry of these regions which determine the position of the elementary loops on the temperature scale. Indeed, the elementary loops with the largest size, which form asym-

metric total hysteresis loop, have simultaneously the lowest position on the temperature scale. This results in the relative broadening of the low-temperature part of the hysteresis loop, i.e., in its asymmetry. If correlation is absent, the loops are symmetrical. This correlation arises in the course of synthesis, because, in all methods of synthesis—anodic oxidation or thermal oxidation in a vacuum chamber at low oxygen pressure (10^{-1} Torr)—the degree of oxidation is always related to the size of oxidized microcrystallite, since the equilibrium oxygen pressure over VO_2 strongly depends on the size of a crystallite [9]. At the same time, the conditions for additional oxidation in air at atmospheric pressure exceed the equilibrium to such an extent that the degree of oxidation is actually independent of the size of a crystallite. Such a situation destroys the correlation, so that the grain-size distribution over the width of the elementary loops and the temperatures of the phase equilibrium become uncorrelated, which results in the symmetrization of the total hysteresis loop.

The constancy in a large extent of the branches for the total loop is associated with the preservation of the high spread of grain imperfections in a polycrystalline film despite the small spread in grain sizes (Fig. 3). As a result, the distribution of elementary loops retains an appreciable width on the temperature scale.

ACKNOWLEDGMENTS

This study was supported by CONACYT and by the International Science and Technology Center, grant no. 1454.

REFERENCES

1. A. A. Bugaev, B. P. Zakharchenya, and F. A. Chudnovskiĭ, *The Metal–Semiconductor Phase Transition and Its Applications* (Nauka, Leningrad, 1979), p. 183.
2. N. F. Mott, *Metal–Insulator Transitions* (Taylor and Francis, London, 1974; Nauka, Moscow, 1979).
3. I. A. Khakhaev, F. A. Chudnovskiĭ, and E. B. Shadrin, Fiz. Tverd. Tela (St. Petersburg) **36**, 1643 (1994) [Phys. Solid State **36**, 898 (1994)].
4. E. B. Shadrin, Doctoral Dissertation (St. Petersburg, 1997).
5. W. Bruckner, H. Opperman, W. Reichelt, E. I. Terukov, F. A. Tschudnovskii, and E. Wolf, *Vanadiumdioxide* (Akademie, Berlin, 1983), p. 252.
6. V. Yu. Zerov, Yu. V. Kulikov, and V. N. Leonov, Opt. Zh. **66** (5), 8 (1999) [J. Opt. Technol. **66**, 387 (1999)].
7. V. P. Belousov, I. M. Belousova, and O. B. Danilov, Proc. SPIE **3263**, 124 (1998).
8. G. B. Stefanovich, Doctoral Dissertation (Petrozavodsk, 1998).
9. V. A. Klimov, I. O. Timofeeva, S. D. Khanin, *et al.*, Zh. Tekh. Fiz. **72** (9), 67 (2002) [Tech. Phys. **47**, 1134 (2002)].
10. A. L. Roĭtburd, Usp. Fiz. Nauk **113**, 69 (1974) [Sov. Phys. Usp. **17**, 326 (1974)].
11. A. Leone, A. Trione, and F. Junga, IEEE Trans. Nucl. Sci. **37**, 1739 (1990).
12. T. Horlin, T. Niklevsky, and M. Nygren, Mater. Res. Bull. **8**, 179 (1973).
13. P. Wuz, A. Miyashita, and S. Yamamato, J. Appl. Phys. **86**, 5311 (1999).
14. N. A. Kolobov and M. M. Samokhvalov, *Diffusion and Oxidation in Semiconductors* (Metallurgiya, Moscow, 1975).

Translated by A. Zalesskiĭ

Semiconductors, Vol. 37, No. 4, 2003, pp. 375–379. Translated from Fizika i Tekhnika Poluprovodnikov, Vol. 37, No. 4, 2003, pp. 393–397.

ELECTRONIC AND OPTICAL PROPERTIES OF SEMICONDUCTORS

Recombination Current Instability in Epitaxial p^+–n Structures with Impurity Atoms Locally Incorporated into the n-type Region and Determination of the Deep Center Parameters

B. S. Muravskiĭ†, O. N. Kulikov*, and V. N. Chernyi

Kuban State University, ul. Stavropol'skaya 149, Krasnodar, 350040 Russia

** e-mail: oleg_kulikov@pochtamt.ru*

Submitted June 25, 2002; accepted for publication July 2, 2002

Abstract—The physical processes causing the recombination current instability in silicon epitaxial p^+–n structures with a local contact formed in the n-type region of the structure and produced by incorporation of impurity atoms that introduced deep energy levels in the silicon band gap were studied. Based on the study of the current instability, the parameters (density, energy position, and cross section of electron capture) of deep-level centers generated by tin, lead, cadmium, and nickel in silicon, were determined. © *2003 MAIK "Nauka/Interperiodica".*

1. INTRODUCTION

Dynamic inhomogeneities in semiconductors or semiconductor structures and the related current instability (CI) are of significant interest for developing fundamentally new devices. Among all the CI types, the least studied is the class of instabilities caused by charge recombination in semiconductors, i.e., the recombination current instability (RCI).

Recently, the CI of this type has not only been studied in materials and structures typical of modern electronics [1–4], but has also been detected in high-resistance PbTe:Ga crystals [5]. Recombination processes in semiconductor plasma depend on many factors, which can not always be controlled because of their variety (see monograph [6]). As a result, among other CI types, the largest number of papers are dedicated to the RCIs, and the obtained data are most controversial. We conducted a comprehensive analysis of virtually all of the RCI studies and came to the following conclusion. The necessary condition for oscillations is the existence of traps whose energy levels are within the band gap. These levels arise due to incorporated impurities, as well as lattice defects or surface states.

Another necessary condition is the existence of processes disturbing the quasi-equilibrium distribution of carriers. In [7, 8], the CI is related to periodic population and depopulation of surface states and corresponding changes in the height of the potential barrier controlled by these states. This allows one to distinguish the specific CI type, i.e., the surface-barrier current instability (SBCI).

Considering the processes causing the SBCI, it should be taken into account that samples with surface-barrier junctions (SBJ) in the absence of external factors already contain a local region of an intense electric field, which can be likened to the existence of a static domain (SD). The SD formation in the surface region of n-Ge and n-Si is caused by acceptor surface states. Within this concept, the CI is interpreted as periodic SD generation and destruction under the electric field [7].

An SD can be generated in a local surface region of an n-type semiconductor by diffusion of atoms that introduce deep acceptor levels into the SD band gap [9]. As in the case of an SD generated due to surface states and impurity atoms incorporated into the semiconductor surface layer, the SBCI is most simply, steadily, and controllably excited in structures representing a p^+–n junction distributed over the entire crystal area. In particular, this junction can represent a p^+–n epitaxial structure whose n-type region contains incorporated impurity atoms (active contact (AC)) [4, 9]. In such structures, the periodic SD destruction due to tunnel electron emission from impurity atoms and the initiation of instability are promoted by hole accumulation in the n-type region, which compensates the charge of electrons localized at deep acceptor levels. The periodic change in the hole concentration in the n-type region causes a parametric change in the barrier capacitance of the AC and the distributed p^+–n junction. This in turn initiates not only oscillations of the current flowing through the AC, but also intense voltage oscillations at the p^+–n junction [9, 10].

The promising application of the RCI microelectronic components arising in structures with a distributed p^+–n junction is confirmed by the development of pilot models of simple devices that efficiently convert an analog change in the emission, capacitance, voltage, and current into a repetition rate of electric pulses. The devices have several control channels and are charac-

† Deceased.

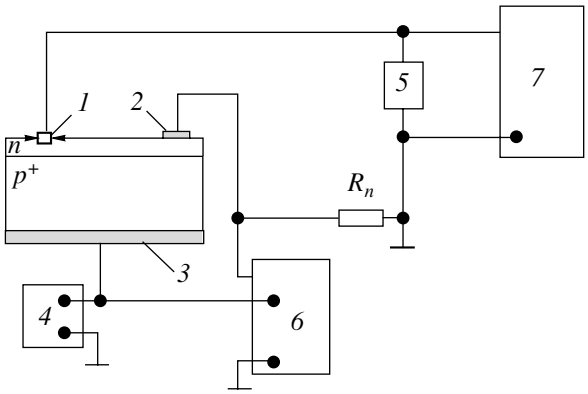

Fig. 1. Sample structure and measuring circuit: (*1*) local contact with impurity atoms incorporated into the *n*-type region (active contact), (*2*, *3*) ohmic contacts, (*4*, *5*) VU-15 voltmeters, (*6*) double-beam oscilloscope, (*7*) B5-9 power unit; R_n is the load resistor.

terized by a high input sensitivity, a strong output signal, and wide tuning ranges of current pulses and sawtooth voltage [4, 10, 11].

In [4, 9–11], the RCI in the structures with a distributed p^+–n junction was considered mainly from the viewpoint of the possibility of developing fundamentally new devices; the physical processes causing existence of the CI were not discussed in detail. Furthermore, the possibility of determining the parameters of deep centers (DC) (responsible for CI existence) by a periodic change in the impurity center charges was also not considered.

The aim of this study was to gain insight into physical processes that cause the RCI in silicon structures with an epitaxial p^+–n junction, whose *n*-type region contained an AC produced by local incorporation of impurity atoms, as well as to determine the density, energy position, and trapping cross section for DCs responsible for CIs.

2. RESULTS AND DISCUSSION

2.1. The samples were prepared by epitaxial growth of an *n*-type layer 10–15 μm thick (ρ = 2–4 Ω cm) on *p* regions (ρ = 10^{-2} Ω cm) of silicon structures. The AC incorporating tin, lead, and cadmium impurity atoms was produced by placing weighed portions (small balls 0.5 mm in diameter) of these materials onto the *n*-type region of the structure. After ion–plasma treatment of the structure in a vacuum chamber at 10^{-5} Torr, the structure was annealed at a temperature of 700–750°C for 15 min followed by 20-min cooling to 25°C. The contacts with incorporated nickel atoms were prepared by metal sputtering in vacuum onto the *n*-type region of the structure after preliminary ion–plasma treatment of its surface followed by annealing at 350°C for 0.5–1 h. The 0.5 × 0.5-mm ACs were formed using photolithography. The sample structure and the measuring circuit are shown in Fig. 1.

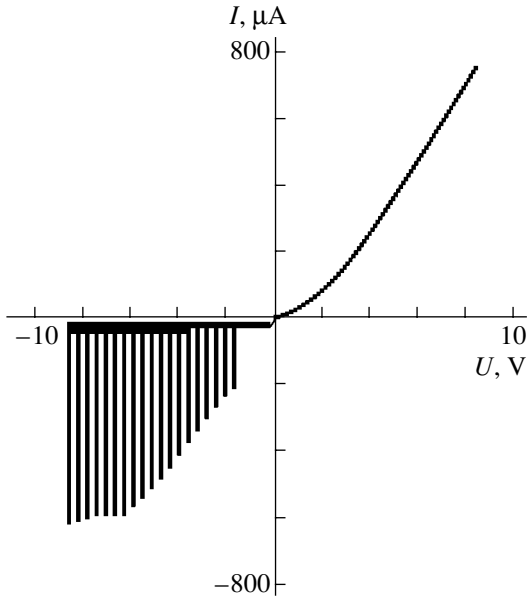

Fig. 2. Typical *I*–*V* characteristic of the active contact.

2.2. A typical current–voltage (*I*–*V*) characteristic of the AC at the open p^+–n junction is shown in Fig. 2. The specific feature of the *I*–*V* characteristic consists in the fact that intense pulsed current oscillations arise in the AC circuit starting with a certain reverse voltage U_{ac} (U_{ac} = 2–8 V for various samples) (see the typical spread in the *I*–*V* characteristic in Fig. 2). Simultaneously, high-amplitude sawtooth oscillations with respect to the base contact arise in the potential of the *p* region. Typical oscillograms of the AC current and p^+–n junction voltage are shown in Fig. 3.

The physical processes controlling the features of electrical characteristics of the structures were briefly considered in [4]. One of the most important processes promoting the structure features is the hole accumulation in the *n*-type region, stimulated by positive current and voltage feedbacks. This significantly changes the structure of the AC space charge and p^+–n junction region, in particular, it significantly narrows it.

We now consider the physical processes controlling the features of electrical properties of the structures. The energy-band diagram of a structure with a disconnected p^+ region at $U_a = 0$ and $U_a = U_{ac}$ and various time intervals (see Fig. 3) is shown in Fig. 4. As a reverse voltage U_a with respect to the base is applied to the AC at the open p^+–n junction, a negative gradient of the hole concentration over the base arises due to hole extraction from the base (contact 2 in Fig. 1) through the AC. As a result, the hole flow from the base to the p^+ region, which was in an equilibrium state, decreases and the hole counterflow from the p^+ region to the base becomes unbalanced. This circumstance gives rise to a hole current i_{p-n} from the p^+ region to the base (see Fig. 4a) and hole accumulation in the base, and the p^+

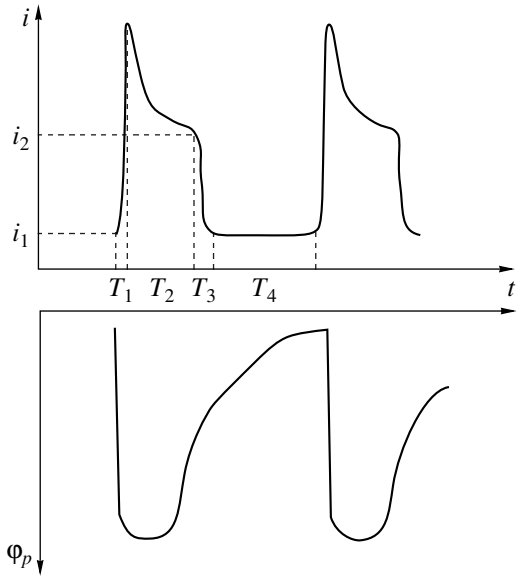

Fig. 3. Typical combined oscillogram of the current (top) and voltage (bottom) oscillations at the p^+–n junction.

region of the distributed p^+–n junction acquires a negative (floating) potential φ_p.

As is known, the emitter floating potential in ordinary transistors, arising when a reverse voltage is applied to the collector (when the emitter is open), does not exceed several tens of millivolts. In the structures under consideration, the value of φ_p at U_a = 3–15 V can be as large as 0.5–2 V. This is indicative of a significant increase in the hole concentration in the base, which is caused by a special feature of the structure "geometry" giving rise to some positive current feedback, which promotes minority carrier accumulation in the base, hence, an increase in φ_p. The higher rate (than in ordinary transistors) of hole accumulation in the structure base and in the AC space charge region (SCR) is promoted by the voltage drop across the distributed resistance of the base, which reaches several kiloohms in the structures under study. Since the p^+ region potential is independent of the coordinate due to the high conductivity ($10^2\ \Omega^{-1}\ \mathrm{cm}^{-1}$]) of this region, the potential along the distributed p^+–n junction changes as the current flows through the AC. The closer the distributed junction region to the AC, the smaller the negative value of φ_p, hence, the higher the excess concentration of carriers in the base. In the local region immediately under the AC, the value of φ_p can vanish or become positive. Thus, the voltage U_p arising at the p^+–n junction is caused by hole extraction by the AC from the base and the voltage drop across the distributed resistance of the base; the value of U_p depends on the voltage applied to the AC. The AC current increases with the hole concentration in the base; this causes an increase in U_p, which, in turn, causes Δp to increase; i.e., a positive current feedback arises, maintaining hole accumulation in the base. The processes causing the minority carrier accumulation in the structures with a distributed p^+–n junction are described in [4] in more detail.

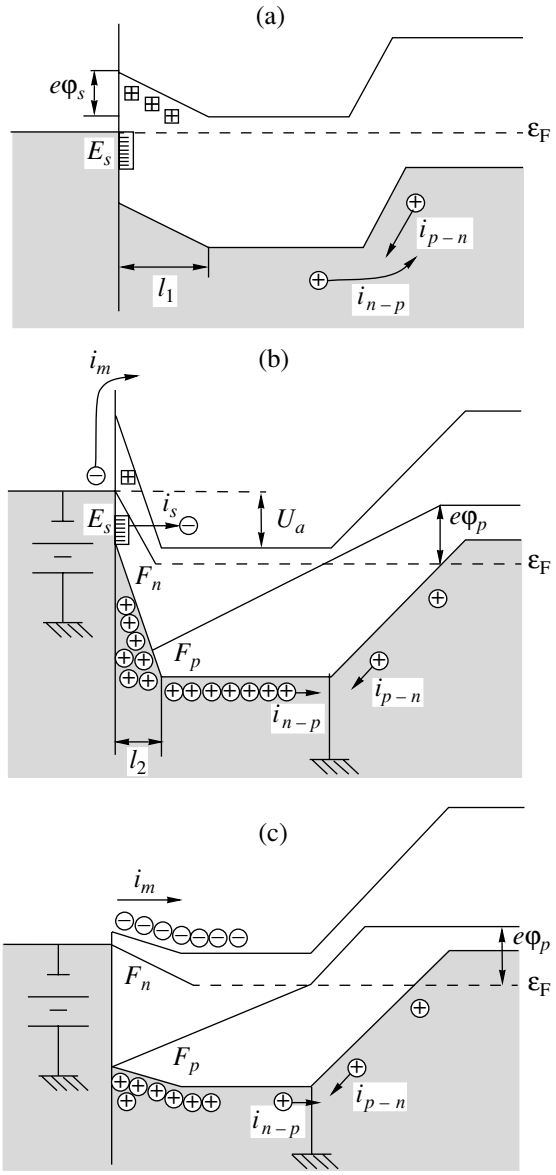

Fig. 4. Energy-band diagram of the structure at (a) $U_a = 0$, (b) $U_a = U_{ac}$, and $t = \tau_1$; (c) $U_a = U_{ac}$ and $t = \tau_3$; E_s are the energy levels of deep centers, $e\varphi_s$ is the barrier height, l_1 and l_2 is the barrier width, ε_F is the Fermi level, and F_n and F_p are the quasi-Fermi levels of electrons and holes.

It must be specially emphasized that the processes described are caused by the conditions for electroneutrality retention in each structure region and the equilibration of diffusion and drift currents through these regions, in particular, the equality of the currents i_{p-n} and i_{n-p}.

The increase in the hole concentration in the structure base is related to the processes considered above, narrows the SCR of the AC, and results in the strengthening of the AC field (Fig. 4b). At a certain critical volt-

Table

Impurity	N_s, cm^{-2}	E_s, eV	c_n, cm^2
Sn, Pb	5×10^{11}–10^{12}	0.17	5×10^{-14}–10^{-14}
Cd	10^{12}	0.45	10^{-14}
Ni	2×10^{11}	0.35	2×10^{-13}
Ni	10^{12}	0.95	5×10^{-14}

age (U_{ac} = 3–15 V for different samples) at the AC, the SCR tunneling breakdown caused by tunnel electron emission from the DCs controlling the AC potential barrier is observed. The AC tunneling breakdown mechanism was previously discussed in [8, 12] in detail and was directly confirmed by the experimental studies of AC capacitance–voltage characteristics [4]. Indeed, the AC SCR width (determined from the AC barrier capacitance measured at U_a values close to the breakdown voltage U_{ac}) narrows to 5×10^{-6}–10^{-5} cm due to hole accumulation. At an applied voltage of 3–15 V, the field in the SCR appears sufficient for tunnel electron emission from the DCs controlling the AC potential barrier (current i_s, see Fig. 4b). This lowers the barrier height and drastically increases the current from metal to the *n*-type region (current i_m, see Fig. 4c). As a result, the structure is transferred to the state shown in Fig. 4b. Then, as a result of recombination of excess electrons and holes, as well as trapping of electrons at DCs, after hole accumulation in the *n*-type region, the structure transforms (through the state shown in Fig.4a) into the state shown in Fig. 4b, etc. According to the studies carried out, the time intervals T_1–T_4 in various regions of the oscillograms shown in Fig. 3 correspond to the following times of the processes: τ_1 is the time of electron tunneling from DCs, τ_2 is the time of recombination of electrons emitted from DCs and metal with holes accumulated in the *n*-type region (and related SCR broadening), τ_3 is the time of electron trapping at DCs (and AC barrier restoration), and τ_4 is the time of hole accumulation in the *n*-type region up to the initial prebreakdown concentration (and a corresponding decrease in the SCR width).

2.3. A method for estimating the parameters of surface centers, creating the surface potential barrier in the metal–semiconductor contact, from the parameters of oscillations caused by the SBCI was briefly described in [13, 14]. In the case we studied, the surface potential barrier was also formed due to incorporated DCs; therefore, that method is also applicable to the samples under consideration.

As indicated above, the change in the oscillation current from i_1 to i_2 over the time τ_3 corresponds to DC charging. Since the current decrease in time is linear, the total charge localized under the AC is given by

$$q_s = \frac{i_2 - i_1}{2}\tau_3 \qquad (1)$$

and the surface density of centers is written as

$$N_s = \frac{q_s}{eS_a}, \qquad (2)$$

where S_a is the AC area.

The surface charge determined by the known solution to the Poisson equation for the surface region,

$$q_s = 2en_iL_D\left[\gamma^{-1}\exp\left(\frac{e\varphi_s}{kT}\right) - \gamma + \gamma\frac{e\varphi_s}{kT}\right]^{1/2}, \qquad (3)$$

makes it possible to calculate the barrier height φ_s. Then, knowing the energy position ε_F of the Fermi level in the *n*-type region, we can estimate the energy position E_s of the deep level in the semiconductor band gap,

$$E_s = e\varphi_s + \varepsilon_F, \qquad (4)$$

where n_i is the intrinsic concentration, L_D is the Debye length, $\gamma = n_n/n_i$, and n_n is the electron concentration in the *n*-type region of the structure.

The energy position of deep levels was also calculated on the basis of the field E_c corresponding to the initiation of tunnel electron emission from DCs and causing the onset of oscillations. The value of E_c was determined by the critical voltage U_c and the AC SCR width l_c (see Fig. 4),

$$E_c = \frac{U_c}{l_c}. \qquad (5)$$

The width l_c was calculated using the measured barrier capacitance of the AC. The level depth E_s was calculated by the relation derived in [12].

As is known, the time of the barrier capacitance response to an applied voltage significantly increases in the presence of DCs in the SCR [15]. Therefore, the barrier capacitance charging in the nonequilibrium mode over the time τ_3 (see Fig. 3) is related to the capacitance C_d calculated as

$$C_d = \frac{c_n u_n n_n \tau_3 N_s e S_a}{\varphi}, \qquad (6)$$

where c_n is the cross section of electron trapping at DCs and u_n is the thermal velocity of electrons [13, 14]. The capacitance C_d was measured using the technique described in [14], and c_n was calculated using Eq. (6).

The samples with an AC containing Sn, Pb, or Cd impurities were characterized by a single oscillation mode at critical voltages 4–4.5 V (Sn and Pb) and 8–8.5 V (Cd). Two oscillation modes at U_{ac1} = 4.5–5 V and U_{ac2} = 7–9 V were observed in the samples with an AC containing a nickel impurity. The first-mode oscillations had a rather small amplitude *i* of current oscillations (4–5 mA), whereas the values of *i* for the second mode reached 50 mA. This suggests that Ni atoms introduce two types of acceptor centers into the Si surface region. The DC parameters calculated by the tech-

nique described above are listed in the table (the level depth E_s is measured from the conduction band edge).

3. CONCLUSION

The studies carried out have ascertained that the special feature in the electric characteristics of the structures is caused in many respects by the accumulation of excess holes in the *n*-type region of the structure. The accumulation of a high hole concentration (10^{16}–10^{18}) in the *n*-type region is caused by the special features of the structure configuration and connection method (a reverse voltage is fed to the active contact of area 10^{-3}–10^{-5} cm^2; the p^+–n junction distributed over the whole sample area is open). This process takes place due to the necessity of maintaining a zero current through the p^+–n junction.

The holes accumulated in the *n*-type region significantly narrow the space-charge region of the active contact. Therefore, the tunnel emission from deep centers, which give rise to the potential barrier in the active contact and initiate oscillations, is observed at low voltages. This allows specific tunneling spectroscopy of the deep center parameters. The values of the parameters listed in the table correlate well enough with the known values [15]. It must be specially emphasized that two oscillation modes were observed in the nickel-based active contacts, since nickel atoms introduce two deep levels with a large cross section of electron trapping into the silicon band gap. This confirms the validity of the method considered as applied in determining the deep center parameters.

REFERENCES

1. A. A. Kokin, Mikroélektronika **20**, 424 (1991).
2. M. K. Bakhadyrkhanov, Kh. Azimkhuzhaev, N. F. Zikrillaev, *et al.*, Fiz. Tekh. Poluprovodn. (St. Petersburg) **34**, 177 (2000) [Semiconductors **34**, 171 (2000)].
3. M. K. Bakhadyrkhanov, U. Kh. Kurbanova, and N. F. Zikrillaev, Fiz. Tekh. Poluprovodn. (St. Petersburg) **33**, 25 (1999) [Semiconductors **33**, 20 (1999)].
4. B. S. Muravskiĭ, G. P. Rubtsov, L. R. Grigor'yan, and O. N. Kulikov, Zh. Radioélektron., No. 10 (2000); http://jre.cplire.ru/win/oct00/2/text.html.
5. B. A. Akimov, N. B. Brandt, A. V. Abdul, and L. I. Ryabova, Fiz. Tekh. Poluprovodn. (St. Petersburg) **31** (2), 197 (1997) [Semiconductors **31**, 100 (1997)].
6. Yu. K. Pozhela, *Plasma and Current Instabilities in Semiconductors* (Nauka, Moscow, 1976).
7. B. S. Muravskiĭ, V. I. Kuznetsov, G. I. Frizen, and V. N. Chernyĭ, Fiz. Tekh. Poluprovodn. (Leningrad) **6**, 2114 (1972) [Sov. Phys. Semicond. **6**, 1797 (1972)].
8. B. S. Muravskiĭ, V. N. Chernyĭ, I. L. Yamanov, *et al.*, Mikroélektronika **18**, 304 (1989).
9. B. S. Muravskiy and O. N. Kulikov, in *Proceedings of International Semiconductor Device Research Symposium* (Univ. of Virginia, 1999), p. 160.
10. L. R. Grigor'yan, B. S. Muravskiĭ, and I. L. Yamanov, in *Proceedings of International Forum on Problems in Science, Engineering, and Education* (Moscow, 1997), p. 48.
11. B. S. Muravskiy and L. R. Grigorian, in *Proceedings of 1997 International Semiconductor Device Research Symposium* (Univ. of Virginia, 1997), p. 233.
12. V. T. Doludenko and B. S. Muravskiĭ, Poverkhnost **18**, 28 (1985).
13. B. S. Muravskiĭ, Fiz. Tverd. Tela (Leningrad) **7**, 334 (1965) [Sov. Phys. Solid State **7**, 273 (1965)].
14. B. S. Muravskiĭ, Fiz. Tekh. Poluprovodn. (Leningrad) **11**, 1010 (1977) [Sov. Phys. Semicond. **11**, 601 (1977)].
15. A. G. Milnes, *Deep Impurities in Semiconductors* (Wiley, New York, 1973; Mir, Moscow, 1977).

Translated by A. Kazantsev

Semiconductors, Vol. 37, No. 4, 2003, pp. 380–383. Translated from Fizika i Tekhnika Poluprovodnikov, Vol. 37, No. 4, 2003, pp. 398–401.

ELECTRONIC AND OPTICAL PROPERTIES OF SEMICONDUCTORS

Optical Reflection in $(Pb_{0.78}Sn_{0.22})_{1-x}In_xTe$ Solid Solutions with a High Indium Content

A. N. Veĭs* and A. V. Nashchekin**

** St. Petersburg State Polytechnical University, St. Petersburg, 195251 Russia*

*** Ioffe Physicotechnical Institute, Russian Academy of Sciences, St. Petersburg, 194021 Russia*

Submitted June 3, 2002; accepted for publication September 6, 2002

Abstract—Optical reflectance spectra of $(Pb_{0.78}Sn_{0.22})_{1-x}In_xTe$ with a high indium content have been studied at $T = 300$ K. Spectral features related to composition heterogeneity in the solid solutions were revealed. An assumption has been made that these heterogeneities are manifested as systems of ordered "threads." Direct evidence of the existence of heterogeneities in $(Pb_{0.78}Sn_{0.22})_{1-x}In_xTe$ has been obtained by studying the surface morphology using optical and scanning electron microscopy. *© 2003 MAIK "Nauka/Interperiodica".*

The study of $(Pb_{0.78}Sn_{0.22})_{1-x}In_xTe$ solid solutions with a high indium content have lately attracted increasing interest owing to specific features of their electrical properties (see [1] and references therein). These features were explained in terms of hopping conduction via indium impurity states [1]. The model was based on the assumption [2] that all In atoms occupy equivalent sites in the $(Pb_{0.78}Sn_{0.22})_{1-x}In_xTe$ lattice (at the metal sublattice sites) and form a quasilocal level E_0. However, at $x \gtrsim 0.03$ the level is broadened due to the overlapping of wave functions of separate impurity atoms; a band of quasilocal states is formed which merges with the conduction band bottom at $x = 0.05$.

It is these assumptions that are inconsistent with the results obtained in studying optical absorption in the closest analogues of the solid solutions under study: $Pb_{1-x}In_xTe$ and $(Pb_{0.7}Sn_{0.3})_{1-x}In_xTe$ [3–5]. An analysis of data obtained in [3–5] shows that the solubility of indium impurity at the metal sublattice sites is not high, not exceeding several atomic percent. Moreover, no noticeable broadening of indium impurity bands was revealed up to $x = 0.09$ [3–5].

The results obtained in [3–5] lead to the assumption that the behavior of the solubility of In impurity in lead chalcogenides and their solid solutions is complex. This was first noticed in [6]. Therefore, it seemed appropriate to study the optical properties of $(Pb_{0.78}Sn_{0.22})_{1-x}In_xTe$ in detail to reveal specific features of the energy spectrum in a wide range of indium concentrations and to estimate the concentration of impurities at the metal sublattice sites. This information cannot be found in [7, 8], which were concerned with the optical properties of $(Pb_{0.78}Sn_{0.22})_{1-x}In_xTe$ with a lower x. The present communication reports the results obtained in a spectral study of the optical reflectance R.

The studied samples were fabricated by hot pressing and then homogenized by annealing in evacuated quartz cells at $T_a = 650°C$ for 100 h [9]. The typical size of grains was ~100 μm. The content of indium is given according to its amount in the stock. All of the indium-containing samples studied had *n*-type conduction. The electrical properties of such samples were investigated in [1]. For comparison, we have also studied a *p*-type In-free $Pb_{0.78}Sn_{0.22}Te$ sample with a Hall density of holes $p_H = 1.2 \times 10^{18}$ cm^{-3}. All the experiments were performed at the temperature $T = 300$ K.

The results of a study of the reflectance for $(Pb_{0.78}Sn_{0.22})_{1-x}In_xTe$ with a high indium content were more than unexpected. As seen in Fig. 1, two, rather than one, dips are observed in the experimental $R(\lambda)$ reflectance spectra for all the samples under study at the wavelengths $\lambda_1 = 1$–2 μm and $\lambda_2 = 25$–30 μm.

The nature of the long-wavelength dip in reflectance spectra was studied in [8]. It was established that this dip is related to plasma oscillations of free carriers. It was also shown that the insignificant depth of the plasma dip for $(Pb_{0.78}Sn_{0.22})_{1-x}In_xTe$ may be due to the combination of the small effective mass of free electrons and their low mobility, equal to ~100 cm^2 V^{-1} s^{-1} for the samples studied in [8].

Turning to the results of the present study, we must note that the spectral position of the long-wavelength dip does not change noticeably with increasing x (see Fig. 1). This means that the free electron density n is nearly the same in all samples. Indeed, estimates based on the assumptions made in [8] show that n lies in the range $(1.3–2.5) \times 10^{18}$ cm^{-3} for the samples studied, with an In content in the stock $x \geq 0.05$.

In contrast to the long-wavelength dip, a short-wavelength dip in reflectance has been observed for $(Pb_{0.78}Sn_{0.22})_{1-x}In_xTe$ for the first time. Its depth increases with rising x. However, $R(\lambda_1)$ values at the short-wavelength dip in reflectance for all the samples studied are close to corresponding experimental data

1063-7826/03/3704-0380$24.00

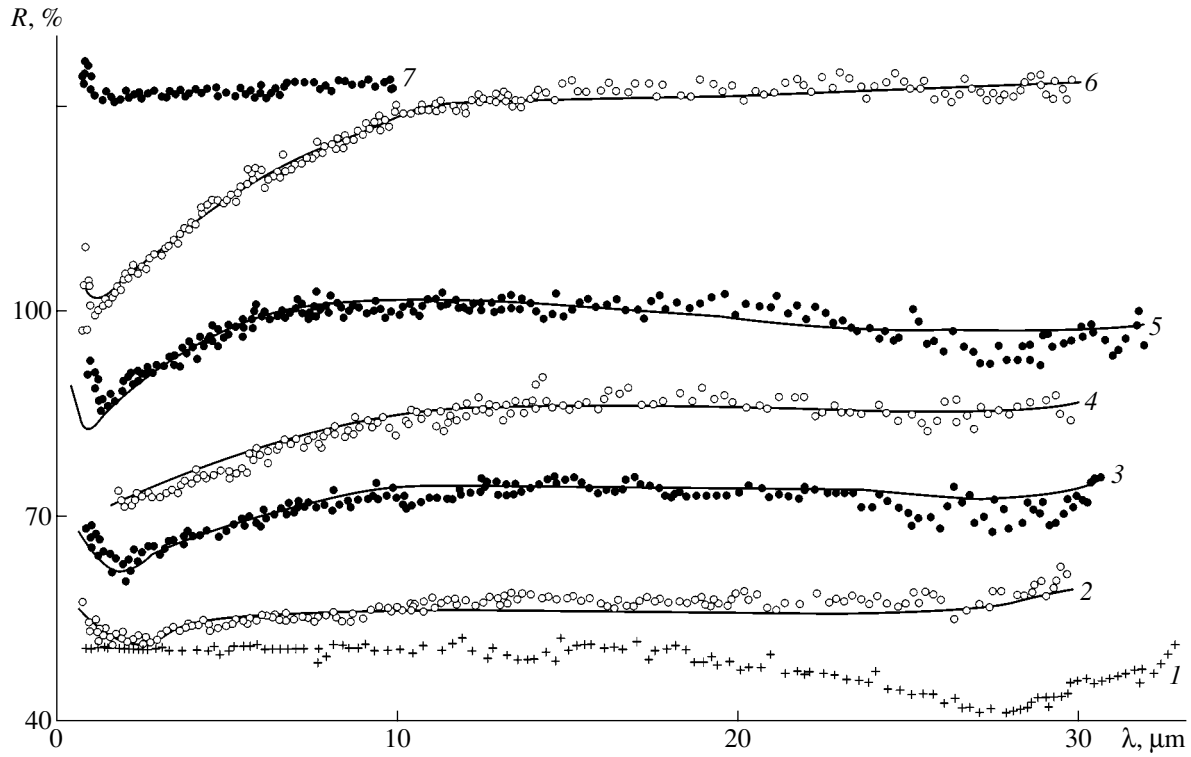

Fig. 1. Reflectance R spectra of $(Pb_{0.78}Sn_{0.22})_{1-x}In_xTe$ at T = 300 K. Points, experiment; x: (*1*) 0, (*2*) 0.05, (*3*) 0.07, (*4*) 0.10, (*5*) 0.15, (*6*) 0.20, and (*7*) 0.03. The dependence $R(\lambda)$ for sample 6 at $\lambda \geq 6$ μm was presented in [8]. Lines, calculation; period of the inductive grid: (*2*) 1.9, (*3*) 1.6, (*4*) 1.7, (*5*) 0.8, (*6*) 1.25 μm. For sample nos. *3–7*, R values are increased by 10, 20, 30, 50, and 80%, respectively.

for "pure" In-free $Pb_{0.78}Sn_{0.22}Te$ (curve *1* in Fig. 1). It is also worth noting that the variation of reflectance near the short-wavelength dip has resonance nature and R does not reach 100% in any of the samples.

These data lead to the conclusion that the short-wavelength dip in $R(\lambda)$ spectra is related to microinclusions with rather high conductivity. Taking into account the data of [10], we may suppose that these microinclusions either consist of indium or are enriched in indium. In this situation, the fraction of the sample surface, occupied by microinclusions, must increase with rising x.

Now we discuss possible mechanisms of the formation of the short-wavelength dip in reflectance. The most natural cause of its appearance in the $R(\lambda)$ spectrum might be plasma oscillations of free carriers inside the microinclusions. However, such a behavior of $R(\lambda)$ is not typical of metallic In. At the angle of incidence close to the normal, the reflectance of indium in the spectral range λ = 0.55–10.00 μm varies within 88.5–97.5% [11], which is due to the influence of interband transitions. We may assume, however, that the microinclusions are formed by an In-containing phase. In particular, an InTe (II) cubic phase demonstrates metallic properties [12]. However, in this case, again, problems arise when explaining the observed effects. Based on the structure of the experimental $R(\lambda)$ spectra in Fig. 1, one would assume that the contribution of microinclusions to the reflectance of $(Pb_{0.78}Sn_{0.22})_{1-x}In_xTe$ is close to zero in the range of the short-wavelength dip. This means (see [13]) that the carrier relaxation frequency in these heterogeneities may be substantially lower than the frequency of the probing radiation. In this case, according to [13], the rate of R variation in the experimental spectra at wavelengths longer than λ_1 must be significantly higher than that observed in the experiment.

Another possible reason for the appearance of the short-wavelength dip in the $R(\lambda)$ spectra may be the sufficiently regular arrangement of heterogeneities throughout the bulk (and, correspondingly, over the surface as well) of the samples under study. These may be impurity microinclusions in the form of "droplets" or "threads."

To the authors' knowledge, no theory exists which could describe optical properties of semiconductors with heterogeneities of this kind. It can be shown, nevertheless, that the obtained experimental data for $(Pb_{0.78}Sn_{0.22})_{1-x}In_xTe$ do not contradict this hypothesis. To do this, we can use the results of theoretical and experimental studies of infrared mesh filters [14, 15]. The comparison of the data presented in Fig. 1 with the data from [14, 15] shows that the optical properties of $(Pb_{0.78}Sn_{0.22})_{1-x}In_xTe$ in the range of the short-wave-

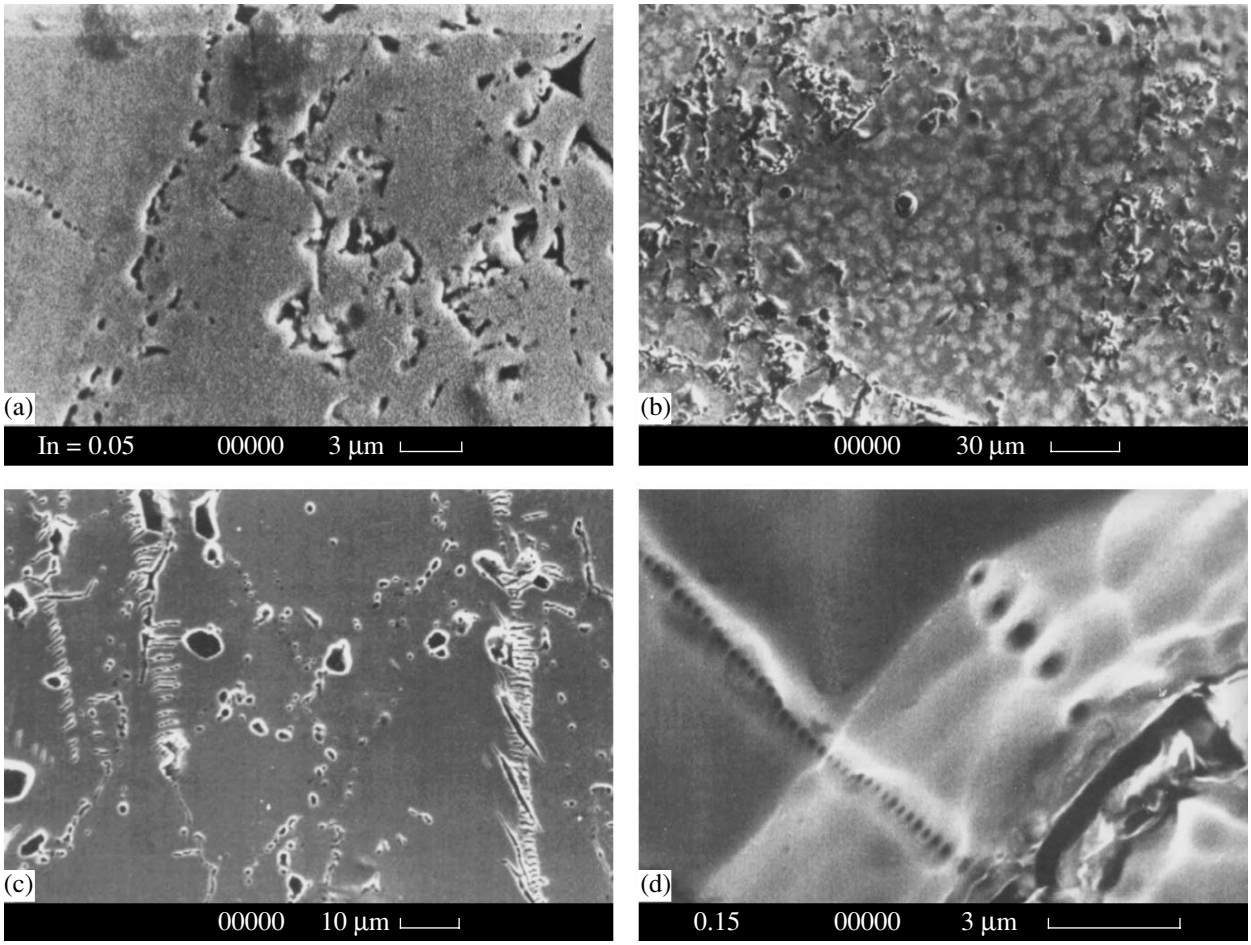

Fig. 2. SEM images of the $(Pb_{0.78}Sn_{0.22})_{1-x}In_xTe$ surface in the reflection mode. *x*: (a) 0.05, (b) 0.20, (c) 0.03, and (d) 0.15.

length dip are similar to those of an inductive grid. This leads to the assumption that the heterogeneities can form regular threads on the sample surface. This is also confirmed by the calculation of the $R(\lambda)$ spectrum on the assumption of additivity of contributions made to the reflectance R by $(Pb_{0.78}Sn_{0.22})_{1-x}In_xTe$ (R_2) and heterogeneities (R_1), in accordance with the relation $R = R_2 + \beta R_1$ (β is a fitting coefficient on the order of unity). The R_2 components were calculated by the method described in detail in [8], and, for R_1, we used the relations for the reflectance of inductive grids listed in Table 3 of [5].

The calculated data are represented by lines in Fig. 1. Satisfactory agreement between experiment and theory is observed. This indicates that the short-wavelength dip in the reflectance spectrum of $(Pb_{0.78}Sn_{0.22})_{1-x}In_xTe$ may be due to a regular arrangement of heterogeneities in the bulk (and on the surface) of the studied samples.

To obtain direct evidence of the existence of heterogeneities, we applied optical and scanning electron microscopy (SEM) to study the surface of $(Pb_{0.78}Sn_{0.22})_{1-x}In_xTe$. To reveal the specific features, the sample surfaces were treated with a polishing etchant based on potassium ferrocyanide. The composition of the etchant and the procedure for its application were described in detail in [16].

The pattern of heterogeneities observed in $(Pb_{0.78}Sn_{0.22})_{1-x}In_xTe$ appear to be much more complicated than what might have been supposed based on an analysis of the reflectance spectra. First, dark and bright areas were revealed on the sample surface by SEM in the reflection mode (Figs. 2a, 2b). We believe that this contrast results from differences in atomic numbers, with the dark and bright areas attributed to phases enriched in light and heavy elements, respectively. Second, unusual topographic defects were found on the sample surface in the form of systems of parallel grooves (Fig. 2c) or pores (Fig. 2d) stretched into lines up to 170 μm long. We do not exclude that these specific features of the $(Pb_{0.78}Sn_{0.22})_{1-x}In_xTe$ surface morphology could belong to a single type of linear defects with different orientations in the sample bulk. It is necessary to note that various regularly arranged linear defects on the $(Pb_{0.78}Sn_{0.22})_{1-x}In_xTe$ surface, including those shown in Fig. 2c, were also observed by optical microscopy.

The study of specific features of the $(Pb_{0.78}Sn_{0.22})_{1-x}In_xTe$ surface morphology has shown that these solid solutions are heterogeneous; i. e., they contain phases of different compositions. The data on $R(\lambda)$ spectra also lead to the assumption that ordered systems of heterogeneities exist in the samples under study. However, direct experimental evidence confirming this assumption has not yet been obtained.

ACKNOWLEDGMENTS

We are grateful to S.A. Nemov, who presented study samples, and to V. A. Zykov, for helpful consultations concerning the treatment of the sample surface.

REFERENCES

1. S. A. Nemov and Yu. I. Ravich, Fiz. Tekh. Poluprovodn. (St. Petersburg) **36**, 3 (2002) [Semiconductors **36**, 1 (2002)].
2. V. I. Kaĭdanov and Yu. I. Ravich, Usp. Fiz. Nauk **145**, 51 (1985) [Sov. Phys. Usp. **28**, 31 (1985)].
3. A. N. Veĭs, V. I. Kaĭdanov, Yu. I. Ravich, *et al.*, Fiz. Tekh. Poluprovodn. (Leningrad) **10**, 104 (1976) [Sov. Phys. Semicond. **10**, 62 (1976)].
4. T. V. Bocharova, A. N. Veĭs, Z. M. Dashevskiĭ, *et al.*, Fiz. Tekh. Poluprovodn. (Leningrad) **15**, 175 (1981) [Sov. Phys. Semicond. **15**, 103 (1981)].
5. T. V. Bocharova, A. N. Veĭs, N. A. Erasova, and V. I. Kaĭdanov, Fiz. Tekh. Poluprovodn. (Leningrad) **16**, 1462 (1982) [Sov. Phys. Semicond. **16**, 933 (1982)].
6. A. J. Rosenberg, R. Grierson, J. C. Woolley, and P. Nicolič, Trans. Metall. Soc. AIME **230**, 342 (1964).
7. A. N. Veĭs, Fiz. Tekh. Poluprovodn. (St. Petersburg) **36**, 183 (2002) [Semiconductors **36**, 176 (2002)].
8. A. N. Veĭs and S. A. Nemov, Fiz. Tekh. Poluprovodn. (St. Petersburg) **32**, 1047 (1998) [Semiconductors **32**, 937 (1998)].
9. S. A. Nemov, Yu. I. Ravich, A. V. Berezin, *et al.*, Fiz. Tekh. Poluprovodn. (St. Petersburg) **27**, 299 (1993) [Semiconductors **27**, 165 (1993)].
10. G. A. Kalyuzhnaya and K. V. Kiseleva, Tr. Fiz. Inst. im. P. N. Lebedeva, Akad. Nauk SSSR **177**, 5 (1987).
11. G. P. Motulevich, Tr. Fiz. Inst. im. P. N. Lebedeva, Akad. Nauk SSSR **55**, 3 (1971).
12. M. D. Banus, R. E. Hanneman, M. Strongin, and K. Gooen, Science **142**, 662 (1963).
13. M. N. Noskov, *Optical and Magneto-Optical Properties of Metals* (UNTs Akad. Nauk SSSR, Sverdlovsk, 1983).
14. J. P. Casey and E. A. Lewis, J. Opt. Soc. Am. **42**, 971 (1952).
15. R. Ulrich, Infrared Phys. **7**, 37 (1977).
16. V. V. Robzerov, V. A. Zykov, and T. A. Gavrikova, Neorg. Mater. **36**, 177 (2000).

Translated by D. Mashovets

Semiconductors, Vol. 37, No. 4, 2003, pp. 384–389. Translated from Fizika i Tekhnika Poluprovodnikov, Vol. 37, No. 4, 2003, pp. 402–407.

ELECTRONIC AND OPTICAL PROPERTIES OF SEMICONDUCTORS

Effect of Lattice Deformation on Semiconducting Properties of $CrSi_2$

A. V. Krivosheeva*, V. L. Shaposhnikov, A. E. Krivosheev, A. B. Filonov, and V. E. Borisenko

Belarussian State University of Informatics and Radioelectronics, Minsk, 220013 Belarus

**e-mail: anna@nano.bsuir.edu.by*

Submitted September 2, 2002; accepted for publication September 6, 2002

Abstract—The effect of isotropic and anisotropic deformation on electronic and optical properties of semiconducting chromium disilicide $CrSi_2$ is studied by the method of augmented plane waves. The compound is found to be an indirect-gap semiconductor with a band gap width of about 0.3 eV. It is found that the deformation affects the transitions similarly; however, for anisotropic deformation this effect is strongly nonlinear, and the stretching of the lattice up to 106% along the axis *a* results in the occurrence of a direct transition.

1. INTRODUCTION

The increasing attention being given to transition-metal silicides in recent years is caused by the possibility of their use in silicon technology. The majority of such compounds are metallic, and only a few of them are semiconductors. The latter are mostly Si-enriched silicides of the metals of Groups VI and VIII. These materials are attractive due to their compatibility with Si technology and have high thermal and chemical stability. Chromium disilicide $CrSi_2$ is the most studied representative of this type of semiconductors [1]. The potential possibility of its application for optoelectronic elements in the IR region, as well as insignificant—in contrast to other silicides of high-melting metals –mismatch of lattice parameters of $CrSi_2$ and Si (0.14% at the orientation $CrSi_2(0001)/Si(111)$ [2, 3]) stimulated attempts to epitaxially grow thin films of this silicide on Si substrate [4, 5]. However, the stresses arising in the course of epitaxial growth can result in displacement of atoms from their equilibrium sites, i.e. in the lattice deformation of contacting materials, which, in turn, can change the band structure of a material.

In this paper, the results of calculations of the band structure and optical properties of semiconducting chromium disilicide with a strained crystal lattice are presented. In studying this problem, we considered both isotropic (i.e. uniform along all directions) and anisotropic (uniaxial) deformation.

2. METHOD

Chromium disilicide has a hexagonal structure *C*40 described by space group $P6_222(D_6^4)$. Its unit cell contains three formula units with three crystallographically equivalent sites for chromium atoms and six sites for silicon atoms. The spread in experimental values for lattice parameters *a* and *c* can be explained by the possible variation in composition within the range from $CrSi_{1.98}$ to $CrSi_{2.02}$. The most appropriate values of the parameters for stoichiometric $CrSi_2$ are $a = 0.4428$ nm and $c = 0.6369$ nm [1].

In this study, the electronic and optical properties of $CrSi_2$ were investigated in terms of the theory of a local density functional, i.e. by the first-principle self-consistent method of linear augmented plane waves with the use of the generalized gradient approximation [6]. As a rule, local density functional methods underestimate the gap energy in semiconductors. The magnitude of error depends on the shift of the energy eigenvalues due to the so-called correlation effects. However, if the extrema in the conduction and valence bands are formed by the same orbital components, as takes place in most silicides of transition *d* metals, the above method demonstrates not only good qualitative but also reasonable quantitative agreement with the experimental data. The results of calculations of the electronic properties of silicides obtained in [7–11] support this fact.

The matching procedure in this study was performed using 198 *k* points uniformly distributed in the irreducible part of the Brillouin zone (2000 *k* points in the entire cell). The electron density of states and optical functions were calculated on a grid consisting of 280 *k* points. The number of *k* points for the band structure calculations was varied from 10 to 20 along each high-symmetry direction. The radius of the "muffin-tin" sphere R_{MT} was taken to be equal to 2.0 au, and the

1063-7826/03/3704-0384$24.00

convergence parameter $R_{MT}K_{max}$ was equal to 8 (K_{max}^2 is the boundary condition for the choice of plane waves in the calculation of pseudopotentials, the so-called plane-wave cutoff parameter). The wave function expansion in terms of lattice harmonics for partial waves within atomic spheres was performed up to $l = 10$. The cycles of self-consistency were completed when the difference between total energies of the system for two succeeding iterations became smaller than 0.0001 Ry/atom.

The main characteristic in the theoretical simulation of optical properties of compounds is a complex dielectric function consisting of real ε_1 and imaginary ε_2 parts. Calculation begins with the determination of the imaginary part of the dielectric function ε_2 [12]:

$$\varepsilon_2(\omega) = \frac{8\pi^2 e^2}{m^2\omega^2}\sum_{n\neq n'}\sum_{n'}\int_{\Omega}|P_{nn''}(\mathbf{k})|^2 \times \delta(E_n^k - E_{n'}^k - \hbar\omega)\frac{d^3\mathbf{k}}{(2\pi)^3}. \quad (1)$$

The interband contributions to the imaginary part of the dielectric function were calculated in a random-phase approximation based on the matrix element of transition probability. The integration was performed over all states in the Brillouin zone Ω, where $P_{nn'}(\mathbf{k})$ in Eq. (1) is the projection of the dipole matrix element onto the Cartesian directions of the electric field. The transitions occur between the valence band n and conduction band n'. The real part of the dielectric function (ε_1) was calculated using the Kramers–Kronig relation

$$\varepsilon_1(\omega) = 1 + \frac{2}{\pi}P\int_0^{\infty}\frac{\varepsilon_2(\omega')\omega' d\omega'}{\omega'^2 - \omega^2}, \quad (2)$$

where P is the principal integral value, $P\int_0^{\infty} = \lim_{a\to 0}\left(\int_0^{\omega-a} + \int_{\omega+a}^{0}\right)$.

Isotropic and axial tension/compression were simulated by changes in the lattice parameters. At first, the band structure of chromium disilicide with an undeformed lattice was calculated. Next, the effect of tension and compression of the lattice in chromium disilicide on its electronic and optical properties under isotropic and axial strains was studied.

For studying isotropic tension and compression, the lattice parameters a and c were correspondingly gradually increased and decreased in the range 94–106% from their initial values (a_0 and c_0) with a step of 1%. The effect of uniaxial deformation was studied along the [0001] direction. This is the most promising direction from the standpoint of epitaxial growth of $CrSi_2$ films on Si substrate with an orientation in the (111) plane [4]. In contrast to isotropic deformation, uniaxial deformation changes the shape of a unit cell; therefore, the simulation requires data on the elastic properties of a material subjected to deformation. Since experimental data on the elastic constant for $CrSi_2$ are unavailable, the lattice parameters of deformed material were determined from the minimization of the total energy of the system. During this procedure, the lattice constant a was varied with the same step as for isotropic deformation, while the parameter c was varied with the aim of finding the value corresponding to the minimum of the total energy of the system. Figure 1 shows the variation of the total energy of the system E_{tot} as a function of the value of c. Numerical values of the optimized lattice parameters a and c used for further calculations and corresponding to the minimum of the total energy of the structure under consideration are listed in the table.

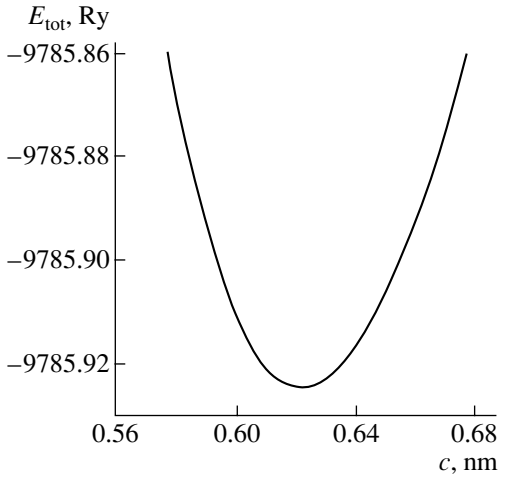

Fig. 1. The effect of variation of lattice parameter c on the total energy E_{tot} of a system.

Optimized values of lattice parameters at uniaxial deformation

a/a_0, %	a, nm	c, nm
94	0.4165	0.6525
95	0.4209	0.6769
96	0.4254	0.6537
97	0.4298	0.6482
98	0.4342	0.6424
99	0.4387	0.6363
100	0.4431	0.6364
101	0.4475	0.6301
102	0.4520	0.6297
103	0.4564	0.6227
104	0.4608	0.6237
105	0.4653	0.6321
106	0.4697	0.6230

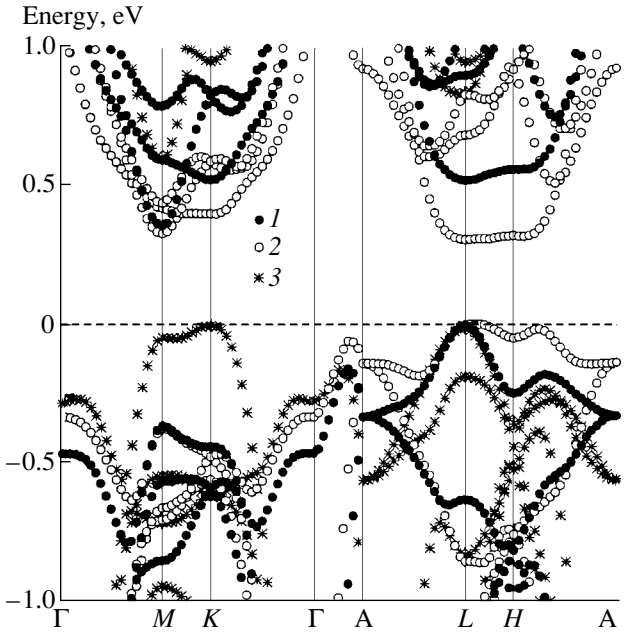

Fig. 2. Energy-band structure of $CrSi_2$ with (*1*) undeformed lattice, (*2*) with uniaxially stretched lattice along the *a* axis to 106%, and (*3*) with uniaxially compressed lattice along the *a* axis to 94%.

3. RESULTS

The energy-band diagram for $CrSi_2$ with an undeformed and uniaxially deformed crystal lattice is shown in Fig 2. The band structure of chromium disilicide under isotropic deformation qualitatively reproduces the features of the band structure of the undeformed compound. Therefore, we will not discuss in detail the former structure. Anisotropic deformation profoundly affects the properties of a material and will be considered in greater detail.

3.1. Properties of an Undeformed Material

In this subsection, the electronic properties of an undeformed material will be analyzed. Points *1* in Fig. 2 correspond to the undeformed material. Chromium disilicide is an indirect gap semiconductor with a band gap of about 0.35 eV, which is formed between extrema of the 21st and 22nd bands at the points *L* and *M* of Brillouin zone. The Fermi level coincides with the valence band top. At point *L* the compound has a direct gap with an energy of ~0.52 eV. The data obtained for undeformed material are in good agreement with other theoretical calculations and experimental studies [11–13]. This suggests that the simulation of a strained structure of $CrSi_2$ should correctly describe the real behavior of the properties of this semiconductor.

An analysis of the density of states (Fig. 3) shows that the low-energy part of the valence band is primarily characterized by the *s* states of silicon. Close to the

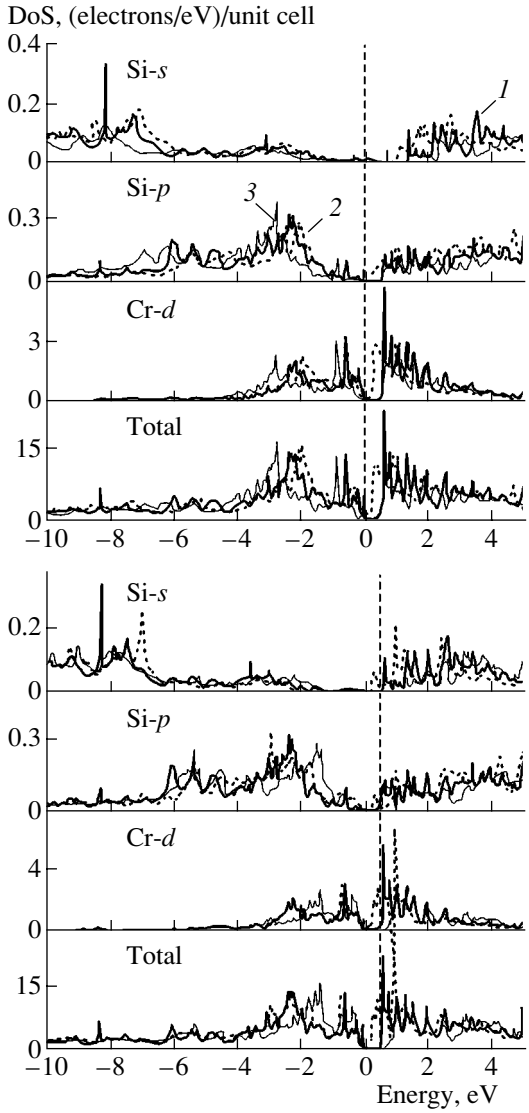

Fig. 3. Density of states (DoS) in $CrSi_2$ under isotropic (top) and anisotropic (bottom) deformations: (*1*) undeformed lattice, (*2*) stretched to 106% lattice, and (*3*) compressed to 94% lattice.

Fermi level, the hybridization of the *p* states of silicon with the *d* states of chromium takes place, while the conduction band is formed mainly by the *d* states of chromium. It is precisely because the extrema of the valence and conduction bands are almost completely (up to 97%) formed by the *d*-sates of chromium that good agreement for the energy gaps with the experiment can be attained. As a consequence, there is no need for introducing correlation corrections for matching the experimental data, since the eigenvalues of functions at the points of extrema undergo almost the same correlation shift [7, 9]. The contribution of *d* orbitals of silicon, as well as *s* and *p* orbitals of chromium, is negligible within the energy range under study, and thus the distribution of their density of states is not shown in Fig. 3.

3.2. Properties of Deformed Material

The data on energy gaps obtained for isotropic deformation as a function of the lattice parameter are shown in Fig. 4. The isotropic stretching of the $CrSi_2$ lattice along all directions affects the dispersion of bands and results in lowering the energy both for indirect *L*–*M* and direct *L*–*L* transitions. In the course of such deformation, the upper valence and lower conduction bands decrease in slope, and the extrema of the bands become less pronounced. Such "smoothing" of bands makes the energy of the direct *L*–*L* transition almost equal to the energy of a nearby indirect *L*–*H* transition; i.e., a flat portion between the *L* and *H* points in the conduction band is formed. Isotropic compression of the unit cell of chromium disilicide, in turn, results in an increase in the transition energies.

As is evident from Fig. 3, the lattice compression shifts (compared with undeformed material) the basic peaks of the density of states into the valence band, while the stretching shifts them into the conduction band. This is indicative of a reduction of the probability of electron transition to the conduction band during compression and of an increase of this probability at stretching, which manifests itself in the corresponding increase and decrease in the intensity of basic transitions. It is significant that the dependences representing the effect of isotropic deformation on the intensity of the transitions under consideration are virtually linear.

Uniaxial deformation profoundly affects both the valence and conduction bands. This effect is most pronounced in the case of compression when the energy of the Fermi level increases with growing pressure under compression and decreases under stretching. The change in the position of the Fermi level causes a considerable shift of bands with respect to their position in undeformed material. A lattice compression up to 95% shifts the top of the valence band from the point *L* to the point *K*; i.e., it is the *K*–*M* and *K*–*K* transitions that now become indirect and direct transitions, respectively. Stretching of the lattice by more than 5% percent from the initial state makes the *L*–*L* transitions dominant over the *L*–*M* transitions; i.e., $CrSi_2$ becomes a direct gap semiconductor with an energy gap of about 0.31 eV. In this case, the first conduction band and, to a lesser extent, the upper valence band become virtually flat in the direction *L*–*H*. The dependences of energies of direct and indirect transitions on the parameter *a* under anisotropic deformation are shown in Fig. 4. Obviously, the tendencies in the variation of gaps are similar to those taking place under isotropic deformation; however, the dependences are markedly nonlinear. Such behavior is caused by a more complex deformation accompanied by an increase in the interatomic distance within the (0001) plane and its simultaneous reduction in the perpendicular direction. A similar behavior of transition energies was also observed in magnesium silicide MgSi in [14]; there it was shown that isotropic compression of a lattice causes a linear increase in the energy of direct and indirect transitions, whereas, for anisotropic deformation, the corresponding dependences are nonlinear.

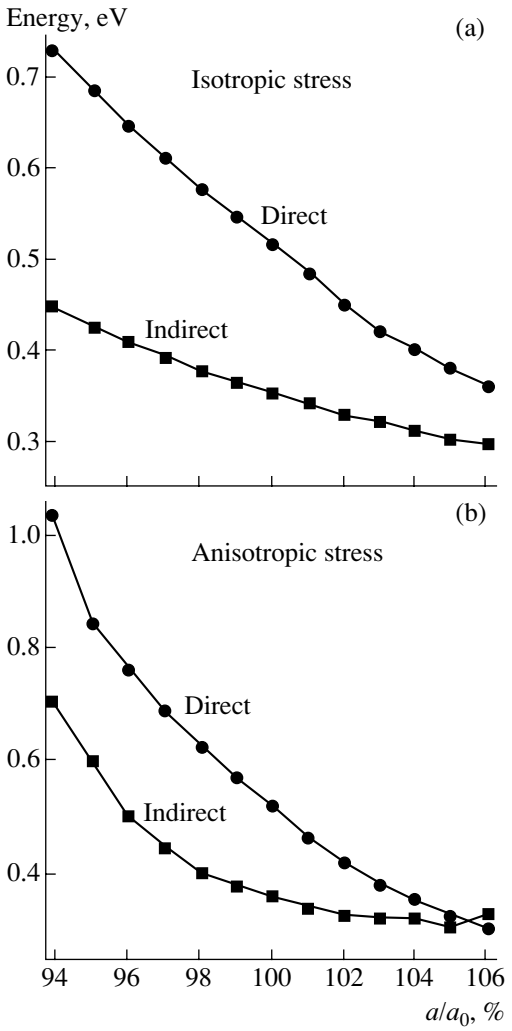

Fig. 4. Variations in basic direct and indirect electron transitions under the effect of (a) isotropic and (b) anisotropic deformations.

The changes in band structure affect the spectra of the total and partial density of states (Fig. 3). Uniaxial deformation results in a shift of the basic peaks for different crystallographic directions. It should be mentioned that compression of the lattice mostly affects the states of the valence band, while lattice stretching mostly affects the states of the conduction band. The shift of the basic peaks reflects variations in energy gaps, while the change in their shapes is related to the differences in the dispersion of bands. Analysis shows that the orbital composition of wave functions in the extrema of bands changes insignificantly under the anisotropic deformation of the lattice. Both the valence

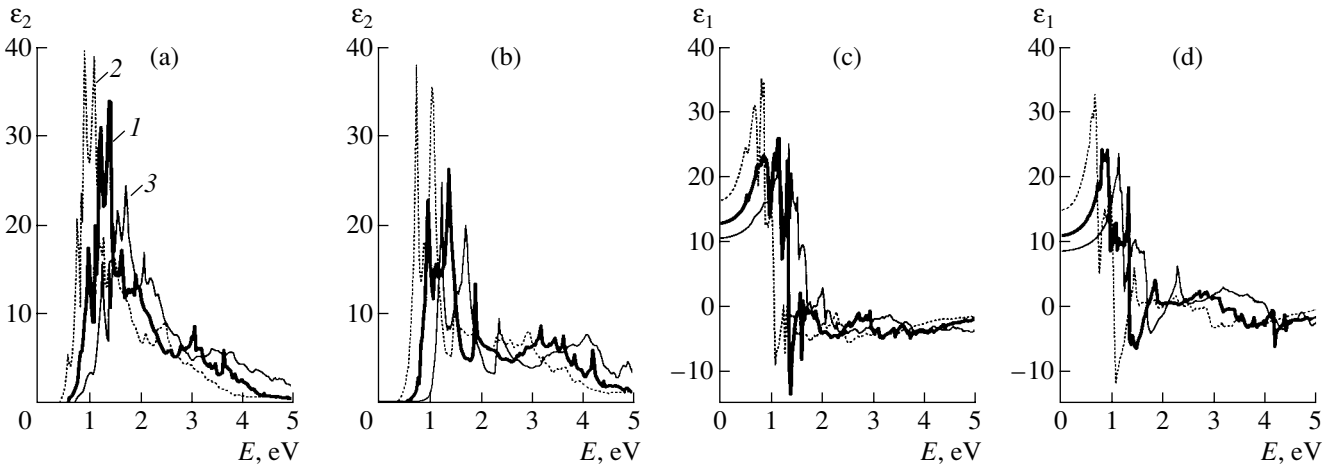

Fig. 5. Variations in (a, b) imaginary and (c, d) real parts of dielectric function for $CrSi_2$ along (a, c) the *a* axis and (b, d) the *c* axis under the isotropic lattice deformation: (*1*) undeformed lattice, (*2*) stretched to 106% lattice, and (*3*) compressed to 94% lattice.

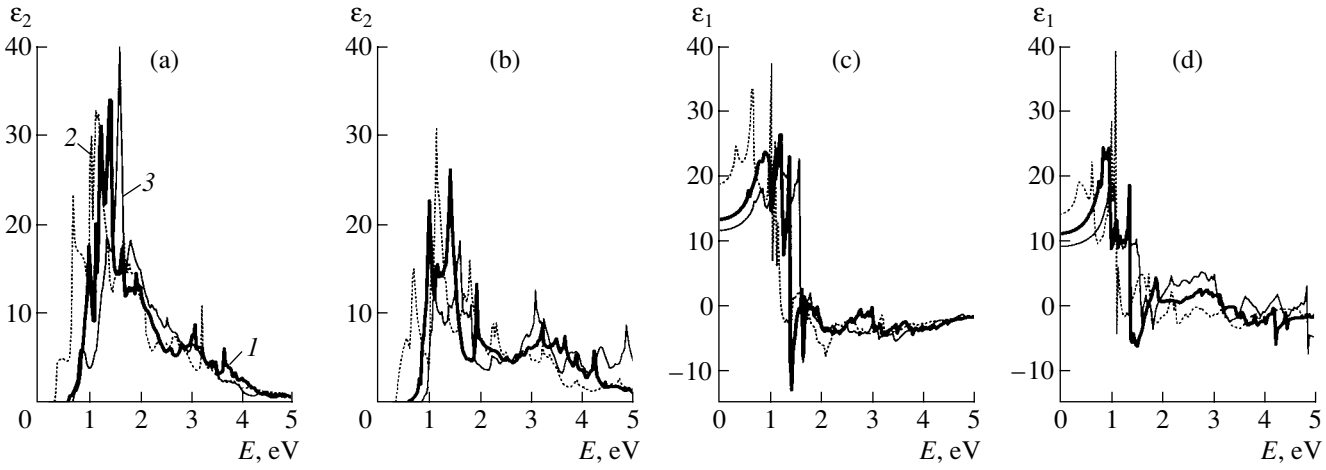

Fig. 6. Variations in (a, b) imaginary and (c, d) real parts of dielectric function for $CrSi_2$ along (a, c) the *a* axis and (b, d) the *c* axis under the uniaxial lattice deformation: (*1*) undeformed lattice, (*2*) stretched to 106% lattice, and (*3*) compressed to 94% lattice.

band top and the conduction band bottom are formed almost entirely by the *d* electrons of chromium.

The optical properties of $CrSi_2$ determined by the imaginary (ε_2) and real (ε_1) parts of the dielectric function in relation to photon energies *E* for two directions of light polarization are shown in Figs. 5 and 6. Good correlation between experimental [12] and theoretical data obtained in this study is evident from Fig. 7. As was mentioned above, of greatest interest for applications in optoelectronics is the uniaxial tension which transforms chromium disilicide into a direct gap semiconductor. In this case, the range where the imaginary part of the dielectric function (ε_2) begins to increase corresponds to the first direct transition at the point *L*. The first peak is formed by the transitions from the upper valence band to the first conduction band in the *L–H* direction. The peaks near 0.8 eV are formed due to the transitions in the direction *M–K* with a higher intensity. Analysis of the optical matrix element allows one to conclude that the probability of the first direct transition at the point *L* is extremely low (by two orders of magnitude lower than the transition probability along the *M–K* direction). The former probability does not increase either under isotropic or under uniaxial deformation of $CrSi_2$. This inference is supported by an analysis of the orbital composition of the wave functions in the extrema of the bands. According to this analysis, the transition formed mainly by the *d* electrons of chromium (95%) should be forbidden in the dipole approximation. The first intense peak at the level of 0.35 eV in a direct gap material seems to arise due to the increase in the density of states in this energy range. Lattice stretching increases the amplitude of the basic peak of the imaginary part of the dielectric function if the polarized light is directed along the *c* axis, and reduces this amplitude under isotropic or anisotropic compression.

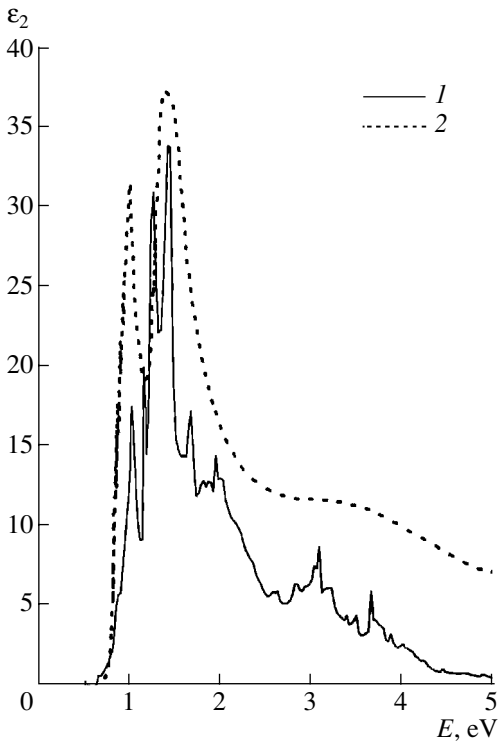

Fig.7. (1) Calculated and (2) experimental spectra of the imaginary part of dielectric function along the *a* axis for unstrained $CrSi_2$.

The variation in ε_2 along the *c* axis is more complex: isotropic compression and anisotropic stretching decrease the amplitude of the basic peak, while isotropic stretching and anisotropic compression increase this amplitude. Such distinctions are likely caused by the fact that, under anisotropic deformation, the compression of the lattice along one of the directions causes the stretching of the lattice in the other direction.

4. CONCLUSION

Changes in the energies of electron bands in semiconducting chromium disilicide are controlled by the type of deformation of its lattice. Isotropic lattice deformation is accompanied by a linear change in the transition energies, and chromium disilicide remains an indirect gap semiconductor. Uniaxial deformation causes more complicated transformations, e.g., under the stretching of the lattice along the *c* axis up to 106%, the direct transition becomes dominant. Analysis of optical properties confirms the small intensity of the direct transition and the low probability of its increase during lattice deformation.

REFERENCES

1. *Semiconducting Silicides*, Ed. by V. E. Borisenko (Springer, Berlin, 2000).
2. F. Y. Shiau, H. C. Cheng, and L. J. Chen, J. Appl. Phys. **59**, 2784 (1986).
3. H. Lange, Phys. Status Solidi B **201**, 3 (1997).
4. N. G. Galkin, T. A. Velichko, S. V. Skripka, and A. B. Khrustalev, Thin Solid Films **280**, 211 (1996).
5. N. G. Galkin, A. M. Maslov, S. I. Kosikov, A. O. Talanov, and K. N. Galkin, in *Physics, Chemistry and Application of Nanostructures: Reviews and Short Notes to NANOMEETING-2001* (World Sci., Singapore, 2001), p. 190.
6. P. Blaha, K. Schwarz, and J. Luitz, in *WIEN97* (Vienna Univ. of Technology, 1997) [Improved and updated Unix version of the original copyright WIEN code: P. Blaha, K. Schwarz, P. Sorantin, and S. B. Trickey, Comput. Phys. Commun. **59**, 399 (1990)].
7. A. B. Filonov, D. B. Migas, V. L. Shaposhnikov, *et al.*, Phys. Rev. B **60**, 16494 (1999).
8. A. B. Filonov, D. B. Migas, V. L. Shaposhnikov, *et al.*, Europhys. Lett. **46**, 376 (1999).
9. A. B. Filonov, D. B. Migas, V. L. Shaposhnikov, *et al.*, Appl. Phys. Lett. **70**, 796 (1997).
10. A. B. Filonov, D. B. Migas, V. L. Shaposhnikov, *et al.*, J. Appl. Phys. **79**, 7708 (1996).
11. A. B. Filonov, I. E. Tralle, N. N. Dorozhkin, *et al.*, Phys. Status Solidi B **186**, 209 (1994).
12. V. Bellani, G. Guizetti, F. Marabelli, *et al.*, Phys. Rev. B **46**, 9380 (1992).
13. M. C. Bost and J. E. Mahan, J. Appl. Phys. **63**, 839 (1988).
14. A. V. Krivosheeva, A. N. Kholod, V. L. Shaposhnikov, *et al.*, Fiz. Tekh. Poluprovodn. (St. Petersburg) **36**, 528 (2002) [Semiconductors **36**, 496 (2002)].

Translated by A. Zalesskiĭ

Semiconductors, Vol. 37, No. 4, 2003, pp. 390–395. Translated from Fizika i Tekhnika Poluprovodnikov, Vol. 37, No. 4, 2003, pp. 408–413.

ELECTRONIC AND OPTICAL PROPERTIES OF SEMICONDUCTORS

Electrical Properties of InAs Irradiated with Protons

V. N. Brudnyĭ*, N. G. Kolin, and A. I. Potapov***

** Kuznetsov Physicotechnical Institute, pl. Revolyutsii 1, Tomsk, 634050 Russia*

e-mail: brudnyi@ic.tsu.ru

*** State Research Center at the Karpov Institute of Physical Chemistry (Obninsk Branch), Obninsk, Kaluga oblast, 249033 Russia*

Submitted August 5, 2002; accepted for publication September 6, 2002

Abstract—The results of studying the electrical properties of InAs irradiated with 5-MeV H^+ ions at a dose of 2×10^{16} cm^{-2} are reported. It is shown that, independently of the doping level and the conductivity type of the as-grown InAs, InAs always has the n^+-type conductivity after irradiation ($n \approx (2–3) \times 10^{18}$ cm^{-3}). The phenomenon of pinning of the Fermi level in the irradiated material is discussed. The thermal stability of radiation damage in InAs subjected to postirradiation annealing at temperatures as high as 800°C was studied. © *2003 MAIK "Nauka/Interperiodica".*

1. INTRODUCTION

Determination of the relation between radiation-stimulated variations in the characteristics of semiconductors (as well as of corresponding devices) and fundamental parameters of crystals is very important in the development of radiation-technology methods (such as radiation-induced modification of materials and also ion-implantation and neutron transmutation doping), in studies of the radiation resistance of semiconductors and relevant devices, and in the design of radiation-resistant systems. It is important to clarify both the role played in these effects by conditions of irradiation and the history of the material under study and the contribution of fundamental parameters of the semiconductor itself to the observed phenomena. Special attention should be focused on the phenomenon of stabilization (pinning) of the Fermi level in irradiated semiconductors and on estimating the corresponding "ultimate" parameters of the crystal [1]. Knowledge of these characteristics makes it possible not only to predict in which direction the electrical properties of a semiconductor should be expected to vary but also to choose the doping level and the conductivity type of the initial material so that this material will be resistant to high-energy radiation.

Among the diamond-like and III–V semiconductors, special attention has been drawn to InAs. In contrast to other materials in which the Fermi level shifts within the band gap as a result of irradiation, the Fermi level in InAs is observed to shift in the direction towards the conduction-band bottom (and, ultimately, enters into the conduction band) as radiation defects are accumulated. Even in the very first studies of polycrystalline InAs, Aukerman [2] observed an increase in the concentration of free electrons in the *n*-InAs samples ($n_0 < 10^{17}$ cm^{-3}) and the *p*–*n* conversion for *p*-InAs as a result of irradiation with 4.5-MeV electrons. Subsequent similar studies of InAs single crystals [3, 4] confirmed the data obtained in [2]. It was ascertained that irradiation lead to an increase in the concentration of electrons if the initial free-electron concentration was lower than 10^{18} cm^{-3}. Many researchers attempted to relate the aforementioned special features of InAs to preferential formation of hydrogen-like donor radiation defects in InAs crystal lattice. However, studies of heavily doped n^+-InAs ($n = 2 \times 10^{19}$ cm^{-3}) irradiated with fast neutrons showed that the concentration of free electrons decreased as a result of irradiation, which was related to preferential formation of acceptor-type radiation defects in this material [5]. These data were used to infer that the efficiency of formation of the donor- or acceptor-type radiation defects in InAs depended on both the doping level and the conductivity type of as-grown InAs.

2. RESULTS OF STUDIES

In this paper, we report the results of studying electrical characteristics of InAs with a high concentration of radiation defects introduced by irradiation with protons. We report (i) the results of studying the dose dependences of the electrical parameters of InAs crystals irradiated with 5-MeV protons with integral fluxes (doses) as high as 2×10^{16} cm^{-2}; (ii) experimental and calculated data on the limiting (steady-state) position of the Fermi level in irradiated InAs and on electrical parameters of this material; and (iii) the results of studying the postirradiation isochronous annealing (at temperatures as high as 800°C) in relation to the integral flux and initial doping level. It should be noted that the properties of InAs with a high radiation-defect concentration attained in this study by irradiation with protons, to our knowledge, have not yet been reported.

1063-7826/03/3704-0390$24.00 © 2003 MAIK "Nauka/Interperiodica"

Table 1. Electrical parameters of InAs samples before and after irradiation with 5-MeV protons ($D = 2 \times 10^{16}$ cm^{-2}). The parameters were measured at a temperature $T_{test} = 295$ K

Sample no.	$R_H(0)$	$R_H(D)$	$\sigma(0)$	$\sigma(D)$	$\mu_H(0)$	$\mu_H(D)$
	cm^3/C		Ω^{-1} cm^{-1}		cm^2 V^{-1} s^{-1}	
1	–284	–3.1	83.4	1000	23665	3100
2	–6.1	–2.2	2000	1272	12200	2800
3	+300	–2.1	1.26	1071	360	2250
4	+8.0	–2.5	33.7	852	270	2130
5	+6.2	–2.0	40.3	910	250	1820

Note: $R_H(0)$, $\sigma(0)$, and $\mu_H(0)$ are the Hall coefficient, electrical conductivity, and the Hall mobility before irradiation; $R_H(D)$, $\sigma(D)$, and $\mu_H(D)$ are the corresponding quantities after irradiation with protons.

2.1. Experimental Data

We studied InAs crystals grown by the Czochralski method. The electrical parameters of these crystals before and after irradiation with 5-MeV protons with a dose $D = 2 \times 10^{16}$ cm^{-2} are listed in Table 1. The 100-μm-thick samples were irradiated with 5-MeV protons using a cyclotron at the Tomsk Polytechnical University; the ion-current density was $j \approx 5 \times 10^{-8}$ A/cm^2, and the temperature of samples during irradiation was about 320 K. The samples were irradiated from both sides, and the integrated fluxes were summed. Electrical parameters of irradiated samples were measured after these samples had been kept at a temperature close to 295 K for a week or up to a year, depending on the integrated flux of protons. The samples were annealed in a vacuum chamber if annealing temperatures (T_{ann}) were no higher than 400°C and in a chamber with equilibrium pressure of As vapors if $T_{ann} > 450$°C.

Dependences of the Hall coefficient R_H and electrical conductivity σ in the *n*- and *p*-InAs samples on the dose of irradiation with 5-MeV H^+ ions are illustrated in Fig. 1. As follows from the data shown in Fig. 1 and those listed in Table 1, the quantity R_H tends to a common value of about –2.5 cm^3/C (at $T_{test} = 295$ K) for all studied crystals as the irradiation dose increases; this value of R_H corresponds to the limiting (steady-state) electron concentration $n_{lim} \approx 2.6 \times 10^{18}$ cm^{-3}. The corresponding variations in electrical conductivity of InAs crystals as the irradiation dose increases are also shown in Fig. 1 and are listed in Table 1. The obtained limiting values of electrical conductivity σ and the Hall mobility $\mu_H = R_H\sigma$ are equal to about 10^3 Ω^{-1} cm^{-1} and 2400 cm^2 V^{-1} s^{-1}, respectively (at 295 K). Special features of variations in the temperature dependences of R_H in the *n*- and *p*-InAs samples irradiated with protons also indicate that the material under investigation is transformed into a degenerate (n^+) state as a result of irradiation (Fig. 2).

Variations in the Fermi level position for initially *n*-type InAs (sample 1) and *p*-type InAs (sample 5) as a result of proton irradiation are shown in Fig. 3. The Fermi level position F was calculated in the three-band approximation using the expression

$$n = N_C[(1 + \delta 2/3)^{3/2}/(1 + \delta)]J_{3/2,0}(\eta, \beta, \delta),$$

where $\delta = \Delta_{SO}/E_G$, $\eta = F/kT$, $\beta = kT/E_G$, N_C is the effective density of states in the conduction band, and $J_{3/2,0}(\eta, \beta, \delta)$ is the Kane integral. We assumed in calculations that the InAs band gap is $E_G = [0.426 - \gamma T^2/(93 + T)]$, where $\gamma = 3.158 \times 10^{-4}$ eV/K, and that the magnitude of the spin–orbit splitting of the valence band is equal to $\Delta_{SO} = 0.38$ eV. According to the data shown in Fig. 3, the Fermi level in all studied InAs samples shifts deeper into the conduction band bottom and becomes pinned at $F_{lim} \approx E_V + (0.49–0.52)$ eV in the

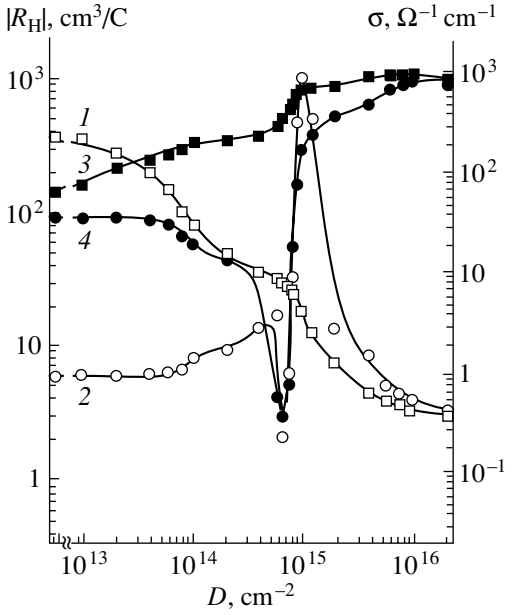

Fig. 1. Dependences of (*1*, *2*) the Hall coefficient R_H and (*3*, *4*) the electrical conductivity σ in InAs on the dose D of irradiation with 5-MeV protons for samples (*1*, *3*) 1 and (*2*, *4*) 4. The parameters were measured at $T_{test} = 295$ K.

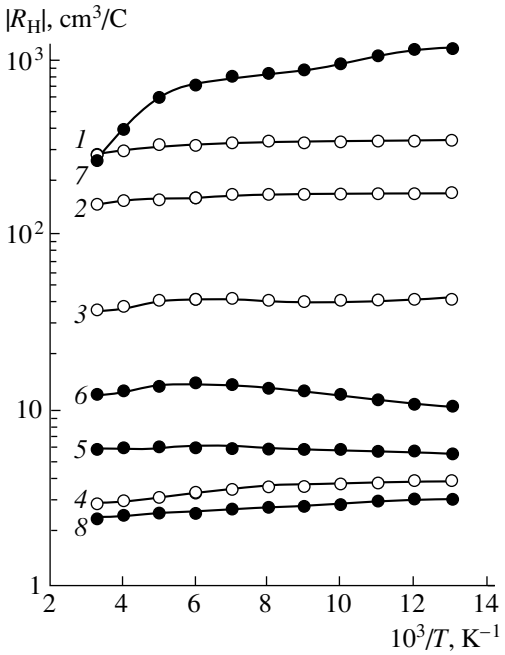

Fig. 2. Temperature dependences of R_H in samples (*1–4*) 1 and (*5–8*) 5 irradiated with 5-MeV protons. The irradiation doses D (expressed in 10^{16} cm^{-2}) were equal to (*1*, *5*) 0, (*2*) 0.02, (*3*) 0.05, (*4*, *8*) 2, (*6*) 0.06, and (*7*) 0.1.

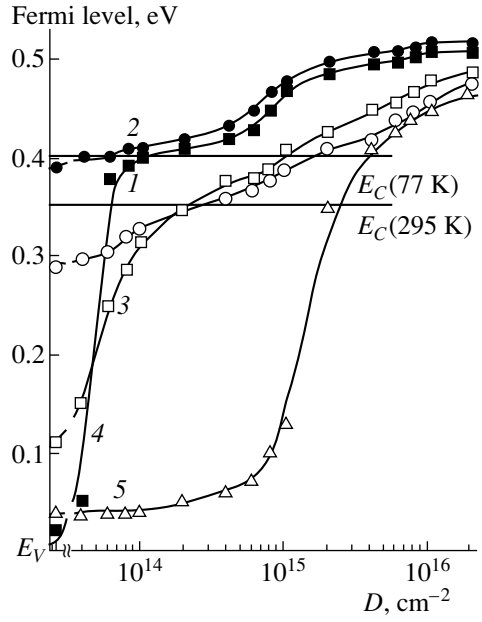

Fig. 3. Dependences of the Fermi level position on the dose of irradiation D of samples (*1*, *2*) 1, (*3*, *4*) 4, and (*5*) 5 with 5-MeV protons. The temperatures of samples during measurements were T_{test} = (*2*, *4*) 77 and (*1*, *3*, *5*) 295 K.

temperature range of 77–295 K. We also used experimental data to estimate the temperature coefficient $\partial F_{lim}/\partial T \approx 1.5 \times 10^{-4}$ eV/K in the range of 77–295 K.

These results, combined with previously published data [1–5], show that introduction of radiation defects into the InAs crystal lattice brings about a shift of the Fermi level closer to (and deeper into) the conduction band; as a result, n^+-GaAs is formed ($n^+ \approx$ (2–3) $\times 10^{18}$ cm^{-3}) for the as-grown InAs samples of both *n*- and *p*-types. The data show that the efficiency of irradiation-induced doping of the *n*- and *p*-InAs crystals with donor-type defects decreases as the initial concentration of free electrons increases from n_0 to $n_{lim} \approx$ (2–3) $\times 10^{18}$ cm^{-3}. Corresponding studies of n^+-InAs irradiated with fast neutrons [5] show that the efficiency of radiation-induced doping of this material with donor-type defects decreases as the free-electron concentration increases from n_0 to n_{lim} as a result of irradiation. Thus, much the same as in other diamond-like semiconductors and III–V compounds, both the donor- and acceptor-type defects are produced in InAs as a result of irradiation; in addition, the electrical activity of these defects in the material under consideration is governed by the Fermi level position in the band structure of the sample under investigation with respect to the limiting Fermi level position F_{lim} in irradiated InAs. As the Fermi level shifts to its limiting position F_{lim}, the efficiency of the irradiation-induced doping of InAs with both the donor- and acceptor-type defects decreases as a result of the equalization of the production rates of these defects; it is this circumstance that leads to stabilization (pinning) of the Fermi level in the band structure of irradiated material. Due to irradiation-induced doping, the initial concentration of free electrons (n_0) or the corresponding concentration of free holes (p_0) in the semiconductor can be varied from n_0 to n_{lim} (or from p_0 to p_{lim}) according to the expressions

$$n_{lim} = n_0 \exp(\Delta E/kT), \quad p_{lim} = p_0 \exp(-\Delta E/kT).$$

Here, $\Delta E = (F_0 - F_{lim})$, where F_0 is the initial (before irradiation) position of the Fermi level. This consideration shows that the concentration of free electrons increases in irradiated InAs if the free-electron concentration n_0 is lower than n_{lim} = (2–3) $\times 10^{18}$ cm^{-3} and decreases if $n_0 > n_{lim}$. It is worth noting that radiation-induced doping differs from doping with chemical impurities in that the limiting electrical parameters of irradiated material are governed by the Fermi level position F_{lim}, whereas they are governed by the type and solubility of impurity in the semiconductor in the case of doping with chemical impurities.

2.2. Estimates Based on the Model

In theoretical estimations, we used the results of corresponding studies of other diamond-like semiconductors and III–V semiconducting compounds; in these compounds, the Fermi level is pinned as a result of irradiation within the narrowest band gap of the crystal. It is assumed that pinning of the Fermi level in irradiated InAs is caused by fulfillment of the condition for charge (local) neutrality for the crystal with defects rather than

by special features of defect formation in a specific material. According to this concept, the position of the level of the charge (local) electroneutrality E_{lnl} is determined from the balance between the charged defects of the donor and acceptor types. In fact, calculations of the E_{lnl} position (the branching points in a complex energy-band structure of the crystal) for InAs according to the previous models [6, 7] yield results which are close to experimental values of $F_{\lim}$ in an irradiated InAs crystal (Table 2). This circumstance indicates that irradiated InAs has a high concentration of charged radiation defects which greatly exceeds the value of $n_{\lim}$. It is in this case that the Fermi level position is bound to be mainly governed by the balance between charged radiation defects of the donor and acceptor types. In fact, the concentration of radiation donors introduced by irradiation with 5-MeV protons into *p*-InAs and estimated from initial rates of free-hole removal on the assumption that the radiation-defect concentration increases linearly with dose yields the value of about 2×10^{19} cm^{-3} for $D = 2 \times 10^{16}$ cm^{-2}. Similarly, in the case of irradiation of heavily doped n^+-InAs ($n = 2 \times 10^{19}$ cm^{-3}) with neutrons, the estimated concentration of irradiation-introduced acceptors for borderline fast-neutron fluxes corresponding to pinning of the Fermi level in the vicinity of $F_{\lim}$ is as high as about 1.8×10^{19} cm^{-3} [5]. Thus, the concentrations of irradiation-introduced donors and acceptors in InAs for the case of $F \approx F_{\lim}$ are close to each other (to within $(2–3) \times 10^{18}$ cm^{-3}), and the irradiated crystal can be treated as almost completely compensated material. The high degree of compensation of such a material is also confirmed by relatively small values of mobility $\mu_H \approx 2.4 \times 10^3$ cm^2 V^{-1} s^{-1} (at 295 K) and 3.6×10^3 cm^2 V^{-1} s^{-1} (at 77 K) compared to the theoretical estimates obtained by Karataev *et al.* [8].

Taking into account that the branching point for a one-dimensional crystal is found to be at the midgap [9], we also estimated the value of $\langle E_G \rangle/2$ in InAs [7]. Here, the value of $\langle E_G \rangle$ was calculated as the mean energy interval between the lower conduction band and the upper valence band of a semiconductor within the entire Brillouin zone. When choosing a crystal model with an isotropic energy gap $\langle E_G \rangle$, we take into account that the $\langle E_G \rangle/2$ position is governed by averaged integral characteristics of the energy-band spectrum of a semiconductor. In fact, studies of irradiated semiconductors subjected to hydrostatic compression showed that radiation defects (independently of the position of their energy levels in the band gap) correspond to deep (highly localized) states, which makes it possible to use a model of a crystal with an isotropic energy gap $\langle E_G \rangle$ to describe the experimental data [10]. The value of $\langle E_G \rangle/2$ reckoned from the top of the InAs valence band (the Γ_{8V} level) is listed in Table 2. The aforementioned studies also make it possible to treat the energy position $F_{\lim}$ as the deepest state related to defects E_B in the crystal within an energy interval in the vicinity of the narrowest band gap. The calculated values of E_B obtained by Brudnyi *et al.* [11] are listed in Table 2.

Table 2. Experimental value of $F_{\lim}$ and calculated values of E_{lnl}, E_B, and $\langle E_G \rangle/2$ for InAs (the values are expressed in eV and are reckoned from the Γ_{8V} level)

$F_{\lim}$	E_{lnl} [7]	E_{lnl} [14]	E_B [11]	$\langle E_G \rangle/2$ [7]
0.52	0.50	0.55	0.52	0.50

According to the models considered, the response of a crystal to irradiation with high-energy particles can be considered as the phenomenon of radiation-induced self-compensation, in which case the Fermi level is pinned in the vicinity of the deepest state of defects, i.e., near the middle of the energy gap $\langle E_G \rangle$ of the crystal. Figure 4 shows calculated values of $\langle E_G \rangle$, $\langle E_G \rangle/2$, and E_{lnl} for InAs. According to the data shown in Fig. 4, it is the low position of Γ_{6C} in reference to the energy $F_{\lim}$ ($\equiv \langle E_G \rangle/2, F_{lnl}, E_B$) that gives rise to the n^+-type conductivity of irradiated InAs. Thus, the model studies show that the Fermi level position $F_{\lim}$ and corresponding electrical properties of irradiated InAs (as in the case of other elemental and III–V compound diamond-like semiconductors) are governed by the energy spectrum of ideal crystal rather than by the special features of defect production in a given material. The only special feature of radiation defects in InAs is the fact that the majority of their energy levels are located above the conduction-band bottom and, thus, form states of the resonance type. In this situation, the defect states are the deepest (localized to the highest degree) states in the energy interval near the narrowest band gap of InAs.

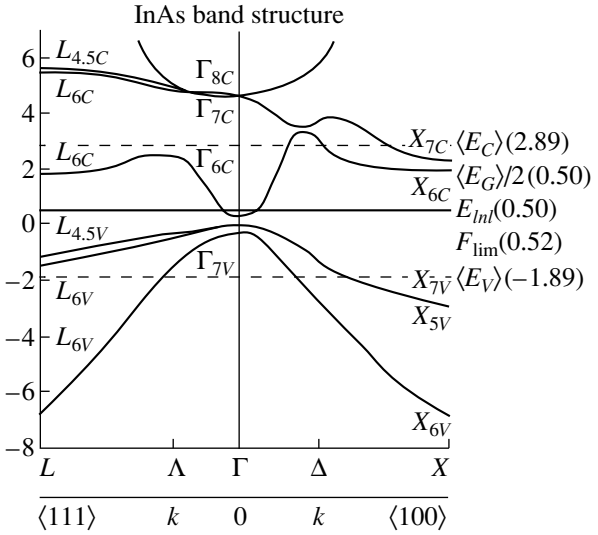

Fig. 4. The energy-band diagram of InAs crystal; experimental value of $F_{\lim}$ and calculated values of E_{lnl} and $\langle E_G \rangle/2$ expressed in eV are indicated.

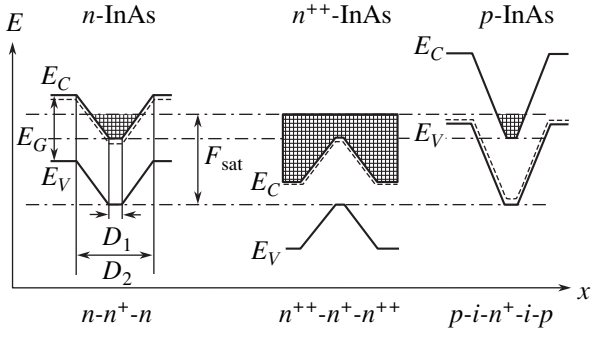

Fig. 5. Energy-band diagrams for defect clusters in InAs samples that had various initial levels of doping and were irradiated with fast neutrons or heavy ions.

On the basis of experimental studies and theoretical calculations, we can draw the energy diagrams of defect clusters, which are formed in InAs samples with various doping levels and conductivity types as a result of irradiation with fast neutrons or heavy ions (Fig. 5). According to the model, the Fermi level is pinned at the limiting (steady-state) position $F_{\lim}$ ($\equiv E_{lnl}, E_B, \langle E_G \rangle/2$) in the central part of these clusters (within the region D_1, see Fig. 5), where the radiation-defect concentration is higher than the concentration of doping impurity. In the peripheral region of the zone D_2 in Fig. 5, the conductivity type of irradiated material is governed by the initial doping level of this material and by the radiation dose. In the case of as-grown *p*-InAs crystals, it is expected that high-resistivity zones (*p*–*n* junctions) will form in the space-charge region. According to the obtained results, sequential irradiation of InAs is bound to lead to a decrease in the potential fluctuations owing to superposition of the defect clusters; ultimately, we obtain a highly compensated ("intrinsic") material, which has a uniform distribution of electrical parameters.

2.3. Studies of Annealing

The special features of annealing of radiation defects in InAs with a low concentration of radiation defects have been studied adequately [12, 13]. Therefore, here we give primary consideration to highly irradiated InAs with a high concentration of radiation defects (Figs. 6, 7). It is found that the efficiency of annealing (removal) of radiation defects is proportional to the level of initial doping of InAs and that this annealing proceeds mainly at temperatures no higher than 500°C. At higher annealing temperatures, quenched-in donors are efficiently formed. This phenomenon is well known and is often related to contamination of the material with rapidly diffusing chemical impurities (for example, Cu) [12]. Heat treatment of nominally undoped *n*-InAs ($n = 2 \times 10^{16}$ cm^{-3}) at temperatures as high as 800°C (Fig. 6) gives rise to InAs with *n*-type conductivity ($n > 10^{17}$ cm^{-3}). In the case of

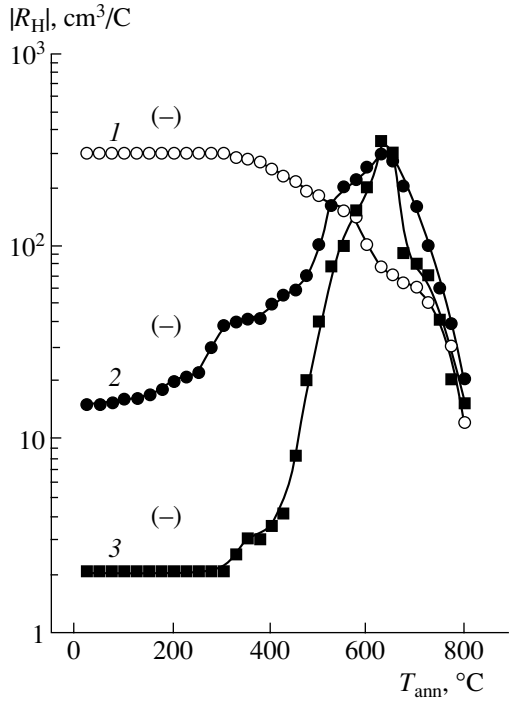

Fig. 6. Dependences of the Hall coefficient on the temperature of isochronous annealing (for 10 min) of *n*-InAs sample 1 irradiated with integrated proton fluxes of (*1*) 0, (*2*) 2×10^{15}, and (*3*) 2×10^{16} cm^{-2}.

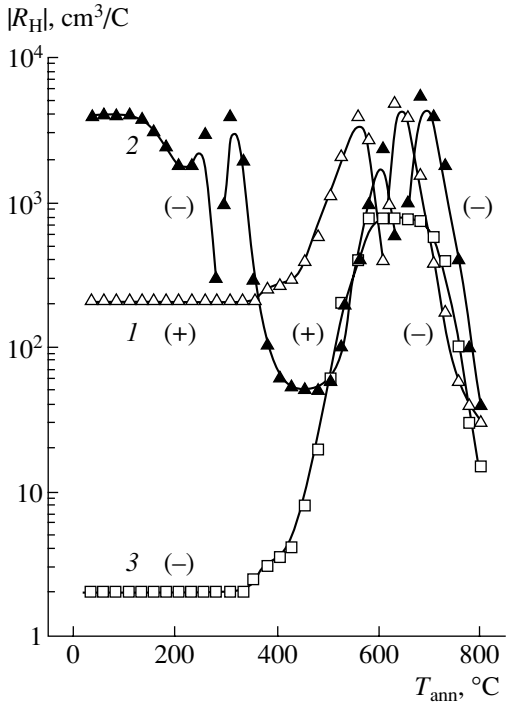

Fig. 7. Dependences of the Hall coefficient on the temperature of isochronous annealing (for 10 min) of *p*-InAs sample 3 irradiated with the integrated proton fluxes of (*1*) 0, (*2*) 5×10^{13}, and (*3*) 2×10^{16} cm^{-2}.

lightly doped *p*-type samples ($p \approx 10^{16}$ cm^{-3}) irradiated with high integrated fluxes of protons, it is impossible to attain the reverse *n*–*p* conversion by annealing the samples; the reason for this is the formation of quenched-in donors as a result of high-temperature heat treatment (Fig. 7). These studies show that variations in electrical parameters of InAs as a result of irradiation and annealing are qualitatively similar; in both cases, the Fermi level shifts towards the conduction band owing to a more efficient introduction of donors in the samples with $n \lesssim 10^{18}$ cm^{-3}. Moreover, similarly to what occurs in the irradiated material, a partial recovery of the electrical parameters of heat-treated InAs (to the values which are close to the initial ones) is observed as a result of subsequent low-temperature annealing ($T_{ann} < 250$°C) [12]. As shown by Kolin *et al*. [14], "residual" acceptors are observed in *n*-InAs crystals irradiated with fast neutrons and subjected to subsequent annealing at temperatures as high as 900°C; the concentration of these acceptors is proportional to the initial doping level of InAs. Most likely, the aforementioned acceptors do not have a radiation-related origin; rather, they are probably formed in the course of annealing of irradiated InAs with an efficiency that increases as the initial doping level increases. All of the above reasoning indicates that the cause of variations in the InAs properties as a result of annealing is the process of self-compensation of this material; this process is similar to that occurring in the course of irradiation with high-energy particles.

3. CONCLUSION

We showed that variation in the electrical parameters of InAs subjected to irradiation can be considered as a process of radiation-induced self-compensation, in which case the Fermi level shifts to the middle of the energy gap $\langle E_G \rangle$ of this material. As a result, the characteristic features of behavior of InAs exposed to radiation are caused by the narrowness of the narrowest band gap due to the presence of a heavy In cation rather than by specific features of defect production in this material. It is this circumstance that defines the limiting position F_{lim} ($\equiv \langle E_G \rangle/2$, F_{lnl}, E_B) in the region of allowed energies in the conduction band and, correspondingly, in the region of n^+-type conductivity of InAs. It can be noted that, as for other semiconductors, there is a close correspondence between F_{lim} in irradiated bulk InAs and the Fermi level position at the interfaces [15]; at the same time, the properties of irradiated crystal are close to those of the InAs surface layer [16, 17]. These observations are indicative of a "rigid" pinning of the Fermi level in the bulk damaged InAs and at interfaces and verify the basic origin of the parameter F_{lim}, which governs the properties of the irradiated semiconductor; it is also clear that this parameter is related to special features of the energy-band spectrum in an ideal semiconductor rather than to the type of structural lattice defects formed as a result of irradiation.

ACKNOWLEDGMENTS

This study was supported by the project "High-Stability Radiation-Resistant Semiconductors" of the International Science & Technology Center, grant no. 1630.

REFERENCES

1. V. N. Brudnyĭ, Izv. Vyssh. Uchebn. Zaved. Fiz. **29** (8), 84 (1986).
2. L. W. Aukerman, Phys. Rev. **115**, 1133 (1959).
3. M. Ladjemi, Le Titre de Docteur Ingenieur (Univ. Paris-Sud, Centre D'Orsay, Paris, 1982).
4. V. N. Brudnyi, S. A. Vorobiev, and A. A. Tsoi, Phys. Status Solidi A **72**, 529 (1982).
5. N. G. Kolin, V. B. Osvenskiĭ, N. S. Rytova, and E. S. Yurova, Fiz. Tekh. Poluprovodn. (Leningrad) **21**, 521 (1987) [Sov. Phys. Semicond. **21**, 320 (1987)].
6. J. Tersoff, Phys. Rev. B **30**, 4874 (1984).
7. V. N. Brudnyi, S. N. Grinyaev, and V. E. Stepanov, Physica B (Amsterdam) **212**, 429 (1995).
8. V. V. Karataev, M. G. Mil'vidskiĭ, N. S. Rytova, and V. I. Fistul', Fiz. Tekh. Poluprovodn. (Leningrad) **11**, 1719 (1977) [Sov. Phys. Semicond. **11**, 1009 (1977)].
9. J. J. Rehr and W. Kohn, Phys. Rev. B **10**, 448 (1974).
10. V. N. Brudnyĭ, Fiz. Tekh. Poluprovodn. (St. Petersburg) **33**, 1290 (1999) [Semiconductors **33**, 1166 (1999)].
11. V. N. Brudnyĭ, S. N. Grinyaev, and N. G. Kolin, Materialovedenie (2002) (in press).
12. V. V. Karataev, G. A. Nemtsova, N. S. Rytova, and T. G. Yugova, Fiz. Tekh. Poluprovodn. (Leningrad) **11**, 1670 (1977) [Sov. Phys. Semicond. **11**, 982 (1977)].
13. N. G. Kolin, V. B. Osvenskiĭ, N. S. Rytova, and E. S. Yurova, Fiz. Tekh. Poluprovodn. (Leningrad) **20**, 822 (1986) [Sov. Phys. Semicond. **20**, 519 (1986)].
14. N. G. Kolin, V. B. Osvenskiĭ, N. S. Rytova, and E. S. Yurova, Fiz. Khim. Obrab. Mater., No. 4, 3 (1986).
15. V. N. Brudnyĭ and S. N. Grinyaev, Fiz. Tekh. Poluprovodn. (St. Petersburg) **32**, 315 (1998) [Semiconductors **32**, 284 (1998)].
16. O. K. Gusev, V. P. Kirienko, A. A. Lomtev, and V. B. Yarzhembitskiĭ, Fiz. Tekh. Poluprovodn. (Leningrad) **17**, 1153 (1983) [Sov. Phys. Semicond. **17**, 727 (1983)].
17. V. V. Karataev, M. I. Reznikov, and V. I. Tal'yanskiĭ, Poverkhnost, No. 4, 57 (1986).

Translated by A. Spitsyn

Semiconductors, Vol. 37, No. 4, 2003, pp. 396–398. Translated from Fizika i Tekhnika Poluprovodnikov, Vol. 37, No. 4, 2003, pp. 414–416.

ELECTRONIC AND OPTICAL PROPERTIES OF SEMICONDUCTORS

Influence of Pulsed Laser Radiation on the Morphology and Photoelectric Properties of InSb Crystals

V. A. Gnatyuk* and O. S. Gorodnychenko**

** Research Institute of Electronics, Shiyuoka University, 3-5-1 Johoka, 432-8011 Hamamatsu, Japan*

e-mail: gnatyuk@mailcity.com

*** Shevchenko National University, Kiev, Vladimirskaya ul. 64, Kiev, 252017 Ukraine*

Submitted September 10, 2002; accepted for publication September 11, 2002

Abstract—Modifications in the surface morphology and photoelectric properties of InSb crystals irradiated with nanosecond pulses of ruby laser are studied. The threshold energy density corresponding to the onset of surface melting was determined to be 0.14 J/cm^2. Laser-induced changes in the spectra and photoconduction kinetics are analyzed. It is demonstrated that the irradiation of InSb crystals with ruby laser pulses within a certain range of energy densities slows down the surface recombination, increases the nonequilibrium carrier lifetime, and, as a consequence, enhances the photosensitivity of crystals. © *2003 MAIK "Nauka/Interperiodica".*

InSb-based photodetectors are widely used to measure the parameters of radiation in the medium infrared spectral region (from 0.2 to 1.24 eV). Fabrication of such sensitive elements involves a variety of surface-treatment procedures aimed at modifying the electrical properties of the semiconductor. Pulsed laser irradiation is appropriate for the optimization of photoelectric properties of semiconductors due to the local character and short time of irradiation, high energy density, and high manufacturability and reproducibility of the conditions of treatment. Laser irradiation of InSb is used for the annealing of structural defects and stresses, for oxide layer desorption [1, 2], and for the formation of accumulation or depletion surface regions up to the inversion of the conductivity type and the appearance of *p–n* junctions as a result of rearrangement in the system of point defects [3].

An essential point for understanding the mechanisms behind the laser-induced transformation of the defect structure in a semiconductor crystal is the determination of its radiation resistance [4]. Analysis of this property yields the data required for the proper choice of optimal irradiation conditions and can be of interest for the elaboration of applied methods in semiconductor photoelectronics technology. Radiation resistance is characterized quantitatively by the damage threshold, which, in terms of laser treatment technologies implies a pulse energy density E_{th} corresponding to the onset of the surface melting [5]. There is no consensus on the magnitude of E_{th} in the case of InSb irradiation [2, 3, 6, 7]. Thus, the values obtained from the circumstantial observations in the experiment with InSb irradiated with nanosecond pulses of ruby laser (0.14–0.22 J/cm^2 [2, 6]) are appreciably higher than that theoretically calculated for similar conditions ($E_{th} \approx 0.08$ J/cm^2) [7].

The aim of this study is to measure the melting threshold of InSb and to establish the optimal laser operation modes that enable modification and optimization of the photoelectric properties of single-crystal InSb irradiated with ruby laser pulses of nanosecond duration. In our experiment, Czochralski-grown *n*-InSb(112) single crystals were subjected to single pulses of ruby laser ($h\nu = 1.78$ eV, $\tau = 20$ ns). A matt-surface lens was used for the homogenization of the beam. The energy density of pulses was varied using neutral filters. We observed the kinetics of photoconductivity and measured the photoconductivity spectra at 77 K at the end of each experimental run.

Ruby laser pulses with an energy density above $E = 0.15$ J/cm^2 were found to produce a change in the morphology of the InSb single-crystal surface subjected to radiation. At first, the changes appear as "islets" characterized with a specific metallic luster. With an increase in E, they spread over the entire laser-spot area (Fig. 1). These effects are likely to be caused by the local and, then, the overall melting of the surface layer [2, 6]. It is known that irreversible damage to the surface morphology of a compound semiconductor may also be caused by the removal of material as a result of intense evaporation [8] and decomposition due to the radiation-induced heating to $T < T_m$ [9]. In the case of InSb, such a process is accompanied by the loss of the volatile component (Sb) and the melting of the fusible component (In). Therefore, we believed it would be possible to determine the threshold energy E_{th} corresponding to the start of the InSb surface melting from direct observations; specifically, the sealing (smoothing) of a preliminarily deposited surface microrelief due to melting was observed [10]. After the final chemicodynamical polishing of the InSb surface, a grid of microscratches with the depth of cut ranging from

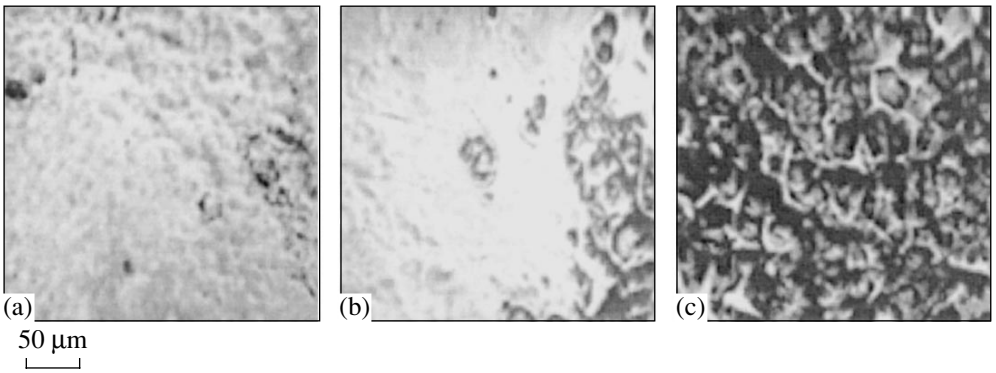

Fig. 1. Morphology of the polished surface of InSb single crystals (a) before and (b, c) after irradiation with nanosecond pulses of ruby laser with energy densities E = (b) 0.15 and (c) 0.18 J/cm^2.

0.04 to 0.06 μm was formed on the surface. In our conditions, such a relief was sealed over at E = 0.14 J/cm^2. Thus, a change in the surface morphology of InSb single crystals at $E \geq E_{th}$ (Fig. 1) should be attributed to melting and subsequent dissociation of the molten material.

Figure 2 shows the photoconductivity spectra of the initial InSb crystal (curve *1*) and the samples (curves *2–5*) subjected to successively higher doses of irradiation $D = E \cdot N$ (where N is the number of pulses) at energy densities below the threshold $E < E_{th}$. The decimals near the curves *2–5* are the factors by which the spectra have been multiplied for their peaks to be close to unity. Curves *2–5* in Fig. 2b were obtained by normalization of the photoconductivity spectra of the irradiated samples (Fig. 2a, curves *2–5*) to the initial spectrum (curve *1*). After irradiation of InSb crystals, their photoconductivity signal increases over the entire spectral range; this growth is especially pronounced in the short-wavelength region (curves *2–5*). A maximal increase in the photoconductivity of the samples was observed at the dose D =0.7 J/cm^2 (curve *5*). A further increase in the radiation dose or irradiating with a dose $E \geq E_{th}$ leads to a reduction of photoconductivity within the entire photosensitivity range $h\nu$ = 0.2–1.24 eV.

Analyzing the shape of the photoconductivity spectra and the appearance of the photoconductivity relaxation curves obtained for InSb crystals under the nanosecond pulsed excitation, we can explain an increase in the photoconductivity of samples after irradiation by the reduction of the surface-recombination rate S (Fig. 3a) and an increase in the lifetime of nonequilibrium carriers τ (Fig. 3b). It is assumed that the laser treatment of the InSb surface leads to the annealing of residual structural defects and lowers the number of recombination centers in the surface layer. This statement is supported by the observed growth of nonequilibrium carrier lifetime and an increasing role of the "slow" component in the relaxation of photocurrent (Fig. 3b). Such effects may also be related to the formation of a surface inversion layer, which hinders the motion of carriers onto the surface and, hence, slows down the surface recombination. As a result of the pulsed laser heating of samples up to T_m, an inversion layer is produced due to the "freezing" of the nonequilibrium high-temperature concentration of thermal-fluctuation defects, which act as acceptors in indium

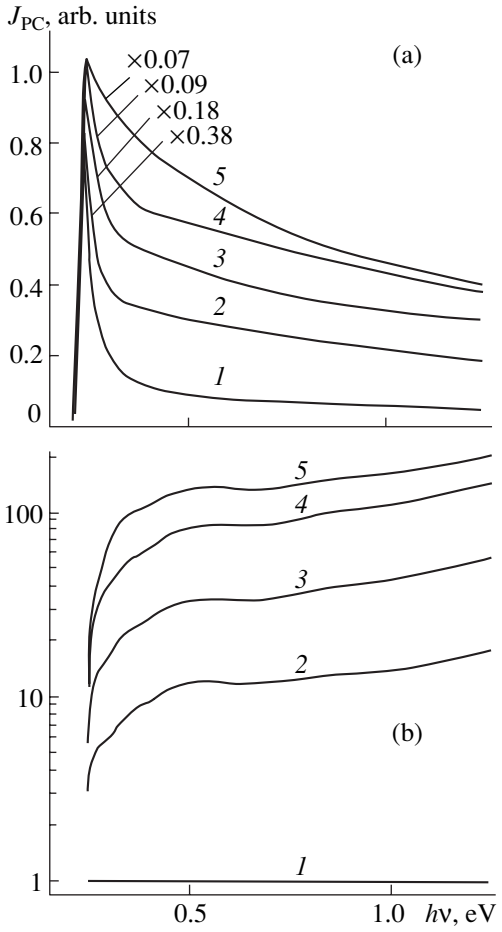

Fig. 2. (a) Spectral dependences and (b) comparative spectra of photoconductivity of InSb single crystals subjected to different radiation doses: (*1*) as-prepared sample, D = (*2*) 0.03, (*3*) 0.22, (*4*) 0.39, and (*5*) 0.70 J/cm^2.

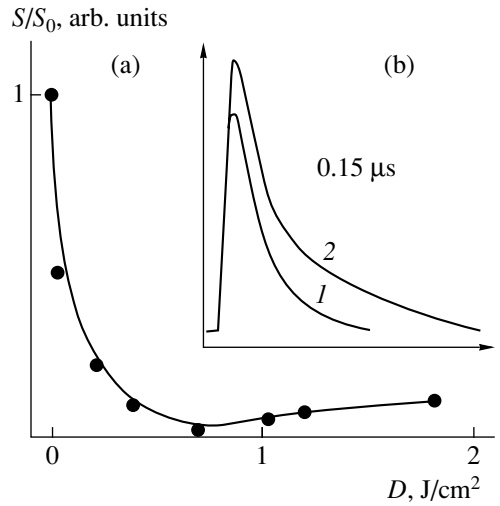

Fig. 3. (a) Surface recombination rate S vs. the dose of laser irradiation D and (b) relaxation of photoconductivity in InSb single crystals (curve *1*) before and (curve *2*) after laser irradiation with a dose $D = 0.4$ J/cm^2.

antimonide [11]. It was also found that the dark resistance of the irradiated InSb crystals exceeds that of as-prepared samples by more than 10%, which seems to be due to an increase in the thickness of the inversion layer and its growing influence on the total resistance of the samples.

Thus, we ascertained that, in a certain range of the pulse energy densities $E < E_{th}$, the irradiation of InSb single crystals with ruby laser pulses with a certain dose D slows down the surface recombination and prolongs the nonequilibrium-carrier lifetime. These circumstances result in a pronounced enhancement of photoconductivity. The observed phenomenon of the laser photosensitization of InSb crystals may be of use in the context of improving the operation of infrared photodetectors.

REFERENCES

1. L. L. Fedorenko, V. K. Malyutenko, and S. S. Bolgov, Ukr. Fiz. Zh. **20**, 2041 (1975).
2. V. A. Gnatyuk, J. Phys. D: Appl. Phys. **32**, 2687 (1999).
3. E. A. Gorin, A. I. Berezhnaya, and G. I. Yanko, Poverkhnost, No. 9, 47 (1982).
4. P. K. Kashkarov and V. Yu. Timoshenko, Poverkhnost, No. 6, 5 (1995).
5. R. V. Arutyunyan, V. Yu. Baranov, L. A. Bol'shov, and A. Yu. Serbant, *Effect of Laser Radiation on Materials* (Nauka, Moscow, 1983).
6. M. Birnbaum and T. L. Stoker, J. Appl. Phys. **39**, 6032 (1968).
7. C. R. Meyer, M. R. Kruer, and F. J. Bartoli, J. Appl. Phys. **51**, 5513 (1980).
8. G. M. Gusakov, A. A. Komarnitskiĭ, and A. S. Ém, Poverkhnost, No. 6, 86 (1991).
9. K. K. Dzhamanbalin, A. G. Dmitriev, É. N. Sokol-Nomokonov, and Yu. I. Ukhanov, Fiz. Khim. Obrab. Mater., No. 2, 20 (1990).
10. V. N. Abakumov, O. V. Zelenova, Yu. V. Koval'chuk, *et al.*, Pis'ma Zh. Tekh. Fiz. **8**, 1365 (1982) [Sov. Tech. Phys. Lett. **8**, 586 (1982)].
11. V. V. Gavrushko and O. V. Kosogov, Fiz. Tekh. Poluprovodn. (Leningrad) **4**, 2373 (1970) [Sov. Phys. Semicond. **4**, 2041 (1970)].

Translated by A. Sidorova

Semiconductors, Vol. 37, No. 4, 2003, pp. 399–403. Translated from Fizika i Tekhnika Poluprovodnikov, Vol. 37, No. 4, 2003, pp. 417–421.

ELECTRONIC AND OPTICAL PROPERTIES OF SEMICONDUCTORS

IR Birefringence in Artificial Crystal Fabricated by Anisotropic Etching of Silicon

E. V. Astrova*^, T. S. Perova, V. A. Tolmachev*, A. D. Remenyuk*, J. Vij**, and A. Moore****

** Ioffe Physicotechnical Institute, Russian Academy of Sciences, St. Petersburg, 194021 Russia*

*** Department of Electronic & Electrical Engineering, Trinity College, Dublin 2, Ireland*

^ e-mail: east@mail.ioffe.ru

Submitted September 11, 2002; accepted for publication September 11, 2002

Abstract—Periodic structures of deep narrow grooves with vertical walls have been fabricated by liquid anisotropic etching of silicon. It has been shown experimentally that the medium obtained behaves as a negative uniaxial crystal with an optical axis parallel to the wafer plane and exhibits an extremely high optical anisotropy in the mid-IR spectral range. The difference in the effective refractive indices for the ordinary and extraordinary rays, Δn, is about 1.5. *© 2003 MAIK "Nauka/Interperiodica".*

1. INTRODUCTION

Interest in the optical properties of silicon-based porous periodic structures is due to their potential in the fabrication of micro-optical elements in a silicon chip. Air gaps in a semiconductor with high permittivity open the way for fabricating an artificial medium with a refractive index n varying in one, two, or three dimensions. If the period a of these variations is comparable with the wavelength of the light wave, a 1D, 2D, or 3D photonic crystal can be produced [1]. Furthermore, these periodic structures exhibit artificial optical anisotropy. Its emergence in an optically isotropic crystal is due to the presence of cavities with a preferential orientation along one of the directions, the so-called shape anisotropy [2]. For example, in a 2D photonic crystal of macroporous silicon, the cavities are cylindrical channels parallel to the ⟨100⟩ crystallographic axis [3]. In this case, the refractive index of the medium has a high anisotropy. However, since its optical axis is perpendicular to the wafer plane, working with such a crystal is somewhat difficult, because the sample must be illuminated from the side with a rather thin end face. A more convenient object was proposed in [4, 5]. This was microporous and mesoporous Si produced by the anodizing of Si oriented in the (110) plane. In this case, the optical axis of a crystal lies in the wafer plane, which is much more convenient, although the anisotropy is smaller.

In the present study, we have fabricated and investigated a medium which is a periodic system of deep and narrow grooves with vertical walls (see Fig. 1a). In this medium, birefringence is observed at the normal incidence of light onto the wafer, whereas under illumination from the end face the material behaves as a 1D photonic crystal [6, 7].

2. EXPERIMENTAL

The structures were fabricated using the technology of liquid anisotropic etching of (110) Si wafers [8, 9]. The grooves are directed along the ⟨111⟩ direction and form a lattice with the period a which equals 4, 5 and 6 μm for different samples. Vertical walls of the thickness d_{Si} = 1.0, 1.2 and 1.4 μm, respectively, alternate with 30-μm-deep air gaps, and the overall thickness of the wafer is 200 μm (Fig. 1b). To enhance the mechanical strength of thin Si walls, solid Si strips, with a surface width of 20 μm, are left between the 400-μm-long grooves. Owing to the specifics of anisotropic etching, the width of these strips grows with depth, becoming 120 μm near the interface with the Si substrate.

Optical properties of the grooved structures were studied with a Digilab FTS-60A Fourier spectrometer in the spectral range of 450–6000 cm^{-1} with 8 cm^{-1} resolution. The transmission and reflection spectra in polarized light were recorded under the normal incidence of light onto the wafer surface. The electric field vector **E** of the incident wave was oriented either parallel or perpendicular to grooves (Fig. 1b), which corresponds to the propagation of ordinary (o) or extraordinary (e) rays in an artificial crystal, respectively. The difference Δn between the effective refractive indices for o- and e-rays was measured using a standard configuration for the transmission of diagonally polarized light. In this case, the polarizer P, placed before the sample, was turned by 45° with respect to the principal axes of the artificial crystal, and the analyzer A behind the sample was oriented either in parallel with or perpendicularly to the polarizer (Fig. 2) [see, *e.g.*, 10].

1063-7826/03/3704-0399$24.00

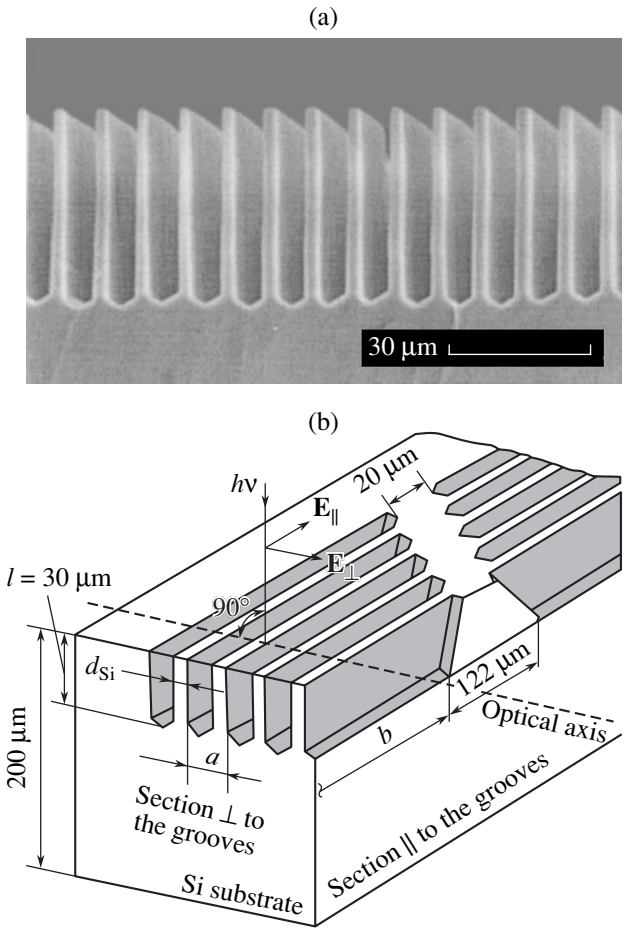

Fig. 1. Grooved silicon: (a) cross-sectional (perpendicular to grooves) SEM image and (b) cross section of a sample and a scheme of optical measurements in polarized light.

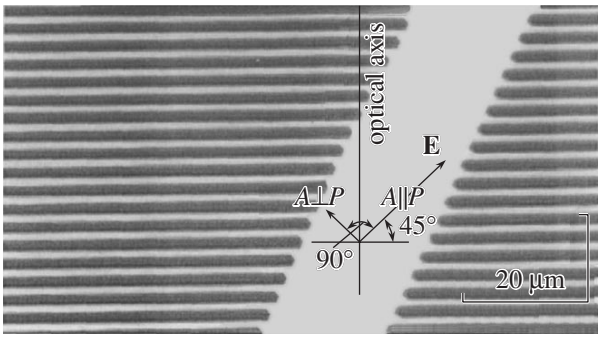

Fig. 2. Plan view in an optical microscope. Arrows indicate the positions of the polarizer and analyzer for the study of transmission of diagonally polarized light.

3. RESULTS AND DISCUSSION

As an example, we discuss the spectra of grooved Si with a period $a = 6$ μm. Figures 3a and 3b show, respectively, the reflection and transmission spectra recorded at different polarizations of light, with the electric field vector parallel $\mathbf{E}_\parallel$ with or perpendicular $\mathbf{E}_\perp$ to the

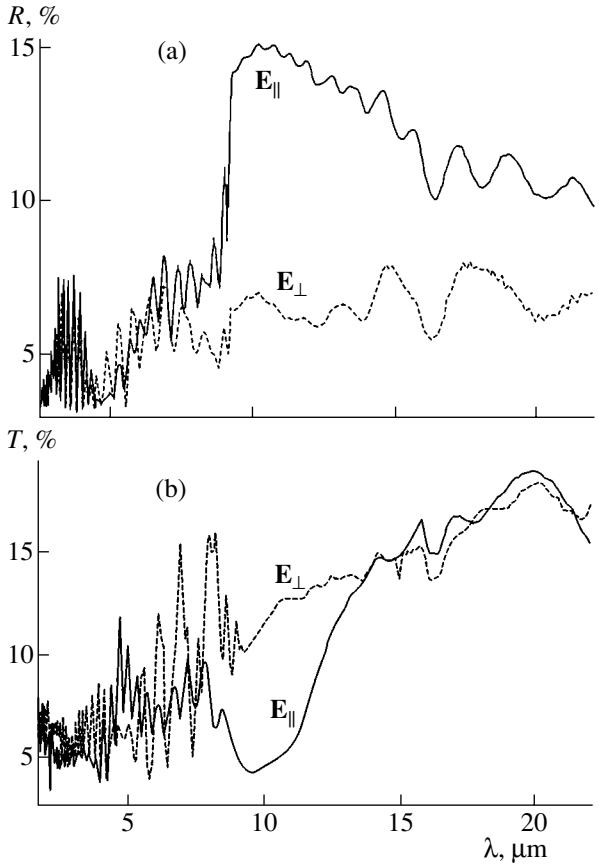

Fig. 3. (a) Reflection and (b) transmission spectra of sample 24*a*6 for two polarizations, $\mathbf{E}_\parallel$ and $\mathbf{E}_\perp$, corresponding to the propagation of ordinary and extraordinary rays.

grooves, which corresponds to the propagation of ordinary and extraordinary light waves. The spectra demonstrate beats in the short-wavelength range, which disappear on passing to the range where the radiation wavelength exceeds the lattice constant of the artificial crystal, $\lambda > a$. The band at $\lambda = 16$ μm is due to absorption associated with multiphonon transitions in crystalline Si. It can be seen that the spectra recorded at different polarizations differ dramatically: the reflection at $\mathbf{E}_\parallel$ is much stronger than at $\mathbf{E}_\perp$. We may conclude therefrom that the refractive index for an ordinary ray is much higher than for an extraordinary one, $n_0 > n_e$, i.e., grooved Si is an effective medium in the form of a negative uniaxial crystal whose axis is perpendicular to silicon walls. In general, the effective medium approximation is valid at $\lambda \gg a$. In our case, even in the long-wavelength spectral range and for the smallest $a = 4$ μm, $\lambda \approx 5a$, and, therefore, we shall mainly discuss the range $\lambda > 12$ μm when characterizing grooved Si by effective refraction indices. Under close examination, the transmission and reflection spectra show, in some places, shallow fine oscillations related to the interference of light on the substrate. Moreover, the reflection spectra at $\lambda > 8$ μm are modulated with long-period oscillations related to the interference on the

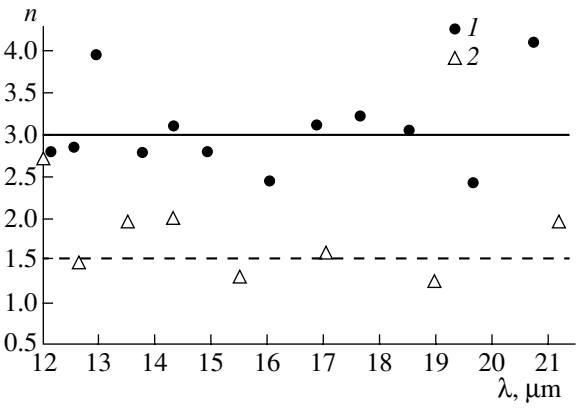

Fig. 4. Spectra of the effective refractive indices for ordinary and extraordinary rays obtained from the reflection spectra in Fig. 3a. (*1*) n_0 and (*2*) n_e. Sample *R*24*a*6.

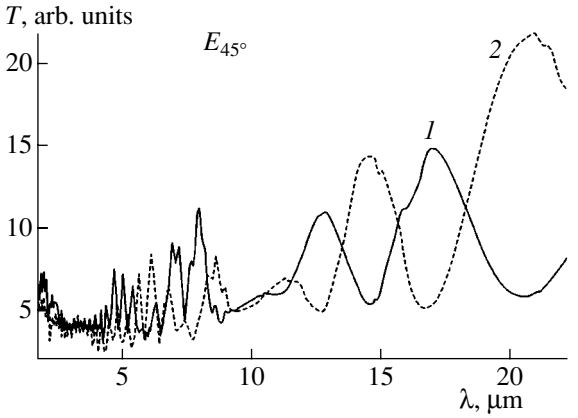

Fig. 5. Transmission spectra of sample 24*a*6 for diagonally polarized light for two positions of the analyzer: (*1*) parallel and (*2*) perpendicular to the polarizer.

30-μm-thick grooved layer (Fig. 1b). The positions of neighboring extrema of these oscillations were used to calculate the effective refractive indices for ordinary and extraordinary rays, n_0 and n_e, using the relation

$$n_{o,e} = \frac{10^4}{4l(\nu_1 - \nu_2)}, \quad (1)$$

where the wave number ν_1 corresponds to a crest, and ν_2, to the closest trough. Figure 4 shows the obtained n_0 and n_e as functions of the wavelength.

The transmission measured in diagonal polarization for parallel and crossed *A* and *P* is shown in Fig. 5. As seen, the observed oscillations are in antiphase: the spectral positions of the crests for $A \perp P$ coincides with the positions of troughs for $A \parallel P$; this results from different velocities of ordinary and extraordinary wave propagation in the crystal and the phase difference arising at the output of the grooved layer. For $A \parallel P$,

$$\Delta_\parallel = \frac{2\pi l}{\lambda}(n_0 - n_e) = \frac{2\pi l}{\lambda}\Delta n. \quad (2)$$

For $A \perp P$,

$$\Delta_\perp = \frac{2\pi l}{\lambda}\Delta n + \pi. \quad (3)$$

Thus, for any two neighboring extrema at λ_1 and λ_2 for either two of these spectra, the phase difference is π

$$\frac{2\pi l}{\lambda_1}\Delta n - \frac{2\pi l}{\lambda_2}\Delta n = \pi, \quad (4)$$

i.e.,

$$\Delta n = \frac{10^4}{2l(\nu_1 - \nu_2)}. \quad (5)$$

Figure 6 shows thus-obtained values of $\Delta n = f(\lambda)$. It appears that $\Delta n = 1.5$ at $\lambda > 12$ μm, which nearly equals the difference $n_0 - n_e$ determined from the reflectance spectra for $E_\parallel$ and $E_\perp$ (Fig. 3a), and characterizes the medium as strongly anisotropic. It is noteworthy that the structures whose artificial lattice has other constants, $a = 4$ and 5 μm, show similar results (see table).

The problem of the shape anisotropy was considered theoretically in [2] in an approximation of a system of thin parallel plates. Assuming that the sizes of silicon ribs, *l* and *b* (Fig. 1b), are large and that the wall thickness d_{Si} and wall spacings $d_{air} = a - d_{Si}$ are much less than λ, we can obtain simple relations for the effective permittivity:

for $\mathbf{E}_\perp$,

$$\varepsilon_\perp = \frac{\varepsilon_1\varepsilon_2}{f_1\varepsilon_2 + f_2\varepsilon_1}, \quad (6)$$

and for $\mathbf{E}_\parallel$,

$$\varepsilon_\parallel = f_1\varepsilon_1 + f_2\varepsilon_2, \quad (7)$$

where

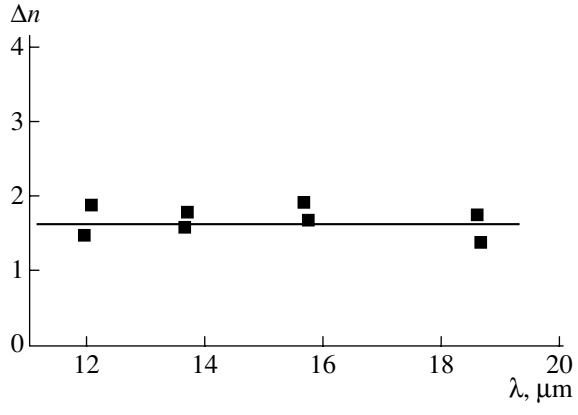

Fig. 6. Spectral dependence of the difference of effective refractive indices for ordinary and extraordinary rays, Δ*n*, obtained from the transmission spectra for diagonally polarized light (Fig. 5). Sample 24*a*6.

Table

Sample no.	a, μm	d_{Si}, μm	p	Calculation for $\lambda \gg a$, $l \gg \lambda$			Experiment			
				n_0	n_e	n_0–n_e	n_0	n_e	n_0–n_e	Δn
24*a*4	4	1	0.75	1.92	1.14	0.78	2.9	1.4	1.5	1.4
24*a*5	5	1.2	0.76	1.89	1.13	0.76	2.8	1.3	1.4	1.5
24*a*6	6	1.4	0.77	1.86	1.12	0.74	3.0	1.5	1.5	1.6
24*a*6*LC**	6	1.4		2.16	1.77	0.39	–	–	–	1.0

* $n_{LC} = 1.6$.

$$f_1 = 1 - p = \frac{d_{Si}}{a}, \quad (8)$$

$$f_2 = \frac{d_{air}}{a} = p, \quad (9)$$

and p is the air filling factor, or porosity.

The difference of two effective dielectric constants is always positive:

$$\varepsilon_\parallel - \varepsilon_\perp = \frac{f_1 f_2 (\varepsilon_1 - \varepsilon_2)^2}{f_1 \varepsilon_2 + f_2 \varepsilon_1} \geq 0, \quad (10)$$

which corresponds to a negative uniaxial crystal with $n_e - n_0 < 0$.

As follows from these relations, the maximum birefringence in such a system, $\Delta n = 1.24$, would be expected at the porosity $p = 0.325$ (see Fig. 7), which corresponds, for a structure with $a = 6$ μm, to $d_{Si} = 4.05$ μm and $d_{air} = 1.95$ μm, i.e., to thicker Si-walls and narrower grooves than those fabricated for the present study.

The n_0, n_e, and p values calculated with formulas (6)–(9) and the experimental data for n_0, n_e, and Δn are listed in the table. The sign of Δn is in agreement with the experiment, whereas the measured magnitudes of n_0, n_e, and Δn are much higher than the calculated values. The wide scatter in the experimental dependences of $n_{o,e}$ and Δn does not allow us to trace how the effective refractive indices vary between structures with different periods and porosities. However, filling the grooves in sample 24*a*6 with liquid crystal *E*7 strongly changed its dielectric constant from $\varepsilon_2 = 1$ for air to $\varepsilon_{LC} = 2.56$ (because $n_{LC} = 1.6$ for the isotropic state of this liquid crystal). The anisotropy of this composite material was noticeably reduced, to $\Delta n \approx 1$. The calculation also yields a weaker anisotropy at lower contrast of the refractive index (see table). The source of the large difference between the calculated and experimental n_0, n_e, and Δn values, with the experimental data being higher, is not yet clear. If higher experimental n_0 and n_e can be related in part to incomplete filling of the sample area with grooves (95% near the surface and 71% near the bottom of grooves), then the same factors must lead to weaker, rather than stronger, anisotropy Δn with respect to the calculated value. It seems that it is not quite correct to compare values calculated in the approximation of $\lambda \gg a$ and $l \gg \lambda$ with the data obtained in our experiment.

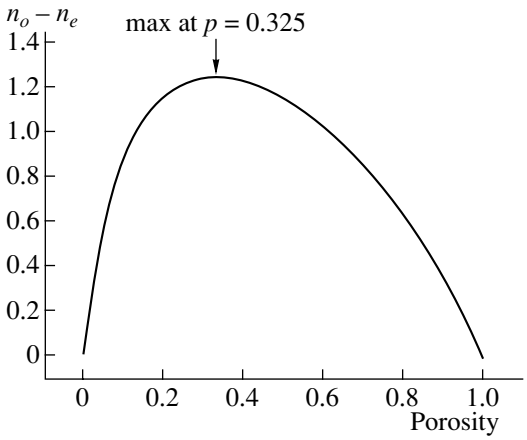

Fig. 7. Calculated Δn vs. the porosity p for an artificial crystal comprising a system of equidistant narrow infinite planes of silicon. Calculation with relations (6)–(9).

4. CONCLUSION

A negative uniaxial crystal has been designed and fabricated, and extremely strong optical anisotropy has been observed experimentally in this crystal. The anisotropy $\Delta n \approx 1.5$ at a porosity $p = 0.77$ or, in relative units, $\frac{\Delta n}{(n_0 + n_e)/2} \approx 66\%$, which is substantially higher than the values obtained earlier for macro- and mesoporous silicon: $\Delta n = 0.366$ [2] and $\Delta n = 0.25$ [3, 4], respectively. For comparison, it may be pointed out that a natural crystal of Iceland spar $CaCO_3$ has $\Delta n = 0.172$ (~11%) [11]. An important advantage of the material obtained in this study is the fact that its optical axis lies in the wafer plane. Moreover, even higher anisotropy can be obtained when a proper choice is made of the structure parameters.

ACKNOWLEDGMENTS

The authors are grateful to colleagues from Lomonosov State University (Moscow, Russia), V. Timoshenko, P. Kashkarov, and L. Golovan', and also from the Ioffe Institute, L. Belyakov, I. Lang, and L. Korovin, for helpful discussions. We also thank L. Granitsyna, R. Dmitrieva, and D. Potapova for assistance in the preparation of samples and participation in the experiments.

This study was supported by the International Cooperation Program (grant IC/2001/042 Enterprise Ireland), INTAS (project no. 01-0642), the Russian Foundation for Basic Research (project no. 00-15-96770), and the Ministry of Industry and Science of the Russian Federation programs "Physics of Solid-State Nanostructures" and "Design of Components for Communication Networks, Software, and Databases for Fundamental Science and Education."

REFERENCES

1. J. D. Joannopoulos, R. D. Meade, and R. D. Winn, *Photonic Crystals* (Princeton Univ. Press, Princeton, N.J., 1995).
2. M. Born and E. Wolf, *Principles of Optics*, 4th ed. (Pergamon, Oxford, 1969; Nauka, Moscow, 1970).
3. F. Genereux, S. W. Leonard, H. M. van Driel, *et al.*, Phys. Rev. B **63**, 161101 (2001).
4. D. Kovalev, G. Polisski, J. Diener, *et al.*, Appl. Phys. Lett. **78**, 916 (2001).
5. L. P. Kuznetsova, A. I. Efimova, L. A. Osminkina, *et al.*, Fiz. Tverd. Tela (St. Petersburg) **44**, 780 (2002) [Phys. Solid State **44**, 811 (2002)].
6. V. A. Tolmachev, L. S. Granitsyna, E. N. Vlasova, *et al.*, Fiz. Tekh. Poluprovodn. (St. Petersburg) **36**, 996 (2002) [Semiconductors **36**, 932 (2002)].
7. V. Tolmachev, T. Perova, J. Vij, *et al.*, Proc. SPIE **4876** (2003) (in press).
8. D. L. Kendall, Annu. Rev. Mater. Sci. **9**, 373 (1979).
9. E. G. Guk, A. G. Tkachenko, N. A. Tokranova, *et al.*, Pis'ma Zh. Tekh. Fiz. **27** (9), 64 (2001) [Tech. Phys. Lett. **27**, 381 (2001)].
10. S. É. Frish and A. V. Timoreva, *Course in General Physics*, Vol. 3: *Optics, Atomic Physics* (Fizmatgiz, Moscow, 1961), p. 192.
11. G. S. Landsberg, *Optics* (Nauka, Moscow, 1976), p. 496.

Translated by D. Mashovets

Semiconductors, Vol. 37, No. 4, 2003, pp. 404–413. Translated from Fizika i Tekhnika Poluprovodnikov, Vol. 37, No. 4, 2003, pp. 422–431.

ELECTRONIC AND OPTICAL PROPERTIES OF SEMICONDUCTORS

Energy Levels of Vacancies and Interstitial Atoms in the Band Gap of Silicon

V. V. Lukjanitsa

Physics Department, Belarussian State Medical University, Minsk, 220116 Belarus

Submitted May 13, 2002; accepted for publication July 22, 2002

Abstract—Based on the analysis of the secondary processes of radiation-induced defect formation in Si crystals with charge-dependent selective traps for vacancies and interstitial atoms, the energy levels of vacancies and interstitial atoms were identified; these level were determined previously from the effect of the irradiation conditions on the annihilation rate of elementary primary defects. It is ascertained that the levels at $\sim E_c - 0.28$ eV and at $\sim E_c - 0.65$ eV in the band gap of Si belong, most likely, to vacancies; the levels at $\sim E_c - 0.44$ eV, at $\sim E_c - 0.86$ eV, and, presumably, at $\sim E_c - 0.67$ eV belong to intrinsic interstitial atoms. © *2003 MAIK "Nauka/Interperiodica".*

1. INTRODUCTION

A paradoxical situation has arisen in the studies of defects in Si: the properties of elementary primary defects (EPDs), vacancies *V* and interstitial atoms *I*, have not been studied as thoroughly as the properties of a number of complex defects, in the formation of which EPDs are involved [1–5]. Characteristic evidence of this fact is the open problem of determining the spectrum of the EPD energy levels [1–7]. The difficulties in the determination of this spectrum result from the short lifetime of *V* and *I* in the free state, which is due to the high mobility of these defects under irradiation conditions and to their high reactivity (EPDs intensively interact with each other and with the atoms of doping and background impurities in Si).

The decrease in the irradiation temperature to $T \lesssim 20$ K made it possible to immobilize the free vacancy and to study some of its properties, in particular, to ascertain that the vacancy *V* has five charge states (V^{2-}, V^-, V^0, V^+, V^{2+}) [8]; to determine the annealing temperature (T = 70–200 K) and the migration energy (0.18–0.45 eV), depending on the charge state [9, 10]; and to determine the positions of two energy levels in the band gap of *p*-Si [9, 11] (regarding the levels of *V* in the band gap of *n*-Si, there is no agreement yet [3–6]). In addition, it was shown that the vacancy in *p*-Si (charge states V^{2+}, V^+, and V^0) has properties of Anderson systems with negative correlation energy, which lead to inversion of the positions of its donor levels [12, 13]. Also, the experiments aimed to justify and determine the energy parameters (ε_L, U_C, E_{JT}) for the model of such a system [12, 14–16] were carried out. Nevertheless, the existing data are not complete; hence, the number of studies concerned with the properties of the vacancy in Si and its role in the processes of radiation-induced formation of defects in the *n*- and *p*-Si crystals progressively increases [6, 10].

Attempts to "freeze" the intrinsic interstitial atoms produced by irradiation and, thus, to increase their lifetime in the free state have failed. Indeed, even at rather low irradiation temperatures (T_{irr} = 0.5–20 K), radiation-induced changes in the properties of Si crystals were revealed [17]. Afterwards, these changes were attributed to ionization-induced athermal diffusion of *I* [18]. Calculations performed later corroborated that the so-called migration barrier for interstitial Si atoms is low [19]. The alternate trapping of radiation-produced electrons and holes changes the charge state of the intrinsic interstitial atom $I^{2+} \longrightarrow I^0 \longrightarrow I^{2+}$, which is accompanied by the transition of the interstitial atom from a tetrahedral to a hexagonal site and then to a new tetrahedral site. Such long-range migration may come to an end by the displacement of the atoms of substitutional impurities of Group III (B, Al, Ga) and C atoms from the lattice sites to interstices (Watkins mechanism) [8, 20, 21].

The analysis of the experimental studies on quenching and irradiation of Si in the context of amphoteric properties of *I* in the theoretical Blount model [22] led Zeeger and Frank [23] to conclude that the self-interstitial atom in *p*-Si has a donor level at $\sim E_V + 0.4$ eV. However, it was determined later that the same level belongs to the interstitial Fe atom, which represents a quenched-in impurity defect [24]. This fact threw doubt on the conclusions made in [23], where a level at $\sim E_V + 0.4$ eV was attributed to the interstitial Si atom. Indeed, it was shown later that the defects experimentally observed in the ESR spectra (Si-*P*6, Si-*B*3, Si-*G*25, and Si-*L*l), which are related to intrinsic interstitial atoms [8, 25–27], have a complex origin and, in the simplest case, represent paired interstitial centers in different geometrical configurations [5, 27, 28]. Therefore, the question about the energy levels and charge states of the Si interstitial atom I^-, I^0, I^+, and I^{2+} still remains open

[5, 6]. It is believed that the states I^0, I^+, and I^{2+} can also form a system with negative correlation energy.

Recently, investigations aimed at determining the spectrum of the energy levels of EPDs in the band gap of Si were reported [29]. These studies, free of the drawbacks and complexities of the experiments on quenching and low-temperature irradiation of Si, were based on determining the dependence of the direct-annihilation rate of EPDs on their charge state. Joint analysis of the states of the atomic and electronic subsystems of the crystal upon varying the conditions of its irradiation with fast electrons (intensity J or temperature T_{irr} showed that the free components of the Frenkel pairs have levels at $E_1 \approx E_c - 0.28$ eV, $E_2 \approx E_c - 0.86$ eV, $E_3 \approx E_c - 0.44$ eV, and $E_4 \approx E_c - 0.65$ eV with an average accuracy of ±0.04 eV.

The aim of this study is to identify the determined EPD levels; i.e., to ascertain whether they belong to V or I defects.

2. EXPERIMENTAL

The energy levels of EPDs were determined by analyzing the secondary processes of radiation-induced defect formation, in which charge-dependent selective sinks (traps) for free vacancies and interstitial atoms are involved. As is known [1], changes in the charge states of the reacting components affect the efficiency of capturing EPDs by such traps. This phenomenon manifests itself in experiments as a drastic (steplike) increase or decrease in the production rates (η) of secondary radiation defects (RDs) or even as a change in the dominant channel of defect production. It was taken into account that the secondary processes under consideration may be obscured by the primary processes of direct annihilation of EPDs. The probability (rate) of direct annihilation also depends on the charge state of EPDs and governs the yield of free defects V and I, which may be involved in secondary-defect production. In order to isolate the secondary processes in an explicit form, the production rates of the secondary RDs were normalized to the rate (efficiency) of the yield of free V and I after their direct annihilation.

The P and B impurities were used as selective traps for free vacancies and self-interstitial atoms, respectively. Being donors in Si, P atoms are positively charged (P_s^+) while B atoms, being acceptors, are negatively charged (B_s^-). The atoms of both impurities have shallow energy levels near the edges of the Si band gap, due to which they do not change their charge states under the conditions of our experiment. Therefore, the observed changes in the efficiency of interaction of P and B with EPDs are unambiguously related to the recharging of the latter. The interaction of V with P^+ ions results in the formation of stable E centers (acceptor level at $E_c - 0.42$ eV), while the I defects displace the B atoms from the lattice sites via the Watkins mechanism ($B_s + I \longrightarrow B_I$) and convert them to an electrically inactive state. Notably, both the formation of the E centers and the loss of electrical activity of B atoms can be easily detected experimentally.

In addition to the impurity P and B atoms, traps of other types were also used for the V and I defects. Clusters consisting of impurities and defects of the interstitial type, which formed in the bulk of the dislocation-free Si grown by the floating-zone method, serve as rather efficient traps for free vacancies [30]. Located in the space-charge region and surrounded by the fields of elastic stresses and by the impurity cloud, which consists mainly of O and C atoms, impurity–defect clusters (IDCs) capture mobile vacancies. Due to the subsequent interaction of vacancies V with O atoms, A centers (RDs with an acceptor level at $E_c - 0.18$ eV) accumulate in the impurity cloud of IDCs, which is characterized by a higher concentration of oxygen ($N_0 \approx 3 \times 10^{16}$ cm^{-3}) in comparison with the crystal matrix ($N_0 > 8 \times 10^{17}$ cm^{-3}). It is expected that the recharging of vacancies will lead to a change in the efficiency of their capture by the IDC defects having a negative charge, which, in turn, will change the formation rate of the A centers (η_A). Self-interstitial atoms can be captured by native defects of two types, with energy levels at $\sim E_v + 0.18$ eV and $\sim E_v + 0.30$ eV [31]. The former are typical of p-Si crystals grown by the Czochralski method and are believed [31] to represent C_s–O_I complexes. These complexes interact with I defects to form C_I–O_I complexes (with a level at $E_v + 0.35$ eV) according to the quasi-chemical reaction $(C_s\text{–}O_I) + I \longrightarrow (C_I\text{–}O_I)$. The defects with an energy level at $\sim E_v + 0.35$ eV are present in p-Si crystals grown by the floating-zone method; they can interact only with interstitial atoms that are in a certain charge state (this fact is important for the purpose of this study) [31]. Due to such interaction, the native defects are transformed into electrically inactive complexes and are removed from the irradiated crystal.

In this context, we used n- and p-Si crystals, dislocation-free and with a low density of dislocations ($N_V = 10^{-4}$ cm^{-2}), with a resistivity $\rho = 4.5$–$40000\ \Omega$ cm, crucible-grown by the Czochralski method, and grown by the floating-zone method in vacuum or in Ar atmosphere.

The EPDs in the samples under investigation ($12 \times 2.5 \times 1.5$ mm in size) were produced by electrons ($E_e = 9.8$ MeV, $t_{imp} = 1$ μs, on–off time ratio $\sim 10^4$) or gamma-ray photons ($E_\gamma = 1.25$ MeV). Under these conditions, the stabilization and necessary changes of the charge states of V and I were obtained in the course of irradiation by changing the nonequilibrium concentration of charge carriers (varying the irradiation intensity) or by changing the initial equilibrium concentration of charge carriers (n_0, p_0) in the crystals (using preliminary compensation).

The results are obtained from the Hall measurements and subsequent analysis (using the electroneu-

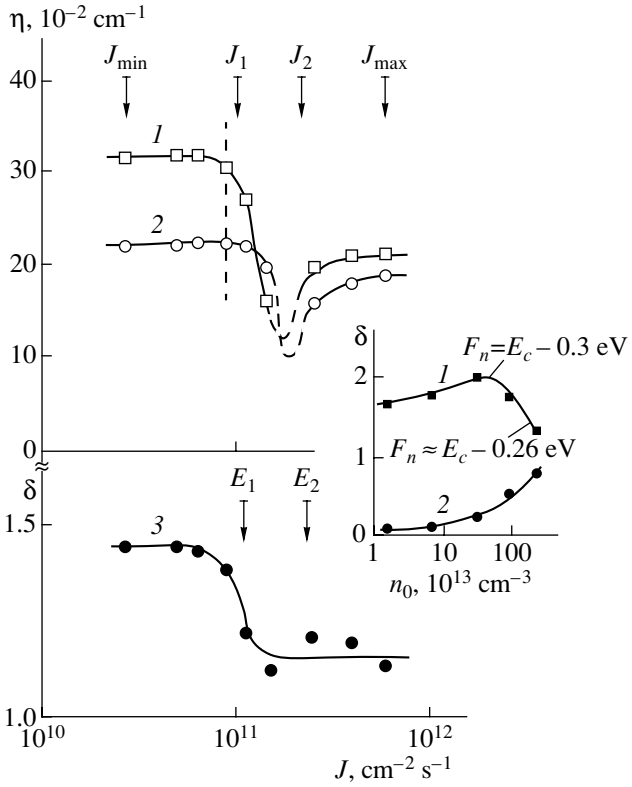

Fig. 1. Dependences of the production rates of RDs with the levels at $\sim E_c - 0.17$ eV in floating-zone *n*-Si ($n_0 = 2 \times 10^{13}$ cm^{-3}) on the intensity of electron radiation: (*1*) for the crystals with IDCs, (*2*) for the reference crystals, and (*3*) normalized dependence δ for the crystals with IDCs. The inset shows normalized dependences of the production rates of (*1*) RDs with levels at $\sim E_c - 0.17$ eV and (*2*) *E* centers in gamma-ray-irradiated crystals with IDCs on the initial concentration of charge carriers.

trality equation) of the temperature dependences of the concentration of charge carriers (T = 80–400 K) in the as-grown and irradiated samples [32]. We determined the production rates of RDs ($\eta = N/\Phi$, where N is the concentration of RDs and Φ is the integrated flux of radiation) and the rates of the radiation-induced change in the carrier concentration $K_n = (n_0 - n_\Phi)/\Phi$ and $K_p = (p_0 - p_\Phi)/\Phi$.

3. EXPERIMENTAL RESULTS AND DISCUSSION

3.1. The E_1 level

The EPD level at $E_1 \approx E_c - 0.28$ eV, which is located in the upper half of the band gap of Si, can manifest itself in the processes of radiation-induced formation of complexes in *n*-Si:P crystals. Since vacancies in *n*-Si have the charge states V^{2-}, V^-, and V^0, and P^+ ions are dominant sinks for vacancies in the floating-zone crystals, the change of the vacancy charge state virtually does not affect the formation rate of the *E* centers in this material. The latter circumstance makes it impossible to obtain necessary data when carrying out experiments with recharging vacancies in *n*-Si. For the same reason, crucible-grown *n*-Si, in which neutral O atoms serve as major traps for vacancies, also cannot be used. In order to overcome this difficulty, we decided to use extra charge-sensitive sinks for vacancies, which could noticeably compete with P in capturing free vacancies. As such competing sinks, IDCs were used, which are present in the dislocation-free floating-zone *n*-Si crystals.

Figure 1 shows typical dependences of the production rates of RDs with levels at $\sim E_c - 0.17$ eV ($\eta_{0.17}$) on the intensity of the electron radiation for the dislocation-free crystals with IDCs (curve *1*) and for the control samples of *n*-Si with a low density of dislocations (curve *2*) grown by the floating-zone method in Ar atmosphere and in vacuum, respectively. In the control material, the formation of IDCs is prevented by the presence of growth dislocations [30], and the RDs with levels $\sim E_c - 0.17$ eV are largely interstitial-type complexes consisting of interstitial and substitutional carbon atoms, C_i–C_s, with a level at $E_c - 0.16$ eV [33]. In the dislocation-free *n*-Si grown in Ar, RDs with levels at $\sim E_c - 0.17$ eV represent a set of C_i–C_s complexes and *A* centers, which are formed at comparable (nearly equal) rates [34]. Due to this, the production rate of these RDs, $\eta_{0.17}$, in the dislocation-free crystals (η_{df}) exceeds that for the control crystals (η_{contrl}) at any radiation intensity.

As the evaluations [29] show, when the radiation intensity increases, at first (at the intensity J_1) recharging of EPDs with a level at $E_1 \approx E_c - 0.28$ eV occurs, and then (at the intensity J_2) EPDs with a level at $E_2 \approx E_v + 0.24$ eV recharge. Due to the recharging processes, the efficiency of direct annihilation of EPDs changes nonmonotonically (see minima in Fig. 1, curves *1, 2*). The analysis we performed shows that, in this case, the efficiency of the secondary processes involving the recharging EPDs also changes. The decrease in the ratio $\delta = \eta_{df}/\eta_{contrl}$ from 1.44 to 1.14 with the increase in the radiation intensity from J_{min} to J_{max} also points to this fact. In addition, it can be seen that, in the region of minima in the curves *1* and *2*, the point at which η_{df} begins to decrease is shifted to smaller values of J in comparison with η_{contrl} (Fig. 1). Both of these experimental facts can be explained from a unified point of view if we assume that, when the charge state of the vacancy becomes more negative, the formation rate of the *A* centers in the impurity cloud of IDCs decreases. The latter phenomenon may be attributed to either the decrease in the flux of vacancies to IDCs due to Coulomb repulsion or to the increasing attachment of vacancies at the interface between the inclusion (IDC) and the crystal matrix [34]. In any case, the abrupt decrease in the formation rate of the *A* centers η_A, which is caused by the recharging of vacancies, not only leads to a decrease in η_{df} and, consequently, to a decrease in δ in the leveling-off portion at $J = J_{max}$, but also, in combination with a decrease in the rate $\eta_{0.17}$ caused by an increase in the annihilation rate of EPDs

upon the recharging of *V*, manifests itself in the experiment as the aforementioned shift of the point at which η_{df} begins to decrease, in comparison with a similar decrease in η_{contrl}.

Assuming that the dependence $\eta_{0.17} = f(J)$ for the reference material (curve *2*) represents the yield of free EPDs after their direct annihilation, we will normalize the dependence $\eta_{df} = f(J)$ (curve *1*) to the dependence $\eta_{0.17} = f(J)$. Due to this normalization, we obtain the function $\delta = (\eta_{df}/\eta_{contrl}) = f(J)$ (curve *3*), which allows us to disregard the changes in η_{df} caused by the dependence of the direct-annihilation rate of EPDs on *J*; i.e., this function characterizes only the secondary processes of accumulation of *A* centers in the crystals with IDCs. As can be seen, the abrupt change in the formation rate of *A* centers, which include *V*, occurs when the radiation intensity varies near the value of J_1, i.e., when the EPD level, denoted as E_1, recharges.

It follows from the above discussion that the level at $E_1 \approx E_c - 0.28$ eV belongs to vacancies.

This conclusion is confirmed by the data on accumulation of RDs with the levels at $\sim E_c - 0.17$ eV and the *E* centers (P-atom–vacancy complexes) in the gamma-ray-irradiated crystals with IDCs and in the reference crystals, depending on the initial concentration of charge carriers n_0 (see inset in Fig. 1). The shown curves represent the dependences $\eta_{0.17} = f(n_0)$ and $\eta_E = f(n_0)$ for the crystals with IDCs; these dependences are normalized to the dependences on n_0 of the production rates of similar RDs in the reference material, in which IDCs do not arise during the material growth because of dislocations. It is expected that, when the vacancy level at E_1 recharges (with an increase in n_0 from 5×10^{14} to 2×10^{15} cm^{-3}), the normalized dependence $\delta_{0.17} = f(n_0)$ should descend (due to η_A) with a simultaneous ascent in the normalized dependence $\delta_E = f(n_0)$. This was confirmed experimentally: in the crystals with $n_0 < 5 \times 10^{14}$ cm^{-3}, the normalized production rates of the *E* centers (δ_E) and RDs with levels at $\sim E_c - 0.17$ eV ($\delta_{0.17}$) are substantially different, which is due to the efficient capture of vacancies by IDCs. However, at $n_0 > 2 \times 10^{15}$ cm^{-3}, these normalized production rates become comparable with each other and nearly as high as the production rates of these RDs in the reference material. This phenomenon is due to the fact that, with an increase in n_0, the Fermi level F_n shifts from $E_c - 0.30$ eV to $E_c - 0.26$ eV (see inset) and crosses the vacancy level at $E_c - 0.28$ eV; as a result, the charge state of this vacancy becomes more negative. Consequently, the efficiency of interaction between vacancies and IDCs decreases, while the efficiency of interaction between vacancies and positively charged P ions, accordingly, increases.

3.2. The E_2 level

The recharging of the EPD level E_2 under variation of the electron-radiation intensity near the value of J_2 does not manifest itself explicitly in the results of experiments with accumulation of vacancy-type RDs in the *n*-Si crystals, including the crystals with IDCs (Fig. 1). This may indicate that the level at E_2 belongs to self-interstitial atoms. In this case, the level at E_2 manifests itself in *p*-Si because this material contains charge-dependent traps for the *I* defects.

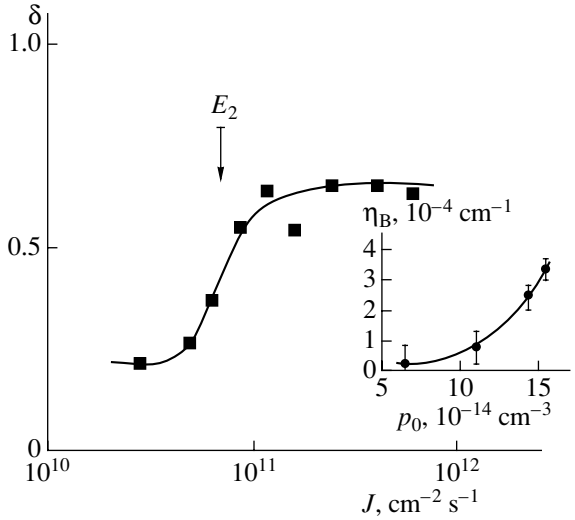

Fig. 2. Dependence (normalized to the dependence of the yield of free EPDs) of the production rate of RDs with a level at $E_V + 0.35$ eV in the crucible-grown *p*-Si ($p_0 = 1.5 \times 10^{15}$ cm^{-3}), on the intensity of the electron radiation. The dependence of the rate of displacement of B atoms from the lattice sites due to gamma-ray irradiation on the initial concentration of holes in *p*-Si is shown in the inset.

Figure 2 shows the dependence (normalized to the yield of free EPDs) of the production rate of the RDs with a level at $E_V + 0.35$ eV on the electron-radiation intensity *J* for the crucible-grown *p*-Si ($p_0 \approx 10^{15}$ cm^{-3}). The observed step shape of the dependence $\delta_{0.35} = f(J)$ is typical of the threshold complex formation upon changing the charge state of one of the interacting components [1]. The RDs with a level at $E_V + 0.35$ eV are C_i–O_i complexes of the interstitial type [35], and the mechanism of their formation in the crystals under investigation is as follows: C_s–$O_i + I \longrightarrow C_iO_i$ [31]. Taking this circumstance into account, we conclude that the observed shape of the dependence is due to the recharging of the *I* defects because, according to the estimations, neither C_i–O_i nor C_s–O_i complexes (with a level at $\sim E_V + 0.18$ eV [31]) recharge under the conditions of our experiments. Judging from the character of the dependence shown in Fig. 2, the EPD level, which is the first to recharge when the radiation intensity increases from J_{min} to J_{max}, corresponds to the energy level of the *I* defects. The calculations we performed showed that, in the used *p*-Si crystals with relatively low resistivity, the level E_2 recharges first followed by the level E_1. Specifically, with an increase in *J*, the quasi-Fermi level for holes F_p^* first crosses the level E_2,

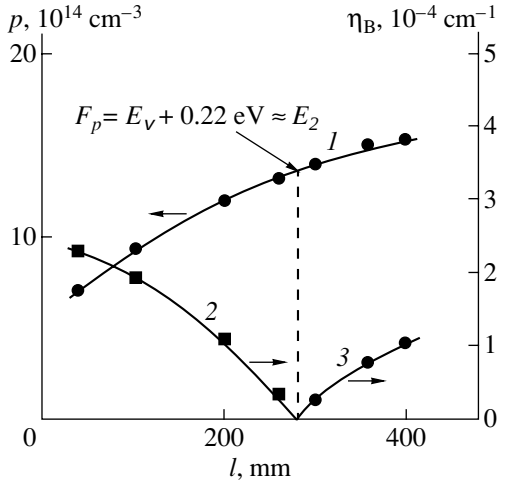

Fig. 3. Distributions of (*1*) the initial concentration of holes *p* and (*2*, *3*) the rates of radiation-induced change in the concentration of electrically active B impurity η_B under gamma-ray irradiation along the axis of a crucible-grown *p*-Si ingot of large diameter. (*2*) Rate of radiation-induced "introduction" of electrically active boron and (*3*) rate of radiation-induced "removal" of electrically active boron.

and only then does the quasi-Fermi level for electrons F_n^* cross the level E_1 [29].

It follows from the above discussion that the level at $E_2 \approx E_v + 0.24$ eV belongs to intrinsic interstitial Si atoms.

As is known [4, 5], interstitial Si atoms may interact with impurity B atoms, displacing the latter from the lattice sites to interstitials. With allowance made for this fact, the recharging of interstitial Si atoms should affect the efficiency of this interaction. The inset in Fig. 2 shows how the rate of displacement of B atoms η_B from the lattice sites in the gamma-ray-irradiated crucible-grown *p*-Si crystals changes under variations in the position of the Fermi level near E_2 due to changing p_0. As can be seen, with an increase in the initial concentration of charge carriers (p_0) in a rather narrow range, η_B sharply increases. Notably, with the increase in p_0 in this range, the Fermi level shifts from $E_v + 0.255$ eV to $E_v + 0.217$ eV, i.e., crosses the level E_2 [29]. In other words, the obtained result also indicates that the level E_2 belongs to free interstitial Si atoms.

In our opinion, this suggestion is also confirmed by the fact that, when the level E_2 recharges, there occurs a change of the channels of the radiation-induced defect production, in which *I* defects and doping B impurity are involved, in the same *p*-Si crystal (ingot) of large diameter (∅ = 150 mm) (Fig. 3). As was noted, due to the irradiation, B atoms are generally displaced from the lattice sites via the Watkins mechanism ($B_s + I \longrightarrow B_i$), which is accompanied by the loss of their electrical activity in *p*-Si. However, in the large-diameter Si ingot, some portion of the doping B impurity is in the electrically inactive state and may be activated by thermal treatment or irradiation of the crystal with ^{60}Co gamma-ray photons [36]. As can be seen from Fig. 3, in the studied large-diameter *p*-Si ingot ($\rho \approx 12\ \Omega$ cm), the B impurity may both gain (at the beginning of the ingot, curve *2*) and loose (at the end of the ingot, curve *3*) its electrical activity due to irradiation. Notably, the former process is replaced by the latter process (curves *2*, *3*) as the initial concentration of charge carriers increases along the ingot axis (curve *1*), i.e., as the Fermi level shifts to the top of the valence band. This change of the processes occurs when the Fermi level crosses the level E_2 (Fig. 3)[1] and, in our opinion, is caused by the recharging of self-interstitial atoms. Indeed, the transition of the *I* defects to the more positive charge state (for example, to the I^+ or I^{++} state) due to Coulomb attraction increases the efficiency of their interaction with negatively charged B ions according to the reaction $B_s^- + I^+ \longrightarrow B_I$ or $B_s^- + I^{++} \longrightarrow B_I$.

Incidentally, this phenomenon may account for the known fact that the Watkins mechanism works more efficiently at low (liquid-nitrogen) temperatures, when the Fermi level in *p*-Si is close to the valence band, rather than at room temperature.

3.3. The E_3 Level

In order to recharge the level E_3, we changed the initial concentration of charge carriers from 3×10^{13} to 4×10^{10} cm^{-3} (compensating them by preliminary introduced RDs) in the high-resistivity floating-zone *n*-Si crystals, which were then subjected to irradiation. The secondary processes were controlled by varying the coefficient $K_n = \Delta n/\Delta\Phi$ of the radiation-induced change in the concentration of charge carriers in the crystals under investigation measured at room temperature.

The inset in Fig. 4 shows a typical dependence of K_n on the initial carrier concentration (n_0) in the *n*-Si crystals irradiated in steps by low-intensity electron fluxes. It can be seen that this dependence represents a two-step curve rising with an increase in n_0. Notably, the first (large) step is related to the change in the annihilation rate of EPDs upon the recharging of the level E_3 [29], whereas the second (small) step is related to the recharging of the levels at $E_c - 0.40$ eV and $E_c - 0.42$ eV, which belong to arising divacancies and *E* centers, respectively. As can be seen, in the latter case, K_n changes exactly by a factor of 2, while, in the former case, K_n changes by more than two orders of magnitude. Comparative analysis of the dependences of K_n on the initial concentration of charge carriers in the crystals with IDCs and in the control crystals (where the value of K_n is several times larger) did not reveal any features pointing to the recharging of vacancies. This may be caused either by the fact that the level of the *E*

[1] With allowance made for the irradiation temperature (45°C), we have $F_p \approx E_v + 0.22$ eV $\longrightarrow$ $F_p \approx E_v + 0.24$ eV.

center (E_c – 0.42 eV), the major compensating RD, is located close to the level E_3 or by the fact that the level E_3 belongs to intrinsic interstitial atoms.

In order to check the latter suggestion, we used the floating-zone *p*-Si crystals which contained native defects with a level at ~E_v + 0.30 eV and serving as charge-dependent sinks for the *I* defects [31]. Although the level at $E_3 \approx E_c - 0.44$ eV is in the upper half of the band gap of Si, it can be recharged by changing the nonequilibrium concentration of charge carriers in the crystals using gamma-ray fluxes of various intensities. Notably, as the measurements of the nonequilibrium conductivity in the *p*-Si samples showed, the concentration of nonequilibrium charge carriers ($\Delta p = \Delta n = 4.5 \times 10^{11}$–$1.1 \times 10^{12}$ cm^{-3}) in the course of irradiation with fluxes of various intensities is, at least, by an order of magnitude lower than the equilibrium concentration of holes ($p_0 = 2.2 \times 10^{13}$ cm^{-3}) in the starting crystals.

It follows from the above data that the position of the quasi-Fermi level for holes F_p^* almost does not change, and possible variations in the course of the secondary processes of the radiation-induced defect formation in *p*-Si at various *J* are due only to the shift of the quasi-Fermi level for electrons F_n^*, which crosses the level E_3 and causes recharging of this level.

The major compensating RDs in the studied *p*-Si are the interstitial carbon atom (C_i) with a level at E_v + 0.30 eV and the vacancy-type defect with a level at $\gtrsim E_v$ + 0.43 eV [31]. Figure 4 shows the dependences of the production rates of these defects on the intensity of the gamma-ray radiation. The nonmonotonic curve *1* represents the total rate of introduction and removal of C_I due to the irradiation of native defects with a level at E_v + 0.30 eV. As can be seen, at low *J*, the process of removal of the native defects is dominant ($\eta_{0.30} < 0$), whereas, at high *J*, the process of accumulation of C_i in the crystals becomes dominant ($\eta_{0.30} > 0$). In our opinion, this phenomenon is due to the change of the defect-production channels involving self-interstitial atoms during their recharging.

When *J* varies from 9.6×10^{10} to ~5×10^{11} cm^{-2} s^{-1}, self-interstitial atoms are in the charge state, which facilitates their interaction with the electrically active native defects. Due to this interaction, complexes, which are electrically neutral during the experiment, are formed. Evidently, the formation of these defects is accompanied by a decrease in the concentration of native defects present in the as-grown crystals [31]. With a further increase in *J* ($J > 5 \times 10^{11}$ cm^{-2} s^{-1}), the charge state of self-interstitial atoms changes; as a result, the probability of their interaction with substitutional (neutral) carbon atoms (C_s) with the formation of the C_I defects ($C_s + I \longrightarrow C_I$) increases.

In other words, curve *1* in Fig. 4 characterizes the reactivity of the *I* defects in different charge states and exhibits the change of the dominant interstitial mechanism of secondary defect formation under the recharging of *I*.

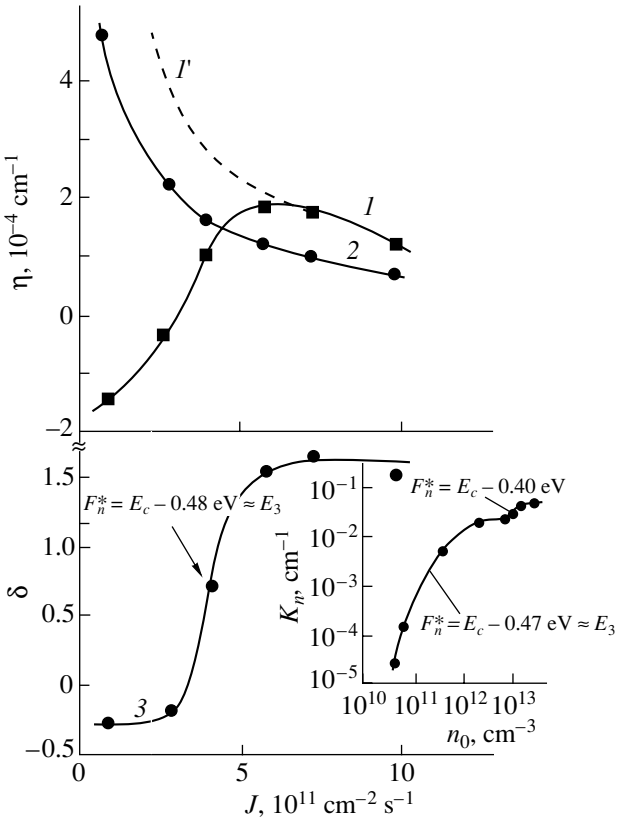

Fig. 4. Dependences of defect-production rates in floating-zone *p*-Si ($p_0 = 2.2 \times 10^{13}$ cm^{-3}) on the intensity of gamma-ray radiation: (*1*, *1'*) for defects with a level at E_v + 0.30 eV, (*2*) for RDs with levels at $\gtrsim E_v$ + 0.43 eV, and (*3*) normalized dependence of the production rate of defects with a level at E_v + 0.30 eV. The dependence of the coefficient of radiation-induced change in the concentration of charge carriers K_n on the initial concentration of electrons in the dislocation-free *n*-Si crystals is shown in the inset.

Concerning the vacancy mechanism of the defect formation, the free vacancies *V*, as was noted, are involved in the formation of RDs with a level at $\gtrsim E_v$ + 0.43 eV, and $\eta_{0.43}$ steadily decreases with an increase in *J* from 9.6×10^{10} to 9.9×10^{11} cm^{-2} s^{-1} (Fig. 4, curve *2*). Such a run of the dependence $\eta_{0.43} = f(J)$ is caused by the effect of *J* on the annihilation rate of the EPDs (Frenkel pairs) [31], which governs the yield of free *V* and *I* that can be involved in the vacancy and interstitial mechanisms of secondary defect formation, respectively. Therefore, the dependence $\eta_{C_i} = f(J)$ (curve *1'*) would have had the same form as $\eta_{0.43}$ if the interstitial mechanism of the defect formation had not changed (curve *1*).

Normalizing curve *1* to curve *2*, we obtain the dependence of the secondary processes involving intrinsic interstitial atoms on the radiation intensity in

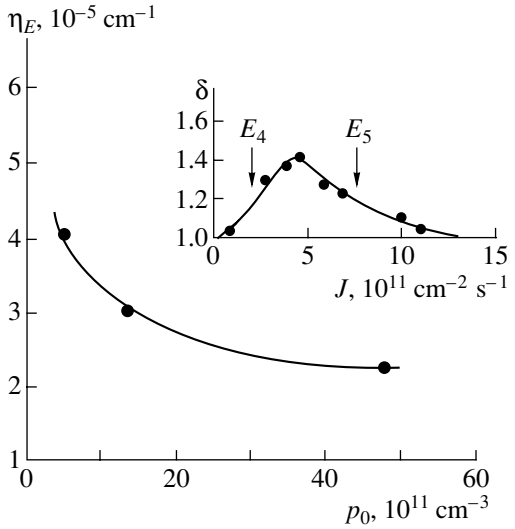

Fig. 5. Dependence of the formation rate of *E* centers in floating-zone *p*-Si on the initial hole concentration. Normalized dependence of the production rate of RDs with levels at $\sim E_c - 0.17$ eV in the floating-zone *n*-Si crystals with IDCs ($n_0 = 2 \times 10^{13}$ cm^{-3}) on the intensity of gamma-ray radiation is shown in the inset.

an explicit form (curve *3*, $\delta = \eta_{0.30}/\eta_{0.43}$). It can be clearly seen that the recharging of *I* occurs at $J \approx 4 \times 10^{11}$ cm^{-2} s^{-1}; i.e., when (according to the estimations performed) F_n^* is near the level at $E_c - 0.48$ eV. This value of the quasi-Fermi level F_n^* can be used to estimate the energy level of interstitial atoms (E_I) in the band gap, under the assumption that the recharging of *I* occurs when F_n^* crosses the level E_I. The value obtained for E_I ($\sim E_c - 0.48$ eV) is in good agreement with the position of the level $E_3 = [(E_c - 0.44) \pm 0.04]$ eV, which was determined previously in the studies on electron irradiation of *n*-Si at various temperatures [29], and with the value of $E_3 \approx E_c - 0.47$ eV, obtained from analysis of the dependence $K_n(n_0)$ in high-resistivity *n*-Si (see the inset in Fig. 4).

Thus, the level E_3 belongs to interstitial Si atoms.

3.4. The E_4 level

In order to recharge the level E_4, we varied the initial concentration of charge carriers in high-resistivity ($\rho \approx 10^4$ Ω cm) *p*-Si. EPDs were produced in the crystals by gamma-ray irradiation. We took into account the features of the radiation-caused changes in the concentration of charge carriers in this material; i.e., when high-resistivity ultrapure *p*-Si is irradiated, in contrast to *n*-Si, the concentration of free charge carriers increases with an increase in the irradiation flux with subsequent levelling-off [37]. Under these conditions, the Fermi level shifts from the midgap to the position at $\sim E_v + 0.39$ eV, which is stable in a wide range of radiation fluxes. As shown in [38], this phenomenon is due to the accumulation of *E* centers formed in *p*-Si and to the ensuing decompensation of high-resistivity *p*-Si, which initially contains the compensating P impurity. In this context, there arises the possibility of determining η_E in the irradiated *p*-Si by measuring the coefficient of radiation-induced change in the hole concentration $K_p = \eta_E$ [38].

The dependence of the formation rate of the *E* centers in the high-resistivity *p*-Si on the initial hole concentration p_0 is shown in Fig. 5. Under varying p_0 in the shown range, the position of the Fermi level ranges from $\sim E_v + 0.43$ eV to $\sim E_v + 0.38$ eV, which corresponds to the completion of recharging of the level E_4. The observed decrease in η_E with an increase in p_0 may be interpreted as the result of the decrease in the efficiency of the reaction $P^+ + V \longrightarrow E$ center upon converting free vacancies to a more positive charge state (for example, to the V^0, V^+, or V^{++} states).

However, such an interpretation of the obtained results is valid only if the annihilation rate of the EPDs produced by the gamma-ray irradiation does not increase with an increase in p_0 in the aforementioned range. At the same time, the validity of this interpretation is indirectly confirmed by the fact that pinning of the Fermi level near $\sim E_v + 0.39$ eV, observed for a large number of high-resistivity *p*-Si crystals [37], is governed, in our opinion, not only by the depletion of the compensating P impurity, but also by the transition of almost all free vacancies to the positive charge state. As a result, due to the Coulomb repulsion, the vacancies completely cease to combine with positively charged P ions; i.e., *E* centers are no longer formed.

Thus, the level at E_4 most likely belongs to vacancies.

In order to verify this conclusion, we performed a comparative analysis of the accumulation of RDs with levels at $\sim E_c - 0.17$ eV in the crystals with IDCs and the reference crystals of floating-zone *n*-Si with a low density of dislocations, using irradiation with gamma-ray fluxes of various intensities. The inset in Fig. 5 shows the dependence $\eta_{0.17}(J)$ for the crystals with IDCs, which is normalized to the dependence $\eta_{0.17} = f(J)$ for the reference crystals. The fact that the curve runs above unity indicates that some of the vacancies produced by irradiation interact with IDCs (the capture of vacancies by IDCs), and the nonmonotonic run of the curve shows that the character of this interaction changes due to the recharging of IDCs, which occurs with an increase in *J*.

The measurements we carried out showed that $\Delta n^* \ll n_0$, due to which the recharging of EPDs occurs if the quasi-Fermi level for holes (F_p^*) shifts. As follows from the data shown in the inset and the estimations performed, the value of $\eta_{0.17}$ changes most radically when F_p^* crosses the energy levels $E_4 = E_c - 0.65$ eV and $E_5 = E_c - 0.67$ eV. In other words, these are the lev-

els that may belong to vacancies, which are recharged when intersected by the quasi-level F_p^* (the recharging changes the efficiency of the interaction between the vacancies and IDCs with the formation of *A* centers). The important circumstance is that, first, the position of one of these levels coincides with the position of the previously determined level $E_4 = E_c - 0.65$ eV [29]. Second, the recharging of the vacancy level E_4, which occurs when F_p^* shifts with an increase in *J*, results in an increase in η_A for the crystals with IDCs (see the inset in Fig. 5), which may occur only when vacancies *V* transfer to a more positive charge state. The latter is in agreement with the above interpretation of the decrease in η_E with an increase in p_0 in floating-zone *p*-Si. Thus, the level E_4 actually belongs to vacancies.

As for the obtained level E_5, the situation concerning its assignment is not so unambiguous (which is indicated by the question mark in Fig. 6). Generally speaking, this level may belong to defects that are constituents of IDCs, i.e., to vacancies or to self-interstitial atoms. Notably, independently of the nature of the level at E_5, its recharging may lead to a decrease in $\delta_{0.17}$. Taking into account that a dependence of similar character, $\delta_{0.17}(J)$, is observed in the control crystals, in which IDCs are absent, we concluded that the level E_5 belongs to EPDs rather than to any of the defects that are constituents of IDCs. In addition, even if we assume that vacancies *V* have properties of systems with negative correlation energy, it is unlikely that this level is related to the vacancy (dash-dotted line in Fig. 6), since another vacancy level (E_4) is located quite close to it, while the other level (E_1) is located fairly far from it (Fig. 6). In addition, the appearance of one more vacancy level, E_5, in combination with the two previously determined, E_1 and E_4, and with two already known, suggests that vacancies have six charge states, whereas, as is known, there are only five. Hence, in our opinion, this level most likely belongs to self-interstitial atoms (the level E_5', dotted line in Fig. 6). This suggestion is in agreement with the experimental data shown in the inset in Fig. 5 because, in the dislocation-free floating-zone crystals, the RDs with levels at $\sim E_c - 0.17$ eV represent not only *A* centers, but also C_i–C_s complexes located near IDCs, in the formation of which *I* defects are involved [30, 33].

4. ENERGY SPECTRUM OF THE LEVELS OF ELEMENTARY PRIMARY DEFECTS

Figure 6 shows the results of determination of the energy levels E_1–E_4 and the position in the band gap of the newly determined EPD level $E_5 \approx E_c - 0.67$ eV, which we tentatively assigned to the *I*-type defects. The shown spectrum of the EPD levels can be expanded by adding two vacancy levels at $\sim E_v + 0.13$ eV and $\sim E_v + 0.05$ eV, which are assumed to be known [3–5, 9, 11].

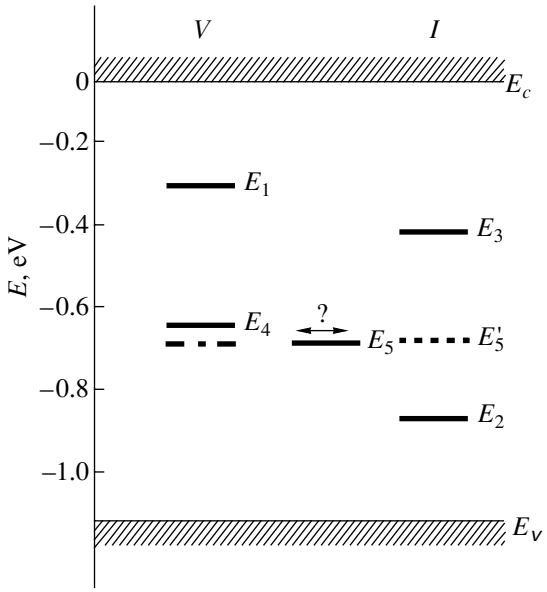

Fig. 6. Energy spectrum of the levels of vacancies and interstitial atoms in the band gap of Si.

It is reasonable to compare the obtained results with the data in the literature, which, in most cases, are ambiguous (hypothetical) in assigning the detected levels to a specific type of EPD.

Naber *et al.* [39] studied how the electrical properties of *n*-Si change under pulsed electron irradiation ($E_e = 30$ MeV, $T = 77$ K) and subsequent annealing of intrinsic defects. It was assumed that the found acceptor defect with a level at $E_c - 0.39$ eV belongs to vacancies, although, in the previous study concerned with diffusion [40], as well as in the later studies related to the low-temperature irradiation of *n*-Si [8, 41], it was suggested that self-interstitial atoms may serve as defects with this energy level (or potential barrier for interaction of the *I* defect with nonorientable vacancies). The levels of these intrinsic defects correlate, although rather vaguely, with the level at E_3, which was identified as corresponding to interstitial atoms in our experiments.

It is believed that, in well-known studies [23, 28, 42], the self-interstitial atom (albeit being in the split dumb-bell configuration, i.e., representing a diinterstitial) has an acceptor level at $\sim E_c - 0.4$ eV and a donor level at $\sim E_v + 0.4$ eV. In contrast to this, the levels at $E_c - 0.25$ eV and $E_c - 0.39$ eV, determined using deep-level transient spectroscopy (DLTS) in the experiments with irradiation of *p*-Si with α particles at $T =$ 77–350 K, were assigned to interstitial atoms in [43]. Although the positions of the former levels correlate with those of the levels E_3 and E_4, and the positions of the latter levels correlate with those of the levels E_1 and E_3, nevertheless, according to our data, the levels E_1 and E_4 belong to vacancies rather than to interstitial atoms.

In study [44], on the basis of data on the diffusion of intrinsic defects obtained by the method of photoelectron emission, the levels at $\sim E_c - 0.15$ eV and at $\sim E_c - 0.31$ eV were attributed to vacancies. The position of the latter correlates with the position of the level E_1, which we also identified as a vacancy level.

It was believed [45], where the DLTS data on accumulation of vacancy and interstitial defects in the space-charge regions of Schottky diodes were interpreted, that the vacancy level is located near $E_c - (0.27–0.30)$ eV. The energies in this range are very close to the value of $E_1 = E_c - 0.28$ eV.

With the use of Hall [46] and DLTS [47] measurements, the effect of the doping level on the production rates of the vacancy-type RDs in high-resistivity (n_0, $p_0 = 5 \times 10^{11}$–3×10^{13} cm^{-3}) and low-resistivity (n_0, $p_0 = 10^{15}$–10^{17} cm^{-3}) Si was studied. On the basis of the obtained results, it was concluded that, presumably, the levels at $\sim E_c - 0.24$ eV and $\sim E_v + 0.19$ eV [47], as well as at $\sim E_c - 0.50$ eV [46], belong to vacancies. The positions of the first two levels are in good agreement with E_1 and E_2, however, with a significant difference: the level E_2 is of another nature. According to our data, this level belongs to interstitial atoms. The position of the third level, as can be seen from Fig. 6, coincides neither with the vacancy levels E_1 and E_3 nor with the interstitial levels E_2, E_4, and E_5. In our opinion, this is caused by incorrect use of the equilibrium value of the Fermi level for evaluation of the positions of the EPD levels in the band gap of high-resistivity Si [46], where, under irradiation, the concentration of nonequilibrium charge carriers is on the same order of magnitude or even exceeds the concentration of equilibrium charge carriers. Thus, in a number of cases, there is partial correlation of the positions and nature of the EPD levels determined here with the data obtained by other researchers using various experimental methods. This validates the results reported here. At the same time, there are discrepancies which, in our opinion, suggest that a new approach is needed both to some published data and to the problem in general.

5. CONCLUSION

On the basis of the experiments we carried out, the nature of energy levels previously found (E_1, E_2, E_3 and E_4) of elementary primary defects was determined. It was ascertained that interstitial Si atoms have energy levels near $E_c - 0.44$ eV and $E_c - 0.86$ eV, while the energy levels at $\sim E_c - 0.28$ eV and $\sim E_c - 0.65$ eV belong to free vacancies. The new experimental data indicate that one more EPD level (presumably, the level of the interstitial I defect) is located near the midgap of Si (at $E_5 \approx E_c - 0.67$ eV). The comparison performed here with the data in the literature, while showing some agreement also showed a number of discrepancies, which, in our opinion, supplement the current state of the problem under consideration.

REFERENCES

1. L. S. Smirnov, in *Physical Processes in Irradiated Semiconductors*, Ed. by L. S. Smirnov (Nauka, Novosibirsk, 1977).
2. J. W. Corbett and J. C. Bourgoin, in *Point Defects in Solids* (Plenum, New York, 1975; Mir, Moscow, 1979).
3. *Problems of Radiation Technology of Semiconductors*, Ed. by L. S. Smirnov (Nauka, Novosibirsk, 1980).
4. V. V. Emtsev and T. V. Mashovets, *Impurities and Point Defects in Semiconductors* (Radio i Svyaz', Moscow, 1981).
5. V. S. Vavilov, V. F. Kiselev, and B. N. Mukashev, *Defects in Silicon and on Its Surface* (Nauka, Moscow, 1990).
6. V. V. Emtsev, T. V. Mashovets, and V. V. Mikhnovich, Fiz. Tekh. Poluprovodn. (St. Petersburg) **26**, 20 (1992) [Sov. Phys. Semicond. **26**, 12 (1992)].
7. Z. V. Basheleĭshvili and T. A. Pagava, Fiz. Tekh. Poluprovodn. (St. Petersburg) **33**, 924 (1999) [Semiconductors **33**, 845 (1999)].
8. G. D. Watkins, in *Lattice Defects in Semiconductors* (Inst. of Physics, London, 1975), p. 1.
9. G. D. Watkins, J. R. Troxell, and A. P. Chatterjee, in *Defects and Radiation Effects in Semiconductors* (Inst. of Physics, London, 1979), p. 16.
10. G. D. Watkins, in *Radiation Damage in Silicon* (Mater. Sci. Forum, London, 1993), Part 2, p. 143.
11. L. C. Kimerling, in *Radiation Effects in Semiconductors* (Inst. of Physics, London, 1977), p. 221.
12. G. D. Watkins and J. R. Troxell, Phys. Rev. Lett. **44**, 593 (1980).
13. G. A. Baraff, E. O. Kane, and M. Schulter, Phys. Rev. B **21**, 5662 (1980).
14. G. D. Watkins, A. P. Chatterjee, and R. Harris, in *Defects and Radiation Effects in Semiconductors* (Inst. of Physics, London, 1981), p. 199.
15. B. N. Mukashev, V. V. Frolov, and L. G. Kolodin, Phys. Lett. A **96**, 358 (1982).
16. V. V. Emtsev, M. A. Margaryan, and T. V. Mashovets, Fiz. Tekh. Poluprovodn. (Leningrad) **18**, 1516 (1984) [Sov. Phys. Semicond. **18**, 950 (1984)].
17. P. S. Gwozdz and J. S. Kochler, Phys. Rev. B **6**, 4571 (1972).
18. J. C. Bourgoin and J. W. Corbett, Radiat. Eff. **36**, 157 (1978).
19. Y. Bar-Yam and J. D. Joannopouls, Phys. Rev. B **30**, 1844 (1984).
20. G. D. Watkins, in *Radiation Damage in Semiconductors* (Dunod, Paris, 1965), p. 97.
21. G. D. Watkins and K. L. Brower, Phys. Rev. Lett. **36**, 1329 (1976).
22. E. I. Blount, J. Appl. Phys. **30**, 1218 (1959).
23. A. Zeeger and W. Frank, in *Radiation and Defects in Semiconductors* (Inst. of Physics, London, 1973), p. 262.
24. Y. H. Lee, R. L. Kleinhenz, and J. W. Corbett, in *Defects and Radiation Effects in Semiconductors* (Inst. of Physics, London, 1979), p. 521.
25. Y. H. Lee, N. N. Gerasimenko, and J. W. Corbett, Phys. Rev. B **14**, 4506 (1976).
26. K. L. Brower, Phys. Rev. B **14**, 872 (1976).

27. R. D. Harris and G. D. Watkins, in *Proceedings of 13th International Conference on Defects in Semiconductors, Coronado, California, 1984* (Metallurgical Soc. of AIME, Warrendale, Pa, 1985), p. 799.
28. A. Zeeger, H. Föll, and W. Frank, in *Radiation Effects in Semiconductors* (Inst. of Physics, London, 1977), p. 56.
29. V. V. Luk'yanitsa, Fiz. Tekh. Poluprovodn. (St. Petersburg) **33**, 921 (1999) [Semiconductors **33**, 842 (1999)].
30. I. I. Kolkovskii, P. F. Lugakov, V. V. Lukjanitsa, and V. V. Shusha, Phys. Status Solidi A **118**, 65 (1990).
31. P. F. Lugakov and V. V. Lukjanitsa, Phys. Status Solidi A **83**, 521 (1984).
32. V. V. Luk'yanitsa, Fiz. Tekh. Poluprovodn. (St. Petersburg) **35**, 513 (2001) [Semiconductors **35**, 491 (2001)].
33. L. I. Murin, Phys. Status Solidi A **83**, 147 (1986).
34. I. I. Kolkovskiĭ and V. V. Luk'yanitsa, Fiz. Tekh. Poluprovodn. (St. Petersburg) **31**, 405 (1997) [Semiconductors **31**, 340 (1997)].
35. R. S. Newman, *Infrared Studies of Crystal Defects* (Taylor and Francis, London, 1973).
36. I. I. Kolkovskiĭ, F. F. Komarov, and V. V. Luk'yanitsa, Dokl. Akad. Nauk Belarusi **45** (3), 59 (2001).
37. I. D. Konozenko, A. K. Semenyuk, and V. I. Khivrich, *Radiation Effects in Silicon* (Naukova Dumka, Kiev, 1974).
38. P. F. Lugakov, V. V. Luk'yanitsa, and V. V. Shusha, Fiz. Tekh. Poluprovodn. (Leningrad) **20**, 1894 (1986) [Sov. Phys. Semicond. **20**, 1188 (1986)].
39. J. A. Naber, C. E. Mallon, and R. E. Leadon, in *Radiation Damage and Defects in Semiconductors* (Inst. of Physics, London, 1973), p. 26.
40. K. P. Chic, Radiat. Eff. **4**, 33 (1970).
41. W. Frank, in *Lattice Defects in Semiconductors* (Inst. of Physics, London, 1975), p. 23.
42. W. Frank, Radiat. Eff. **21**, 119 (1974).
43. Kh. A. Abdullin, B. N. Mukashev, and M. F. Tamendarov, Fiz. Tekh. Poluprovodn. (Leningrad) **25**, 684 (1991) [Sov. Phys. Semicond. **25**, 412 (1991)].
44. V. A. Panteleev, S. N. Ershov, V. V. Chernyakhovskiĭ, and S. N. Nagornykh, Pis'ma Zh. Éksp. Teor. Fiz. **23**, 688 (1976) [JETP Lett. **23**, 633 (1976)].
45. V. V. Bolotov and V. A. Stuchinskiĭ, Fiz. Tekh. Poluprovodn. (Leningrad) **25**, 2168 (1991) [Sov. Phys. Semicond. **25**, 1305 (1991)].
46. P. F. Lugakov and T. A. Lukashevich, Fiz. Tekh. Poluprovodn. (Leningrad) **23**, 581 (1989).
47. V. I. Gubskaya, P. V. Kuchinskii, and V. M. Lomako, Phys. Status Solidi A **85**, 585 (1984).

Translated by Yu. Sin'kov

Semiconductors, Vol. 37, No. 4, 2003, pp. 414–416. Translated from Fizika i Tekhnika Poluprovodnikov, Vol. 37, No. 4, 2003, pp. 432–434.

SEMICONDUCTOR STRUCTURES, INTERFACES, AND SURFACES

Photosensitive Structures Based on $ZnIn_2Se_4$ Single Crystals

A. A. Vaipolin*, Yu. A. Nikolaev*, V. Yu. Rud', Yu. V. Rud'*, and E. I. Terukov***

** Ioffe Physicotechnical Institute, Russian Academy of Sciences, St. Petersburg, 194021 Russia*

*** St. Petersburg State Polytechnic University, St. Petersburg, 195251 Russia*

Submitted July 15, 2002; accepted for publication July 22, 2002

Abstract—Photosensitive structures of surface-barrier and homojunction types have been fabricated for the first time on the basis of $ZnIn_2Se_4$ single crystals. The spectral dependence of the quantum efficiency of photoconversion has been studied and discussed. It is concluded that the structures are promising for commercial applications. *© 2003 MAIK "Nauka/Interperiodica".*

The current interest in studying the physical properties of $A^{II}B_2^{III}C_4^{VI}$ compounds, $ZnIn_2Se_4$ included, is due to their high photosensitivity, high-efficiency photoluminescence, and unique nonlinear optical properties [1–3], which provide the potential for their application in modern optoelectronics. Following this line, our study is devoted to the problem of fabricating photosensitive structures based on single-crystal $ZnIn_2Se_4$.

Single-crystal $ZnIn_2Se_4$ was grown in evacuated (~10^{-5} Torr) quartz ampules by the method of chemical transport reactions, with crystalline iodine as the transport agent. The crystals grown were ~0.1 to 0.2-mm-thick wafers with an area ~ 3×3 mm^2. The dark resistivity of crystals was $\rho \approx 10^5$–10^6 Ω cm, and the free electron density was $n \approx 10^{15}$ cm^{-3} at the temperature $T = 300$ K. With crystals of the same batch, elongated prisms also occurred with a natural faceting typical of ternary compounds with a chalcopyrite lattice [4]. According to [5, 6], $ZnIn_2Se_4$ crystallizes as thiogallate (defective chalcopyrite) with $I4(S_4^2)$ symmetry. According to X-ray diffraction data, our crystals have a tetragonal lattice with unit cell parameters $a = (5.709 \pm 0.002)$ Å and $c = (11.454 \pm 0.05)$ Å. Our measurements of the lattice constants, which are more accurate than those in [5], revealed a slight tetragonal stretching of the $ZnIn_2Se_4$ lattice, which occurs rather infrequently in crystals of ternary compounds with tetrahedral atomic coordination and chalcopyrite or thiogallate-type structures [6].

A characteristic feature in the morphology of $ZnIn_2Se_4$ crystals is the predominant development of the (112) face, which is also typical of other ternary compounds grown from nonstoichiometric melts or from the gas phase. On the whole, the faceting of the grown $ZnIn_2Se_4$ crystals (both lamellar and prismatic) was similar to that observed for crystals with a chalcopyrite structure, e.g., $A^{II}B_2^{III}C_4^{VI}$ compounds. The shape of these crystals was described in detail in [4]. This shape does not correspond to the point symmetry group of the thiogallate structure, which directly contradicts the crystallographic rule stating that the faceting of a crystal must correspond to its symmetry. This may be due to bond dynamics at relatively high crystal growth temperature and to the resulting difference between the real and ideal configurations of tetrahedral bonds [7].

It is necessary to stress that the $ZnIn_2Se_4$ lattice parameters, which were determined with high precision, allowed us to relate this material to semiconductors with a lattice stretched in the [001] direction and characterized by tetragonal strain $\tau = 1 - c/2a \approx -0.3\%$, even though it has been assumed up to now that there is no intrinsic deformation in the $ZnIn_2Se_4$ lattice [5, 6]. The fact that $\tau \neq 0$ is very important because it relates this compound to substances with a pronounced anisotropy of their physical properties.

To fabricate photosensitive structures on the basis of $ZnIn_2Se_4$ crystals, which, until now, have only been obtained with *n*-type conduction [1, 8, 9], we studied contact phenomena and natural doping. These studies have shown that the photovoltaic effect can be obtained upon (i) thermal deposition of pure indium layers onto a mirrorlike (112) surface and (ii) modulation of the deviation from stoichiometry in the surface layer of the crystals. The obtained structures demonstrate a rectification by a factor of ~2–5 at the voltage $U \approx 5$ V, with the forward bias always corresponding to negative voltage applied to the $ZnIn_2Se_4$ crystal. The sign of the photovoltage is independent of the geometric characteristics of structure illumination and the photon energy $\hbar\omega$; it corresponds to the rectification polarity. When the structures are illuminated from the side of the barrier contact or doped surface layer of the $ZnIn_2Se_4$ crystal, the photosensitivity is higher. The maximum

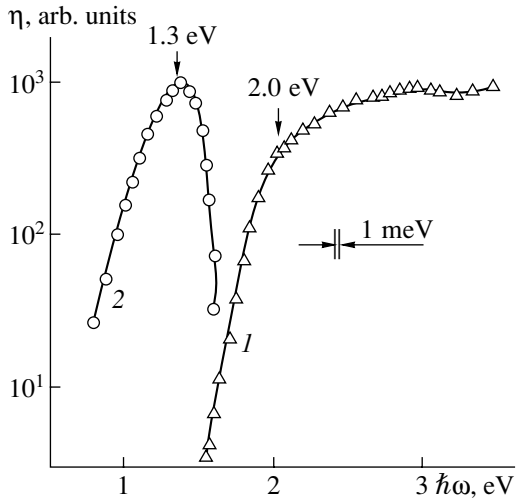

Fig. 1. Spectra of the relative quantum efficiency of photoconversion in the (n' – n)-$ZnIn_2Se_4$ structure. T = 300 K. Sample no. 7. Illumination: (*1*) from the side of the n'-region, (*2*) from the rear side of the n-$ZnIn_2Se_4$ crystal.

voltage responsiveness obtained in the best structures, In/n-$ZnIn_2Se_4$ and (n' – n)-$ZnIn_2Se_4$, was $S_U^m \approx 10$ V W^{-1} at T = 300 K.

Figure 1 shows a typical spectrum of the relative quantum efficiency η of an isotype (n' – n)-$ZnIn_2Se_4$ homojunction illuminated from the doped layer side.

It is necessary to stress that In/$ZnIn_2Se_4$ structures fabricated with the same crystals exhibit similar spectral dependences of the photosensitivity η(ħω). A specific feature of these structures is that the range of a sharp rise of photosensitivity near the photon energy ħω ≈ 1.5 eV coincides with the onset of fundamental absorption in $ZnIn_2Se_4$ crystals [1, 10]. The absence of a decrease in η high above the fundamental absorption edge, up to 3.6 eV, indicates a high efficiency of collection of photogenerated electron–hole pairs. Figure 2 shows the results of a graphical analysis of the photosensitivity spectrum of the structures, obtained in terms of the theory of band-to-band absorption in semiconductors [11]. It can be seen that the long-wavelength portion of the photoactive absorption spectra in the range ħω = 1.7–2.1 eV is well approximated by the dependence $(\eta\hbar\omega)^{1/2} = f(\hbar\omega)$, typical of indirect interband optical transitions, whose extrapolation $(\eta\hbar\omega)^{1/2} \longrightarrow 0$ yields the band gap for indirect optical transitions, $E_G^{in} \approx 1.61$ eV. In the high-energy range, at 2.2–2.8 eV, the η(ħω) spectra for structures of both types are approximated with the relation $(\eta\hbar\omega)^2 = f(\hbar\omega)$, which is typical of direct interband optical transitions, and its extrapolation $(\eta\hbar\omega)^2 \longrightarrow 0$ yields an estimate of the band gap for direct optical transitions, $E_G^d \approx 2.1$ eV at T = 300 K.

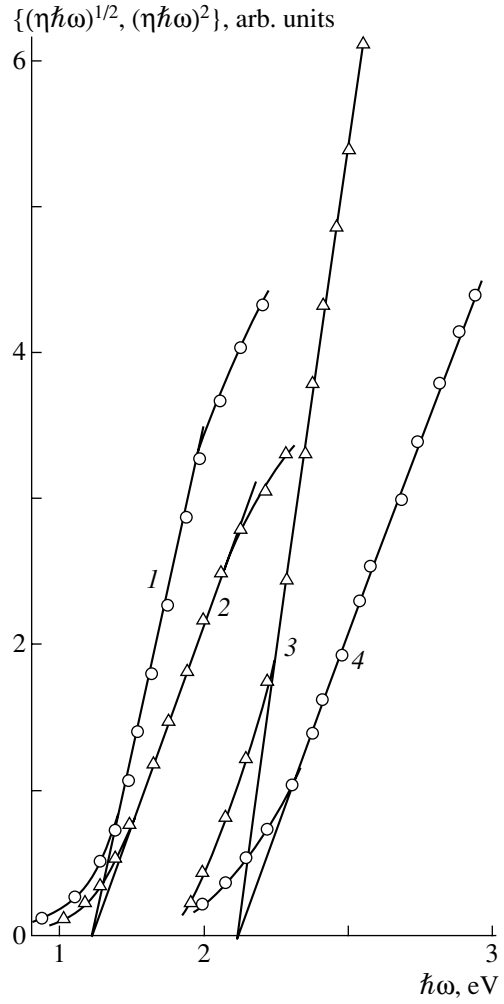

Fig. 2. (*1, 2*) $(\eta\hbar\omega)^{1/2} = f(\hbar\omega)$ and (*3, 4*) $(\eta\hbar\omega)^2 = f(\hbar\omega)$ dependences for (*1, 3*) In/n-$ZnIn_2Se_4$ structure, sample no. 5 and (*2, 4*) (n' – n)-$ZnIn_2Se_4$ structure, sample no. 6. T = 300 K.

It is worth noting that E_G^{in} estimated from the photosensitivity spectra of structures based on $ZnIn_2Se_4$ crystals coincides with the value obtained from the spectra of optical absorption α [1, 8]. With respect to the approximation of the high-energy portion of the η(ħω) curves, the conclusion concerning the type of the transitions is also in agreement with the results of α(ħω) analysis [8]; however, the E_G^d value found from the η(ħω) spectra is higher than that obtained from α(ħω). This may be due to difficulties encountered in the fabrication of thin $ZnIn_2Se_4$ samples and to the inaccuracy of α(ħω) measurement in the range of strong absorption, associated with the onset of direct optical transitions.

The photosensitivity spectrum of $ZnIn_2Se_4$ surface-barrier structures and homojunctions illuminated from the rear side of the crystal (Fig. 1, curve *2*) differs in the appearance of the short-wavelength falloff, which cor-

relates corresponds to the beginning of the sharp rise of η in the spectra recorded under illumination from the side of the energy barrier (Fig. 1, curve *1*). The short-wavelength falloff of η is due to a decrease, with increasing photon energy, in the thickness of the layer in which photoexcited carriers are generated, so that it becomes increasingly remote from the active region of a structure.

The obtained photosensitive surface-barrier and homojunction structures based on *n*-$ZnIn_2Se_4$ single crystals can find application as detectors of unpolarized radiation in the spectral range from 0.6 to 3.6 eV. Taking into account the discovered intrinsic deformation of the $ZnIn_2Se_4$ unit cell, it is necessary to note the possibility of applying these structures as detectors of linearly polarized radiation.

REFERENCES

1. A. N. Gergobiani, S. I. Radautsan, and I. M. Tiginyanu, Fiz. Tekh. Poluprovodn. (Leningrad) **19**, 193 (1985) [Sov. Phys. Semicond. **19**, 121 (1985)].
2. A. N. Gergobiani, V. S. Donu, Z. P. Plyukhina, *et al.*, Fiz. Tekh. Poluprovodn. (Leningrad) **17**, 1524 (1983) [Sov. Phys. Semicond. **17**, 970 (1983)].
3. B. F. Levine, C. G. Bethea, and N. M. Kasper, IEEE J. Quantum Electron. **10**, 904 (1972).
4. *II–IV–V_2 Semiconductors*, Ed. by Yu. A. Valov and N. A. Goryunova (Sovetskoe Radio, Moscow, 1968).
5. H. Hahn, G. Frank, and W. Klinger, Z. Anorg. Allg. Chem. **279**, 241 (1955).
6. *Handbook on Physicochemical Properties of Semiconductor Materials* (Nauka, Moscow, 1975).
7. A. A. Vaĭolin, Fiz. Tverd. Tela (Leningrad) **32**, 2086 (1990) [Sov. Phys. Solid State **32**, 1212 (1990)].
8. N. M. Mekhtiev, Z. Z. Guseĭnov, and É. Yu. Salaev, Fiz. Tekh. Poluprovodn. (Leningrad) **18**, 1088 (1984) [Sov. Phys. Semicond. **18**, 677 (1984)].
9. N. M. Mekhtiev, Doctoral Dissertation (Inst. Fiz. Akad. Nauk Azerb., Baku, 1991).
10. R. Tzykorko and J. Filipowcz, Jpn. J. Appl. Phys., Suppl. **49** (19-3), 153 (1980).
11. S. Sze, *Physics of Semiconductor Devices* (Wiley, New York, 1981; Mir, Moscow, 1984).

Translated by D. Mashovets

Semiconductors, Vol. 37, No. 4, 2003, pp. 417–425. Translated from Fizika i Tekhnika Poluprovodnikov, Vol. 37, No. 4, 2003, pp. 435–442.

SEMICONDUCTOR STRUCTURES, INTERFACES, AND SURFACES

Special Features of Electron Scattering at $Al_xGa_{1-x}As/AlAs(001)$ Interfaces

S. N. Grinyaev, G. F. Karavaev*, and V. N. Chernyshov

Kuznetsov Physicotechnical Institute, Tomsk State University, pl. Revolyutsii 1, Tomsk, 634050 Russia

** e-mail: karavaev@elefot.tsu.ru*

Submitted September 2, 2002; accepted for publication September 3, 2002

Abstract—The effect of total reflection of an electron wave from an interface was investigated for $Al_xGa_{1-x}As/AlAs$ structures. Analysis was performed on the basis of calculations by the pseudopotential method as well as analytically and numerically in terms of the three-valley model. The appearance of zero in the coefficient of electron transmission through the $Al_xGa_{1-x}As/AlAs$ interface was observed at a certain energy in the interval between the bottom of the X_1 valley in AlAs and the bottom of the X_1 valley in $Al_xGa_{1-x}As$ and was shown to be induced by the multivalley character of the electron energy spectrum. It is ascertained that this total reflection is due to the mutual compensation of contributions from various valleys and is not related to any resonance interface state. © *2003 MAIK "Nauka/Interperiodica".*

1. INTRODUCTION

Much attention is being given to the investigation of electron processes in semiconductor heterostructures. Of special interest is the study of the so-called Γ–*X* mixing of electrons at $Al_xGa_{1-x}As/Al_yGa_{1-y}As(001)$ interfaces. Various manifestations of this mixing were investigated both theoretically and experimentally [1–15]. However, the total reflection of an electron wave from a heterointerface for a certain specific electron energy, which was found in theoretical calculations, has remained unstudied experimentally. We discuss this effect in more detail by the example of the GaAs/AlAs heterostructure. The conduction-band minimum is located in GaAs at the point Γ of the Brillouin zone; an additional minimum of interest is located near the point *X*(001) forming a so-called "camel-back" (CB) structure. In AlAs, the conduction-band minimum is at the point *X* of the Brillouin zone, whereas an analogue of the CB structure is observed in the region of complex values of wave vectors at lower energies. Due to the inequality $E_\Gamma(GaAs) < E_X(AlAs) < E_X(GaAs)$, there is an energy interval from the conduction-band bottom in AlAs to the minimum E_0 of the CB structure in GaAs in which two propagating waves can exist from the left and from the right of the GaAs/AlAs(001) interface—Γ in the GaAs layer and *X* in the AlAs layer. Electron-wave propagation through the GaAs/AlAs(001) heterostructure has to be accompanied by its Γ–*X* conversion; therefore, this conversion plays an important role and, thus, attracts much great attention. It is within this interval of energies where the electron wave undergoes total reflection from the heterointerface. First evidence for the appearance of a zero in the transmission coefficient was reported by Ando and Akera [11], who found this effect in calculations of the transmission coefficient for an electron through the interface in the $Al_{0.32}Ga_{0.68}As/Al_{0.5}Ga_{0.5}As$ structure. It was assumed [11] that the appearance of a zero was associated with the existence of a resonance interface state formed from damped waves at energies located near the bottom of the CB structure of $Al_{0.32}Ga_{0.68}As$ and near the *X* level in $Al_{0.5}Ga_{0.5}As$. In our calculations, a zero in the transmission coefficient is also observed for the electron waves traveling through the $Al_xGa_{1-x}As/AlAs(001)$ structures in the energy interval from the X_1 level in AlAs to the X_1 level in $Al_xGa_{1-x}As$. This study is devoted to investigating the reasons for the appearance of this zero on the basis of calculations by the pseudopotential method, as well as analytically and numerically in terms of the simplified three-valley model.

2. PSEUDOPOTENTIAL CALCULATION

Electron tunneling through the GaAs/AlAs(001) interface was calculated using a model with a potential discontinuity at the heterointerface. As the heterointerface for this system, we choose a crystal plane ($z = 0$) composed of arsenic atoms, which are common for both components of the heterostructure. We will now outline the basic points in solving the problem. The calculation method is explicitly described elsewhere [12, 13]. We assume that GaAs is located to the left of the heterointerface (in the region $z < 0$), and AlAs, to the right. The general solutions Ψ^n to the Schrödinger equation in the regions with the number n ($n = \alpha$ for GaAs and $n = \beta$ for AlAs) for the given values of the energy E and the wave-vector component $\mathbf{k}_\parallel$, which is parallel to the interface, can be represented as

$$\Psi^n = \sum_\nu A_\nu^n \Psi_{\mathbf{k}_\nu^n} + \sum_\mu B_\mu^n \Psi_{\mathbf{k}_\mu^n}, \qquad (1)$$

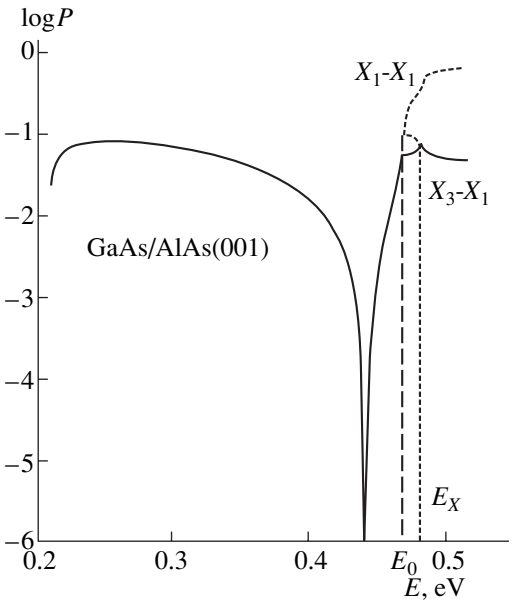

Fig. 1. The coefficient of electron transmission $P(E)$ through a single GaAs/AlAs(001) interface from Γ_1, X_1, and X_3 valleys in GaAs to the X_1 valley of AlAs. The energies E_0 and E_X correspond to the bottom of the CB structure and to an extremum of the conduction band at the point X of GaAs, respectively.

where $\mathbf{k}^n_{\nu(\mu)} = \mathbf{k}_\parallel + \mathbf{k}^n_{z\nu(\mu)}$ are the wave vectors for the nth subsystem, $\mathbf{k}^n_{z\nu(\mu)} = k^n_{z\nu(\mu)}\mathbf{n}_z$, $\mathbf{n}_z$ is the vector of the normal to the interface, the numbers $k^n_{z\nu(\mu)}$ can be complex, and $\Psi_{\mathbf{k}^n_{\nu(\mu)}}$ are the partial solutions to the Schrödinger equation in the medium with the number n corresponding to the wave vector $\mathbf{k}^n_{\nu(\mu)}$. The subscript ν designates the waves propagating (damped) from left to right, and the subscript μ designates those propagating (damped) from right to left. The coefficients A^n_ν and B^n_μ in (1) can be found from the matching conditions at the heterointerface and the conditions at infinity. The matching conditions, i.e., the continuity conditions for the wave functions and their first derivatives at the heterointerface, can be written using the scattering matrix S [2, 12–15] as

$$\begin{pmatrix}\mathbf{A}^\beta\\ \mathbf{B}^\alpha\end{pmatrix} = \mathbf{S}\begin{pmatrix}\mathbf{A}^\alpha\\ \mathbf{B}^\beta\end{pmatrix}, \tag{2}$$

where $\mathbf{A}^n$ and $\mathbf{B}^n$ are column vectors with components A^n_ν and B^n_μ, respectively. The dimension of the matrix S is equal to the number of partial solutions appearing in (1).

Relationship (2) can be represented as

$$\begin{aligned}\mathbf{A}^\beta &= \mathbf{S}_{11}\mathbf{A}^\alpha + \mathbf{S}_{12}\mathbf{B}^\beta,\\ \mathbf{B}^\alpha &= \mathbf{S}_{21}\mathbf{A}^\alpha + \mathbf{S}_{22}\mathbf{B}^\beta,\end{aligned} \tag{3}$$

where $\mathbf{S}_{ij}$ ($i, j = 1, 2$) are square matrices with a dimension twice as low as that of $\mathbf{S}$. We now consider the problem of an electron wave traveling from left to right, i.e., from GaAs to AlAs. In this case, solution (1) contains no waves traveling from right to left in AlAs and also no solutions $\Psi_{\mathbf{k}^n_{\nu(\mu)}}$ increasing indefinitely when receding from the heterointerface. In order to satisfy these conditions, we have to set $\mathbf{B}^\beta = 0$, $A^n_\nu = \delta_{\nu\nu_0}$, where ν_0 is the number of the incident wave. In this case, relationships (3) can be written as

$$\begin{aligned}\mathbf{A}^\beta &= \mathbf{S}_{11}\mathbf{A}^\alpha,\\ \mathbf{B}^\alpha &= \mathbf{S}_{21}\mathbf{A}^\alpha.\end{aligned} \tag{4}$$

The electron transmission coefficient corresponding to a transition from the state with the number ν_0 in GaAs to the state with the number ν in AlAs (provided that the wave functions of these states are normalized to the group velocities in media) is equal to

$$P_{\nu\nu_0} = \left|A^\beta_\nu\right|^2 = \left|(\mathbf{S}_{11})_{\nu\nu_0}\right|^2. \tag{5}$$

Thus, for solving the problem of the electron tunneling, it is necessary to calculate the matrix elements $\mathbf{S}_{11}$. These matrix elements can be written as [12]

$$\begin{aligned}(\mathbf{S}_{11})_{\nu\nu_0} &= (\mathbf{Q}_2^{-1}\mathbf{Q}_1)_{\nu\nu_0},\\ \mathbf{Q}_2 &= (\mathbf{P}_2^\alpha)^{-1}\mathbf{P}_1^\beta - (\mathbf{D}_2^\alpha)^{-1}\mathbf{D}_1^\beta,\\ \mathbf{Q}_1 &= (\mathbf{P}_2^\alpha)^{-1}\mathbf{P}_1^\alpha - (\mathbf{D}_2^\alpha)^{-1}\mathbf{D}_1^\alpha,\end{aligned} \tag{6}$$

where $\mathbf{D}^n_i$ and $\mathbf{P}^n_i$ ($i = 1, 2$) are the matrices whose elements are the Fourier components of the projections onto the interface for the partial solutions $\Psi_{\mathbf{k}^n_\nu}$ ($i = 1$) and $\Psi_{\mathbf{k}^n_\mu}$ ($i = 2$) and also their first derivatives, respectively.

In order to find the functions $\Psi_{\mathbf{k}^n_{\nu(\mu)}}$, we applied the pseudopotential method using local atomic pseudopotentials defined in [16] on the basis of experimental data and the results of *ab initio* calculations of the band spectrum for GaAs and AlAs. Using these potentials for $\mathbf{k}_\parallel = 0$, we obtain 42 independent partial solutions $\Psi_{\mathbf{k}^n_{\nu(\mu)}}$ to the Schrödinger equation in each medium and, consequently, the scattering matrix $\mathbf{S}$ has the dimension of (42×42). For improving the accuracy of the calculations, we took into account approximately 150 plane waves in the expansion of wave functions in addition to

the plane-wave basis according to the Levdin perturbation theory.

Figure 1 shows the coefficients $P(E)$ of transmission from the Γ and X valleys of the lower conduction band for GaAs into the X_1 valley of AlAs for the case of $\mathbf{k}_{\|} = 0$, which corresponds to the propagation of electrons in the direction normal to the heterointerface. The energies are reckoned from the bottom of the GaAs conduction band. The extrema of the X_1 valleys in GaAs and AlAs are located at energies E_X equal to 0.4818 and 0.2082 eV, respectively, while the bottom of the CB structure of GaAs is at the energy $E_0 = 0.4672$ eV. At the energy $E_d = 0.441$ eV, the total reflection (TR) of the electron wave takes place. The states with this energy are designated further as the TR states.

In Fig. 2, we show the probability-density distribution averaged over the interface plane for two TR states corresponding to the electron incidence on the heterointerface both from the left (the solid line) and from the right (the dotted line). When the electrons are scattered from the Γ_1 valley of GaAs into the X_1 valley of AlAs, the probability density oscillates in the GaAs region away from the interface due to the interference of the incident and reflected Γ waves. Oscillations with a large period depend on the behavior of envelope wave functions, and frequent oscillations are associated with a variation in periodic functions. When electrons are scattered from the X_1 valley of AlAs to the Γ_1 valley of GaAs, the TR-state density increases due to decreasing electron group velocity; in addition, due to the closeness of envelope-function periods to those of the periodic parts of the Bloch functions, beats arise in this density. As can be seen from Fig. 2, only a small burst in the density amplitude near the heterointerface is observed in both cases; therefore, the TR states can hardly be considered as resonance interface states. Calculations show that there are no features in the electron density near the heterointerface also for the states with energies close to E_d.

It is known that the resonance states manifest themselves in a characteristic way in the scattering matrix; specifically, if there are resonance states, the scattering matrix must have a pole near the real energy axis. As applied to our problem, this statement follows from relationships (2) and (4). In order to clarify the character of the TR states, we considered an Argand diagram for the scattering-matrix element $(S_{11})_{X\Gamma}$, which relates the amplitude of the wave traveling in the X_1 valley of AlAs to that of the wave incident from the Γ_1 valley of GaAs [17]. If the structure has an isolated resonance state, this diagram must constitute a circle whose parameters are related to the position of the scattering-matrix pole in the complex energy region. In the case under consideration, the diagram resembles only a part of a circle (Fig. 3); therefore, the completely formed resonance does not correspond to this diagram. Direct calculations of the scattering matrix in the complex-energy region verified that this matrix actually has no pole near the real energy axis.

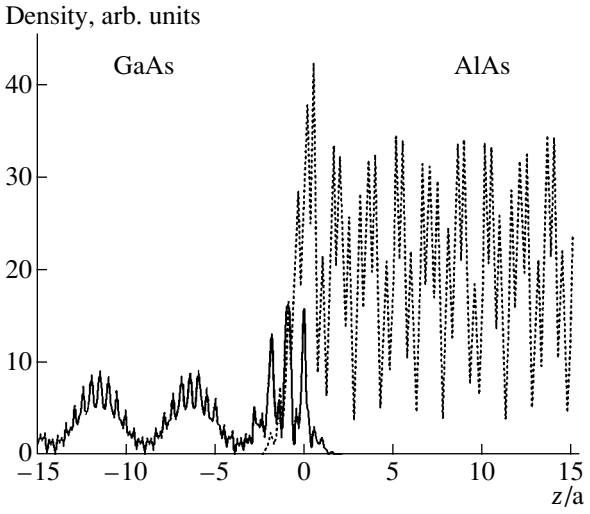

Fig. 2. The probability density for the TR states averaged over the (001) interface plane for Γ_1(GaAs) ⟶ X_1(AlAs) (solid line) and X_1(AlAs) ⟶ Γ_1(GaAs) (dotted line) electron scattering. Here, a is the lattice constant, and z is the coordinate along the heterostructure axis.

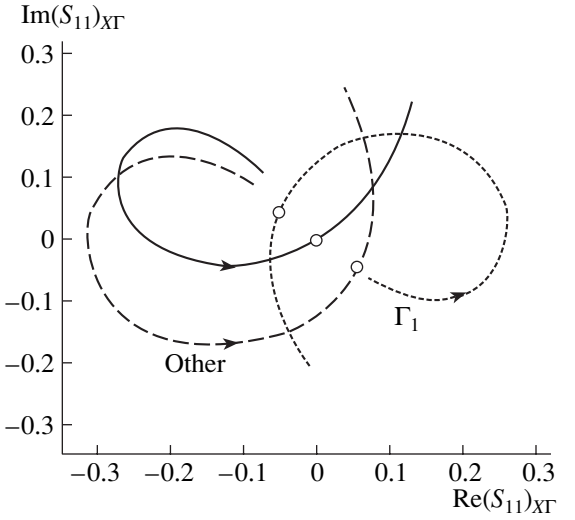

Fig. 3. Argand diagram for the scattering-matrix element $(S_{11})_{X\Gamma}$ in the energy interval E_X(AlAs) < E < E_0(GaAs) (solid line). The arrow indicates the direction of the energy increase. The circles correspond to the energy E_d. The dashed lines designate the contributions from the "virtual" processes (scaled down by a factor of five) related to the Γ_1 wave and all of the other waves.

The passage of the electron wave through the interface can be considered a result of the interaction between various virtual processes. From formula (6) for the matrix element $(S_{11})_{X\Gamma}$, it follows that the incident Γ_1 wave is first transformed into the reflected waves in GaAs (according to the matrix $\mathbf{Q}_1$), which are

thereafter transformed into the transmitted X_1 wave in AlAs (according to the matrix $\mathbf{Q}_2$). Various terms in the product of matrices $(\mathbf{Q}_2^{-1}\mathbf{Q}_1)_{X\Gamma}$ correspond to virtual processes. The major contributions to this sum are made by the terms associated with the transformation of the reflected Γ_1, X_1, and X_3 waves, the major role being played by the X waves in the neighborhood of the energy E_d. For energies lower than E_0, the designations X_1 and X_3 correspond to two states of the CB structure in GaAs. Figure 3 shows the partial contributions from the Γ waves and from all the remaining reflected waves in GaAs to the Argand diagram. The summarized amplitude $(S_{11})_{X\Gamma}$ is seen to be the result of the compensation of these contributions. It is simpler to ascertain the compensation mechanism by taking into account only Γ_1, X_1, and X_3 waves in (6). In this approximation, after inverting the matrix $\mathbf{Q}_2$, we obtain

$$(\mathbf{S}_{11})_{X\Gamma} = \{[(\mathbf{Q}_2)_{X_1\bar{X}_3}(\mathbf{Q}_2)_{X_3\bar{\Gamma}} - (\mathbf{Q}_2)_{X_3\bar{X}_3}(\mathbf{Q}_2)_{X_1\bar{\Gamma}}](\mathbf{Q}_1)_{\Gamma\Gamma} + [(\mathbf{Q}_2)_{\Gamma\bar{\Gamma}}(\mathbf{Q}_2)_{X_3\bar{X}_3} - (\mathbf{Q}_2)_{\Gamma\bar{X}_3}(\mathbf{Q}_2)_{X_3\bar{\Gamma}}](\mathbf{Q}_1)_{X_1\Gamma} - [(\mathbf{Q}_2)_{\Gamma\bar{\Gamma}}(\mathbf{Q}_2)_{X_1\bar{X}_3} - (\mathbf{Q}_2)_{\Gamma\bar{X}_3}(\mathbf{Q}_2)_{X_1\bar{\Gamma}}](\mathbf{Q}_1)_{X_3\Gamma}\}/\det(\mathbf{Q}_2). \quad (7)$$

Here, the bar marks the states in AlAs; and the left and right symbols correspond to the reflected and incident waves, respectively. The wave functions of the reflected X states of the GaAs CB band structure are mutually complex conjugate. As can be seen from formula (7), the contributions of these waves appear with opposite signs. In the difference of these wave projections on the interface, the principal components for the surface plane waves are canceled; therefore, the major contributions in (7) of the virtual X_1 and X_3 processes compensate one another to a great extent. Similar compensation also takes place in the virtual Γ process. The remaining contributions of the X and Γ processes also appear with opposite signs and compensate one another due to the closeness of the projection of Γ functions for GaAs to that for AlAs.

We also considered the oblique incidence of electrons on the heterointerface for various directions of $\mathbf{k}_\parallel$ for values $|\mathbf{k}_\parallel| < 0.04 \cdot 2\pi/a$. In all of the cases, we observed total reflection, with the energy E_d increasing steadily with $|\mathbf{k}_\parallel|$. At the end of this interval, the variation in the energy E_d amounted to 0.03 eV, which approximately corresponded to the thermal energy at room temperature and to the interval of small values of the transmission coefficient (see Fig. 1). Therefore, we can expect that this feature of $P(E)$ will be observed in the GaAs/AlAs(001) heterostructures at reasonably low temperatures.

3. THREE-VALLEY MODEL

The above circumstances make it possible to perform a more careful analysis of the appearance of a zero in the coefficient of electron transmission through an abrupt GaAs/AlAs(001) heterointerface for $\mathbf{k}_\parallel = 0$ on the basis of simpler models. These are the models based on the envelope-function method and a correct choice of the matching conditions for such functions. To determine the matching-matrix elements for the envelope functions, we used the procedure described in detail previously [18, 19]. This approach is based on the use of the three-valley approximation (the Γ_1, X_1, and X_3 valleys) and the choice of corresponding real Bloch functions. Under these matching conditions, if the heterointerface passes through As atoms (the plane $z = 0$), the envelope functions for the Bloch wave functions of the Γ_1 and X_1 levels and the derivative of the envelope functions for the Bloch function of the X_3 level are linked by three linear relationships with real coefficients, while the derivatives of the Γ_1 and X_1 envelopes and the X_3 envelope are linked by three other relationships with real coefficients. Consequently, there are 18 different matching-matrix elements altogether.

The matching condition for the envelope functions can be represented as

$$\begin{pmatrix} F^\alpha_{\Gamma_1} \\ F^\alpha_{X_1} \\ a\frac{\partial}{\partial z}F^\alpha_{X_3} \end{pmatrix} = T_1 \begin{pmatrix} F^\beta_{\Gamma_1} \\ F^\beta_{X_1} \\ a\frac{\partial}{\partial z}F^\beta_{X_3} \end{pmatrix} \begin{pmatrix} a\frac{\partial}{\partial z}F^\alpha_{\Gamma_1} \\ a\frac{\partial}{\partial z}F^\alpha_{X_1} \\ F^\alpha_{X_3} \end{pmatrix} = T_2 \begin{pmatrix} a\frac{\partial}{\partial z}F^\beta_{\Gamma_1} \\ a\frac{\partial}{\partial z}F^\beta_{X_1} \\ F^\beta_{X_3} \end{pmatrix}, \quad (8)$$

where the envelope functions F_γ and their derivatives normal to the interface are calculated at the heterointerface plane; the superscripts α and β designate various materials composing the heterostructure; a is the lattice constant; and the matrices T_1 and T_2 for the $Al_xGa_{1-x}As/AlAs$ heterostructures were determined by using the pseudopotentials from [20] and have the form

$$T_1 = \begin{pmatrix} 1 - 0.0144y & 0.0732y & -0.0058y \\ 0.0649y & 1 + 0.0601y & 0.0051y \\ -1.5182y & -0.3072y & 1 - 0.1261y \end{pmatrix},$$
$$T_2 = \begin{pmatrix} 1 - 0.1245y & -0.0042y & -0.1483y \\ 0.4270y & 1 - 0.0082y & -0.0113y \\ -0.0519y & -0.0028y & 1 + 0.0411y \end{pmatrix}. \quad (9)$$

Here, $y = 1 - x$, where x is the Al content; and the superscripts α and β designate the solid solution and AlAs, respectively. It should be noted that, for the $GaAs/Al_xGa_{1-x}As$ heterostructures (the superscripts α and β correspond to GaAs and $Al_xGa_{1-x}As$), the matrices T_1 and T_2 are determined for $y = x$. We performed calculations using this model and, in all of the cases, obtained results virtually coinciding with the data of exact pseudopotential calculations.

However, a descriptive representation of the factors leading to the appearance of a zero in the transmission coefficient for the three-valley model is hampered due to the exceptionally cumbersome expressions obtained using the computer systems of analytical calculations. Therefore, we adopt simplified matching conditions for the envelope functions suggested by Ando and Akera [11] and refined in [21, 22]. These matching conditions have the form

$$F_\Gamma^\alpha = F_\Gamma^\beta, \quad a\frac{m_0}{m_\Gamma^\alpha}\frac{\partial}{\partial z}F_\Gamma^\alpha = a\frac{m_0}{m_\Gamma^\beta}\frac{\partial}{\partial z}F_\Gamma^\beta + tF_{X_3}^\beta,$$

$$F_{X_3}^\alpha = F_{X_3}^\beta, \quad a\frac{m_0}{m_{X_3}^\alpha}\frac{\partial}{\partial z}F_{X_3}^\alpha = a\frac{m_0}{m_{X_3}^\beta}\frac{\partial}{\partial z}F_{X_3}^\beta + tF_\Gamma^\beta, \quad (10)$$

$$F_{X_1}^\alpha = F_{X_1}^\beta, \quad a\frac{m_0}{m_{X_1}^\alpha}\frac{\partial}{\partial z}F_{X_1}^\alpha = a\frac{m_0}{m_{X_1}^\beta}\frac{\partial}{\partial z}F_{X_1}^\beta,$$

where $m_\Gamma^{\alpha,\beta}$, $m_{X_3}^{\alpha,\beta}$ and $m_{X_1}^{\alpha,\beta}$ are the effective masses; t is the dimensionless parameter of the Γ–X mixing; and m_0 is the free-electron mass. Here, the superscript α corresponds to quantities in GaAs, and β, to those in AlAs. It is clear that these matching conditions markedly differ from "exact" conditions (8) and (9) that we found; nevertheless, it turns out that they lead to qualitatively valid results.

In the context of the model under consideration, the envelope functions have the form

$$F_\Gamma(z) = A_\Gamma\exp(ik_\Gamma z) + B_\Gamma\exp(-ik_\Gamma z),$$

$$F_{X_1}(z) = \sum_{j=1,2}[A_j\exp(ik_j z) + B_j\exp(-ik_j z)], \quad (11)$$

$$F_{X_3}(z) = \sum_{j=1,2}[\eta(k_j)A_j\exp(ik_j z) - \eta(k_j)B_j\exp(-ik_j z)].$$

Here, the coefficients A are the amplitudes of the waves propagating (damped) from left to right, and the coefficients B are the amplitudes of the waves propagating (damped) from right to left; the wave numbers k_j and the coefficients η_{k_j} in the exponents are determined for the given energy E from the solution to the corresponding problem in terms of the kp model. It should be noted that the coefficients A and B are somewhat different here from the corresponding coefficients in (1), while the numbers k_j have the same meaning as $k_{z\nu(\mu)}^n$ introduced in (1).

The envelope X functions satisfy the set of equations

$$\begin{pmatrix} E_{X_3} + \dfrac{p^2}{2m_{X_3}} - E & \dfrac{\langle X_3|p|X_1\rangle p}{m_0} \\ \dfrac{\langle X_1|p|X_3\rangle p}{m_0} & E_{X_1} + \dfrac{p^2}{2m_{X_1}} - E \end{pmatrix}\begin{pmatrix} F_{X_3} \\ F_{X_1} \end{pmatrix} = 0, \quad (12)$$

which accounts for the interaction between the X_1 and X_3 valleys; the interaction with the remaining valleys is taken into account in the effective masses m_{X_1} and m_{X_3}, $p = -i\hbar\dfrac{\partial}{\partial z}$; E_{X_1} and E_{X_3} are the energies of the X_1 and X_3 valleys; and $\langle X_1|p|X_3\rangle$ is the matrix element of the momentum for the Bloch wave functions. From the solution to equation (12), we can find two wave numbers, k_1 and k_2, involved in the expressions for F_{X_1} and also the factors

$$\eta(k_j) = -\frac{\langle X_3|p|X_1\rangle\hbar k_j}{(E_{X_3} + \hbar^2k_j^2/2m_{X_3} - E)m_0} = \frac{(E_{X_1} + \hbar^2k_j^2/2m_{X_1} - E)}{\langle X_3|p|X_1\rangle\hbar k_j}, \quad (13)$$

involved in the envelope function F_{X_3}. In order to describe the Γ electrons, we use the single-valley approximation with allowance for nonparabolicity, which enables us, for a given energy E, to find two solutions $\sim\exp[\pm ik_\Gamma z]$ with the complex wave numbers $k_\Gamma(E)$ in the general case.

From the six matching conditions (10), we obtain six equations for the coefficients $A_\Gamma^{\alpha,\beta}$, $A_j^{\alpha,\beta}$, $B_\Gamma^{\alpha,\beta}$, and $B_j^{\alpha,\beta}$ for the waves propagating from left to right and from right to left:

$$\begin{aligned} A_\Gamma^\alpha + B_\Gamma^\alpha &= A_\Gamma^\beta + B_\Gamma^\beta, \\ \frac{am_0}{m_\Gamma^\alpha}ik_\Gamma^\alpha[A_\Gamma^\alpha - B_\Gamma^\alpha] &= \frac{am_0}{m_\Gamma^\beta}ik_\Gamma^\beta[A_\Gamma^\beta - B_\Gamma^\beta] \\ &\quad + t\sum_{j=1,2}\eta^\beta(k_j^\beta)[A_j^\beta - B_j^\beta], \\ \sum_{j=1,2}\eta^\alpha(k_j^\alpha)[A_j^\alpha - B_j^\alpha] &= \sum_{j=1,2}\eta^\beta(k_j^\beta)[A_j^\beta - B_j^\beta], \\ \frac{am_0}{m_{X_3}^\alpha}i\sum_{j=1,2}k_j^\alpha\eta^\alpha(k_j^\alpha)[A_j^\alpha + B_j^\alpha] &= \frac{am_0}{m_{X_3}^\beta}\sum_{j=1,2}k_j^\beta\eta^\beta(k_j^\beta)[A_j^\beta + B_j^\beta] + t[A_\Gamma^\beta + B_\Gamma^\beta], \end{aligned} \quad (14)$$

$$\sum_{j=1,2}[A_j^\alpha + B_j^\alpha] = \sum_{j=1,2}[A_j^\beta + B_j^\beta],$$

$$\frac{am_0}{m_{X_1}^\alpha}\sum_{j=1,2} ik_j^\alpha[A_j^\alpha - B_j^\alpha] = \frac{am_0}{m_{X_1}^\beta}\sum_{j=1,2} ik_j^\beta[A_j^\beta - B_j^\beta].$$

Assuming the coefficients for all the waves incident on the heterointerface to be equal to zero except the Γ waves in the GaAs semiconductor, we find that

$$A_\Gamma^\alpha + B_\Gamma^\alpha = A_\Gamma^\beta,$$

$$\frac{am_0}{m_\Gamma^\alpha} ik_\Gamma^\alpha[A_\Gamma^\alpha - B_\Gamma^\alpha] = \frac{am_0}{m_\Gamma^\beta} ik_\Gamma^\beta A_\Gamma^\beta + t\sum_{j=1,2}\eta^\beta(k_j^\beta)A_j^\beta,$$

$$-\sum_{j=1,2}\eta^\alpha(k_j^\alpha)B_j^\alpha = \sum_{j=1,2}\eta^\beta(k_j^\beta)A_j^\beta,$$

$$\frac{am_0}{m_{X_3}^\alpha} i\sum_{j=1,2} k_j^\alpha\eta^\alpha(k_j^\alpha)B_j^\alpha = \frac{am_0}{m_{X_3}^\beta} i\sum_{j=1,2} k_j^\beta\eta^\beta(k_j^\beta)A_j^\beta + tA_\Gamma^\beta, \quad (15)$$

$$\sum_{j=1,2} B_j^\alpha = \sum_{j=1,2} A_j^\beta,$$

$$-\frac{am_0}{m_{X_1}^\alpha}\sum_{j=1,2} ik_j^\alpha B_j^\alpha = \frac{am_0}{m_{X_1}^\beta}\sum_{j=1,2} ik_j^\beta A_j^\beta.$$

We call attention to the fact that the third, fifth, and sixth equations involve no coefficients for the Γ waves. We write these equations separately:

$$-[\eta^\alpha(k_1^\alpha)B_1^\alpha + \eta^\alpha(k_2^\alpha)B_2^\alpha] = \eta^\beta(k_1^\beta)A_1^\beta + \eta^\beta(k_2^\beta)A_2^\beta,$$

$$B_1^\alpha + B_2^\alpha = A_1^\beta + A_2^\beta, \quad (16)$$

$$-i\frac{am_0}{m_{X_1}^\alpha}[k_1^\alpha B_1^\alpha + k_2^\alpha B_2^\alpha] = i\frac{am_0}{m_{X_1}^\beta}[k_1^\beta A_1^\beta + k_2^\beta A_2^\beta].$$

Now, if we express the quantity $A_2^\beta = B_1^\alpha + B_2^\alpha - A_1^\beta$ from the second equation and substitute it into the remaining two equations, we obtain

$$-[\eta^\alpha(k_1^\alpha) + \eta^\beta(k_2^\beta)]B_1^\alpha - [\eta^\alpha(k_2^\alpha) + \eta^\beta(k_2^\beta)]B_2^\alpha$$
$$= [\eta^\beta(k_1^\beta) - \eta^\beta(k_2^\beta)]A_1^\beta,$$
$$-i\left[\frac{am_0}{m_{X_1}^\alpha}k_1^\alpha + \frac{am_0}{m_{X_1}^\beta}k_2^\beta\right]B_1^\alpha - i\left[\frac{am_0}{m_{X_1}^\alpha}k_2^\alpha + \frac{am_0}{m_{X_1}^\beta}k_2^\beta\right]B_2^\alpha \quad (17)$$
$$= i\frac{am_0}{m_{X_1}^\beta}[k_1^\beta - k_2^\beta]A_1^\beta.$$

For definiteness, let us assume that the vector k_1^α has the positive real part and the positive imaginary part in the energy region below the CB structure for gallium arsenide and that the vector k_2^α has the negative real part and the positive imaginary part. For the case of aluminum arsenide, we assume that the vector k_1^β is real, while the vector k_2^β is purely imaginary. In this case, the quantity $\eta^\beta(k_2^\beta)$ is real, and it turns out that the coefficients for B_1^α and B_2^α are mutually complex conjugate in the first equation of set (17). In the second equation, the coefficients of these quantities are also mutually complex conjugate. If we now construct the determinant from the coefficients of B_1^α and B_2^α in these two equations, then it turns out to be a purely imaginary quantity

$$\Lambda = i\left[\frac{am_0}{m_{X_1}^\alpha}k_2^\alpha + \frac{am_0}{m_{X_1}^\beta}k_2^\beta\right][\eta^\alpha(k_1^\alpha) + \eta^\beta(k_2^\beta)]$$
$$-i\left[\frac{am_0}{m_{X_1}^\alpha}k_1^\alpha + \frac{am_0}{m_{X_1}^\beta}k_2^\beta\right][\eta^\alpha(k_2^\alpha) + \eta^\beta(k_2^\beta)],$$

which can vanish for a certain real value of the energy $E = E_d$. For $\Lambda = 0$, the quantity A_1^β can also evidently vanish in the general case. Actually, the condition for vanishing of the quantity Λ coincides with the condition for vanishing of the electron transmission coefficient for an abrupt GaAs/AlAs(001) heterointerface, which is corroborated by the corresponding numerical and analytical calculations. From the expression for the quantity Λ, it can be seen that it in no way involves parameters characterizing Γ electrons and the Γ–*X* mixing (in reality, this parameter is present as a common multiplier in the transmission coefficient). Thus, in the context of this simple model of matching the envelope functions at the heterointerface, the total reflection of the Γ wave incident from GaAs on the heterointerface with AlAs is caused by the properties of X electrons and by the interaction between *X* electrons in both materials. This conclusion agrees with the results of the pseudopotential calculation (see above), which show that the X_1 and X_3 states predominantly contribute to the scattering-matrix element $(S_{11})_{X\Gamma}$.

Let us analyze whether the vanishing of the quantity Λ is accidental and whether this effect disappears for another choice of the band-spectrum parameters. We substitute explicit expressions for the quantities η^α and η^β into Λ provided that

$$k_1^\alpha = h + if, \quad k_2^\alpha = -h + if,$$
$$k_2^\beta = i\sigma; \quad h, f, \sigma > 0.$$

We then obtain

$$\Lambda = 2i\frac{a^3 m_0^2 h}{\hbar^2 P^\alpha}\left\{(E-E^\alpha_{X_1})\left(\frac{2f}{m^\alpha_{X_1}}+\frac{\sigma}{m^\beta X_1}\right)\frac{1}{(f^2+h^2)}\right.$$
$$\left.+(E-E^\beta_{X_1})\frac{P^\alpha}{m^\alpha_{X_1}P^\beta\sigma}+\frac{\hbar^2\sigma}{m^\alpha_{X_1}m^\beta_{X_1}}P^\alpha\left(\frac{1}{P^\beta}-\frac{1}{P^\alpha}\right)\right\}, \quad (18)$$

where $P^{\alpha,\beta}=\frac{ia}{\hbar}\langle X_3^{\alpha,\beta}|p|X_1^{\alpha,\beta}\rangle$.

The first term in the braces of formula (18) is negative in the energy interval under consideration, the second term is positive, and the third term is almost zero because the $P^{\alpha,\beta}$ values are close to one another in GaAs(α) and AlAs(β) semiconductors. The first term is dominant in the energy region $E \approx E^\beta_{X_1}$, while the second term, in the energy region $E \le E_0 < E^\alpha_{X_1}$ if the following inequality is satisfied:

$$(E^\alpha_{X_1}-E_0)\frac{\sigma^2}{m^\beta_{X_1}} < (E_0-E^\beta_{X_1})\frac{h^2P^\alpha}{P^\beta m^\alpha_{X_1}}. \quad (19)$$

Here, the values σ and h are calculated at the energy E_0. Inequality (19) is satisfied with a large margin because the energy difference $(E^\alpha_{X_1}-E_0)$ is much smaller than the difference $(E_0-E^\beta_{X_1})$. Therefore, there is an energy at which the quantity Λ vanishes.

This is the case if the CB structure in GaAs is formed for real wave numbers. If we take the AlGaAs solid solution instead of GaAs, it is possible to obtain an extremum of the CB structure in the region of the imaginary wave numbers. (From now on, by the CB-structure extremum in the region of imaginary wave numbers, we mean an energy E_0 for which the imaginary wave numbers k_1^α and k_2^α become the same.) In this case, the above calculations for Λ are valid at $E < E_0$; however, the condition for the existence of a zero is different for this quantity because this is the quantity h instead of f, which tends to zero as the energy approaches E_0.

Therefore, in this case, the condition for the vanishing of the quantity Λ is the following inequality:

$$(E^\alpha_{X_1}-E_0)\left(\frac{2f}{m^\alpha_{X_1}}+\frac{\sigma}{m^\beta_{X_1}}\right)\frac{1}{f^2} < (E_0-E^\beta_{X_1})\frac{P^\alpha}{m^\alpha_{X_1}P^\beta_\sigma}. \quad (20)$$

Here, f and σ are calculated at the energy E_0. It is more difficult to meet this condition as compared with the previous case, due to the presence of an additional term on the left-hand side of the inequality. Of course, inequality (20) is satisfied for small $(E^\alpha_{X_1}-E_0)$. However, we can consider the energy region above E_0 but below

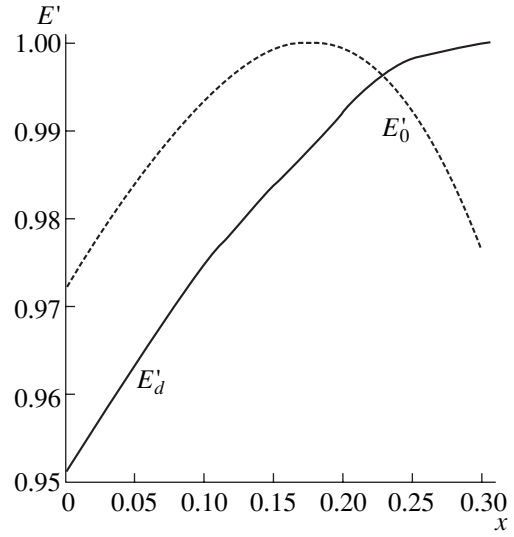

Fig. 4. Dimensionless energies corresponding to the bottom E'_0 of the CB structure in $Al_xGa_{1-x}As$ and to the zero of the transmission coefficient E'_d for the $Al_xGa_{1-x}As/AlAs$ structure as functions of the content x. Here, $E'_d = (E_d - E^\beta_{X_1})(E^\alpha_{X_1} - E^\beta_{X_1})^{-1}$ and $E'_0 = (E_0 - E^\beta_{X_1})(E^\alpha_{X_1} - E^\beta_{X_1})^{-1}$.

$E^\alpha_{X_1}$. In this energy interval, the wave numbers k_1^α and k_2^α are purely imaginary; however, the quantity Λ turns out to be real and, therefore, there is a possibility that it vanishes. In fact, assuming that $k_1^\alpha = if_1$, $k_2^\alpha = if_2$, and $k_2^\beta = i\sigma$, we obtain the expression for Λ in the form

$$\Lambda = -\frac{a^2m_0^2(f_1-f_2)}{P^\alpha}\left\{P^\alpha\frac{E-E^\beta_{X_1}}{P^\beta m^\alpha_{X_1}\sigma\hbar^2}\right.$$
$$\left.+\frac{(E-E^\alpha_{X_1})(m^\beta_{X_1}(f_1+f_2)+m^\alpha_{X_1}\sigma)}{f_1f_2m^\alpha_{X_1}m^\beta_{X_1}\hbar^2}+\sigma\frac{P^\alpha-P^\beta}{2m^\alpha_{X_1}m^\beta_{X_1}P^\beta}\right\}. \quad (21)$$

The last term in braces in (21) can be discarded due to the small difference between the matrix elements for the momentum in AlAs and in AlGaAs. The second term vanishes at $E = E^\alpha_{X_1}$, while the first term is positive. If the energy decreases from $E^\alpha_{X_1}$, the first term decreases, while the second term increases in magnitude and remains negative. If we have

$$\frac{E_0-E^\beta_{X_1}}{P^\beta m^\alpha_{X_1}\sigma}P^\alpha < \frac{(E^\alpha_{X_1}-E_0)}{f^2}\left(\frac{2f}{m^\alpha_{X_1}}+\frac{\sigma}{m^\beta_{X_1}}\right), \quad (22)$$

where the wave numbers are calculated at an energy E_0 and $f_1 = f_2 = f$, the quantity in braces in the expression for Λ (21) vanishes for a certain energy in the interval

under consideration and we have zero for the electron transmission coefficient at this energy. Thus, we find that, if inequality (20) is met, the total reflection of the electron wave takes place on the heterointerface at a certain energy E below the energy E_0 of the CB-structure extremum, whereas, if opposite inequality (22) is met, the total reflection of the electron wave takes place at an energy above E_0 but below $E^{\alpha}_{X_1}$.

The pseudopotential calculations performed with the pseudopotentials [20] for the $Al_xGa_{1-x}As/AlAs$ structures show the presence of zeros in $P(E)$ and corroborate the qualitative conclusions obtained with this simple model. Figure 4 shows the dimensionless energies E'_d and E'_0 calculated from the formula $E' = (E - E^{\beta}_{X_1})(E^{\alpha}_{X_1} - E^{\beta}_{X_1})^{-1}$ as functions of the content x. It is clear that $E' = 1$ for $E = E^{\alpha}_{X_1}$ and $E' = 0$ for $E = E^{\beta}_{X_1}$. The calculations show that, for $x < 0.175$, the CB structure in $Al_xGa_{1-x}As$ is formed for the real wave numbers; for $x > 0.175$, it is formed in the region of imaginary wave numbers; and for $x = 0.175$, there is no CB structure. Up to $x < 0.23$, we have $E_d < E_0$, and $E_d > E_0$ for $x > 0.23$.

It is easy to see that the quantity Λ vanishes due to the common multiplier also at $E = E_0$ because $f_1 = f_2 = f$ in this case. However, it should be remembered that the two chosen solutions to the Schrödinger equation become identical in this case. Such a situation requires special investigation. The analytical consideration in the context of the simple model and the pseudopotential calculation show that, in this case, there is no zero in the transmission coefficient [the transmission coefficient involves the quantity Λ divided by $(f_1 - f_2)$].

It is possible to verify that there is no pure interface localized state responsible for the appearance of a zero in the transmission coefficient. Actually, we obtain the amplitude A^{β}_1 for the transmitted X wave in set (17) equal to zero provided that $\Lambda = 0$ and find that the amplitudes B^{α}_1 and B^{α}_2 of the reflected X waves are related by a phase factor. The second equation of set (16) defines the amplitude A^{β}_2 of another X wave damped deep the GaAs layer. Thus, three of the six equations represented in set (15) are used. In the remaining three equations, the unknowns are three coefficients that can be expressed when being solved in terms of the amplitude of the Γ wave arriving from the GaAs layer. In this case, it turns out that the magnitude of the amplitude B_Γ of the reflected wave is equal to that of the incident wave. If the latter amplitude is zero, all the remaining coefficients are also zero. It follows from this consideration that the quantum state at the energy corresponding to the zero transmission coefficient represents the superposition of the standing Γ wave localized in the half-space occupied by the GaAs layer, the standing X wave damped deep in the GaAs layer, and two waves (one of the X type and another of the Γ type) damped deep in the AlAs layer. Thus, the presence of an electron wave incident on the heterointerface is obligatory for the existence of the considered state. The search for resonance-type states, i.e., those existing for complex energy values, shows that there are no such states.

The consideration of the situation where only the X wave is incident on the heterointerface from the AlAs side leads to similar conclusions. Because of the symmetry relative to the time reversal, the reflection coefficients for the Γ electrons in GaAs and the X electrons in AlAs must coincide in the energy interval under consideration. Therefore, the total reflection of the X wave in AlAs from the AlAs/GaAs(001) heterointerface is observed at the same energy E_d.

The quantum state responsible for the zero transmission coefficient in the case of incidence of the electron X wave from AlAs on the heterointerface involves the standing X_1 wave in the half-space occupied by the AlAs layer, two X waves damped deep in the GaAs layer with identical amplitudes, and one X_3 wave damped deep in the AlAs layer. In contrast to the previous case, there is no contribution from the Γ states at all. Of course, this is valid only in terms of simple matching model (10).

4. CONCLUSION

We considered the scattering of electrons at $Al_xGa_{1-x}As/AlAs(001)$ heterointerfaces in the context of the pseudopotential description and the three-valley approximation for the envelope functions. The use of this model is shown to lead to results virtually coinciding with those calculated with the pseudopotentials. The numerical calculations and analytical formulas obtained in the context of the simplified model enabled us to conclude that the appearance of a zero in the electron transmission coefficient for the GaAs/AlAs(001) heterointerface observed in the energy interval from the bottom of the X_1 valley to the bottom of the CB structure in GaAs is caused by the multivalley character of the energy spectrum of electrons. This phenomenon is due to the mutual compensation of contributions from various “virtual processes”. This compensation turns out to be possible due to the fact that the damped states described by real functions can be formed in the energy interval under consideration. In this case, it is also possible to form the standing wave from the propagating waves, which can be attained for a certain energy value. Such a state corresponds to the zero flux of the electron density. It was shown that interface resonance states are not at all related to the appearance of a zero in the transmission coefficient

ACKNOWLEDGMENTS

This study was supported by the Russian Foundation for Basic Research, project no. 02-02-17848.

REFERENCES

1. E. E. Mendez, W. I. Wang, E. Calleja, and C. E. T. Goncalves da Silva, Appl. Phys. Lett. **50**, 1263 (1987).
2. D. Y. Ko and J. C. Inkson, Phys. Rev. B **38**, 9945 (1988).
3. Xue Fang Shi, Semicond. Sci. Technol. **4**, 150 (1989).
4. E. E. Mendez, E. Calleja, and W. I. Wang, Phys. Rev. B **34**, 6026 (1986).
5. E. E. Mendez and E. Calleja, Appl. Phys. Lett. **53**, 977 (1988).
6. J. J. Finley, M. S. Skolnick, J. W. Cockburn, *et al.*, Superlattices Microstruct. **23**, 513 (1998).
7. Hyunsik Im, P. C. Klipstein, R. Grey, and G. Hill, Phys. Rev. B **62**, 11076 (2000).
8. C. Gourdon, D. Martins, P. Lavallerd, *et al.*, Phys. Rev. B **62**, 16856 (2000).
9. M. Hosoda, N. Ohtani, H. Mimura, *et al.*, Phys. Rev. Lett. **75**, 4500 (1995).
10. T. Ando, S. Wakahara, and H. Akera, Phys. Rev. B **40**, 11609 (1989).
11. T. Ando and H. Akera, Phys. Rev. B **40**, 11619 (1989).
12. S. N. Grinyaev and V. N. Chernyshov, Fiz. Tekh. Poluprovodn. (St. Petersburg) **26**, 2057 (1992) [Sov. Phys. Semicond. **26**, 1157 (1992)].
13. S. N. Grinyaev, G. F. Karavaev, and V. N. Chernyshov, Fiz. Tekh. Poluprovodn. (St. Petersburg) **28**, 1393 (1994) [Semiconductors **28**, 784 (1994)].
14. G. F. Karavaev, S. N. Grinyaev, and V. N. Chernyshov, Izv. Vyssh. Uchebn. Zaved. Fiz., No. 9, 64 (1992).
15. G. F. Karavaev and V. N. Chernyshov, in *Abstracts of International Symposium on Nanostructures: Physics and Technology* (St. Petersburg, 1995), p. 126.
16. K. A. Mader and A. Zunger, Phys. Rev. B **50**, 17393 (1994).
17. S. N. Grinyaev and G. F. Karavaev, Fiz. Tverd. Tela (St. Petersburg) **42**, 752 (2000) [Phys. Solid State **42**, 772 (2000)].
18. G. F. Karavaev and V. N. Chernyshov, Fiz. Tekh. Poluprovodn. (St. Petersburg) **35**, 105 (2001) [Semiconductors **35**, 106 (2001)].
19. G. F. Karavaev and V. N. Chernyshov, Fiz. Tekh. Poluprovodn. (St. Petersburg) **35**, 841 (2001) [Semiconductors **35**, 807 (2001)].
20. V. A. Chaldyshev and S. N. Grinyaev, Izv. Vyssh. Uchebn. Zaved. Fiz., No. 3, 38 (1983).
21. I. A. Aleĭner and E. L. Ivchenko, Fiz. Tekh. Poluprovodn. (St. Petersburg) **27**, 594 (1993) [Semiconductors **27**, 330 (1993)].
22. Y. Fu, M. Willander, E. L. Ivchenko, and A. A. Kiselev, Phys. Rev. B **47**, 13498 (1993).

Translated by V. Bukhanov

Semiconductors, Vol. 37, No. 4, 2003, pp. 426–432. Translated from Fizika i Tekhnika Poluprovodnikov, Vol. 37, No. 4, 2003, pp. 443–449.

SEMICONDUCTOR STRUCTURES, INTERFACES, AND SURFACES

The Charge Accumulation in an Insulator and the States at Interfaces of Silicon-on-Insulator Structures as a Result of Irradiation with Electrons and Gamma-Ray Photons

D. V. Nikolaev, I. V. Antonova*, O. V. Naumova, V. P. Popov, and S. A. Smagulova

Institute of Semiconductor Physics, Siberian Division, Russian Academy of Sciences, pr. Akademika Lavrent'eva 13, Novosibirsk, 630090 Russia

** e-mail: antonova@isp.nsc.ru*

Submitted September 5, 2002; accepted for publication September 5, 2002

Abstract—The accumulation of charge in an insulator and the states at interfaces in silicon-on-insulator structures irradiated with 2.5-MeV electrons and 662-keV gamma-ray photons were studied. It was found that an additional positive charge appears in the buried insulator of the structures as a result of irradiation. The concentration of hole traps generated by radiation in the oxide is higher at the boundary with substrate than at the bonding interface between a split-off silicon layer and oxide. It is shown that the presence of even a weak built-in field in the structures ($F \gtrsim 5 \times 10^3$ V/cm) gives rise to efficient separation of charge carriers. There is no generation of additional states at the Si/SiO_2 interfaces in the silicon-on-insulator structures for both irradiation types, although this generation is observed in the initial thermal oxide. © *2003 MAIK "Nauka/Interperiodica".*

1. INTRODUCTION

The main results of irradiating structures containing insulating and semiconducting layers consist in the introduction of additional (most commonly, positive) charge in the insulator, generation of states at the semiconductor–insulator interface, and generation of defects in the semiconductor bulk. The effects of ionizing radiation (X- and gamma-ray photons, electrons, neutrons, alpha particles, and so on) on the characteristics of metal–insulator–semiconductor (MIS) structures have been studied over several decades [1]. As a result, methods for enhancing the radiation resistance of integrated circuits based on MIS transistors have been developed; these methods involve the use of thin oxide layers [1] and composite oxides ($SiO_2/Si_3N_4/SiO_2$) [2].

In silicon-on-insulator (SOI) structures, the operating silicon layer is thin and is separated by the insulator from radiation defects produced in the substrate; as a result, irradiation mostly affects the SOI properties owing to introduction of charge into the buried insulator and generation of states at the semiconductor–oxide interface [3, 4]. The charge in the buried insulator and the states at the interface between the split-off silicon layer and insulator are the SOI material parameters that directly affect the operation of devices formed in the split-off silicon layer; the aforementioned charge and states give rise to an additional conducting channel near the interface with the semiconductor and to a shift of the threshold voltage of an MIS transistor.

The effect of radiation on SOI has been studied in the greatest detail for the structures formed by oxygen implantation (the so-called SIMOX technology) [5]. Thus, in particular, the following special features are observed in the effects of radiation on SIMOX structures (depending on the technology of production of these structures): (i) a smaller amount of charge is accumulated in the structures with a buried insulator of higher quality (i.e., with an insulator subjected to longer annealing or to annealing at a higher temperature); (ii) both hole and electron traps are formed in the oxide (i.e., both positive and negative charges are accumulated, which results in their partial mutual compensation [6]); and (iii), in the case of SIMOX structures formed by multiple implantation of oxygen, the density of surface states virtually does not change under irradiation, whereas additional surface states are generated in irradiated SIMOX structures produced using a single implantation of oxygen [7, 8].

For the SOI structures obtained using direct bonding of silicon wafers, the published data mainly concern the effect of irradiation on BESOI (bonded and etched back SOI) structures [9]; in these structures, the thickness of one of the bonded wafers is reduced by etching. The behavior of BESOI structures under irradiation is similar to the behavior of metal–oxide–semiconductor (MOS) structures with thermal oxide. As a rule, a positive charge accumulates in the buried oxide of BESOI structures. Hydrogen introduced during hydrophilization of the surface as a preliminary stage in the bonding procedure is present in a BESOI structure. It is believed that hydrogen is responsible for differences between electrical characteristics of the buried oxide and those of the initial oxide [10, 11].

1063-7826/03/3704-0426$24.00

Table 1. Main parameters of the SOI and MOS structures and the value of the charge in the insulator before and after irradiation with electrons and gamma-ray photons

Structure	The insulator-layer thickness, μm	The conductivity type of layers	Q_0, 10^{11} cm^{-2}	Q, 10^{11} cm^{-2}; electrons, 3×10^6 rad	Q, 10^{11} cm^{-2}; γ-ray photons, 3×10^6 rad
SOI-1	0.11	*p*-Si/SiO$_2$/*n*-Si	1.1	7	10
SOI-2	0.28	*n*-Si/SiO$_2$/*p*-Si	3.5	25.3	–
SOI-3	0.40	*n*-Si/SiO$_2$/*n*-Si	1.8	17	23
SOI-4	0.41	*n*-Si/SiO$_2$/*n*-Si	2.4	24	–
SOI-5	0.36	*p*-Si/SiO$_2$/*n*-Si	3.0	–	16
MOS-1	0.13	*n*-Si	1.1	2.83	8.7
MOS-2	0.36	*n*-Si	3.1	3.7	5.2

Note: Q_0 is the initial charge in the oxide, Q is the total fixed charge in the oxide.

There are almost no available published data on the effect of radiation on SOI structures obtained using the method of bonding silicon wafers with subsequent splitting-off of one of these wafers using hydrogen implantation (the so-called Smart-Cut method) [12]. The aim of this study was to gain insight into the process of charge accumulation in the buried oxide of SOI structures produced using hydrogen-assisted splitting-off and to compare this process with similar processes in MOS structures.

2. EXPERIMENTAL

In our studies, we used SOI structures produced using the Dele-Cut technology [13]. This method relies on bonding of a hydrogen-implanted silicon wafer to an oxidized substrate with subsequent splitting of the first wafer over the layer whose cohesion was weakened by hydrogen implantation. The interface between the split-off silicon layer and oxide constitutes the bonding boundary. The oxide–substrate interface was formed in the course of thermal oxidation. All oxides used in the formation of the MOS and SOI structures were grown under the conditions of wet oxidation at a temperature of 1000°C. In order to measure the electrical parameters of devices, we fabricated mesa structures with aluminum contacts to both the split-off silicon layer and the substrate. The area of a mesa structure was equal to 300×300 μm^2 and was the same for all samples under investigation. In Table 1, we list the most important parameters of the studied SOI and MOS structures. We studied SOI structures with different types of electrical conductivity in the split-off silicon layer and in the substrate and also with various thickness values of the buried oxide (0.11–0.41 μm) and split-off silicon layer (0.48–1.70 μm). The charge-carrier concentration in the initial silicon was in the range of $(0.3–1.0) \times 10^{15}$ cm^{-3}. The SOI-4 structure was fabricated from silicon grown by the floating-zone method, whereas the other SOI and MOS structures were formed using silicon grown by the Czochralski method. In order to study the changes in the oxide properties in the course of fabrication of the SOI structures, we also measured the parameters of MOS structures fabricated using the same silicon wafers and oxides as in the case of SOI structures. The charge in the oxide, the charge-carrier concentration, and the density of states at the interfaces were determined from the measurements of high-frequency capacitance–voltage (*C–V*) characteristics. The structures were irradiated with gamma-ray photons and 2.5-MeV electrons. Irradiation with electrons was performed in the pulsed mode with the pulse duration being equal to 400 μs. The current density in a pulse ranged from 0.1 to 0.3 A/cm^2. The pulse-repetition frequency was controlled so that the average temperature of a sample did not exceed 50°C during irradiation. The second source was ^{137}Cs, which provided continuous emission of gamma-ray photons with an energy of 662 keV and a dose rate of 100 rad/s. In both cases, the radiation doses were in the range of $D = 10^5–10^7$ rad. The structures were irradiated without applying an additional bias to them.

3. RESULTS

In Figs. 1a and 1b, we show the *C–V* characteristics of the SOI-1 and SOI-3 structures irradiated with electrons and gamma-ray photons, respectively. The SOI-1 structure has *p*-type conductivity in the split-off silicon layer and *n*-type conductivity in the substrate, which is responsible for the steplike shape of the *C–V* characteristic. In the situation where the conductivity types in the split-off silicon layer and in the substrate coincide (the SOI-3 structure), the *C–V* characteristic also features two portions of capacitance modulation from the largest value C_{max} to the two smallest values. In both structures, the capacitance modulation is related to the formation of a space-charge region (SCR) in the split-off silicon layer if a positive bias is applied, and to the formation of an SCR in the substrate in the case of negative bias. The largest capacitance of the structure is determined by the buried-insulator capacitance. The smallest capacitance (capacitances) and (or) the value of capacitance at a plateau are determined by the

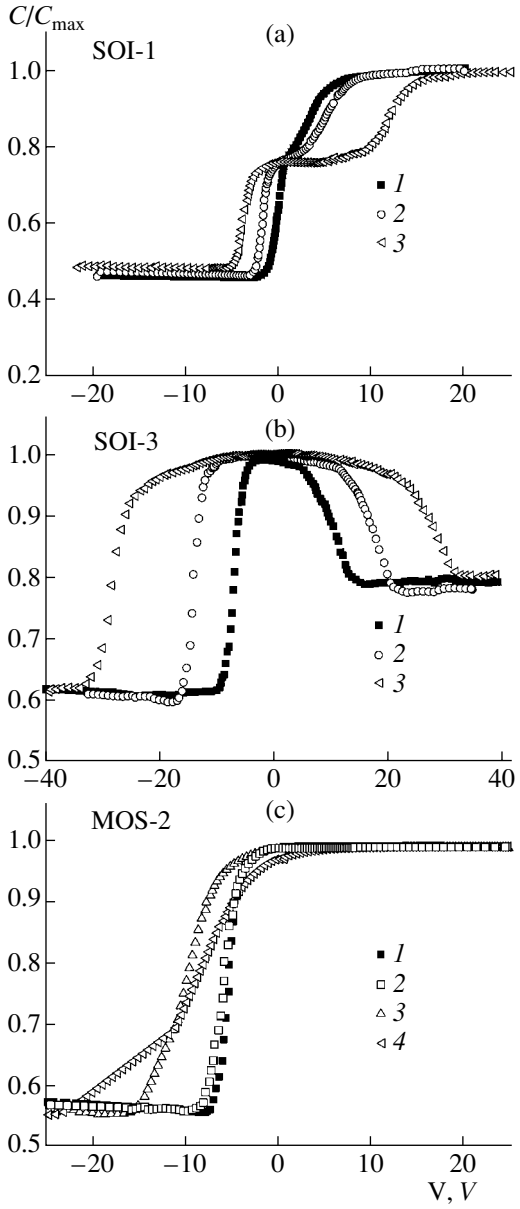

Fig. 1. Capacitance–voltage characteristics of the (a) SOI-1, (b) SOI-3, and (c) MOS-2 structures in relation to the irradiation dose D with (a, c) electrons and (b) gamma-ray photons. (a): D = (*1*) 0, (*2*) 10^5, and (*3*) 10^7 rad; (b): D = (*1*) 0, (*2*) 3×10^5, and (*3*) 10^7 rad; and (c): D = (*1*) 0, (*2*) 10^5, (*3*) 10^6, and (*4*) 10^7 rad.

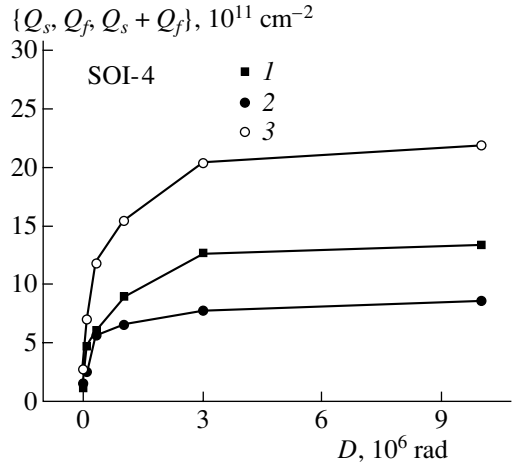

Fig. 2. Dependence of built-in charge in the buried oxide of the SOI-4 structure on the dose of electron irradiation. Curve *1* corresponds to the charge Q_s at the oxide–substrate interface; curve *2*, to the charge Q_f at the interface between the cut-off silicon layer and oxide; and curve *3*, to the total charge $Q_s + Q_f$.

charge-carrier concentrations in the split-off silicon layer and in the substrate.

It follows from the shift of the capacitance-modulation regions along the voltage axis that positive charge accumulates in the buried oxide during irradiation of both SOI-1 and SOI-3 structures. The slope of the curves in the region of capacitance modulation is governed by the density of surface states and remains virtually constant. The smallest value of capacitance and the value of capacitance at a plateau also remain virtually unchanged for the range of radiation doses used in our experiments. This means that the charge-carrier concentrations in the split-off silicon layer and in the substrate are virtually not affected by irradiation.

Figure 1c shows *C–V* characteristics of an MOS structure based on *n*-Si in relation to the dose of electron radiation. In contrast with SOI structures, we observe here not only a shift of the modulation region to higher voltages but also an appreciable change in the slope of the *C–V* characteristic as the dose increases, which corresponds to an increase in the density of surface states as a result of irradiation.

The charge in the insulator was determined from the *C–V* characteristics of the SOI and MOS structures using the flat-band voltage. As an example, Fig. 2 shows dependences of accumulated charge at each of the interfaces (the charge at the oxide–substrate interface is designated by Q_s, and the charge at the interface between the split-off silicon layer and the oxide is designated by Q_f) and the total charge $Q_s + Q_f$ in the buried insulator on the dose of irradiation with electrons. It can be seen that the dose dependence of charge at both interfaces levels off at an electron dose of 3×10^6 rad. This trend is observed for all SOI structures under investigation. The leveling-off of the charge vs. dose plots is observed even at a dose of $(1–3) \times 10^5$ rad for MOS structures.

Figures 3a and 3b show the dependences of accumulated charge on the dose of irradiation with electrons and gamma-ray photons for various SOI and MOS structures. Since we have two interfaces between the oxide and semiconductor in SOI structures (in contrast to MOS structures where there is only a single interface), Figs. 3a and 3b represent the values of charge only at one of the boundaries of the SOI structures in

order to correctly compare the MOS and SOI structures; i.e., the values of the charge at the oxide–substrate interface are given. It can be seen from Figs. 3a and 3b that there are cases both when the charge introduced into the SOI-structure oxide nearly coincides with the charge in similar MOS structure and when the charge in an SOI structure far exceeds that in an MOS structure. Charges at both boundaries and the total charge in the buried insulator for other SOI and MOS structures before and after irradiation with a dose of 3×10^6 rad are listed in Tables 1 and 2.

The density of surface states was calculated from the slope of the *C–V* characteristic in the region of modulation. As an example, Fig. 4 shows the distributions of the surface-state density in the silicon band gap for MOS structures and at one of the boundaries of the SOI structures before and after electron irradiation at a dose of 3×10^6 rad. For a MOS-1 structure, the density of states after irradiation is higher than the initial value by about an order of magnitude. At the oxide–substrate interface in the SOI-4 structure, the initial density of states is almost the same as in an MOS structure; however, this density of states remains virtually unchanged after irradiation. The density of states at the interface between the split-off silicon layer and oxide is also unaffected by irradiation. The same situation also takes place for other studied SOI and MOS structures; specifically, irradiation affects the density of states only in the initial oxide of a MOS structure, whereas this density remains unchanged in an SOI structure.

4. DISCUSSION

The data obtained on the SOI and MOS structures irradiated with electrons and gamma-ray photons show that the most important effect of radiation consists in the introduction of positive charge both into the buried oxide in an SOI structure and into the MOS oxide. This effect is typical of thermal oxide in MOS and BESOI structures. However, the charge accumulated in the buried oxide of SOI structures exceeds, in some instances, the charge in the gate oxide of MOS structures. At the same time, the charge introduced by irradiation into other SOI structures is closely matched by that introduced into the corresponding MOS structure.

In Table 2, we list the values of the contact potential difference (φ_c) and the electric-field strength (F) in the buried insulator of SOI and MOS structures; the potential difference and the electric field appear owing to a difference between the work functions for the charge carriers leaving the split-off silicon layer and the substrate in SOI structures and those leaving the metal and silicon in MOS structures. Depending on the sign and magnitude of the field in the buried oxide, the studied SOI and MOS structures can be divided into three groups. Table 3 illustrates the energy-band diagrams that are characteristic of each of the groups. For example, if we have a p-Si/SiO_2/n-Si structure (consisting of a split-off layer, an insulator, and the substrate, respec-

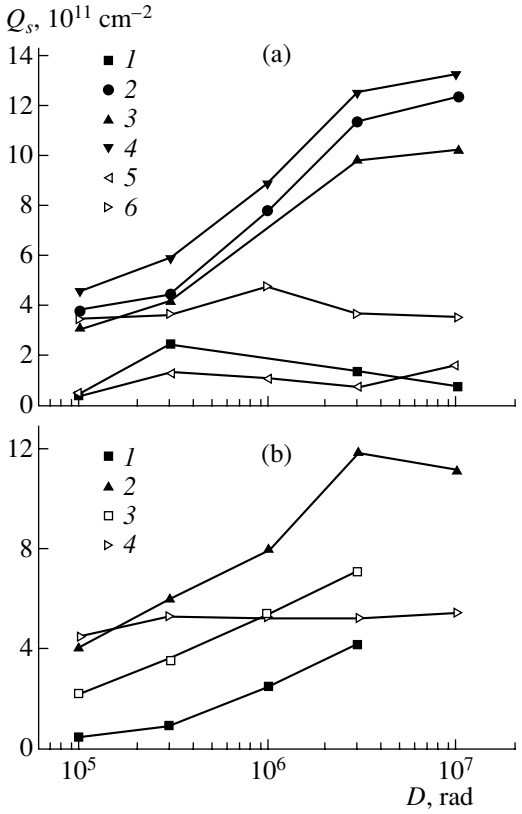

Fig. 3. Dependences of the charge Q_s at the oxide–substrate boundary on the dose of irradiation with (a) electrons and (b) gamma-ray quanta. (a): curve *1* corresponds to the SOI-1 structure; curve *2*, to the SOI-2 structure; curve *3*, to the SOI-3 structure; curve *4*, to SOI-4; curve *5*, to the MOS-1 structure; and curve *6*, to the MOS-2 structure. (b): curve *1* corresponds to the SOI-1 structure; curve *2*, to the SOI-3 structure; curve *3*, to the SOI-5 structure; and curve *4*, to the MOS-2 structure.

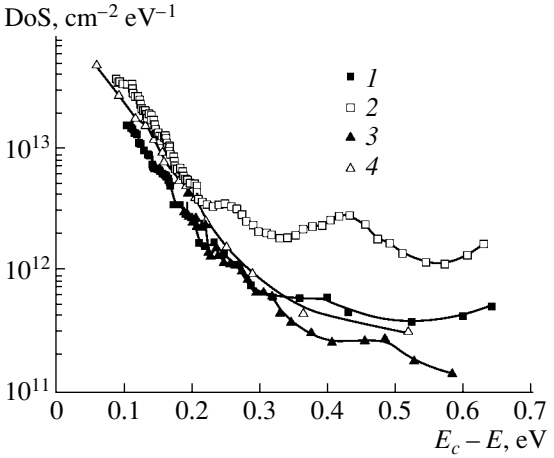

Fig. 4. Distribution of the density of surface states (DoS) in energy E in the silicon band gap at the oxide–silicon interface in the (*1*, *2*) MOS-1 structure and at the oxide–substrate interface in the (*3*, *4*) SOI-4 structure (*1*, *3*) before and (*2*, *4*) after electron irradiation at a dose of 3×10^6 rad.

Table 2. Charges assigned to boundaries in the insulator, the strength of the built-in electric field F, and the contact potential φ_c in the SOI and MOS structures after irradiation with electrons and gamma-ray photons

Structure	Irradiation with electrons		Irradiation with gamma-ray photons		F, V/cm	φ_c, V
	Q_f, 10^{11} cm^{-2}	Q_s, 10^{11} cm^{-2}	Q_f, 10^{11} cm^{-2}	Q_s, 10^{11} cm^{-2}		
SOI-1	4.6	2.3	5.8	4.2	-6.54×10^4	–0.693
SOI-2	10.3	15	–	–	1.93×10^4	0.54
SOI-3	7.1	9.4	11.3	11.8	4.49×10^2	0.018
SOI-4	8.5	15	–	–	4.48×10^3	0.184
SOI-5	–	–	8.8	7.1	-1.91×10^4	–0.69
MOS-1	–	2.83	–	8.7	-2.34×10^4	–0.206
MOS-2	–	3.7	–	5.2	-8.13×10^3	–0.217

Note: Q_s is the fixed charge in the oxide assigned to the oxide–substrate interface; and Q_f is the fixed charge in the oxide assigned to the interface between the oxide and split-off silicon layer.

Table 3. Energy-band diagrams of the SOI and MOS structures in relation to the magnitude and sign of the contact electric field

SOI-1, SOI-5, MOS-1, MOS-2	SOI-3, SOI-4	SOI-2
$F_1 < 0$ $Q_f > Q_s$ – ← + 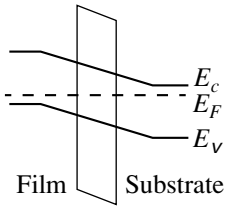 	$0 < F \ll F_2$ $Q_f \approx Q_s$ + → – 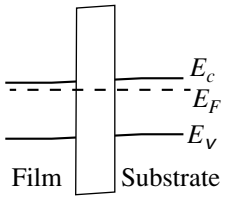 	$F_2 > 0$ $Q_f < Q_s$ + → – 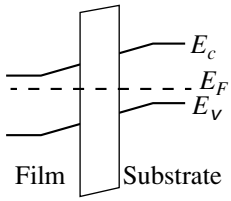

Note: E_c is the conduction-band bottom, E_v is the valence-band top, and E_F is the Fermi level position.

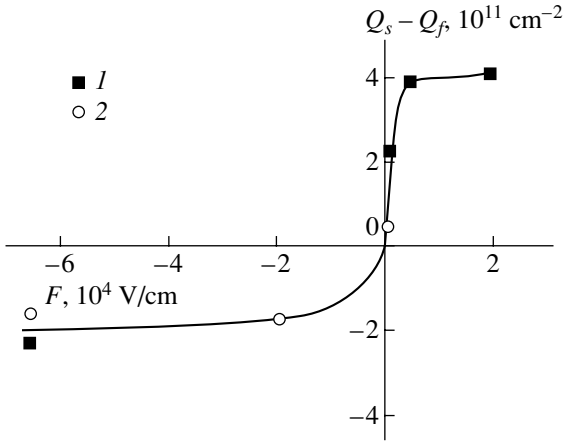

Fig. 5. The difference in the charges $Q_s - Q_f$ accumulated at the interfaces of SOI structures after irradiation with (*1*) electrons and (*2*) gamma-ray photons at a dose of 3×10^6 rad in relation to the strength of the built-in electric field F.

tively), the internal field (F_1) is directed towards the split-off layer. For *n*-Si/SiO_2/*p*-Si structures, the field (F_2) is directed towards the interface with the substrate. If the conductivity types in the split-off silicon layer and the substrate coincide, the sign of the internal electric field and magnitude of the electric-field strength depend on the difference in doping levels of Si; in this situation, the magnitude of F is much smaller than in the first two cases.

As is well known, the main effect of irradiation with electrons and gamma-ray photons on SiO_2 is ionization. This effect induces breakage of bonds (predominantly, strained bonds) in the oxide. The built-in electric field can be conducive to more efficient separation of electrons and holes generated during irradiation. It is clear that, if there are hole traps in the oxide, the charge will be accumulated predominantly at one of the interfaces (depending on the sign of the built-in field in the buried insulator). In Fig. 5, we show the difference between the values of the charge at the interfaces of the buried

oxide in SOI structures irradiated with electrons and gamma-ray photons at a dose of 3×10^6 rad in relation to the strength of the built-in electric field F. It can be seen that differences in the values of accumulated charge in the SOI structures under investigation can be attributed to the effect of the internal electric field. If we compare the values of charge accumulated in the MOS and SOI structures under identical conditions (with respect to the sign and magnitude of F) we can see that, according to the data listed in Table 3, the charge introduced into the SOI structures is somewhat larger. This observation suggests that a certain degradation of the oxide properties occurs during the fabrication of SOI structures; this degradation is the cause of the larger values of the charge generated by irradiation. It is also noteworthy that field tests of oxides in unirradiated SOI structures indicate that there are no charge-carrier traps in these oxides [14].

As was shown previously [10], oxide properties are affected by the bonding procedure; specifically, the generation of surface states and charge trapping in the oxide occur during injection of electrons or holes into the SiO_2 layer. This effect is tentatively caused by incorporation of hydrogen into the thermal-oxide structure [10]: hydrogen interacts with the $O_3Si–SiO_3$ bond and forms the $O_3Si–H$ group; the latter decomposes under irradiation into $O_3Si–$ (the E' center) and H. Hydrogen has a high mobility and diffuses with the formation of H_2; as a result, the probability of recombination is found to be low. Feijoo *et al.* [15] have shown that the concentration of hydrogen bonds is on the order of 10^{15} cm^{-2} when hydrophilized surfaces are bonded. If hydrogen-assisted exfoliation is used, the concentration of hydrogen appearing in an SOI structure in the course of fabrication is higher by an order of magnitude than that in a BESOI structure [16]. Therefore, enrichment of oxide with hydrogen in the course of bonding and subsequent annealing is assumed to be responsible for degradation of thermal oxide in SOI structures.

It can also be seen from Fig. 5 that the curve $Q_s - Q_f$ vs. F levels off at relatively small values of F. This means that a comparatively low electric-field strength ($F \gtrsim 5 \times 10^3$ V/cm) is sufficient for separation of irradiation-generated charge carriers; consequently, the hole traps are produced predominantly in the vicinity of interfaces. This inference is consistent with existing notions about localization of the charge introduced by radiation into thermal oxide and BESOI structure (see, for example, [17]). Large values of $Q_s - Q_f$ for the positive electric-field strength indicate that the concentration of hole traps generated by radiation in the oxide is higher in the vicinity of the substrate boundary than near the bonding boundary (the interface between the split-off silicon layer and oxide). This observation can be related to the higher concentration of strained bonds in the SiO_x transition layer than in the vicinity of the bonding interface, where there is virtually no transition layer [18].

The density of states in an SOI structure at the interface with the substrate approximately equals (and somewhat exceeds at the interface with the split-off silicon layer) the density of states at the initial interface with thermal oxide in MOS structures. A higher density of states at the bonding boundary can be related to the difference in the origin of these states, since the interfaces were formed by different methods. Furthermore, as mentioned above, the presence of hydrogen during the fabrication of an SOI structure may bring about an additional generation of states at the interface between silicon and oxide as a result of heat treatments [19]. It follows from Fig. 4 that an appreciable increase in the density of states occurs in the thermal oxide of MOS structures as a result of irradiation; in contrast, these states are not generated at the interfaces of SOI structures. This invariance of the density of states under the effect of radiation can be caused by passivation of these states with hydrogen released from the bonds in the oxide and (or) by the stability of bonds formed at a high temperature [10]. The appearance of free hydrogen in the course of irradiation is consistent with the aforementioned assumption and with the data [10] on the decomposition of $O_3Si–H$ groups into E' centers and hydrogen atoms.

The total charge introduced into the buried insulator of the SOI and MOS structures as a result of irradiation with gamma-ray photons is larger than the charge introduced by irradiation with electrons. These two types of radiation differ in two main parameters. First, the electron energy is much higher than the energy of gamma-ray photons (2.5 MeV in the case of electrons and 662 keV in the case of gamma-ray photons). This factor should bring about a more efficient introduction of charge into the oxide as a result of irradiation with electrons. Second, there is a high electron-current density in an irradiation pulse, which can give rise to elevated temperatures during an electron pulse (notwithstanding the fact that the average temperature is not high). Heating of structures during an electron pulse with an ensuing increase in the probability of recombination for split (due to ionization) bonds are apparently the causes of the smaller total charge in the oxide after irradiation with electrons.

5. CONCLUSIONS

The obtained results make it possible to draw the following conclusions.

The presence of hydrogen in SOI structures during their fabrication exerts a dual effect. This presence manifests itself as a factor which contributes to an increase in the accumulation of built-in charge and to invariance of surface states in the buried oxide of an SOI structure in the course of irradiation with electrons and gamma-ray photons.

The presence of even a weak built-in electric field ($F \gtrsim 5 \times 10^3$ V/cm) in the SOI structures can bring

about a more efficient accumulation of charge at one of the boundaries of the buried oxide in an SOI structure. The amount of charge accumulated during irradiation and located at the interface between the split-off silicon layer and oxide can be reduced by choosing a conductivity type and doping level of the substrate so that separation of charge carriers would induce holes to drift to the substrate.

The concentration of hole traps generated by radiation in the oxide is higher in the vicinity of the substrate than that near the bonding interface (the interface between the split-off silicon layer and the oxide), which is apparently related to the presence of a more extended transition layer at the interface obtained by thermal oxidation.

ACKNOWLEDGMENTS

This study was supported by the Russian Foundation for Basic Research, project no. 01-02-16986.

REFERENCES

1. E. H. Nicollian and J. R. Brews, *MOS (Metal Oxide Semiconductor) Physics and Technology* (Wiley, New York, 1982).
2. K. Watanabe, M. Kato, T. Okabe, and N. Nagata, IEEE Trans. Nucl. Sci. **33**, 1216 (1986).
3. S. Cristoloveanu and S. S. Li, *Electrical Characterization of Silicon-on-Insulator Materials and Devices* (Kluwer Academic, Boston, 1995).
4. J.-P. Colinge, *Silicon-on-Insulator Technology: Materials to VLSI*, 2nd ed. (Kluwer Academic, Boston, 1997), p. 223.
5. K. Izumi, M. Dokin, and H. Ariyoshi, Electron. Lett. **14**, 593 (1978).
6. H. E. Boesch, Jr., T. L. Taylor, L. R. Hite, and W. E. Bailey, IEEE Trans. Nucl. Sci. **37**, 1982 (1990).
7. F. T. Brady, S. S. Li, and W. A. Krull, IEEE Trans. Nucl. Sci. **37**, 1995 (1990).
8. H. K. Annamalai, J. F. Bockman, N. E. McGruer, and J. Chapski, IEEE Trans. Nucl. Sci. **37**, 2001 (1990).
9. W. P. Maszara, G. Goetz, A. Caviglia, and J. B. McKitterick, J. Appl. Phys. **64**, 4943 (1998).
10. A. G. Revesz and H. L. Hughes, in *Physical and Technical Problems of SOI Structures and Devices*, Ed. by J. P. Colinge, V. S. Lysenko, and A. N. Nazarov (Kluwer Academic, Dordrecht, 1995), p. 133.
11. R. E. Stahlbush, G. J. Campisi, J. B. McKitterick, *et al.*, IEEE Trans. Nucl. Sci. **39**, 2086 (1992).
12. M. Bruel, Electron. Lett. **31**, 1201 (1995).
13. V. P. Popov, I. V. Antonova, L. V. Mironova, and V. F. Stas', RF Patent No. 99,120,527/28(021,735) (28 September 1999).
14. D. V. Nikolaev, I. V. Antonova, O. V. Naumova, *et al.*, Fiz. Tekh. Poluprovodn. (St. Petersburg) **36**, 853 (2002) [Semiconductors **36**, 800 (2002)].
15. D. Feijoo, Y. J. Chabal, and S. B. Christman, in *IEEE International Conference Proceedings* (1994), p. 89.
16. I. V. Antonova, V. P. Popov, V. F. Stas, *et al.*, Microelectron. Eng. **48**, 383 (1999).
17. A. N. Nazarov, *Physical and Technical Problems of SOI Structures and Devices*, Ed. by J. P. Colinge, V. S. Lysenko, and A. N. Nazarov (Kluwer Academic, Dordrecht, 1995), p. 217.
18. V. P. Popov, I. V. Antonova, A. A. Frantsuzov, *et al.*, Fiz. Tekh. Poluprovodn. (St. Petersburg) **35**, 1075 (2001) [Semiconductors **35**, 1030 (2001)].
19. V. V. Afanas'ev and A. Stesmans, Appl. Phys. Lett. **72**, 79 (1998).

Translated by A. Spitsyn

Semiconductors, Vol. 37, No. 4, 2003, pp. 433–438. Translated from Fizika i Tekhnika Poluprovodnikov, Vol. 37, No. 4, 2003, pp. 450–455.

SEMICONDUCTOR STRUCTURES, INTERFACES, AND SURFACES

The Effect of Internal Fields on Tunneling Current in Strained GaN/$Al_xGa_{1-x}N$(0001) Structures

S. N. Grinyaev^ and A. N. Razzhuvalov

Kuznetsov Physicotechnical Institute, pl. Revolyutsii 1, Tomsk, 634050 Russia

^ e-mail: gsn@phys.tsu.ru

Submitted September 2, 2002; accepted for publication September 6, 2002

Abstract—The influence of internal fields on tunnelling current in *w*-GaN/$Al_xGa_{1-x}N$(0001) nitride structures with strained barrier layers is investigated by the pseudopotential and scattering-matrix methods. It is shown that, for symmetric two-barrier structures, spontaneous polarization and a piezoelectric field lead to asymmetry of the current–voltage characteristic when the direction of an external field is varied. Moreover, for asymmetric structures these phenomena cause the current to depend on the position of layers along the polar axis. In confined superlattices, internal fields form a Stark ladder of electron states, which manifests itself in current peaks for a relatively weak external field (~10 kV/cm). Pronounced features in the tunnel current are observed for layer thicknesses which are smaller in comparison with the GaAs/AlGaAs(001) structures by a factor of approximately 2. The dependence of tunnel current on the thickness and position of the layers, temperature, and degree of doping are explained from an analysis of the Stark effect for resonance states. © *2003 MAIK "Nauka/Interperiodica".*

1. INTRODUCTION

The A_3N compounds and corresponding heterostructures are of considerable interest for the development of multifunctional high-power electronic devices and short-wave emitters [1]. Wurtzite polymorphs (*w*-) of nitrides are notable for their high values of the spontaneous polarization vector and piezoelectric tensor [2], which lead to strong internal fields. The latter substantially affect the electron [3] and phonon [4] states. Variations in the electron potential and energies of defect formation, which are caused by internal fields in *w*-GaN/AlGaN(0001) structures, lead to a high density of two-dimensional electron gas; this circumstance made it possible to fabricate power field transistors with characteristics close to those of GaAs/AlGaAs(001)-based transistors [5]. Due to the large band offset and one-valley structure of the lower conduction band, *w*-GaN/AlGaN(0001) structures can also be competitive with GaAs/AlGaAs structures in transverse-transport devices. It was shown that a number of peculiarities caused by internal fields manifest themselves in electron tunneling across *w*-GaN/AlGaN(0001) multibarrier structures [6]. These peculiarities are the dependence of the transmission coefficient on the relative position of the layers, the emergence of a Stark ladder of electron states, and so on. In this study, we investigated the influence of built-in fields on the tunnel current in nitride structures and analyzed Stark shifts of resonance states. Based on this analysis, we interpreted the asymmetry of current peaks. The results are compared with similar characteristics for GaAs/AlGaAs(001) structures.

2. CALCULATION PROCEDURE

The tunnel current density $I(V)$ was calculated similarly to [7] in the ballistic approximation by the effective-mass method with the parameters determined from a pseudopotential-based calculation [6]. Active regions from the thin undoped *w*-GaN layers and the *w*-$Al_{0.3}Ga_{0.7}N$ solid solution with a (0001) heterointerface orientation were formed between the heavily doped contact regions of *w*-GaN. We assumed the field inside the contacts to be equal zero. The position of the Fermi level E_f was determined from the electroneutrality equation. The solid solution was lattice-matched to thick *w*-GaN contacts. A strain-induced (biaxial tension in the interface plane and compression along the hexagonal axis) piezoelectric field emerges in the barrier layers. Along with the spontaneous polarization, this field was also taken into account in the context of the macroscopic approach [8]. The internal field in the active region is inhomogeneous; however, it is unidirectional for all layers. Therefore, with allowance for boundary conditions, the variations in the electron potential, which were caused by both kinds of polarization, are comparable, although the spontaneous polarization in barriers is higher than the piezoelectric polarization by a factor of approximately 3. The conduction band offset at the GaN/$Al_{0.3}Ga_{0.7}N$(0001) heterointerface is also strain-dependent. The interpolation of the results of calculation [8] yields the value 0.81 eV [6]. Other structure parameters and details of calculating the transmission coefficient $P(E)$ are given in [6].

1063-7826/03/3704-0433$24.00

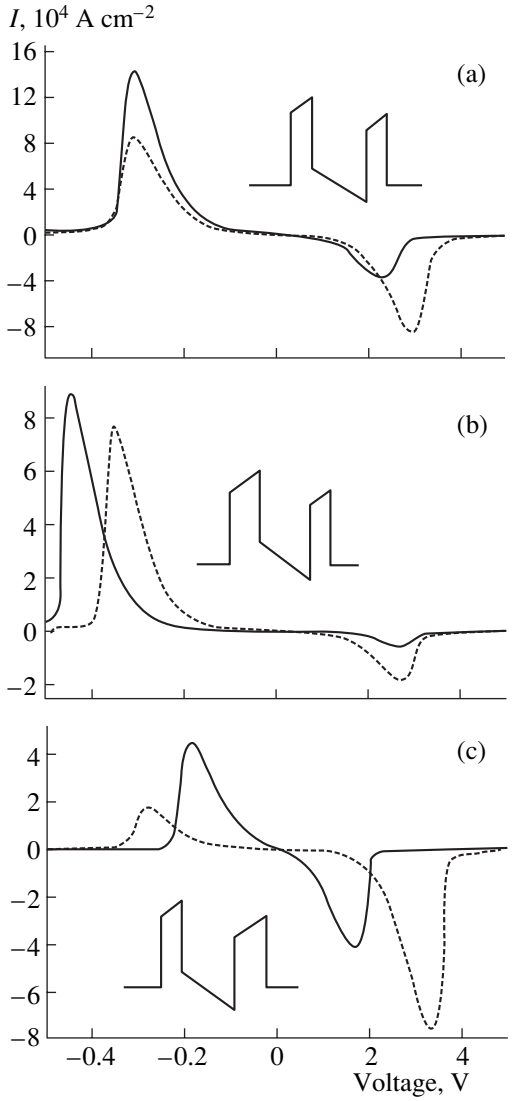

Fig. 1. Tunnel current in the w-$Al_{0.3}Ga_{0.7}N(m)/GaN(5)/Al_{0.3}Ga_{0.7}N(n)(0001)$ two-barrier structures: (a) (m, n = 2), (b) (m = 3, n = 2), and (c) (m = 2, n = 3). Solid and dotted lines represent the results of calculations with and without allowance made for internal fields, respectively. The electron potential profiles along the hexagonal axis for V = 0 are shown in the inset. T = 250 K, and $N_d = 5 \times 10^{18}$ cm^{-3}.

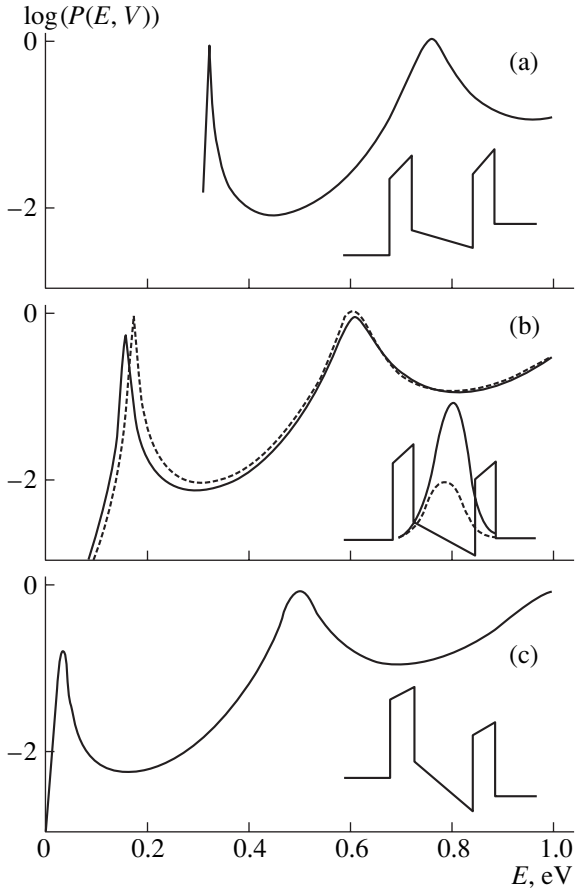

Fig. 2. Electron transmission coefficient $P(E, V)$ for the w-$Al_{0.3}Ga_{0.7}N(2)/GaN(5)/Al_{0.3}Ga_{0.7}N(2)(0001)$ structure: (a) (V_{max} = –0.30 V), (b) (V = 0), and (c) (V_{max} = 0.23 V). Solid and dotted lines show the results of calculations with and without allowance made for internal fields, respectively. Charge densities of lower resonance states correspond to the wave incident from the right.

3. RESULTS AND DISCUSSION

The current–voltage (I–V) characteristics calculated for w-$Al_{0.3}Ga_{0.7}N(m)/GaN(5)/Al_{0.3}Ga_{0.7}N(n)(0001)$ two-barrier structures (n, m are the layer thicknesses expressed in units of the lattice constant along the hexagonal axis) at T = 250°C are shown in Fig. 1. For positive voltages V, the left-hand contact region is negatively charged. The contact regions were Si-doped to the concentration $N_d = 5 \times 10^{19}$ cm^{-3}, with the ionization energy of the donor level E_d = 30.8 meV [9]. The tunnel current peaks I_{max} correspond to voltages V_{max}, for which the Fermi level for the negatively charged contact region $K^{(-)}$ coincides with the energy of the lower resonance E_r for the quantum well $E_r(V_{max}) = E_f$ = 0.018 eV. Due to internal fields, the electron potential and tunnel current possess clearly pronounced asymmetry when the direction of the external field is varied.

Let us consider the special features of the tunnel current of the $Al_{0.3}Ga_{0.7}N(2)/GaN(5)/Al_{0.3}Ga_{0.7}N(2)$ symmetric structure in more detail (Fig. 1a). The strengths of the internal field in the well (w) and barriers (b) of this structure are equal to F_w^{in} = –1418 kV/cm and F_b^{in} = 1819 kV/cm, respectively. The transmission coefficients calculated for voltages V_{max} and V = 0 are shown in Fig. 2. Two resonance states in the well correspond to the $P(E, V)$ peaks. With allowance made for internal fields, the V_{max} and I_{max} quantities decrease for positive voltages. For V < 0, the position of the current peak varies slightly, whereas the amplitude increases. Internal fields lead to greater localization and to a decrease in the potential of the charge density of reso-

nance states in the well (see inset in Fig. 2b). The difference in the amplitudes I_{max} for the forward and reverse biases by almost an order of magnitude is associated with the difference in transmission coefficients (Figs. 2a, 2c). For $V < 0$, the external field compensates the internal field in the well. As a result, the electron potential becomes almost symmetric, whereas the transmission coefficient in the $P(E_r, V_{max})$ resonance is close to unity. For $V > 0$, the directions of the external and internal fields in the well coincide and the asymmetry of the electron potential increases. Therefore, the half-width at half-height of the peak increases, whereas the $P(E_r, V_{max})$ quantity decreases. A similar dependence of the tunnel current on the relative orientation of the external and internal piezoelectric fields in the strained well was observed earlier for a GaAlAs/GaInAs(111) two-barrier structure [10].

The position of current peaks in the $I(V)$ curve can be explained from an analysis of the voltage dependence of the lower resonance level. It is convenient to represent the energy level position relative to the conduction band edge for a negatively charged contact region $E_c^{(-)}$ in the form $E_r(V) = E_r(0) + \Delta E_r(V)$. Here, $E_r(0)$ is the resonance energy relative to contact regions in terms of internal fields for $V = 0$ (for a symmetric two-barrier structure, $E_r(0) = 0.151$ eV), and $\Delta E_r(V)$ is the level shift due to the external field; this shift is equal to the sum of two contributions $\Delta E_r(V) = \Delta\varepsilon_c(V) + \Delta\varepsilon_d(V)$, where $\Delta\varepsilon_c(V)$ is the shift of the potential energy at the well center relative to $E_c^{(-)}$ and $\Delta\varepsilon_d(V)$ is the level shift relative to the well center. The quantity $\Delta\varepsilon_c(V)$, which is associated with the well shift with no allowance made for the well deformation, is equal to the sum of variations in the potential energy in the barrier and at the well half-width $\Delta\varepsilon_c(V) = eV(a/2 + b)/L$, where e is the elementary charge; a is the well width; b is equal to the thickness of the right-hand barrier (b_r) for $V < 0$ and to the thickness of the left-hand barrier (b_l) for $V > 0$, respectively; and $L = a + b_l + b_r$ is the width of the active region. The level shift $\Delta\varepsilon_d(V)$, which is associated with the deformation of potentials of the well and barriers by the external field, leads to asymmetry in the position of tunnel current peaks. The calculated dependence $\Delta\varepsilon_d(V)$ for a symmetric two-barrier structure is shown in Fig. 3. For the range of external field strength, which is bounded by vertical dashed lines, the lower resonance level lies above the conduction band edge for a negatively charged contact region. Outside this range, the level descends below $E_c^{(-)}$ and the wave function subsides into the left-hand region for $V > 0$ and into the right-hand region for $V < 0$. By virtue of low barrier permeability, the $\Delta\varepsilon_d(V)$ dependence is close to the shift of the lower bound level $\Delta\varepsilon_w(V)$ in an isolated quantum well, which is confined by the $Al_{0.3}Ga_{0.7}N$ barriers. It can be seen from the calculated $\Delta\varepsilon_w(V)$ dependence that

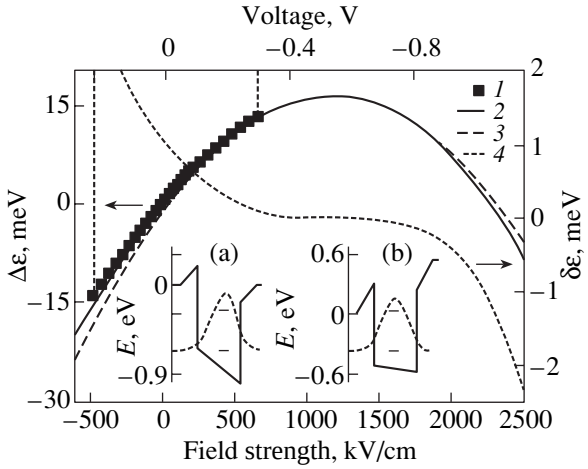

Fig. 3. Shifts of the lower level $\Delta\varepsilon$ relative to the well center: (*1*) the $\Delta\varepsilon_d$ shift for the two-barrier structure, (*2*) the result of calculating the $\Delta\varepsilon_w$ shift for the isolated quantum well, (*3*) the quadratic Stark shift $\Delta\varepsilon_{st}$ displaced to the extremum of the $\Delta\varepsilon_w$ curve, and (*4*) the difference $\delta\varepsilon = \Delta\varepsilon_V - \Delta\varepsilon_{st}$. $V_c = -0.54$ V, $F_c = 1170$ kV/cm. Insets represent the potential profiles for isolated wells, level positions, and charge densities of lower states (dashed lines) for external voltages V: (a) 0 and (b) $V_c = -F_cL$.

this shift is largest for an external field strength F_c = 1170 kV/cm (Fig. 3), at which this field almost completely compensates the internal field in the well. For the fields close to F_c, the wave function of the lower state is almost symmetric (see inset in Fig. 3), while the term which is linear in $F_w = F - F_c$ in the $\Delta\varepsilon_w(V)$ shift is equal to zero. Therefore, for weak fields $F_w \ll 4\hbar^2/|e|m^*a^3\Omega^{3/2}$, the deviation of $\Delta\varepsilon_w(V)$ from the largest value at F_c is described by the quadratic Stark effect [11] $\Delta\varepsilon_{st} = -(\Omega^2/8)(m^*e^2F_w^2a^4/\hbar^2)$, where Ω is a factor that depends on the parameters of the well, barriers, and energy level of the well in the field F_c. For a 30-Å-thick GaAs quantum well, which is bounded by barriers formed from the $Ga_{0.62}Al_{0.36}As$ solid solution, the quadratic Stark effect is valid for the strengths F_w lower than 100 kV/cm [11]. In the nitride structure, this region increases to the fields $F_w \sim 300$ kV/cm, since the well parameters are correlated as $\Omega_{GaAs}/\Omega_{GaN} \sim 2.3$, $m^*_{GaAs}/m^*_{GaN} \sim 0.5$, and $a_{GaAs}/a_{GaN} \sim 1.2$. This is evident from the difference $\Delta\varepsilon_w - \Delta\varepsilon_{st}$ (see Fig. 3), which is close to zero in the field range $F_c \pm 300$ kV/cm. For strong fields F_w, deviations from the quadratic Stark effect, which are associated with variation in the localization of the wave function, are observed. The external-field dependence of the tunnel current peak for $F > 0$ can be used to determine the F_c quantity and estimate the internal field strength in the well.

Figure 4 represents the graphic solution of the equation $E_f - e|V_{max}|(a/2 + b)/L = E_r(0) + \Delta\varepsilon_d(V_{max})$ for a symmetric two-barrier structure and clearly illustrates

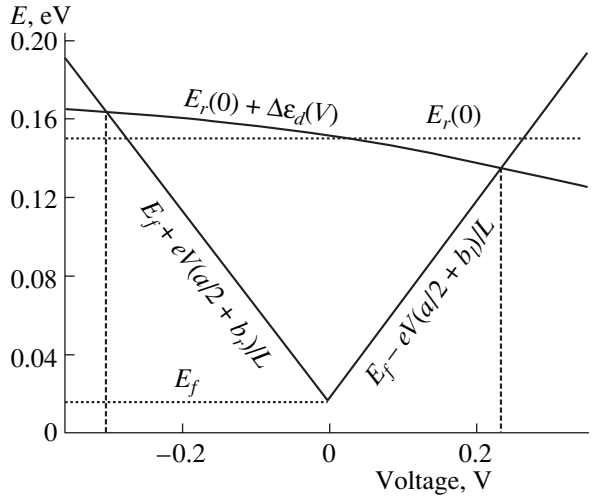

Fig. 4. Graphic solution of the equation $E_f - e|V|(a/2 + b)/L = E_r(0) + \Delta\varepsilon_d(V)$ for the $Al_{0.3}Ga_{0.7}N(2)/GaN(5)/Al_{0.3}Ga_{0.7}N(2)(0001)$ structure. The voltages V_{max}, which correspond to current peaks, are determined from the intersection of curves; they are shown by vertical dashed lines.

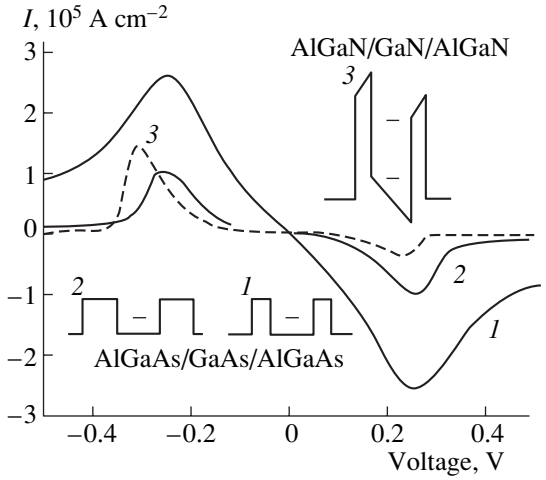

Fig. 5. Tunnel current for structures: (*1*) $Al_{0.3}Ga_{0.7}As(2)/GaAs(5)/Al_{0.3}Ga_{0.7}As(2)$, (*2*) $Al_{0.3}Ga_{0.7}As(4)/GaAs(5)/Al_{0.3}Ga_{0.7}As(4)$, and (*3*) $Al_{0.3}Ga_{0.7}N(2)/GaN(5)/Al_{0.3}Ga_{0.7}N(2)$. Corresponding potential profiles are shown in insets.

the dependence of the tunnel current peaks on the position of the Fermi level, as well as on the resonance level, barrier thicknesses, and internal field in the well. The slope of the $\Delta\varepsilon_d$ curve is determined by the direction of the internal field in the well. We compared this curve with the results of calculation with internal fields disregarded (Fig. 1a, dotted curve). It can be seen from this comparison that the shift of the resonance current peak is noticeable only when the directions of the external and internal fields in the well coincide. This is associated with the fact that it is possible to neglect the shift $\Delta\varepsilon_d$ upon determining V_{max} for the structure with no allowance made for internal fields, whereas the resonance level for this structure is located at an energy $E_r(0) = 0.169$ eV, which almost coincides with the solution of the equation for the structure with internal fields for $V < 0$ (Fig. 4).

For two-barrier structures with various barrier widths, additional asymmetry in the tunnel current emerges. This asymmetry is associated with a difference in the shifts of the resonance level $\Delta\varepsilon_c(V)$ for positive and negative biases. Furthermore, upon varying the relative position of barriers with respect to the polar axis, the electron potential profile varies along with the transmission coefficient and resonance level energy $E_r(0)$, which manifests itself in the *I–V* characteristics (Figs. 1b, 1c).

With increasing temperature and degree of doping, the Fermi energy and the electron density increase. As a result, the amplitudes of the tunnel current for the forward and reverse biases increase, whereas the V_{max} quantity decreases.

As far as we know, no experimental investigations of the tunnel current for thin-film nitride structures have been carried out yet. Therefore, we compared the results obtained with the data for the $GaAs/Al_{0.3}Ga_{0.7}As(001)$ structure, which has been investigated in more detail (Fig. 5). When calculating the tunnel current for the $GaAs/Al_{0.3}Ga_{0.7}As(001)$ structure, we assumed that the GaAs contact regions were impurity-doped to the concentration $N_d = 5 \times 10^{18}$ cm^{-3} and ionization energy $E_d = 5.2$ meV [12]. The conduction band offset at the heterointerfaces is equal to 0.309 eV [12]. For the GaAs/AlGaAs(001) structures, no internal fields occur owing to the cubic symmetry. It follows from the comparison that for close layer thicknesses, the tunnel current for the GaAs/AlGaAs two-barrier structures is considerably heavier, whereas the peaks are wider owing to higher permeability of the $Al_{0.3}Ga_{0.7}As$ barriers. The tunnel currents for the negative voltage portion are leveled with increasing thickness of the $Al_{0.3}Ga_{0.7}As$ barrier by a factor of approximately 2. However, for the nitride structure, the current decreases more rapidly with increasing voltage.

We then considered a confined superlattice formed by 5 $Al_{0.3}Ga_{0.7}N(2)$ barriers and 4 GaN(6) wells. Well dimensions were somewhat increased, while the temperature was lowered ($T = 30$ K) with the aim of attaining pronounced peaks of the tunnel current for relatively weak external fields. Contact regions were doped with shallow-level impurity with an ionization energy $E_d = 0.01$ eV [9] up to a concentration $N_d = 5 \times 10^{19}$ cm^{-3}. In this case, the Fermi energy equals $E_f = 0.003$ eV. Disregarding internal fields, the tunnel current across the superlattice is symmetric (Fig. 6a). The peaks of the transmission coefficient are associated with miniband states, whose levels are shown in the inset to Fig. 6a. The interval between the levels of the lower miniband E_r is equal to ~0.01 eV. If internal fields are taken into

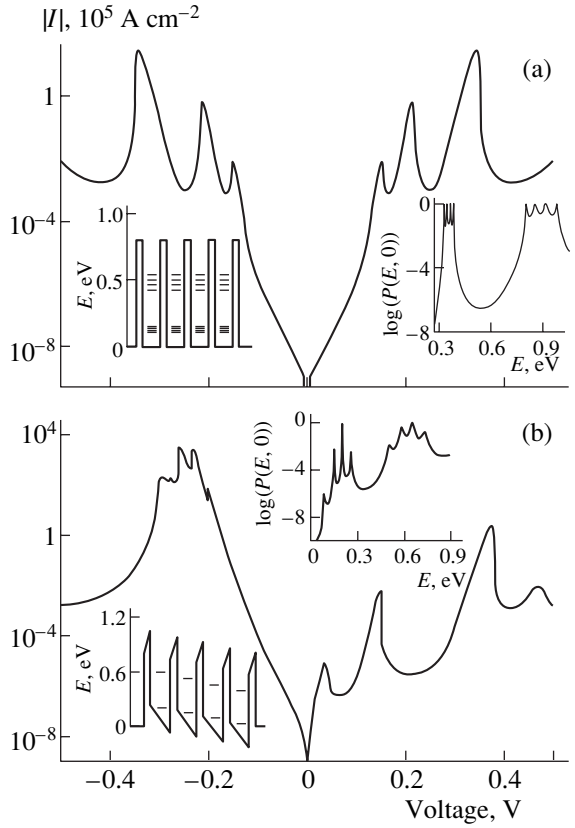

Fig. 6. Tunnel current for the confined superlattice formed by five $Al_{0.3}Ga_{0.7}N(2)$ barriers and four GaN(6) wells: (a) calculation without and (b) with allowance made for internal fields. The electron potential profile with resonance levels in the wells and the transmission coefficient $P(E, V)$ for $V = 0$ are shown in insets. $T = 30$ K, and $N_d = 5 \times 10^{19}$ cm^{-3}.

account ($F_w^{in} = -930$ kV/cm, $F_b^{in} = 2300$ kV/cm), an effective homogeneous field $F_{\text{eff}} = (aF_w^{in} + bF_b^{in})/(a + b) = -140$ kV/cm emerges in the superlattice. This field shifts the resonance levels in neighboring wells by a magnitude of 0.06 eV, which is much larger than E_r (Fig. 6b). As a result, the wave functions of the states are localized mainly within separate wells, and the Stark ladder is formed; the corresponding levels manifest themselves in the peaks of the transmission coefficient $P(E, 0)$ and the tunnel current. For the voltage range considered, the external field is no stronger than ~300 kV/cm, for which $\Delta\varepsilon_d < 0.01$ eV. Therefore, the voltage $V_{\max}^j$ that corresponds to the jth current peak can be estimated by taking into account only the shift of the level $\Delta\varepsilon_c^j$ in the jth well. For this purpose, the equation $E_f - e|V_{\max}^j|(a/2 + d^j)/L_s = E_r^j(0)$ should be used, where L_s is the superlattice thickness, and d^j is the thickness of the layer between the jth well and the contact region $K^{(-)}$; the quantity d^j is equal to $(5 - j)(b + a) - a$ for $V > 0$ and $j(b + a) - a$ for $V < 0$.

For positive voltages, the external and internal fields F_{eff} have the same direction. Therefore, with increasing peak number j, the layer thickness d^j decreases, whereas the resonance energies in the wells $E_r^j(0)$ increase. As a result, the interval between neighboring peaks $I(V)$ increases with increasing voltage. The first peak ($V_{\max} = 0.034$ eV) emerges for the external field ($F = 20$ kV/cm), which is much weaker than the internal field F_{eff}. In this context, note that, for the GaAs/GaAlAs superlattices, the Stark localization sets in for significantly stronger external fields ~100 kV/cm [13].

For negative voltages, the external field is directed opposite to the field F_{eff}. Compared with the case of $V > 0$, the layer thicknesses d^j decrease (increase) for $j = 1, 2$ ($j = 3, 4$), whereas the current peaks shift to larger (smaller) absolute values of voltage by modulus. Furthermore, for the superlattice chosen, the condition $(E_f - E_r^1(0))/e = (b + a/2)F_{\text{eff}}$ is almost satisfied. If this condition is satisfied, the field F_{eff} is completely compensated by the external field ($V = L_sF_{\text{eff}}$), whereas all levels of the Stark ladder coincide with the Fermi level. Owing to the hybridization, these levels are split into a narrow miniband ~0.04 eV wide (Fig. 6a). It is this phenomenon that leads to an increase in the transmission coefficient and a tunnel current as well as to a weak dependence of $V_{\max}^j$ on the peak number.

4. CONCLUSION

In conclusion, we summarize the most important results obtained in this study.

(1) Internal fields give rise to asymmetry of the tunnel current in the w-GaN/AlGaN(0001) symmetric two-barrier structures. This phenomenon has no analogues in GaAs/AlGaAs cubic structures. The current asymmetry is associated with a difference in the total field strength in the layers of the forward- and reverse-biased structures. The peak values of the voltage and current are larger when the external and internal fields in the well are directed opposite to one another. In this case, the current peak is in the voltage region, in which variation of the resonance level is described by the quadratic Stark effect, which permits the determining of the magnitude and direction of the internal field.

(2) For asymmetric two-barrier structures, an additional dependence of the tunnel current on the barrier positions relative to the polar axis emerges. This dependence is associated with variation in the profile of the potential energy, which affects the transmission coefficient.

(3) Stark shifts of the resonance for the two-barrier structure and of the bound state for the quantum well, which are caused by the deformation of the potential by

the external field, are close to each other. These shifts determine the variation in the tunnel current peaks depending on the structure parameters (temperature, doping, and layer thicknesses).

(4) For the superlattices, the internal fields give rise to the Stark localization of electron states in quantum wells. If the external field is directed oppositely to the effective homogeneous field in the superlattice, miniband states, which manifest themselves in pronounced and closely spaced current peaks, are formed. Otherwise, the state localization in the wells becomes stronger and the difference between the levels of the Stark ladder increases. This circumstance gives rise to clearly pronounced asymmetry of the tunnel current in superlattices when the direction of the external field is varied.

(5) The *I–V* characteristics of nitride structures are comparable with the characteristics of the GaAs/AlGaAs(001) structures for barrier layer thicknesses smaller by a factor of approximately 2, which holds promise for the use of nitride materials in the development of thin-film resonance-tunnel diodes.

ACKNOWLEDGMENTS

This study was supported by the Russian Foundation for Basic Research, project nos. 02-02-17848 and no. 02-02-06894.

REFERENCES

1. S. Nakamura, M. Senoh, N. Iwasa, *et al.*, Jpn. J. Appl. Phys., Part 2 **34**, L1332 (1995); A. Yu. Yunovich, Svetotekhnika, Nos. 5–6, 2 (1996); R. Dimitrov, L. Wittmer, H. P. Felsl, *et al.*, Phys. Status Solidi A **168**, R7 (1998).
2. F. Bernardini, V. Fiorentini, and D. Vanderbilt, Phys. Rev. B **56**, R10024 (1997).
3. V. Fiorentini, F. Bernardini, F. D. Sala, *et al.*, Phys. Rev. B **60**, 8849 (1999).
4. J. Gleize, J. Frandon, M. A. Renucci, and F. Bechstedt, Phys. Rev. B **63**, 073308 (2001).
5. C.-H. Chen, K. Krishnamurthy, S. Keller, *et al.*, Electron. Lett. **35**, 933 (1999).
6. S. N. Grinyaev and A. N. Razzhuvalov, Fiz. Tverd. Tela (St. Petersburg) **43**, 529 (2001) [Phys. Solid State **43**, 549 (2001)].
7. R. Tsu and L. Esaki, Appl. Phys. Lett. **22**, 562 (1973).
8. F. Bernardini and F. Fiorentini, Phys. Rev. B **57**, R9427 (1998).
9. H. Wang and A.-B. Chen, J. Appl. Phys. **87**, 7859 (2000).
10. I. H. Campbell, M. D. Joswick, D. L. Smith, and R. H. Miles, Appl. Phys. Lett. **66**, 988 (1995).
11. G. Bastard, E. E. Mendez, L. L. Chang, and L. Esaki, Phys. Rev. B **28**, 3241 (1983).
12. Sadao Adachi, J. Appl. Phys. **58** (3), R1 (1985).
13. E. E. Mendez, F. Agullo-Rueda, and J. M. Hong, Phys. Rev. Lett. **60**, 2426 (1988).

Translated by N. Korovin

Semiconductors, Vol. 37, No. 4, 2003, pp. 439–442. Translated from Fizika i Tekhnika Poluprovodnikov, Vol. 37, No. 4, 2003, pp. 456–459.

SEMICONDUCTOR STRUCTURES, INTERFACES, AND SURFACES

Characteristics of Gallium Arsenide Structures and Gunn Devices Based on Them Fabricated Using the Radiation–Thermal Technology

M. V. Ardyshev* and V. M. Ardyshev

Kuznetsov Physicotechnical Institute, pl. Revolyutsii 1, Tomsk, 634050 Russia

** e-mail: ard.rff@elefot.tsu.ru*

e-mail: detector@mail.tomsknet.ru

Submitted August 5, 2002; accepted for publication September 6, 2002

Abstract—Doped layers were produced by implanting sulphur ions into single-crystal GaAs and also into GaAs epitaxial films grown on semi-insulating substrates, with subsequent thermal annealing. An additional radiation treatment was performed using halogen lamps (photon annealing). Gunn devices and integrated circuits based on them were fabricated by planar technology. The additional treatment was shown to lead to an increase in the electron mobility in the layers due to the reduction of the concentration of scattering center. The Gunn-device structures, which were subjected to photon annealing, are characterized by better homogeneity and higher values of the current drop. Nearly ideal current pulses were generated in such structures, and no effects caused by trapping, as well as by the impact ionization, were observed. © *2003 MAIK "Nauka/Interperiodica".*

1. INTRODUCTION

Gunn devices are known to place the most stringent requirements on the purity, homogeneity, and structural perfection of the material they are made of [1]. To provide a high speed of response, good coherence of oscillations, and high sensitivity to the control-electrode voltage, the following conditions must be satisfied [2]: an electron concentration in the active layer $n \cong (2–4) \times 10^{16}$ cm^{-3}, a layer thickness $d \geq 0.5$ μm, a product $nd \cong 10^{12}$ cm^{-2}, and an electron mobility $\mu \geq 5000$ cm^2 V^{-1} s^{-1} (at 300 K). The fabrication of doped layers with a high charge-carrier mobility (close to theoretical values) by ion implantation is quite a complex problem if one takes into account that the GaAs structure is badly damaged during the implantation.

In this connection, the purpose of this study is to investigate the radiation–thermal treatment of GaAs for the fabrication of structures and planar Gunn devices of high quality.

2. EXPERIMENTAL

The investigations were performed on GaAs(100) single-crystal wafers (with a resistivity higher than 10^7 Ω cm, a dislocation density not higher than 5×10^4 cm^{-2}, an electron mobility of 3000 cm^2 V^{-1} s^{-1}) and also on epitaxial films of undoped GaAs grown by chloride-vapor-phase epitaxy on semi-insulating substrates. The concentration of background impurities in the films was less than 10^{14} cm^{-3}, the electron mobility was not lower than 6300 cm^2 V^{-1} s^{-1}, and the thickness was 1.5–8.0 μm.

Before implantation, the wafers were treated in an etchant $H_2SO_4 : H_2O_2 : H_2O = 1 : 1 : 100$. Sulphur ions (^{32}S) were implanted with an energy of 100 keV and a dose of 2×10^{13} cm^{-2} at 150°C. Thereafter, we deposited an SiO_2 insulating film by the procedure [3] from a film-forming solution with a samarium content of 6–8 wt %. The thermal annealing was performed in the temperature range of 750–850°C for 1.5 h. The radiation treatment of the structures was carried out in an "Impul's-5" system (using halogen lamps) at temperatures of 520–800°C for 10–30 s in nitrogen (with a dew point below –65°C).

After annealing and removing the insulating, film we measured the sheet concentration and mobility in the layers by the van der Pauw method in combination with layer-by-layer etching in the temperature range of 70–400 K.

3. EXPERIMENTAL RESULTS AND DISCUSSION

Figure 1 shows the electron mobility μ in ion-implanted layers as a function of the thickness *d* of the epitaxial films in which the layers were formed. It can be seen that the values of μ decrease with decreasing *d*, tending to the values characteristic of ingot compensated semi-insulating GaAs. Notably, at higher temperatures of thermal annealing, the value of $\mu \geq 3000$ cm^2 V^{-1} s^{-1} is observed for thicker epitaxial films. The result shown indicate that, in contrast to the case of thick films, additional scattering centers for electrons appear in thin epitaxial films. The most probable cause of their appearance is the diffusion of defects (scatter-

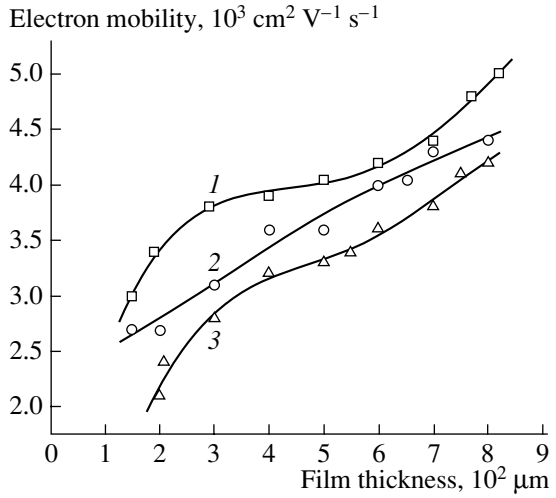

Fig. 1. Electron mobility μ at 300 K in the doped layers fabricated in undoped GaAs epitaxial films of different thicknesses at annealing temperatures T_{ann} = (*1*) 750, (*2*) 800, and (*3*) 850 °C.

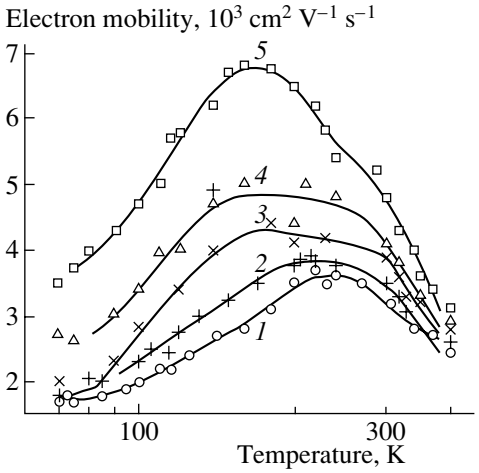

Fig. 2. Temperature dependences of the electron mobility in the ion-implanted layers annealed at T_{ann} = 750°C for t = 1.5 h. The layers are formed in single-crystal GaAs (curve *1*) and in undoped GaAs epitaxial films of a thickness d = (*2*) 2, (*3*) 4, and (*4*), (*5*) 8 μm. Curve (*5*) is for the film subjected to additional radiation treatment

ing centers) from the substrate into the epitaxial film during the film deposition and subsequent thermal annealing. The defect-diffusion length increases with the annealing temperature. Therefore, the undoped portion of the film between the doped layer and the substrate should be rather thick to reduce the influence of the defects on the electron mobility in the doped layer.

It was established [4] that, in order to obtain the value of $\mu > 4500$ cm^2 V^{-1} s^{-1} in doped layers formed by ion implantation in epitaxial films, the thickness of the latter has to satisfy the relation $d \geq 10(D_S t)^{1/2}$, where D_S is the coefficient of diffusion of S from the implanted layer at the annealing temperature and t is the annealing time. This relation was obtained under the condition that the sulphur-diffusion depth is smaller than the distance between the doped layer and the film–substrate interface. In this case, the doped layer must be formed in the region where the content of impurities and defects diffusing from the substrate into the film is the lowest. For the chosen annealing conditions, $D_S \approx 10^{-12}$ cm^2 s^{-1} [5, 6]. Therefore, according to the above relation, the film thickness must be not less than 7.3 μm. In this case, the electron mobility in the doped layer is not less than 4550 cm^2 V^{-1} s^{-1}, which is confirmed by the data in Fig. 1 (curve *1*).

In order to determine the type of the additional scattering centers in the doped layers, we measured the mobility as a function of temperature (Fig. 2). The experimental dependences were optimized by the calculated dependences, using the method of global-extremum search. The calculated dependences were obtained using the known analytical expressions for scattering from the additional centers (dipoles [7], neutral impurities [8], space-charge regions [9], two-dimensional defects [10], and one-dimensional defects [11]).

In Table 1, we list the values of the concentrations of the additional scattering centers, which provide the best agreement between the calculated and experimental dependences. Here, we also list the values of the electron mobility at 300 K, the sheet concentration, and the degree of compensation.

Table 1. Parameters of doped layers fabricated in epitaxial films of different thickness by ion implantation with subsequent annealing at 750°C for 1.5 h

Film no.	Film thickness, μm	n_i, cm^{-3}	N_{dip}, cm^{-3}	N_{Weis}, cm^{-3}	N_S, cm^{-2}	K	μ(300 K), cm^2 V^{-1} s^{-1}
1	Single crystal	2.5×10^{17}	$\sim 7 \times 10^{16}$	1.8×10^{15}	1.2×10^{12}	0.85	3160
2	2	2.0×10^{17}	–	1.4×10^{15}	2.1×10^{12}	0.70	3470
3	4	1.6×10^{17}	–	1.0×10^{15}	2.9×10^{12}	0.54	3930
4	8	1.2×10^{17}	–	4.5×10^{14}	3.8×10^{12}	0.38	4380
5*	8	1.1×10^{17}	–	1.1×10^{14}	4.2×10^{12}	0.27	5060

* Denotes the film subjected to additional radiation treatment.

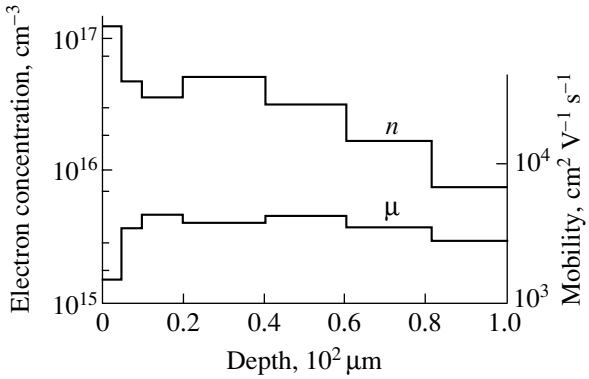

Fig. 3. Depth profiles of the electron concentration and mobility in the GaAs-device structure.

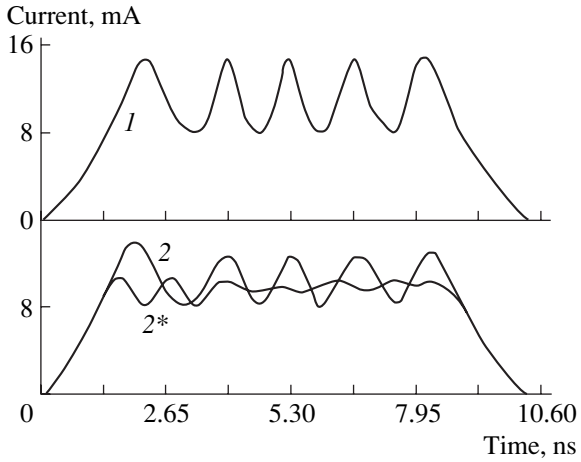

Fig. 4. Oscillograms of currents through Gunn diodes fabricated in epitaxial films (*1*) subjected to an additional radiation treatment, (*2*) without the additional radiation treatment and without illumination, and (*2**) without the radiation treatment but with the illumination.

It can be seen from Fig. 2 and Table 1 that an increase in μ in the doped layer with increasing epitaxial-film thickness can be obtained by decreasing the concentrations of point defects, dipoles, and Weisberg inhomogeneities; N_i, N_{dip}, and N_{Weis}, respectively. The defects of the latter type are probably caused by defect–impurity complexes, in formation of which the substrate defects are involved, because the concentration N_{Weis} decreases with increasing film thickness. The concentration N_i and the degree of compensation K also decrease, while the sheet concentration N_S increases. It is noteworthy that the radiation treatment of the doped layer formed in the 8-μm-thick film leads to an additional increase in the electron mobility, to a decrease in the Weisberg-inhomogeneity concentration, and to an increase in the sheet concentration. In this case, the point-defect concentration is virtually invariable. One may assume that additional radiation–thermal treatment leads to the decomposition of defect–impurity complexes, due to which the concentration and mobility of electrons increase and the degree of compensation decreases; i.e., the structure of the doped layer becomes more perfect.

It is shown in [12–16] that the radiation–thermal treatment of implanted GaAs (rapid thermal annealing using halogen lamps and electron-beam annealing) leads both to enhancement of the diffusion of the impurity and its activation and to the formation of defect complexes. With allowance for the results of this study, it is believed that the decomposition of defect complexes also occurs during radiation treatment. It remains to determine what factors are responsible for the dominance of one or another of the noted processes.

Figure 3 shows typical depth profiles of the electron concentration and mobility in the doped layers intended for Gunn devices. The Hall mobility is no lower than 4600 cm^2 V^{-1} s^{-1}. In the fabricated samples, the product $nd = (1–4) \times 10^{12}$ cm^{-2} and the doped-layer thickness is 0.60–0.95 μm.

The experimental Gunn devices and the integrated circuits based on them were fabricated by planar technology. Ohmic contacts were formed by vacuum deposition of the AuGe + 14%Ni alloy with subsequent alloying in hydrogen at 420°C for 2–5 min. The active elements of the integrated circuits were isolated by successive bombardment of interelement gaps by H, He, and N ions. The samples of Gunn devices were 100 μm in length and 50 μm in width. The measurements were performed with a 5009 sampling oscilloscope. In Fig. 4, we show the oscillograms of currents in the diodes fabricated from two types of structures with ion-implanted layers: those subjected to the additional radiation treatment and those not subjected to it. The main parameters of the diodes (the resistance homogeneity $\Delta R/R$ and the current drop γ) are listed in Table 2.

As can be seen from Table 2 and Fig. 4, the doped layers in the epitaxial films subjected to the photon-radiation treatment are characterized by better homogeneity and higher values of the current drop. Nearly ideal current pulses were generated in these structures, and the effects caused by trapping and impact ionization were completely absent. At the same time, these effects are present in the diodes fabricated from the material that was not subjected to additional radiation treatment.

The above technology was used to fabricate regenerator integrated circuits on the basis of GaAs with planar Gunn devices. The parameters of the fabricated regenerators are as follows: the control signal is 0.3 V, the output signal is 0.3 V (for a load of 50 Ω), the pulse width is 300 ps, the leading-edge time is 80 ps, and the

Table 2. Parameters of Gunn devices

Material	$\Delta R/R$, %	γ, %
Structure before the radiation treatment	13.9	36.4
Structure after the radiation treatment	8.7	43.6

power consumption is 0.19 W. The regenerators provided the product of power consumption and the response speed close to 10 pJ.

ACKNOWLEDGMENTS

We are grateful to G. I. Aĭzenshtat for his help in measuring the characteristics of the Gunn devices and integrated circuits.

REFERENCES

1. G. King, M. P. Wasse, and C. P. Sandbank, in *Gallium Arsenide* (Inst. of Physics, London, 1968; Sovetskoe Radio, Moscow, 1972).
2. M. Shur, *GaAs Devices and Circuits* (Plenum, New York, 1987; Mir, Moscow, 1991).
3. V. M. Ardyshev, L. A. Kozlova, O. N. Korotchenko, and A. P. Mamontov, USSR Inventor's Certificate, No. 235,899 (1 April 1986).
4. V. M. Ardyshev, G. I. Aĭzenshtat, B. S. Azikov, and L. S. Shirokov, USSR Inventor's Certificate, No. 125,682 (3 March 1980).
5. T. T. Lavrishchev and S. S. Khludkov, in *Gallium Arsenide*, Ed. by S. A. Krivov (Tomsk Gos. Univ., Tomsk, 1975), No. 5, p. 57.
6. *Atomic Diffusion in Semiconductors*, Ed. by D. Shaw (Plenum, London, 1973; Mir, Moscow, 1975), Chap. 6.
7. R. Stratton, J. Phys. Chem. Soc. **23**, 1011 (1962).
8. L. M. Falicot and M. Cuevas, Phys. Rev. **164**, 1025 (1967).
9. L. R. Weisberg, J. Appl. Phys. **33**, 1817 (1962).
10. K. L. Chopra, *Thin Film Phenomena* (McGraw-Hill, New York, 1969; Mir, Moscow, 1972), Chap. 1.
11. V. L. Bonch-Bruevich and S. M. Kogan, Fiz. Tverd. Tela (Leningrad) **1**, 1221 (1959) [Sov. Phys. Solid State **1**, 1118 (1959)].
12. M. V. Ardyshev and V. M. Ardyshev, Fiz. Tekh. Poluprovodn. (St. Petersburg) **32**, 1153 (1998) [Semiconductors **32**, 1029 (1998)].
13. M. V. Ardyshev, V. M. Ardyshev, and S. S. Khludkov, Fiz. Tekh. Poluprovodn. (St. Petersburg) **34**, 28 (2000) [Semiconductors **34**, 27 (2000)].
14. M. V. Ardyshev, V. M. Ardyshev, and S. S. Khludkov, Fiz. Tekh. Poluprovodn. (St. Petersburg) **34**, 70 (2000) [Semiconductors **34**, 70 (2000)].
15. M. V. Ardyshev and V. M. Ardyshev, Fiz. Tekh. Poluprovodn. (St. Petersburg) **36**, 164 (2002) [Semiconductors **36**, 157 (2002)].
16. M. V. Ardyshev and V. M. Ardyshev, Fiz. Tekh. Poluprovodn. (St. Petersburg) **36**, 269 (2002) [Semiconductors **36**, 250 (2002)].

Translated by V. Bukhanov

Semiconductors, Vol. 37, No. 4, 2003, pp. 443–447. Translated from Fizika i Tekhnika Poluprovodnikov, Vol. 37, No. 4, 2003, pp. 460–464.

SEMICONDUCTOR STRUCTURES, INTERFACES, AND SURFACES

The Influence of Carbon on the Properties of Si/SiGe Heterostructures

M. Ya. Valakh*, V. N. Dzhagan, L. A. Matveeva, A. S. Oberemok, B. N. Romanyuk, and V. A. Yukhimchuk

Institute of Semiconductor Physics, National Academy of Sciences of Ukraine, Kiev, 03028 Ukraine

** e-mail: valakh@semicond.kiev.ua*

Submitted July 4, 2002; accepted for publication October 4, 2002

Abstract—Si/SiGe/SiGe:C/SiGe/Si heterostructures are investigated by Raman spectroscopy, electroreflectance method, and secondary-neutral mass spectrometry. It is shown that doping of a SiGe layer lying between undoped SiGe layers with C (1.5%) leads to almost complete stress relaxation in the doped layer. It is found that high-temperature photon annealing is responsible for a partial stress relaxation in the lower SiGe buffer layer. However, such annealing increases the Si content in this layer. Low-temperature treatment in the radio-frequency (RF) hydrogen plasma leads to considerable stress relaxation in the lower buffer layer without varying its composition. The results obtained from the electroreflectance and secondary-neutral-mall spectra correlate with the Raman spectroscopy data. *© 2003 MAIK "Nauka/Interperiodica".*

1. INTRODUCTION

More and more interest has been shown in SiGe systems in recent time. This is caused by the development of microwave integrated circuits [1] and optoelectronic devices operating in the near-IR region [2] on the basis of well-developed Si technology. The possibility of obtaining an $Si_{1-x}Ge_x$ solid solution with any value of x between 0 and 1 makes it possible to vary the solution band gap. Furthermore, the mobility of charge carriers in SiGe structures is considerably higher than in pure Si. In the case of thin highly strained Ge layers on Si, self-organized growth of nanoislands is possible [3].

Due to the lattice mismatch between Si and SiGe solid solution, the Si–Ge layers on Si substrates are strained. Upon reaching the critical thickness of the SiGe layer, misfit dislocations, which partially relieve the stress, appear at the interface. However, misfit dislocations substantially degrade device parameters. To solve the related problems, various methods are used. These are growing the SiGe films on gradient layers [4], doping SiGe layers with C [5], and hydrogen ion implantation into the strained layer [6]. Furthermore, in recent years, much attention has been given to the investigation of the influence of elastic stress on diffusion in strained heterostructures. Elastic stress can both accelerate and decelerate diffusion fluxes of atoms [7].

The purpose of this study was to investigate the properties of Si/SiGe heterostructures which were doped with C during growth, as well as analyze the influence of additional treatments on the properties of the hetorostructure layers.

2. EXPERIMENTAL

The epitaxial structures investigated here consisted of a C-doped (1.5%) 100-nm-thick SiGe layer lying between undoped SiGe layers, each 50 nm thick. The Ge content in these layers was 25% ($x = 0.25$). Pure Si was used for the substrate and the upper protective layer (cap). The protective-layer thickness was 50 nm (Fig. 1). One series of the samples was subjected to photon annealing for 1 min at 700, 800, and 900°C, and also to thermal annealing for 15 min at 900°C. Another series included samples treated in the low-temperature RF hydrogen plasma. The main investigation method was Raman spectroscopy. The spectra were recorded at room and liquid-nitrogen temperatures using a spectrometer with a double monochromator. The excitation was performed by the emission of an Ar^+ laser with wavelengths of 457.9, 476.5, 487.9, and 514.5 nm. The use of different wavelengths allowed us to vary the depth of probing the structures. The signal reflected from the structure was detected by a cooled photomultiplier operating in the photon-counting mode. In order to determine the positions of the Raman bands with higher accuracy, the plasma lines of the Ar^+ laser were used. The structures were additionally investigated by the electroreflectance method and secondary-neutral mass spectrometry (SNMS).

3. RESULTS AND DISCUSSION

It is known that three modes manifest themselves in the Raman spectrum of the SiGe solid solution. These are the Ge–Ge, Ge–Si, and Si–Si modes. The band fre-

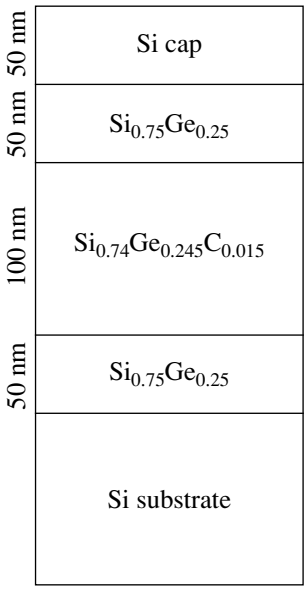

Fig. 1. Schematic representation of the structure under investigation.

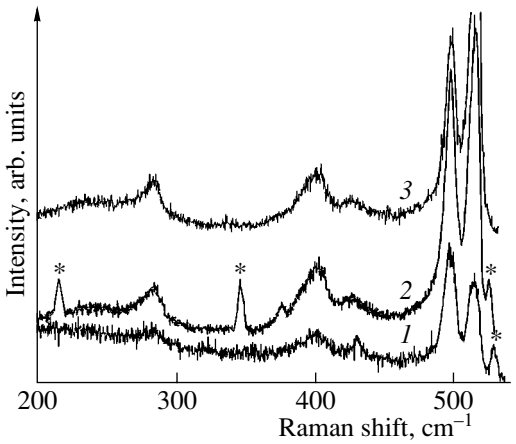

Fig. 2. Raman spectra of starting samples recorded at room temperature. The wavelengths of the exciting radiation λ are (*1*) 476.5, (*2*) 487.9, and (*3*) 514.5 nm. The plasma lines of the Ar^+ laser are denoted by asterisks.

quencies depend on the atomic fraction of Ge x and the elastic strain ε according to the expressions [8]

$$\omega_{Si-Si} = 520.5 - 68x - 815\varepsilon,$$
$$\omega_{Ge-Si} = 400.5 + 14x - 575\varepsilon, \quad (1)$$
$$\omega_{Ge-Ge} = 282.5 + 16x - 385\varepsilon.$$

Solving the system, it is possible to determine x and ε from each pair of Eqs. (1). We should note that the second equation is valid only for $x \le 0.4$. However, for the multilayer structure under consideration, it is difficult to use these equations directly for quantitative analysis. Although the atomic fraction x for the starting sample is known from the epitaxial-growth conditions and the SNMS measurements, it is impossible to determine unambiguously the elastic strain ε in the layers, at least at room temperature. This is due to the fact that the experimental spectrum represents a superposition of contributions from all layers of the structure, and it is impossible to isolate the bands from separate layers at room temperature. However, these expressions can be used to analyze the spectra of SiGe layers that were not doped with C, with the proviso that the bands from the doped layer and undoped layers at low temperatures are isolated with allowance made for the changes in the elastic constants at these temperatures. In this case, the effect of the additional stress arising in the layers under investigation due to an insignificant distinction in their coefficients of thermal expansion can be neglected since the corresponding shift of the Raman bands is less than the measurement error.

The Raman spectra of the starting structure at room temperature are shown in Fig. 2. The bands at ω_1 = 290 cm^{-1}, ω_2 = 406 cm^{-1}, and ω_3 = 502 cm^{-1} (curve *3*) correspond to the Ge–Ge, Ge–Si, and Si–Si vibrations. These bands are governed by the summary contribution to scattering from the SiGe and SiGe:C layers. The band at a frequency of ω_4 = 520 cm^{-1}, which is due to the superposition of contributions of the Si–Si vibrations in the substrate and the protective layer, is characterized by a slight asymmetry (a feature in the low-frequency region). The bands at frequencies of ω_5 = 430 cm^{-1} and ω_6 = 250 cm^{-1} have no unambiguous interpretation in the literature (see, for example, [9, 10]).

To isolate the contributions from separate layers, Raman spectra were obtained at different wavelengths of the exciting radiation (Fig. 2, curves *1*–*3*). With increasing wavelength, the probing depth d increases according to the formula $d = 1/2\alpha$, where α is the absorption coefficient of the substance under investigation [11]. It can be seen from Fig. 2 that the relative intensity of the band peaked at 520 cm^{-1} increases in this case, which is indicative of the increasing contribution of scattering from the Si substrate. We recorded the spectrum in the Si–Si-vibration range with a higher resolution (the spectral width of the gap ~1.2 cm^{-1}). In this case, we succeeded in isolating the components in the asymmetric band at 520 cm^{-1} (from the substrate) and at 517 cm^{-1} (from the protective layer). With an increase in the wavelength of exciting radiation, the relative intensity of the band peaked at 520 cm^{-1} increased due to the increasing contribution of the signal from the substrate.

A more informative picture with respect to the Si–Si vibrations is observed at a low temperature (Fig. 3, curve *1*). In this case, the bands peaked at 523.5, 520.3, and 505 cm^{-1} are clearly observed. The bands at 523.5 and 520.3 cm^{-1} correspond to the substrate and the protective layer, respectively, whereas the band at 505 cm^{-1} is a superposition of the signals from SiGe:C and the upper SiGe transition layer. A weak band at 515 cm^{-1} is

related to the lower SiGe transition layer. The increase in the band frequencies in the spectra recorded at liquid-nitrogen temperature is due to the increase in the elastic constants when the temperature is lowered. The difference in the positions of the bands related to the Si–Si vibrations in the substrate and in the protective Si layer is indicative of the fact that the protective layer is tensile-strained. Evaluation of the tensile stress according to the formula $\sigma(\mathrm{H/m^2}) = 2.49 \times 10^8 \Delta\nu(\mathrm{cm^{-1}})$ [12] yields a value of 1.04×10^9 N/m^2. Such a large tensile stress is caused by the significant lattice mismatch between Si and SiGe layers.

The position of the band corresponding to the undoped lower SiGe transition layer (515 cm^{-1}) indicates that this layer is heavily compressed. Indeed, at room temperature, the band caused by the Si–Si vibrations in the unstrained solid solution should shift with a variation in x according to the expression [10] $\omega_{\mathrm{Si-Si}} = 520 - 70x$, where x is the atomic fraction of Ge in the $Si_{1-x}Ge_x$ solid solution. It was demonstrated [13] that, for the $Si_{1-x}Ge_x$ solid solutions, the dependences of the band frequencies at room and liquid-nitrogen temperatures on the atomic fraction of Ge are similar and differ only by a constant value of ~3 cm^{-1}. Therefore, at liquid-nitrogen temperature, this expression takes the form $\omega_{\mathrm{Si-Si}} = 523–70x$. In our case, for $x = 0.25$, the band position for the completely relaxed SiGe layer should be at 505.5 cm^{-1}, in contrast to the experimental value of 515 cm^{-1}. Using formulas (1) with the above correlation for liquid-nitrogen temperature, we obtained $x = 0.25$ and $\varepsilon = –0.0105$ for the undoped lower SiGe transition layer. At the same time, the SiGe:C layer and the upper SiGe transition layer relaxed almost completely (~505 cm^{-1}).

The depth profiles of Si, Ge, and C in the structure under investigation ((*1*) for the starting sample and (*2*) for the sample annealed at 900°C for 15 min) are shown in Fig. 4. When constructing these profiles, we took into account that a layer ~10 nm thick is removed from the structure surface during the SNMS measurements, whereupon the composition of the sample is analyzed. It can be seen from Fig. 4 that, upon sputtering the surface Si layer in the starting sample, the Ge content increases starting at a depth of 30 nm. The Ge content levels off at a depth of 50 nm, remains virtually constant up to a depth of 180 nm, and then decreases as the depth increases to 240 nm. In the sample bulk, the tail of the Ge distribution is observed. This tail is related to the sputtering of the crater edges, as well as to some diffusion redistribution of Ge during layer deposition. It should be noted that the Ge distribution in the SiGe transition layer adjacent to the substrate is much more gradual compared with the Ge distribution in the upper SiGe transition layer.

After photon annealing at 700, 800, and 900°C for 60 s, the distribution of C atoms does not change. Only insignificant blurring of the Ge-depth profile near to the interface between the lower SiGe transition layer and the substrate is observed (the spectra are not shown). After thermal annealing at $T = 900$°C for 15 min, the Ge and C distributions are blurred considerably (curves *2* in Fig. 4). The SNMS measurements showed that the treatment in the RF hydrogen plasma for 1–5 min leads to the growth of a surface oxide layer ~5–15 nm thick (due to the residual oxygen), as well as to increase in the hydrogen content in the upper layer. The Ge- and C-depth profiles do not change compared with the case of the starting sample.

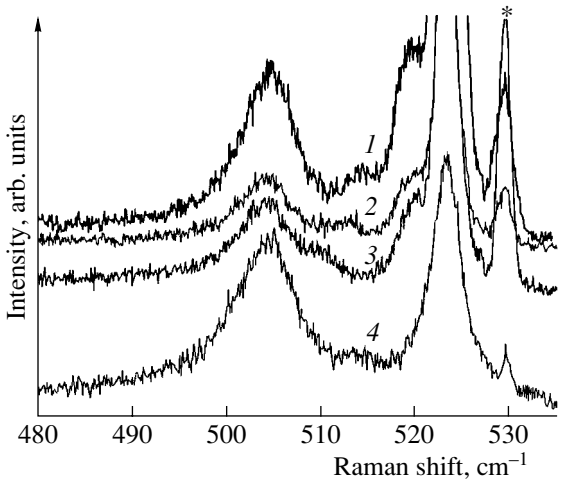

Fig. 3. Raman spectra of (*1*) the starting sample, (*2*) the sample annealed at 800°C for 1 min, (*3*) the sample annealed at 900°C for 1 min, and (*4*) the sample treated in RF plasma for 5 min. The spectra were recorded at 80 K at the wavelength of the exciting radiation $\lambda = 487.9$ nm: The plasma lines of the Ar^+ laser are denoted by asterisks.

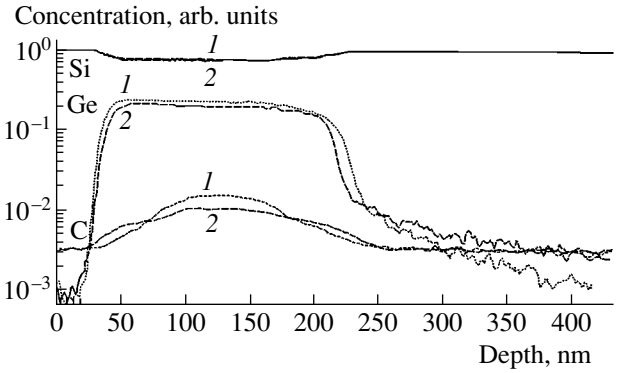

Fig. 4. SNMS profiles of Si, Ge, and C in (*1*) the starting sample and (*2*) the sample annealed at 900°C for 15 min.

Figure 3 shows the Raman spectra (curves *2*, *3*) of the samples annealed at 800 and 900°C. It can be seen that, with an increase in the annealing temperature, the band related to the Si–Si vibrations in the lower Si–Ge transition layer shifts to lower frequencies, which is indicative of partial stress relaxation. However, the position of the band related to the Si–Si mode does not attain a value corresponding to a completely relaxed

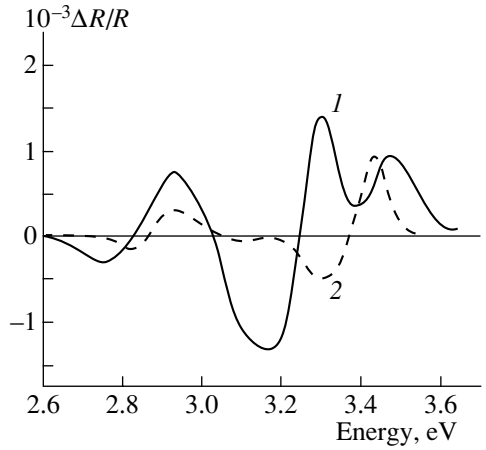

Fig. 5. Electroreflectance spectra of (*1*) the starting sample and (*2*) the sample annealed at 900°C for 15 min.

layer. In this case, we made allowance for some increase in the Si content in the lower transition layer due to the diffusion during the annealing (on the basis of the Raman and SNMS measurements). This increase shifts the band to higher rather than to lower frequencies. At the same time, the composition of the SiGe:C layer between the two SiGe layers is almost invariable during the annealing, which is confirmed by the fact that the position of the scattering band related to the Si–Si vibrations in this layer is constant, as well as by the SNMS data.

It also follows from the Raman spectra that treatment in the low-temperature RF hydrogen plasma, in contrast to high-temperature photon annealing, does not change the composition of the SiGe layers. At the same time, the stress decreases considerably in this case. This manifests itself in a shift of the Si–Si mode related to the protective Si layer to higher frequencies, so that this mode coincides with the Si–Si mode related to the substrate after prolonged (5 min) treatment (Fig. 3, curve *4*). Such treatment of starting samples also reduces the stress in the lower SiGe transition layer, which results in a shift of the corresponding band from 515 to 513.5 cm^{-1} (Fig. 3, curve *4*). The position of the band corresponding to the SiGe:C layer was the same for different parameters of the treatments in the RF plasma, which is indicative of maximum stress relaxation under these conditions.

The electroreflectance spectra of the starting sample and the sample annealed at 900°C for 15 min are shown in Fig. 5. The spectra were recorded at room temperature. The modulation voltage was 1 V, which corresponded to the weak-field mode. In this case, the formulas derived by Aspnes [14] can be used for the calculation of the direct-transition energy E_g and the phenomenological broadening parameter Γ. The depth of radiation penetration into the structures was no greater than 80 nm, due to which only the protective Si layer and the upper SiGe transition layer contributed to the detected signal. It can be seen from Fig. 5 that the considerable stress in the protective Si layer in the starting sample leads to a splitting of the band corresponding to two adjacent direct transitions (curve *1*). The energies of these transitions, calculated from the formulas [14], are equal to E_0 = 3.23 and 3.28 eV, in contrast to the transition energy for the unstrained crystalline Si, which amounts to 3.38 eV. After annealing at 900°C, the stress reduces and the spectral splitting is no longer observed. Furthermore, the phenomenological broadening parameter noticeably decreases after annealing (from 145 to 130 meV). This fact serves as extra evidence of reduced stress in the Si layer because the broadening parameter is inversely proportional to the electron-energy-relaxation time. Concerning the transition energy for the SiGe layer, it is equal to 2.9 eV and does not change after annealing. This value of the transition energy indicates that the upper SiGe layer is unstrained. At the same time, the phenomenological broadening parameter Γ decreased from 170 to 125 meV after annealing, which is indicative of structural ordering in this layer.

4. CONCLUSION

Thus, it is established in this study that doping the SiGe layer lying between undoped SiGe layers with C (1.5%) causes almost complete stress relaxation in it. High-temperature photon annealing causes partial stress relaxation in the lower SiGe transition layer. However, the Si content increases in the lower layer in this case. Low-temperature treatment in the RF hydrogen plasma causes considerable stress relaxation in this layer without changing the layer composition. The investigations of the structures by the electroreflectance method confirm that the protective Si layer in the starting sample is strained, whereas the upper SiGe transition layer is unstrained. It is shown that the results of the electroreflectance measurements correlate with the Raman spectroscopy data.

ACKNOWLEDGMENTS

We are grateful to D. Kryuger and V.P. Mel'nik for supplying the samples, to A.B. Kornete for performing the treatment of the samples in the RF hydrogen plasma, and to R.Yu. Holiney for measuring the electroreflectance spectra.

This study was supported in partly by INTAS-CALL 2001 NANO-0444.

REFERENCES

1. A. Cutalans, Solid State Commun. **39**, 59 (2000).
2. H. Presting, Thin Solid Films **321**, 186 (1998).
3. T. I. Kamins, E. C. Carr, R. S. Williams, and S. J. Rosner, J. Appl. Phys. **81**, 211 (1997).
4. F. Schaffler, Semicond. Sci. Technol. **12**, 1515 (1997).

5. A. Rodriquez, J. Olivares, J. Sangrador, *et al.*, Thin Solid Films **383**, 113 (2001).
6. S. Mantl, B. Hollander, R. Liedtke, *et al.*, Nucl. Instrum. Methods Phys. Res. B **147**, 29 (1999).
7. N. E. B. Cowern, P. C. Zalm, P. van der Sluis, *et al.*, Phys. Rev. Lett. **72**, 2585 (1994).
8. J. Groenen, R. Carles, S. Christiansen, *et al.*, Appl. Phys. Lett. **71**, 3856 (1997).
9. W. J. Brya, Solid State Commun. **12**, 253 (1973).
10. M. I. Alonso and K. Winer, Phys. Rev. B **39**, 10056 (1989).
11. A. C. De Wilton, M. Simard-Normandin, and P. T. T. Wong, J. Electrochem. Soc. **133**, 988 (1986).
12. J. Takahashi and T. Makino, J. Appl. Phys. **63**, 87 (1987).
13. M. A. Renucci, J. B. Renucci, and M. Cardona, in *Proceedings of Second International Conference on Light Scattering in Solids, Paris, 1971*, Ed. by M. Balkanski (Flammarion, Paris, 1971), p. 326.
14. D. E. Aspnes, Surf. Sci. **37**, 418 (1973).

Translated by N. Korovin

Semiconductors, Vol. 37, No. 4, 2003, pp. 448–451. Translated from Fizika i Tekhnika Poluprovodnikov, Vol. 37, No. 4, 2003, pp. 465–468.

SEMICONDUCTOR STRUCTURES, INTERFACES, AND SURFACES

Effect of Irradiation with Low-Energy Ar Ions on the Characteristics of the Working and Rear Sides of Single-Crystal GaAs Substrate

A. S. Alalykin*^, P. N. Krylov*, I. V. Fedotova*, and A. B. Fedotov^^**

** Udmurt State University, Krasnoarmeĭskaya ul. 71, Izhevsk, 426034 Russia*

^e-mail: ftt@uni.udm.ru

*** Nizhni Novgorod State Technical University, ul. Minina 24, Nizhni Novgorod, 603024 Russia*

^^e-mail: fabor@kis.ru

Submitted July 10, 2002; accepted for publication October 4, 2002

Abstract—Contactless methods were used to study the characteristics of the front and rear sides of single-crystal GaAs wafers whose rear side was irradiated with low-energy Ar ions. Variations in the optical and photoelectric properties of irradiated and unirradiated sides were detected. A solitonic mechanism for the penetration of defects into the crystal bulk is suggested. *© 2003 MAIK "Nauka/Interperiodica".*

1. INTRODUCTION

Treatment of various materials with particle beams is widely used in the fabrication of modern electronic devices. Irradiation of the surface gives rise to various kinds of defects and affects the structure not only at the irradiated surface itself but also at distances from the irradiated spot that exceed by three orders of magnitude the characteristic lengths of absorption of primary radiation. This phenomenon has come to be referred to as the long-range effect. Long-range effects have been studied previously (see, for example, [1–4]). These effects can be divided into two groups, i.e., longitudinal and transverse effects. The emergence of excess defects at the surface at a certain distance from the irradiated region should be assigned to transverse effects. Thus, Kol'chenko *et al*. [4] studied the effect of local irradiation with argon ions on the structure, composition, and properties of GaAs surface layers in the vicinity of the pseudointerface between the irradiated and unirradiated surface areas. It was shown that the distribution of dislocations appearing in the unirradiated region had an extremum. A maximum in this distribution was found to be located at a distance of about 1.5 μm from the boundary of the irradiated area.

In this paper, we report the results of studying the longitudinal long-range effect. We studied variations in the optical and electrical characteristics of irradiated (with low-energy argon ions) and unirradiated sides of a single-crystal GaAs wafer. A mechanism for the penetration of defects into the crystal bulk is suggested.

2. EXPERIMENTAL

The *n*-GaAs:Te wafers ($n = 10^{18}$ cm^{-3}) were irradiated with argon ions in a Sapfir setup that is described in detail elsewhere [5]. The ion discharge current in a Radikal-80 ion source was $I = 0.6$–0.7 A at a voltage $U = 2000$ V; the average ion energy was 300–400 eV; and the ultimate vacuum in a chamber corresponded to a pressure of 10^{-5} Torr. The working gas was introduced directly into the ion source.

The wafers were irradiated with argon ions for 10, 20, 30, and 45 min. Before and after irradiation, the samples were studied using contactless methods.

We used an LÉF-3M-1 ellipsometer to measure angular dependences of parameters ψ and Δ for irradiated and unirradiated sides of wafers. The spectral dependence of the reflection coefficient was studied using an SF-26 spectrophotometer equipped with an attachment for measuring the reflectance in the near-infrared and visible regions of the spectrum. The spectral dependence of photoconductivity for both sides of each sample was measured by a contactless high-frequency capacitive method.

3. RESULTS

Using an SF-26 spectrophotometer, we found that the reflection spectra of the front and rear sides of the wafers virtually coincided before irradiation (Fig. 1). However, the spectrum of the rear side becomes much different from that of the front side after irradiation. A decrease in the reflection coefficient of the rear (irradiated) side is observed after irradiation, which indicates that the corresponding surface either loses its specular properties or becomes more rough. Variations in the reflection spectrum for the unirradiated (front) side of the samples are more complex. According to previous inferences [6], reflection at very short wavelengths should be governed by the intrinsic properties of a

material rather than by impurities. It is expected that the surface plays an important role in the near-ultraviolet and visible regions of the spectrum [6]. It can be seen from Fig. 1 that a decrease in the reflection coefficient in the near-infrared region of the spectrum and its increase in the visible spectral region are observed for the unirradiated (front) side after irradiation of the rear surface.

Thus, the properties of the material itself and the quality of the opposite (front) surface of the wafer are affected by irradiation of the rear sides of the wafers. It is worth noting that relative temporal variations in the reflection coefficients are largest for an irradiation duration of 10 min. This circumstance is indicative of a complex character of generation and decomposition of imperfections at both irradiated and unirradiated sides of GaAs wafers.

Studies performed using an LÉF-3M-1 ellipsometer showed that the ellipsometric parameter ψ at the Brewster angle varies as a result of irradiation. This parameter measured at the rear surface varies similarly to that measured at the front surface (Fig. 2), but these variations are less pronounced at the front (unirradiated) surface than at the rear (irradiated) surface.

It is quite evident that before irradiation the surfaces are virtually lacking a damaged layer, the Brewster law is obeyed, the angle between the reflected and refracted rays is equal to 90°, and the parameter ψ equals zero. As a result of irradiation, thin damaged layers begin to grow at the front and rear surfaces; in these layers, the dipole moments of molecules are oriented in a different way than in the wafer bulk. Due to this circumstance, reflected light has a slight elliptic polarization when the incoming light is incident at an angle which is equal to the Brewster angle. The parameter ψ increases and attains a maximum after irradiation for 30 min.

The amplitudes of oscillations in the components of the electric-field vector for the reflected wave A_p and A_s (the subscripts *p* and *s* indicate the components which are parallel and perpendicular to the plane of incidence, respectively) are also changed as a result of irradiation. The difference between these components becomes distinct after irradiation, which indicates that the reflecting system is anisotropic. Dependences of the difference between the magnitudes of these components on the irradiation duration are shown in Fig. 3.

The plot of the difference between the above components for the unirradiated (front) side features the first point of inflection after irradiation of the wafers for 10 min and a maximum after irradiation for 30 min. Judging from the above temporal dependences, we may assume that an anisotropic damaged layer appears at the unirradiated (front) side of the wafers as a result of irradiation. As the irradiation time increases, the anisotropy becomes more pronounced; however, it attains a maximum at the irradiation time which is equal to that corresponding to leveling off of the damaged-layer thickness (see Fig. 2). Thereafter, a secondary rearrangement of the structure occurs.

The most pronounced anisotropy of the films is observed at irradiated sides after irradiation for 10 min,

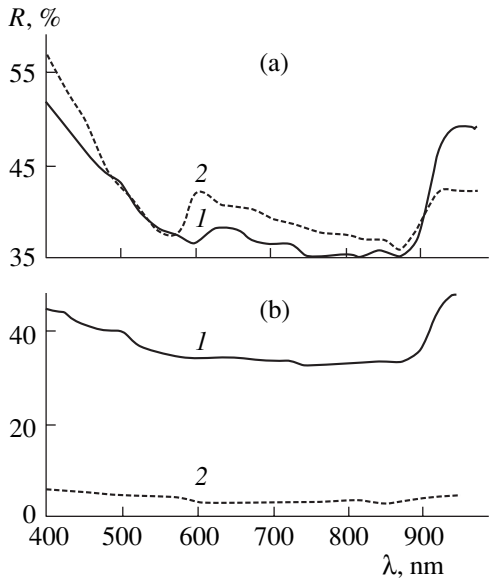

Fig. 1. Reflection spectra of (a) the unirradiated (front) side and (b) the irradiated (rear) side of the sample: (*1*) before irradiation and (*2*) after irradiation for 10 min.

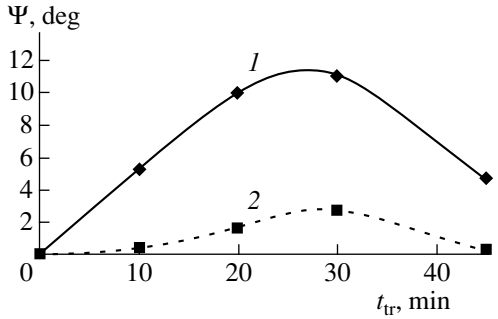

Fig. 2. Ellipsometric parameter ψ as a function of irradiation duration t_{tr} for (*1*) the irradiated (rear) side of the wafer and (*2*) the unirradiated (front) side.

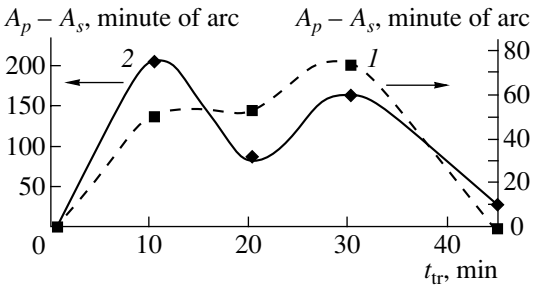

Fig. 3. Dependences of $A_p - A_s$ on the irradiation duration t_{tr} for (*1*) the unirradiated (front) side of the wafer and (*2*) the irradiated (rear) side.

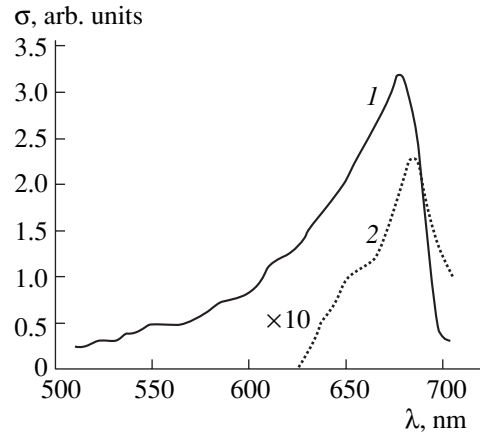

Fig. 4. Spectral dependences of photoconductivity for the irradiated (rear) side of GaAs wafer: (*1*) before irradiation and (*2*) after irradiation for 10 min.

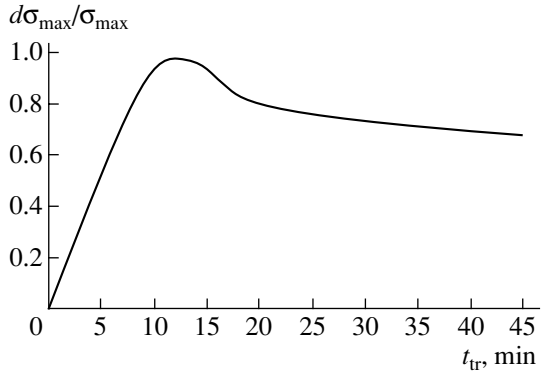

Fig. 5. Relative variation in photoconductivity in relation to the irradiation duration.

which apparently corresponds to an increase in the damaged-layer thickness and to depletion of this layer in arsenic. With further irradiation, gallium is sputtered; accordingly, the concentrations of elements become equal. In this situation, gallium can enter into the damaged layer; as a result, a new increase in the anisotropy is observed. It is quite possible that these variations will recur if the irradiation time increases further.

The special features of variation in the spectral photoconductivity of the front side are similar to those of the rear side (Fig. 4). Ion bombardment brings about a decrease in photoconductivity within an entire spectral range. Variations in the vicinity of the peak in the spectral curve at a wavelength $\lambda = 695$ nm are the most pronounced. The relative variation in photoconductivity as a function of irradiation duration is described by a curve with a peak (Fig. 5). The largest variation in σ (by 93% of the initial value) is observed after irradiation for 10 min.

It has been shown previously [7, 8] that the photoconductivity of submicrometer *n*-GaAs epitaxial films has a predominantly surface origin and can be interpreted as a variation in the dark electrical conductivity due to a decrease in the layer thickness as a result of capture of photogenerated holes by the surface states. The results of studying a decrease in photoconductivity as a result of mechanical treatment [9] made it possible to conclude that an additional recombination channel came into existence in the film; this channel brought about a decrease in the effective lifetime of charge carriers. It is believed that the most likely cause of variation in the electrical properties of epitaxial GaAs film is migration of point defects from the layer damaged by mechanical treatment. In the case under consideration, variations in photoconductivity at the irradiated and unirradiated sides of the wafers can also be attributed to an increase in the defect concentration in the structure.

4. DISCUSSION

Thus, ellipsometric and spectral studies show that variations in the properties of gallium arsenide wafers as a result of irradiation with argon ions are related to the mobility of structural defects. As is well known [10], the mobility of structural defects depends on the distribution of point defects around extended inhomogeneities in the crystal structure. It is also known [10] that extended defects of the crystal lattice (free surfaces, voids, cracks, the grain and block boundaries, and separate dislocations with an edge component) are the potential sources and sinks for vacancies. The position, size, and shape of the aforementioned defects can change if vacancies are absorbed or released.

The formation of a surface layer enriched with vacancies is also quite possible in the case under consideration. Further penetration of vacancies into the crystal bulk occurs owing to their diffusion, which is complicated by the generation and dissociation of both divacancies ($V + V \longleftrightarrow V_2$) and trivacancies ($V_2 + V \longleftrightarrow V_3$ or $V + V + V \longleftrightarrow V_3$). Taking these interactions into account, we obtain the following system of continuity equations:

$$\partial N/\partial t = D\nabla^2 N - 2(A_1 N^2 - A_2 N_d) - 3(A_3 N_d N - A_4 N_t), \quad (1)$$

$$\partial N_d/\partial t = D_d \nabla^2 N_d + A_1 N^2 - A_2 N_d - A_3 N_d N + A_4 N_t, \quad (2)$$

$$\partial N_t/\partial t = A_3 N_d N - A_4 N_t. \quad (3)$$

Here, N_d and N_t are the concentrations of divacancies and trivacancies, respectively; the terms A_1N^2 and A^3N_dN are the divacancy- and trivacancy-generation rates per unit volume; and A_2N_d and A_4N_t are the dissociation rates of divacancies and trivacancies, respectively. The parameters A_1–A_4 are exponential functions of temperature and are referred to as the rate constants for the reactions of generation and dissociation of corresponding defects [11].

In this model, the diffusion flux of trivacancies is assumed to be negligible compared to diffusion fluxes of vacancies and divacancies. Let us assume that the generation rate of divacancies is equal to the rate of their dissociation (local equilibrium with respect to divacancies). In this situation, the condition $A_1N^2 = A_2N_d$ should be satisfied. Since N and N_d are functions of the coordinate r and time t, this condition is in fact an equation of motion (in the crystal) of the point of local equilibrium with respect to divacancies $r = r(t)$ in the implicit form. The parameters A_i are represented as $A_i = A_{i0}\exp(-\mu_i/kT)$, where A_{i0} are constants and μ_i are chemical potentials of defects of the ith type. Consequently, in order to determine the dependence $r(t)$, we have to solve the equation

$$\frac{A_{10}}{A_{20}}\exp\left(\frac{\mu_2 - \mu_1}{kT}\right) = \frac{N^2(r(t))}{N_d(r(t))}. \quad (4)$$

It is reasonable to assume that, in the vicinity of a given coordinate, the generation–dissociation reaction for trivacancies is far from equilibrium and, consequently, $A_3N^3 \gg A_4N_t$. As a result, the system of Eqs. (1)–(3) can be rewritten as

$$\partial N/\partial t = D\nabla^2 N - 3A_3^* N^3, \quad (5)$$

$$\partial N_d/\partial t = D_d\nabla^2 N_d - A_3 N_d N, \quad (6)$$

$$\partial N_t/\partial t = A_3 N_d N, \quad (7)$$

where $A_3^* = A_3(A_1/A_2)$. As a result, Eq. (5) takes the form that allows solitonic solutions. Consequently, solitary (soliton) waves of vacancies can appear in this region. In this situation, the rate of transport of vacancies should be controlled by the velocity of motion of the region of local equilibrium with respect to vacancies rather than by diffusion relation (1).

5. CONCLUSION

Thus, preferential sputtering of As occurs at the irradiated side of a GaAs wafer at the early stage of irradiation of this wafer with Ar ions; the reason for this is that As has a larger sputtering coefficient compared to Ga. As a result, a damaged layer is formed at the sample surface; this layer contains a fairly high concentration of vacancies and is enriched with Ga. The flux of vacancies and divacancies is directed towards the crystal bulk. If the irradiation time is longer than 10 min, the damaged (depleted in As) layer is etched off, so that the structure of this layer becomes similar to that of the initial crystal. The waves of vacancies and divacancies reach the unirradiated side of the wafer. During their motion, these waves interact with linear defects. As a result of these interactions, a point defect can diffuse to a dislocation and completely annihilate at it [12]; however, the largest fraction of point defects reaches the opposite side of the wafer. Vacancies and their complexes are acceptors [13, 14], which brings about a reduction in photoconductivity, variation in the ellipsometric parameter ψ, and a change in the reflection coefficient.

REFERENCES

1. P. V. Pavlov, V. I. Pashkov, V. M. Genkin, *et al.*, Fiz. Tverd. Tela (Leningrad) **15**, 2857 (1973) [Sov. Phys. Solid State **15**, 1914 (1973)].
2. V. A. Panteleev, V. V. Chernyakhovskiĭ, and S. N. Ershov, Fiz. Tverd. Tela (Leningrad) **16**, 2151 (1974) [Sov. Phys. Solid State **16**, 1411 (1974)].
3. T. I. Kol'chenko, V. M. Lamako, and I. E. Maronchuk, Fiz. Tekh. Poluprovodn. (Leningrad) **15**, 580 (1981) [Sov. Phys. Semicond. **15**, 329 (1981)].
4. A. S. Alalykin, A. A. Krasnov, P. N. Krylov, *et al.*, in *Proceedings of IX International Meeting on Radiation Physics of Solid State* (Sevastopol, 1999), p. 132.
5. A. S. Akashkin, V. V. Besogonov, V. M. Vetoshkin, *et al.*, Vak. Tekh. Tekhnol. **9** (2), 17 (1999).
6. B. I. Bednyĭ, A. N. Kalinin, and I. A. Karpovich, Fiz. Tekh. Poluprovodn. (Leningrad) **17**, 1302 (1983) [Sov. Phys. Semicond. **17**, 822 (1983)].
7. *Semiconductors and Semimetals*, Vol. 3: *Optical Properties of III–V Compounds*, Ed. by R. Willardson and A. Beer (Academic, New York, 1967; Mir, Moscow, 1970).
8. B. I. Bednyĭ, A. N. Kalinin, I. A. Karpovich, and A. N. Savinov, Izv. Vyssh. Uchebn. Zaved. Fiz., No. 12, 84 (1984).
9. B. I. Bednyĭ, S. N. Ershov, and V. A. Panteleev, Fiz. Tekh. Poluprovodn. (Leningrad) **19**, 1806 (1985) [Sov. Phys. Semicond. **19**, 1109 (1985)].
10. B. Ya. Lyubov, *Diffusion in Inhomogeneous Solid Media* (Nauka, Moscow, 1981), p. 295.
11. J. R. Manning, *Diffusion Kinetics for Atoms in Crystals* (Van Nostrand, New York, 1968; Mir, Moscow, 1971).
12. S. A. Medvedev, *Introduction to Semiconductor Materials Technology. A Textbook* (Vysshaya Shkola, Moscow, 1970).
13. K. Saarinen, A. P. Seitsonen, P. Hautojarvi, and C. Corbel, Phys. Rev. B **52**, 10932 (1995).
14. V. P. Klad'ko, T. G. Kryshtab, Yu. S. Kleĭnfel'd, *et al.*, Fiz. Tekh. Poluprovodn. (St. Petersburg) **26**, 368 (1992) [Sov. Phys. Semicond. **26**, 208 (1992)].

Translated by A. Spitsyn

Semiconductors, Vol. 37, No. 4, 2003, pp. 452–455. Translated from Fizika i Tekhnika Poluprovodnikov, Vol. 37, No. 4, 2003, pp. 469–472.

SEMICONDUCTOR STRUCTURES, INTERFACES, AND SURFACES

Generation–Recombination Centers in CdTe:V

L. A. Kosyachenko, S. Yu. Paranchich, Yu. V. Tanasyuk, V. M. Sklyarchuk, E. F. Sklyarchuk, E. L. Maslyanchuk, and V. V. Motushchuk

Chernovtsy National University, Chernovtsy, 58012 Ukraine

Submitted September 6, 2002; accepted for publication October 4, 2002

Abstract—Generation–recombination currents in surface-barrier structures based on vanadium-doped CdTe are investigated. The level depth and the capture cross section of the centers responsible for the most efficient generation–recombination processes in the samples examined are determined. © *2003 MAIK "Nauka/Interperiodica".*

1. INTRODUCTION

Cadmium telluride is one of the most well-studied II–VI compound semiconductors. It is a promising material for photodetectors, solar cells, and filters for the infrared spectral range. For several decades, CdTe and $Cd_{1-x}Zn_xTe$ alloys ($x \approx 0.1$) have been utilized in X-ray and γ-ray detectors [1, 2]. Another potentially important application is related to the use of CdTe as a photorefractive material in optical memory and information-processing systems.

Development of CdTe-based devices calls for the solution of several important problems. One of these is determining the parameters of impurity- and defect-related levels in this semiconductor. With respect to photorefractivity-based devices, deep levels of V impurity are of interest. Vanadium forms several recombination and trapping levels in the band gap [3]. A number of techniques (electrical, optical, luminescence, etc.) were used to examine the properties of CdTe:V and $Cd_{1-x}Zn_xTe$ ($x \approx 0.1$) in relation to the influence V doping; however, the parameters of these levels are not accurately known. In particular, this pertains to deep-level generation–recombination centers in the CdTe-based material. Consider, for example, deep levels in the energy range $(E_g/2) \pm 0.1$ eV (0.65–0.85 eV): one study revealed three levels located at 0.75, 0.77, and 0.78 eV [4]; two levels (at 0.76 and 0.79 eV) were found in another study [5]; and no such levels were found in a third one [6]. It is quite possible that differences in level positions reported by different authors are due to limited accuracy of the measurements rather than to a different nature of the levels involved.

In this paper, we report on the study of electrical properties of CdTe:V surface-barrier structures; the results presented make it possible to determine, with sufficiently high accuracy, (±0.01 eV) the level depth and the capture cross section of the centers involved most efficiently in the generation–recombination processes in CdTe:V. We also believe that the results related to the mechanisms of charge transport, which demonstrate very good agreement between the calculations and the experimental data, are of interest in themselves.

2. SAMPLES

Single crystals of CdTe:V were grown by the vertical Bridgman method in a quartz container. The concentration of V, which was loaded into the cell simultaneously with high-purity Cd and Te, was equal to 5×10^{18} cm^{-3}. The resistivity of the material was $(2–3) \times 10^9$ Ω cm in the center part of the ingot and 10^2–10^3 Ω cm at the ends of the ingot. The density and the mobility of holes in the center part of the ingot, determined from Hall effect and conductivity measurements, were $\sim 2 \times 10^7$ cm^{-3} and 70–80 cm^2 V^{-1} s^{-1}, respectively. Away from the center of the ingot, the carrier density increased up to $\sim 10^{15}$ cm^{-3}. Wafers cut from low-resistivity material were used to fabricate the diode structures.

Surface-barrier structures were formed using vacuum deposition of Al on the carefully polished and chemically treated surface of a wafer. Ohmic contacts were prepared by vacuum deposition of Ni. For a bias equal to 5 V, the forward current exceeded the reverse current by more than a factor of 10^2; under illumination, a photovoltage of about 0.5 V was observed.

3. ELECTRICAL PROPERTIES OF SURFACE-BARRIER DIODES

In Fig. 1, the current–voltage (*I–V*) characteristics of Al/CdTe:V diodes at three different temperatures are shown.

One can see that a temperature increase by a mere 33 K leads to an increase of almost an order of magnitude in both forward and reverse current. The shape of the voltage dependence of the reverse current remains unchanged, but only at low bias voltages (see Fig. 2a). Another typical feature of the *I–V* curves is the sublinear voltage dependence of the reverse current in the low-bias region; this is readily demonstrated by Fig. 2b, where (as in Fig. 2a) reverse characteristics of the diode are plotted normalized at $V = -0.2$ V. With an increase in the reverse bias, a sublinear dependence gives way to a superlinear one; the lower the temperature, the lower the voltage corresponding to this transition.

1063-7826/03/3704-0452$24.00 © 2003 MAIK "Nauka/Interperiodica"

A sublinear increase of the reverse current with the voltage is indicative of the thermal-generation current mechanism (saturation should occur in the case of an above-barrier diffusion current). For $|V| > (0.6–0.7)$ V, tunneling is another mechanism that comes into play (avalanche processes cannot take place in CdTe at such low bias voltages). As long as the thermal-generation current varies with temperature more strongly than the tunneling current, the contribution from the latter is reduced with increasing temperature.

The high-current region of the forward *I–V* characteristics is distorted because of the voltage drop across the series resistance R_s, which is always present in the diode structure. From Fig. 3, where the voltage dependence of the differential resistance is shown, one can see that the ohmic resistance R_s in the diodes under study amounts to 400–1000 Ω (and decreases with the temperature). Note that the region $V > 1$ V corresponds to the linear portion of the *I–V* curve plotted on the linear voltage scale; the cutoff voltage on such a plot equals 0.55 V at room temperature and increases to 0.59 V at 336 K. This means that semiconductor band bending at the surface (the barrier height) is, at least, 0.55–0.59 eV (complete compensation of the barrier does not occur, and some "residual" potential difference across the barrier remains).

Figure 4 shows the *I–V* characteristic of an Al/CdTe:V diode replotted to take into account the voltage drop across the series resistance R_s. We chose T = 336 K, since, with increasing temperature, the contribution from tunneling current under reverse bias decreases and, in addition, the influence of the series resistance under forward bias is reduced.

One can see from Fig. 4 that, even with the effect of series resistance taken into account, the forward *I–V* characteristic of the Al/CdTe:V diode is not described by the dependence $I \propto \exp(eV/2kT)$, which is usually considered as an indication of the recombination current-flow mechanism [7]. However, it should be stressed that the current follows this dependence only in the case of a *p–n* junction and under the condition that recombination proceeds via near-midgap levels. In the case of a Schottky diode (a surface-barrier structure), the shape of the forward *I–V* characteristics changes considerably. It becomes dependent on the barrier height, the recombination level depth, and other factors [8].

4. CALCULATION OF THE CURRENT–VOLTAGE CHARACTERISTICS OF THE DIODE

Using the Sah–Noyce–Shockley theory, let us calculate the *I–V* characteristics of a surface-barrier Al/CdTe:V structure in the same way as in [9].

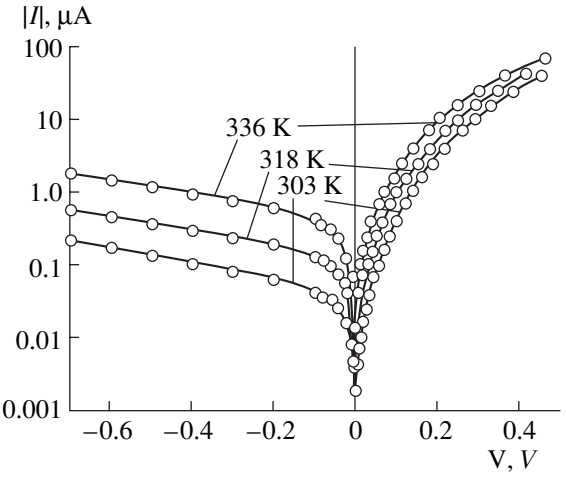

Fig. 1. Current–voltage characteristics of an Al/CdTe:V diode at different temperatures.

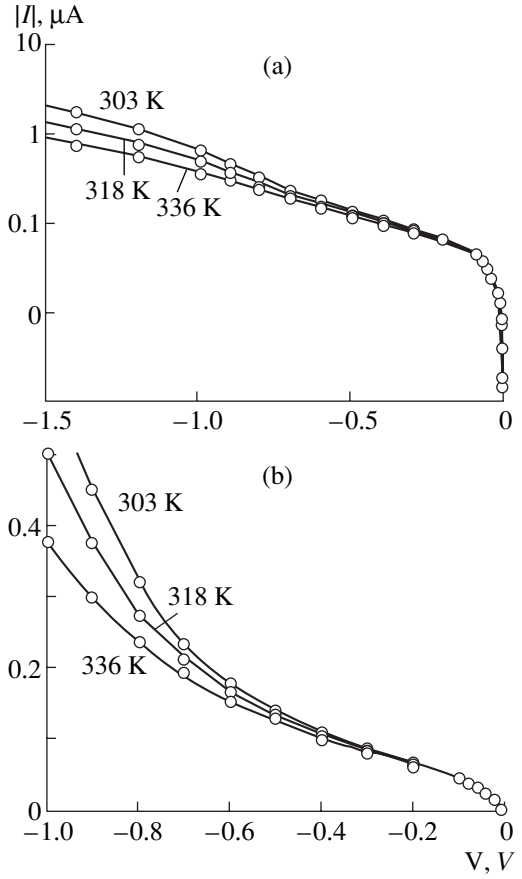

Fig. 2. Reverse current–voltage characteristics of the diode at different temperatures normalized in the low-bias region and plotted on (a) semilog and (b) linear scales.

The generation–recombination rate in any cross section of the depletion layer of the diode structure is given by

$$U(x, V) = \frac{n(x, V)p(x, V) - n_i^2}{\tau_{p0}[n(x, V) + n_1] + \tau_{n0}[p(x, V) + p_1]}; \quad (1)$$

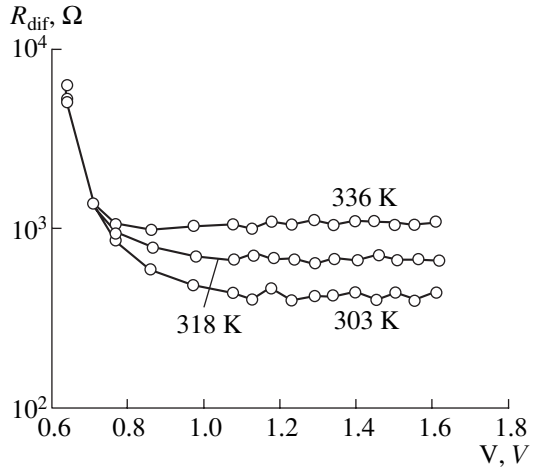

Fig. 3. Voltage dependence of the Al/CdTe:V diode differential resistance under forward bias in the high-current region.

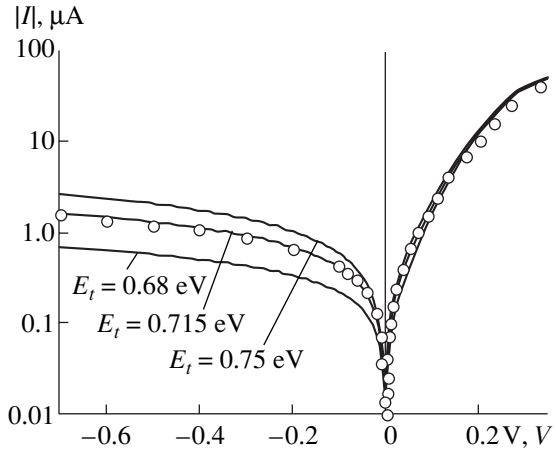

Fig. 4. Current–voltage characteristics of the Al/CdTe:V diode calculated for different values of the generation–recombination level depth E_t (solid lines) in comparison with experimental characteristics (circles); T = 336 K.

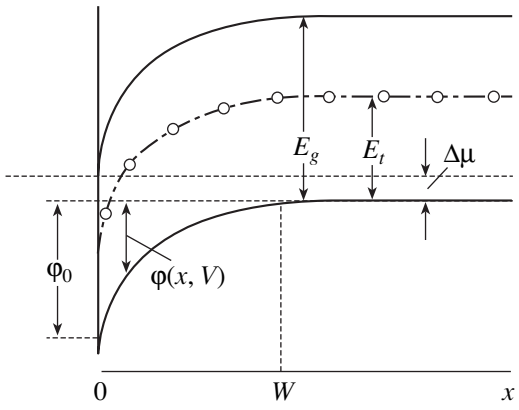

Fig. 5. Energy-band diagram of the surface-barrier structure under consideration.

here, n(x, V) and p(x, V) are the free-carrier densities in the conduction and valence bands, respectively; n_1 and p_1 are equilibrium free-carrier densities when the Fermi level coincides with the recombination level; n_i is the intrinsic carrier density; τ_{n0} and τ_{p0} are the effective electron and hole lifetimes in the space-charge region (SCR), respectively. Note that the generation–recombination level depth enters this expression in terms of n_1 and p_1.

Let us set the energy zero at the top of the valence band and the coordinate zero at the metal–semiconductor interface (see Fig. 5).

Then, n(x, V) and p(x, V) can be written as

$$n(x, V) = N_c \exp\left[-\frac{E_g - \Delta\mu - \varphi(x, V) - eV}{kT}\right], \quad (2)$$

$$p(x, V) = N_v \exp\left[-\frac{\Delta\mu + \varphi(x, V)}{kT}\right], \quad (3)$$

where N_c and N_v stand for the effective density of states in the conduction and valence bands, respectively (other notation is clear from Fig. 5). The potential energy in the SCR of the surface-barrier structure is described by the following expression:

$$\varphi(x, V) = (\varphi_0 - eV)\left(1 - \frac{x}{W}\right)^2; \quad (4)$$

here, φ_0 and W are the barrier height and the SCR width, respectively.

The generation–recombination current is calculated by integrating U(x, V) over the SCR:

$$I = Ae\int_0^W U(x, V)dx, \quad (5)$$

where A is the diode area and e is the electron charge.

Solid lines in Fig. 4 represent the I–V curves of the diode at T = 336 K calculated by formula (5) (taking (1)–(4) into account) for different values of the barrier height φ_0. The effective electron and hole masses were assumed to be $0.11m_0$ and $0.35m_0$, respectively. The hole density is 8×10^{14} cm^{-3}, and we find that $\Delta\mu = kT\ln(N_v/p)$ equals 0.208 eV. The shape of the calculated I–V characteristic under forward bias fits the shape of the experimental curve most closely when the barrier height is taken to be 0.695 eV; the best fit for the magnitude of the current is obtained with $\tau_{n0} = \tau_{p0} = 7 \times 10^{-8}$ s.

The results of calculating the reverse I–V characteristic are quite sensitive to the level depth E_t. The best agreement between calculation results and the experiment is attained for E_t = 0.715 eV. In Fig. 4, we show the calculated curves for $E_t = 0.715 \pm 0.035$ eV; however, a notable discrepancy with the experimental data takes place even when E_t deviates from 0.715 eV by less than ±0.01 eV. Assuming that the band gap of CdTe at 300 K E_g = 1.5 eV and the temperature coefficient of

the band gap variation $\gamma = 4 \times 10^{-4}$ eV/K, we find that $E_g = 1.5 - 36\gamma = 1.49$ eV at $T = 336$ K [10]. Thus, the generation–recombination level is located close to, but not exactly at, the midgap ($E_g/2 = 0.745$ eV). Unfortunately, from the data obtained, it is not possible to determine from which band is the level E_t spaced by 0.715 ± 0.01 eV [10].

Given a vanadium concentration $N_V = 5 \times 10^{18}$ cm^{-3}, one can use the value of the carrier lifetime τ, which was determined above, to find the capture cross section of the generation–recombination centers: $\sigma = 1/v\tau N_V = 2 \times 10^{-15}$ cm^2 (here, $v \simeq 10^7$ cm/s is the mean thermal velocity of the charge carriers).

5. CONCLUSION

Rectifying surface-barrier structures were obtained by vacuum deposition of Al on CdTe:V single crystals. The current–voltage characteristics calculated by Sah–Noyce–Shockley generation–recombination theory agree well with the experimental curves. Comparison of the results of calculation with the experimental data enabled us to determine the parameters of generation–recombination centers: a level depth $E_t = 0.715$ eV and a capture cross section $\sigma = 2 \times 10^{15}$ cm^2, as well as a carrier lifetime $\tau = 7 \times 10^{-8}$ s.

REFERENCES

1. Y. Eisen, Nucl. Instrum. Methods Phys. Res. A **322**, 596 (1992).
2. E. H. Redus, A. C. Huber, and J. A. Pantazis, Nucl. Instrum. Methods Phys. Res. A **458**, 214 (2001).
3. Y. Marfaing, J. Cryst. Growth **197**, 707 (1999).
4. A. Zerrai, G. Marrakchi, G. Bremond, *et al.*, Nucl. Instrum. Methods Phys. Res. A **161**, 264 (1996).
5. A. Castaldini, A. Cavallini, B. Fraboni, *et al.*, J. Appl. Phys. **83**, 2121 (1998).
6. A. Zumbiehl, P. Fougeres, M. Hage-Ali, *et al.*, J. Cryst. Growth **197**, 670 (1999).
7. C. Sah, R. Noyce, and W. Shockley, Proc. IRE **45**, 1228 (1957).
8. L. A. Kosyachenko, V. P. Makhniĭ, and I. V. Potykevich, Ukr. Fiz. Zh. **23**, 279 (1978).
9. L. A. Kosyachenko, I. M. Rarenko, Z. I. Zakharuk, *et al.*, Fiz. Tekh. Poluprovodn. (St. Petersburg) **36**, 1480 (2002) [Semiconductors **36**, 1138 (2002)].
10. S. Sze, *Physics of Semiconductor Devices*, 2nd ed. (Wiley, New York, 1981; Mir, Moscow, 1984).

Translated by M. Skorikov

Semiconductors, Vol. 37, No. 4, 2003, pp. 456–461. Translated from Fizika i Tekhnika Poluprovodnikov, Vol. 37, No. 4, 2003, pp. 473–478.

SEMICONDUCTOR STRUCTURES, INTERFACES, AND SURFACES

Special Features of Formation and Characteristics of Ni/21*R*-SiC Schottky Diodes

V. L. Litvinov*, K. D. Demakov*, O. A. Ageev, A. M. Svetlichny**, R. V. Konakova***, P. M. Lytvyn***, O. S. Lytvyn***, and V. V. Milenin*****

** Institute for Information Technologies, Russian Research Centre Kurchatov Institute, pl. Akademika Kurchatova 1, Moscow, 123182 Russia*

*** Kalmykov State University of Radio Engineering, ul. Chekhova 22, Taganrog, 347915 Russia*

**** Institute of Semiconductor Physics, National Academy of Sciences of Ukraine, pr. Nauki 45, Kiev, 03028 Ukraine*

e-mail: konakova@isp.kiev.ua

Submitted September 10, 2002; accepted for publication October 4, 2002

Abstract—The Ni/*n*-21*R*-SiC(0001) and Ni/*n*-21*R*-SiC($000\bar{1}$) surface-barrier structures formed on 21*R*-SiC crystals doped to a concentration of $(1–2) \times 10^{18}$ cm^{-3} and grown by the Lely method were investigated prior to and after rapid thermal annealing (RTA) in vacuum (10^{-2} Pa) in the temperature range of 450–1100°C. Using X-ray diffraction analysis and Auger analysis, it is shown that cubic $NiSi_2$ and orthorhombic δ-Ni_2Si and NiSi silicides coexist with pure Ni in starting samples. The RTA brings about a polymorphic transformation of these phases, which causes the transformation of a barrier contact to a rectifying one independently of the SiC face type, even at $T \gtrsim 600$°C. The physicochemical mechanisms of degradation of these barrier structures are discussed. © *2003 MAIK "Nauka/Interperiodica".*

1. INTRODUCTION

Recent data on the technology of various types of SiC single crystals and related epitaxial structures confirm that the use of this material for high-temperature electronics is feasible [1–4]. However, the possible application of SiC in fabricating high-power devices, as well as fast-response microelectronic microwave devices, which can operate under extreme conditions, could not be realized without reliable metal–semiconductor contacts. Despite intensive investigations carried out in this field [5–9], a number of problems, which are associated with the specific features of formation, mechanism of degradation, and breakdown of nonrectifying and barrier contacts, still remain unresolved. Even for one metal, contact electrical characteristics vary in a wide range [8–11] and no clear correlation exists between the variation of these characteristics and the structure–phase state of the interface. The contacts for device structures based on wide-gap III–V compounds and Si were developed and fabricated earlier [12, 13]. With allowance made for this experience, it is possible to note that a "pure" metal–semiconductor interaction manifests itself only in the absence of oxide interlayers at the interface. Under real conditions, it is necessary to take into account exchange reactions of a metal with a semiconductor, as well as with oxide and other phases at the metal surface. These phenomena complicate the mechanism of contact formation. Moreover, a variation in the surface composition of a semiconductor over a depth of 5–10 Å is sufficient for the formation of the potential barrier. In this case, the investigations of the mechanism of formation of contacts with single-type metallization upon varying the SiC crystalline structure are of great importance.

In this study, we investigated the characteristics of Ni/*n*-21*R*-SiC contact structures, which were subjected to RTA by noncoherent infrared (IR) radiation in vacuum at 10^{-2} Pa over a wide temperature range. The Ni contacts with other SiC polymorphs were investigated in detail previously [8–11, 14, 15].

2. EXPERIMENTAL

The Ni/*n*-21*R*-SiC contact structures were formed at the (0001)Si and ($000\bar{1}$)C faces of the 21*R*-SiC single-crystal substrates. The 21*R*-SiC single crystals were grown by the Lely method and were doped with nitrogen to $(1–2) \times 10^{18}$ cm^{-3}.

Rectifying contacts to SiC were formed by resistive sputtering deposition of 100-nm-thick Ni film in a single vacuum run onto chemically cleaned (0001) or ($000\bar{1}$) faces of the samples at a substrate temperature of 300°C. Subsequent RTA in vacuum (10^{-2} Pa) for 10 s at a temperature as high as 1100°C was carried out.

Sheet resistance of the Ni films [Ω/□] on various substrates at various temperatures of rapid thermal annealing

Substrate	*T*, °C					
	300	450	600	750	900	1100
21*R*-SiC $(000\bar{1})$	3.25 ± 0.193	1.27 ± 0.007	10.91 ± 0.155	3.64 ± 0.016	3.64 ± 0.036	0.70 ± 0.006
21*R*-SiC (0001)	3.95 ± 0.293	1.30 ± 0.020	2.83 ± 0.131	4.48 ± 0.138	3.56 ± 0.055	1.01 ± 0.019
Polycor	1.40 ± 0.09	1.40 ± 0.10	1.30 ± 0.06	1.20 ± 0.05	1.10 ± 0.07	1.40 ± 0.09

Barrier contacts were also formed at opposite faces of the SiC samples by Ni thermal evaporation onto chemically cleaned sample surfaces at a substrate temperature of 300°C. The Ni layer thickness was the same as for nonrectifying contacts. Then the vacuum RTA of the samples was carried out for 10 s in the temperature range of 450–1100°C. The heating rate was 100 K/s. The RTA was performed by noncoherent IR radiation using an ITO-18MV setup [16].

Samples of two types were investigated, specifically, test and device structures. Test samples were Ni/*n*-SiC/Ni structures with a continuous metallization layer at both sides. Device structures had a Schottky barrier with an area of ~10^{-3} cm^2. These structures were formed using photolithography on an SiC wafer with a continuous metal contact at the opposite side.

The structures fabricated were analyzed using a number of methods. The sheet resistance of the Ni films was measured using the four-probe method. The barrier properties of contacts were investigated by the method of steady-state current–voltage (*I–V*) characteristics. The concentration profiles of components in contacts and processes at interfaces were investigated by the layer-by-layer Auger electron spectroscopy (AES). The phase composition of the heterointerface was monitored by an X-ray diffraction technique. The morphology and topography of surfaces were investigated by atomic-force microscopy (AFM).

3. RESULTS AND DISCUSSION

To obtain information on the character and temperature ranges of varying the electrical properties of contact structures, the sheet resistance of the Ni films was measured for various RTA temperatures. The results of measurements of the sheet resistance of the Ni films at the (0001) and $(000\bar{1})$ faces of the SiC crystals for various RTA temperatures are given in the table. Comparison of these results with the phase analysis data shows good correlation between the reduction of sheet resistance and the onset of the formation of the final phase of nickel silicide. The lowest value of the sheet resistance corresponds to the completion of this process.

Data on the influence of RTA conditions on the sheet resistance of Ni-on-polycor films obtained in a single vacuum run with the Ni/*n*-21*R*-SiC structures are given in the table. It can be seen that, for the Ni/polycor structures, the sheet resistance is lower. In this case, it depends more weakly on RTA temperature compared with the Ni/*n*-21*R*-SiC contacts. This is associated with the absence of interaction of the Ni film with the substrate.

Typical *I–V* characteristics of the Ni/*n*-21*R*-SiC$(000\bar{1})$ barrier contact prior to and after annealing are shown in Fig. 1. Qualitatively similar dependences were also obtained for the contacts formed on the other (0001) face. The specific feature of the characteristics obtained prior to and after the RTA is the absence of current saturation in the reverse portion of the *I–V* characteristic,

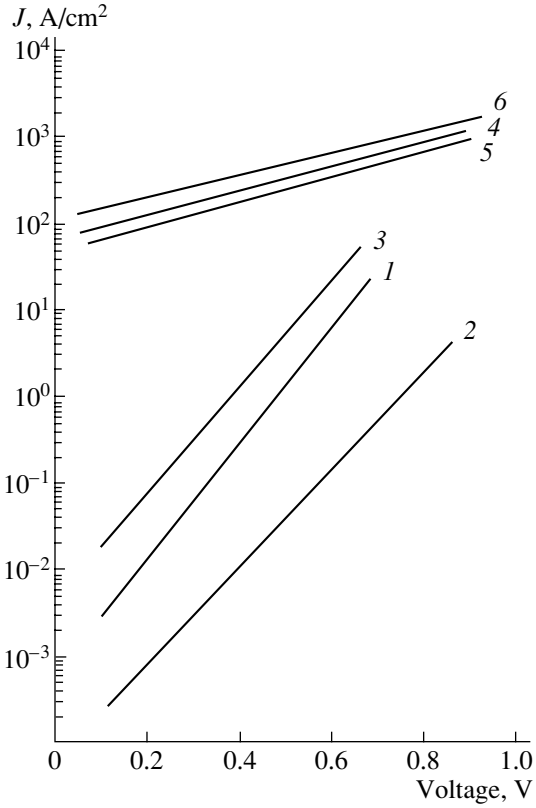

Fig. 1. Current–voltage characteristics of the Ni/*n*-21*R*-SiC(0001) contact measured for the structures (*1*) without annealing (the barrier height φ_B = 0.6 eV; the ideality factor n = 2.6) and after annealing at temperatures (*2*) 450 (φ_B = 0.65 eV, n = 2.1), (*3*) 600 (φ_B = 0.55 eV, n = 2.6), (*4*) 750, (*5*) 900, and (*6*) 1100°C; curves (*4*)–(*6*) correspond to the nonrectifying contact.

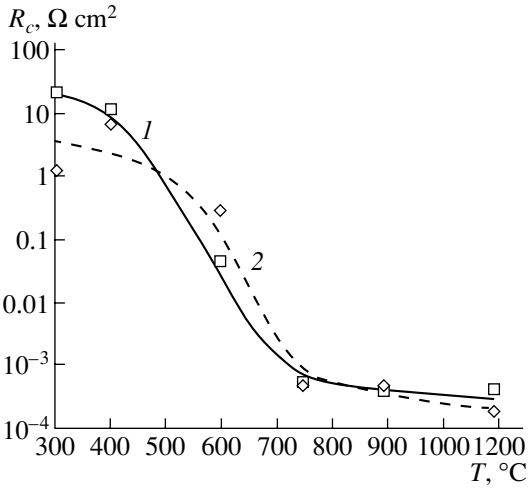

Fig. 2. Dependence of resistance of the Ni/*n*-21*R*-SiC contacts on the temperature of rapid thermal annealing. The structures are fabricated at the SiC faces (*1*) (0001) and (*2*) $(000\bar{1})$.

which can be associated with the conditions of contact formation. In fact, our investigations showed that a fairly high substrate temperature during Ni deposition leads to the partial phase formation in the Ni/*n*-21*R*-SiC system, which determines the formation of the heterointerface with the structure–phase inhomogeneity [17]. Consequently, the current across the Ni/*n*-21*R*-SiC contact flows through the segments with different potential barrier heights, which leads to the absence of a saturation current.

However, the shape of forward portions of the *I–V* characteristic is typical of the metal–semiconductor contact [18]; i.e.,

$$J = J_S \exp\left(\frac{qV}{nkT} - 1\right),$$

where J is the density of current through the contact, J_S is the saturation current density, q is the elementary charge, V is the applied voltage, n is the ideality factor, k is the Boltzmann constant, and T is the temperature.

The *I–V* characteristics obtained were analyzed using conventional procedures [18–20]. Using a modified model [21], which was adapted for SiC [22], the resistivity of the contacts was calculated in relation to the RTA conditions (Fig. 2).

It turned out that the contact resistance for the RTA temperature range of 450–750°C decreases drastically and ceases to depend on the face orientation. This is associated with the predominance of metastable phases of nickel silicides, with the formation of a diffuse heterointerface with an increased structure–phase inhomogeneity, and, consequently, with decreased height of the contact potential barrier. For the RTA at $T \gtrsim 700$°C, stable silicide phases are formed. Silicide phases are responsible for a decrease in resistance by 3–4 orders of magnitude compared with the starting sample and very

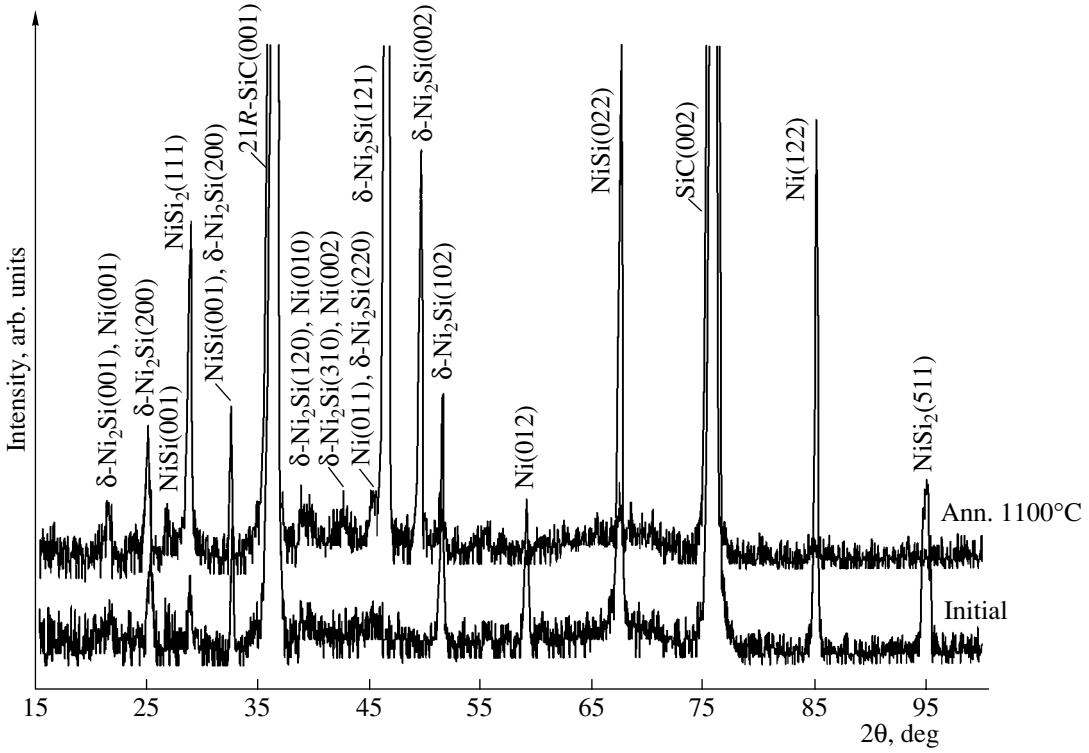

Fig. 3. X-ray diffraction patterns of the Ni/*n*-21*R*-SiC structures at the (0001) face prior to and after annealing at 1100°C.

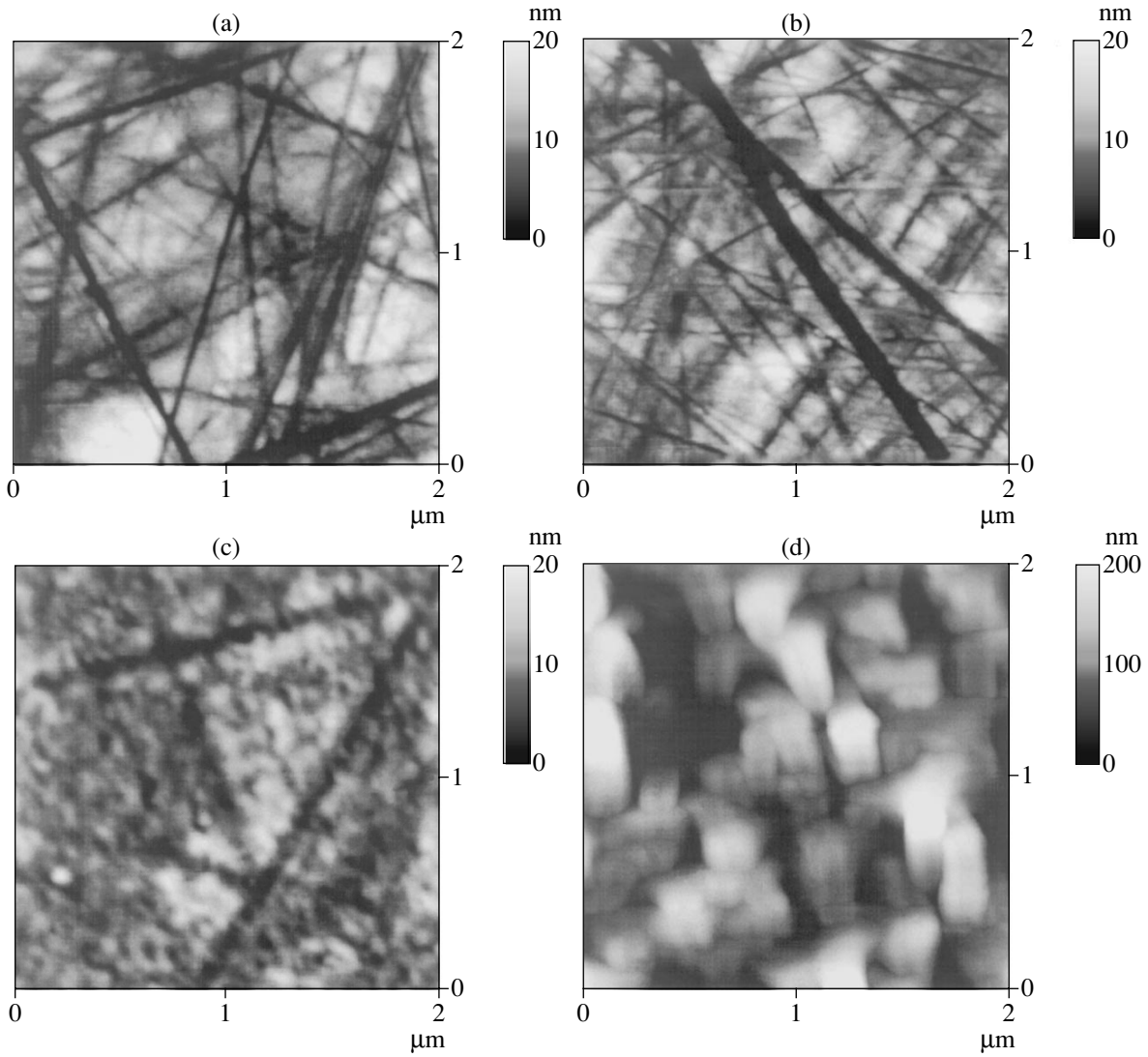

Fig. 4. Transformation of the morphology of the heterointerface surface during annealing: (a) the starting structure; and after annealing at temperatures T = (b) 450, (c) 750, and (d) 1100°C.

small resistance variations in the RTA range T = 750–1100°C. In general, the temperature dependences of resistance reflect the effects of interdiffusion and of formation and transformation of metastable nickel silicide phases at the Ni/*n*-SiC interface during RTA.

Figure 3 shows the results of X-ray diffraction analysis of starting Ni/*n*-21*R*-SiC(0001) contacts prior to and after annealing at 1100°C. It can be seen from the results that, even at the stage of formation of the contact structure, nickel silicides are formed in the diffusion zone of the Ni/*n*-SiC system of the initial sample. The phases formed during this process are identified as cubic $NiSi_2$ and orthorhombic δ-Ni_2Si and NiSi. Along with the hexagonal Ni polymorph, these phases determine the phase composition of the transition region of the contact. The RTA at 1100°C, as follows from Fig. 3, enhances the interaction between the chemically unbound Ni and SiC and leads to the polymorphic transformation of the phases which are formed at the stage of contact formation. Consequently, the fraction of the δ-Ni_2Si phase increases and retains the $NiSi_2$ phase reoriented along the ⟨111⟩ direction. This is conducive to its better incorporation into the rhombohedral SiC lattice.

The investigations of the surface morphology of the Ni film at various annealing temperatures showed that the starting film had a smooth surface (roughness $R_a \approx$ 1.4 nm) with a network of shallow depressions (as deep as 6 nm). The annealing at 450°C causes the formation of fine grains (diameter 17–40 nm, height 4–5 nm), as well as rounded depressions from 3 to 60 nm in depth, at the surface ($R_a \approx$ 1.8 nm). This fact points to the onset of diffusion and recrystallization in the metallized layer at this annealing temperature, which correlates with the

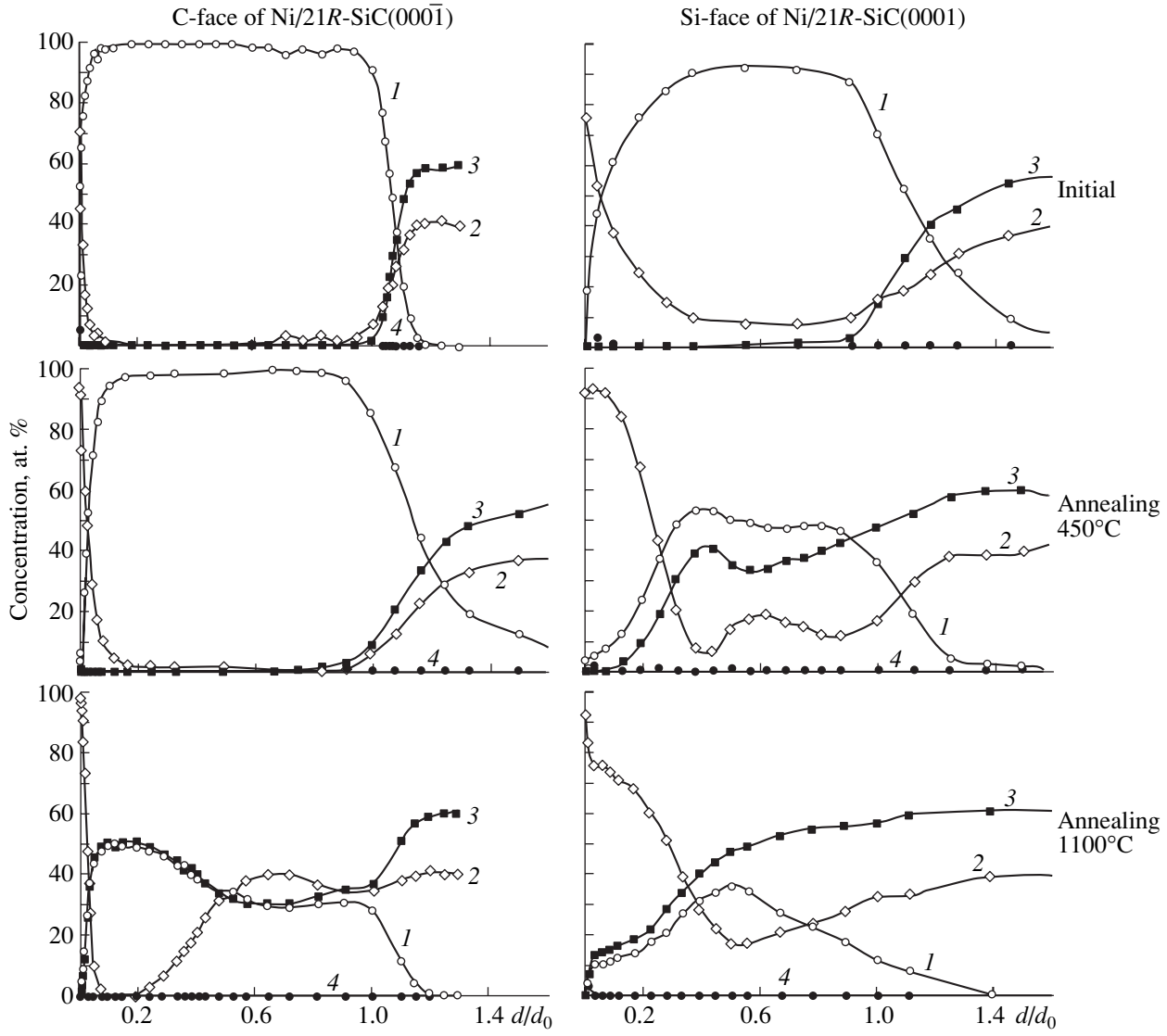

Fig. 5. Auger distribution profiles for the components in the Ni/*n*-21*R*-SiC$000\bar{1}$ and Ni/*n*-21*R*-SiC(0001) structures: (*1*) Ni, (*2*) C, (*3*) Si, and (*4*) O.

X-ray diffraction data. After the annealing at 1100°C, the film surface undergoes more drastic transformations ($R_a \approx 7.1$ nm). Large-size depressions of about 300 nm in diameter with an average depth of about 30 nm are formed at this surface.

Special features of the morphology of the SiC surface layer after removal of the metallized layer by ionic etching are illustrated in Figs. 4a–4d. Assuming that areas with dissimilar chemical compositions are sputtered differently by the Ar^+ beam, we can gain some insight into the planar structural–phase inhomogeneity of the Ni/*n*-SiC interface. As can be seen from Figs. 4a and 4b, after removal of the metal layer, characteristic linear defects are observed at the SiC surface in the heterointerface region at annealing temperatures as high as 750°C. During the RTA at 750°C, linear SiC defects are blurred and the tendency toward grain formation can be noticed. After the annealing at 1100°C, the surface of the exposed heterointerface consists of grains of about 70 nm in height with lateral dimensions from 200 to 800 nm.

The distribution profiles of components for the Ni/*n*-21*R*-SiC(0001) and Ni/*n*-21*R*-SiC($000\bar{1}$) contacts are shown in Fig. 5. It can be seen from the data shown in Fig. 5 that the enhancement of penetration of metal atoms into the semiconductor increases diffusion widening of the phase interface. This process occurs due to weakening and dissociation of Si–C bonds during the charge exchange with the interstitial Ni atom. Comparison of component profiles for the contacts formed at different SiC faces shows that a more

extended transition region is formed at the Si face compared with the C face. This is caused by the formation of Ni–Si chemical bonds even at the stage of metal adsorption onto the SiC substrate heated to 300°C. Such behavior is in agreement with the data on the temperature modes of formation of nickel silicides [23–26]. Therefore, the RTA at 450°C brings about an appreciable redistribution of the atomic components over the entire thickness of the metal cover deposited onto the (0001)SiC face. However, during the Ni deposition onto the $(000\bar{1})$SiC face, such deep penetration of the atomic components of the semiconductor into the metal occurs at much higher annealing temperatures ($\lesssim$600°C). In this case, the role of thermochemical factors, which determine the intense silicide formation, increases sharply. At higher temperatures, the variations are observed in the proportion of components in the film and in the transition contact region. These variations are associated with the conversion of unstable phases, which are formed at early stages, to more stable phases.

4. CONCLUSION

Thus, the above results permit us to make an inference about the structural–phase inhomogeneity of the heterointerface, which is formed during Ni deposition onto *n*-21*R*-SiC substrate heated to 300°C. The heterogeneity of the heterointerface increases during the rapid thermal annealing (RTA) in the temperature range of 450–1100°C. This enables us to explain the *I–V* characteristics of the Ni/*n*-21*R*-SiC contact at the (0001) and $(000\bar{1})$ faces by the current flowing through the segments with various barrier heights, including the nonrectifying regions. With an increase in the RTA temperature, as Ni is consumed, the contribution of the barrier constituent of the current decreases and its nonrectifying component dominates.

REFERENCES

1. R. J. Trew, Jing-Bang Tan, and P. M. Mock, Proc. IEEE **79**, 598 (1991).
2. P. A. Ivanov and V. E. Chelnokov, Semicond. Sci. Technol. **7**, 863 (1992).
3. P. A. Ivanov and V. E. Chelnokov, Fiz. Tekh. Poluprovodn. (St. Petersburg) **29**, 1921 (1995) [Semiconductors **29**, 1003 (1995)].
4. A. A. Lebedev and V. E. Chelnokov, Fiz. Tekh. Poluprovodn. (St. Petersburg) **33**, 1096 (1999) [Semiconductors **33**, 999 (1999)].
5. A. N. Andreev, A. A. Lebedev, M. G. Rastegaeva, *et al.*, Fiz. Tekh. Poluprovodn. (St. Petersburg) **29**, 1833 (1995) [Semiconductors **29**, 957 (1995)].
6. A. A. Lebedev, D. V. Davydov, V. V. Zelenin, and M. L. Korogodskiĭ, Fiz. Tekh. Poluprovodn. (St. Petersburg) **33**, 959 (1999) [Semiconductors **33**, 875 (1999)].
7. S. Yu. Davydov, A. A. Lebedev, O. V. Posrednik, and Yu. M. Tairov, Fiz. Tekh. Poluprovodn. (St. Petersburg) **35**, 1437 (2001) [Semiconductors **35**, 1375 (2001)].
8. L. M. Poter and R. F. Davis, Mater. Sci. Eng. B **34**, 83 (1995).
9. B. Pecz, Appl. Surf. Sci. **153**, 1 (2001).
10. S. Y. Han, K. H. Kim, J. K. Kim, *et al.*, Appl. Phys. Lett. **79**, 1816 (2001).
11. A. Kokanakova-Georgieva, Ts. Marinova, O. Noblanc, *et al.*, Thin Solid Films **343–344**, 637 (1999).
12. V. I. Strikha and E. V. Buzaneva, *Physical Foundations of the Reliability of Metal–Semiconductor Contacts in Integrated Electronics* (Radio i Svyaz', Moscow, 1987).
13. E. F. Venger, R. V. Konakova, G. S. Korochenkov, V. V. Melenin, É. V. Russu, and I. V. Prokopenko, *Interphase Interactions and Degradation Mechanisms in the Metal–InP and Metal–GaAs Structures* (Naychnaya Kniga, Kiev, 1999).
14. M. G. Rastegaeva, A. N. Andreev, A. A. Petrov, *et al.*, Mater. Sci. Eng. B **46**, 254 (1997).
15. H. S. Lee, S.-W. Lee, D. H. Shin, *et al.*, J. Korean Phys. Sci. **34**, 558 (1999).
16. D. A. Sechenov and A. M. Svetlichnyĭ, Élektron. Prom., No. 3, 6 (1991).
17. V. L. Litvinov, K. D. Demakov, O. A. Ageev, *et al.*, in *Abstracts of IV International Seminar on Silicon Carbide and Related Materials* (Novgorod, Russia, 2002), p. 67.
18. E. H. Rhoderick, *Metal–Semiconductor Contacts*, 2nd ed. (Clarendon, Oxford, 1988; Radio i Svyaz', Moscow, 1982).
19. A. Y. C. Yu, Solid-State Electron. **13**, 239 (1970).
20. F. A. Padovani and R. Stattion, Solid-State Electron. **9**, 695 (1966).
21. K. Varahramyan and E. J. Verret, Solid-State Electron. **39**, 1601 (1996).
22. O. A. Ageev, D. A. Sechenov, A. M. Svetlichnyi, and D. A. Izotovs, in *Abstracts of IV International Seminar on Silicon Carbide and Related Materials* (Novgorod, Russia, 2002), p. 67.
23. S. B. Kushchev, Doctoral Dissertation (Voronezh Gos. Tekhnol. Univ., 2000).
24. A. E. Gershinskiĭ, A. V. Rzhanov, and E. I. Cherepov, Mikroélektronika **11** (2), 83 (1982).
25. S. Murarka, *Silicides for VLSI Applications* (Academic, New York, 1983; Mir, Moscow, 1986).
26. O. M. Barabash and Yu. N. Koval', *Handbook on Crystalline Structure of Metals and Alloys* (Naukova Dumka, Kiev, 1986).

Translated by N. Korovin

Semiconductors, Vol. 37, No. 4, 2003, pp. 462–467. Translated from Fizika i Tekhnika Poluprovodnikov, Vol. 37, No. 4, 2003, pp. 479–484.

LOW-DIMENSIONAL SYSTEMS

Properties of Ge Nanocrystals Formed by Implantation of Ge^+ Ions into SiO_2 Films with Subsequent Annealing under Hydrostatic Pressure

I. E. Tyschenko*^, A. B. Talochkin*, A. G. Cherkov*, K. S. Zhuravlev*, A. Misiuk, M. Voelskow***, and W. Skorupa*****

** Institute of Semiconductor Physics, Siberian Division, Russian Academy of Sciences, pr. Akademika Lavrent'eva 13, Novosibirsk, 630090 Russia*

^e-mail: tys@isp.nsc.ru

*** Institute of Electronic Technology, 02-668 Warsaw, Poland*

**** Institute of Ion Beam Physics, Research Center Rossendorf, D-01314 Dresden, Germany*

Submitted July 22, 2002; accepted for publication September 6, 2002

Abstract—The influence of hydrostatic compression on the implantation-induced synthesis of Ge nanocrystals in SiO_2 host was studied. It is found that high-temperature annealing under pressure leads to retardation of Ge diffusion in SiO_2. It is shown that unstressed Ge nanocrystals are formed as a result of conventional annealing (under atmospheric pressure). Annealing under pressure is accompanied by formation of hydrostatically stressed Ge nanocrystals. The stress in Ge nanocrystals was determined from optical-phonon frequencies in the Raman spectra. The shift of Raman resonance energy (E_1, $E_1 + \Delta_1$) corresponds to the quantization of the ground-state energy for a two-dimensional exciton at the critical point M_1 of germanium. It is ascertained that a photoluminescence band peaked at 520 nm is observed only in the spectra of the films which contain stressed Ge nanocrystals. © *2003 MAIK "Nauka/Interperiodica".*

1. INTRODUCTION

Theoretical calculations [1] predict fairly large values of the band gap for Ge nanocrystals (nc-Ge). In addition, the closeness of the energy minimum for direct transitions to that for indirect transitions is expected to ensure high rates of radiative recombination for electrons and holes in nc-Ge [1, 2]. This circumstance was the reason for increased interest in the development and properties of nc-Ge because this material emits in the visible region of the spectrum and can compete with direct-gap semiconductors (for example, GaAs and AlGaAs). However, Ge quantum dots (QDs), which are conventionally produced by molecular-beam epitaxy (MBE) [3], are typically highly stressed. Furthermore, the stresses are distributed nonuniformly in these QDs. Nonuniform stresses can give rise to complex and almost unpredictable changes in the spectrum of electron states in nc-Ge [4]. This circumstance may account for the fact that photoluminescence (PL) of MBE-grown Ge QDs is not observed in the visible region of the spectrum. A PL band in the green–yellow region of the spectrum (520–580 nm) was observed for SiO_2 films that contained Ge nanocrystals [5–9]. However, the origin of this PL band has not been fully ascertained. Controversy about the PL mechanism is mainly due to the fact that there is no correlation between the size of nc-Ge crystallites and the position of the PL peak. At the same time, there is also no consensus about the role of the interface between an nc-Ge crystallite and the surrounding SiO_2 host in the processes of radiative recombination [2, 8, 9]. Hydrostatic compression can be one of the methods for controlling the electronic and structural properties of nc-Ge. Hydrostatic compression is mainly used as an efficient tool for studying the energy-band spectrum of semiconductors, including Si and Ge nanocrystallites. At the same time, there is evidence that hydrostatic compression in the course of high-temperature annealing [10] brings about retardation of diffusion; this circumstance can be conducive to the formation of higher density new-phase nuclei with smaller sizes. Tyschenko *et al.* [11, 12] observed intensification of short-wavelength PL in SiO_2 and SiO_xN_y films implanted with Si^+ and Ge^+ ions after these films were subjected to postimplantation annealing under pressure; this intensification was related to enhanced formation of ≡Si–Si≡, ≡Ge–Si≡, and ≡Ge–Ge≡ centers. In this study, hydrostatic pressure as a parameter of implantation-induced synthesis was used for the first time in order to form Ge nanocrystals in an SiO_2 host which are homogeneously stressed and stable at room temperature. The aim of this study was to investigate the properties of nc-Ge crystallites formed in SiO_2 films implanted with Ge^+ ions and then annealed under conditions of hydrostatic compression.

2. EXPERIMENTAL

Germanium nanocrystals were formed in 500-nm-thick SiO_2 films, which were grown by thermal oxidation on *n*-Si (100) wafers with a resistivity of 5–10 Ω cm. The films were first implanted with Ge^+ ions with energies of 450 and 200 keV at doses of 1.1×10^{15} and 6.6×10^{14} cm^{-2} (0.1 at. % of Ge); 6.6×10^{15} and 4.0×10^{15} cm^{-2} (0.67 at. % of Ge); and 3.0×10^{16} and 1.8×10^{16} cm^{-2} (3 at. % of Ge), respectively. The energies used and ion doses made it possible to form a flat Ge concentration profile in the depth range from about 0.1 to 0.35 μm. In the course of implantation, the ion-current density ranged from 0.5 to 1 $\mu A/cm^2$ and the target temperature was 120–130 K. After implantation, the samples were annealed for 5 h at temperatures T_a = 600 and 1130°C in an Ar atmosphere. Annealing was performed in a high-pressure furnace under the conditions of hydrostatic compression (P = 12 kbar) and, alternatively, in a conventional furnace under atmospheric pressure (1 bar). Concentration profiles of implanted Ge were studied using Rutherford backscattering (RBS) spectroscopy of 1.5-MeV He^+ ions. The Ge nanocrystals formed were analyzed by Raman scattering spectroscopy, high-resolution transmission electron microscopy (HRTEM), and PL spectroscopy. The Raman spectra were measured using a DFS-52 spectrometer and were excited with a 488-nm line of an Ar laser in the backscattering geometry. Resonance dependences of the Raman scattering were studied under excitation with Ar laser radiation at wavelengths of 457, 476, 488, 496, and 514 nm. For HRTEM studies, we used a JEM-4000 EX electron microscope with a resolution of 0.2 nm at an accelerating voltage of 250 keV. The PL in the wavelength range λ_{em} = 340–850 nm was excited with radiation of an N_2 laser with a wavelength λ_{ex} = 337 nm and a power of 10 mW. All measurements were performed at room temperature.

3. RESULTS AND DISCUSSION

In Fig. 1, we show the Ge concentration profiles obtained from an analysis of RBS spectra for the samples implanted with high Ge^+ doses and then annealed at T_a = 1130°C both at atmospheric pressure and at P = 12 kbar. Germanium was not redistributed within the SiO_2 film as a result of annealing under conditions of hydrostatic compression. In this case, the Ge profile in the unannealed samples and that in the samples annealed under pressure coincided. Conventional annealing at P = 1 bar was accompanied with the drain of a fraction of the Ge atoms to the SiO_2 surface. Part of the implanted Ge remained in the layer at a depth of ~150–300 nm, with the Ge concentration being equal to that before annealing. It is also worth noting that a fraction of germanium is transferred from the bulk to the 150 to 300-nm buried layer, which can be related to nucleation and subsequent growth of germanium precipitates.

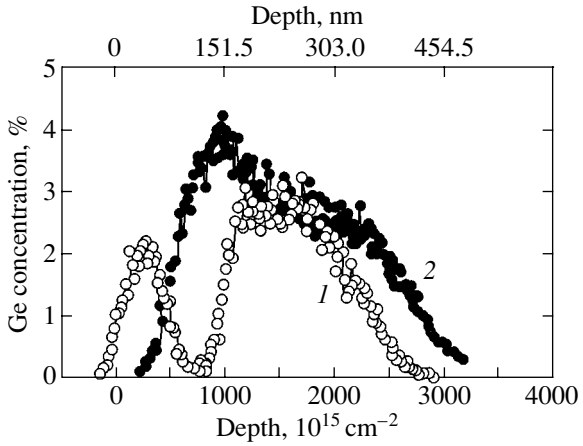

Fig. 1. Germanium concentration profiles obtained by Rutherford backscattering of helium ions from SiO_2 films that contained 3 at. % of Ge and were annealed at T_a = 1130°C under pressure of (*1*) 1 bar and (*2*) 12 kbar.

Information about the structure of the formed nc-Ge crystallites can be derived from the shape and position of peaks in the spectra of Raman scattering by optical phonons. Annealing at T_a = 600°C gives rise to a broad band in the Raman spectra with a peak at about 30 cm^{-1}. The full width at half-maximum (FWHM) of this band was about 30 cm^{-1}, which corresponds to vibrations of Ge–Ge bonds in an unordered host. Figure 2 shows the Raman spectra of SiO_2 films that contain 0.1, 0.67, and 3 at. % of Ge and that were annealed at T_a = 1130°C and P = 12 kbar. A band in the vicinity of 300 cm^{-1} is also observed in the Raman spectra of the films with low Ge content (0.1 at. %); the FWHM of this band is about 15 cm^{-1}. An increase in the Ge content to 0.67 at. % is accompanied by a further decrease in the FWHM of the band peaked at 300 to 10 cm^{-1} and by the appearance of a low-intensity narrow band peaked at about 307 cm^{-1}. This band becomes dominant in the Raman spectra of the films containing 3 at. % of Ge. Its intensity increases by more than two times. The FWHM of this band is about 4.5 cm^{-1}. A weakly pronounced band is observed at about 300 cm^{-1}; the intensity of this band is lower than that observed for the samples containing 0.67 at. % of Ge. The origin of the band at 300 cm^{-1} can be related both to isolated Ge–Ge bonds incorporated in SiO_2 in various positions and to amorphous Ge clusters. The presence of these clusters is confirmed by the fact that the band under consideration is narrower than in the spectra of the samples annealed at 600°C. For the sake of comparison, Fig. 2 also shows the Raman spectrum for a sample with 3 at. % of Ge after annealing at T_a = 1130°C under atmospheric pressure. In this case, a Ge peak with a frequency characteristic of bulk material (300 cm^{-1}) is observed in the Raman spectra; at the same time, the features corresponding to an amorphous component are virtually not observed. The shift of the optical-phonon line to higher frequencies (curve *3*) indicates that there are stresses in the material; as a

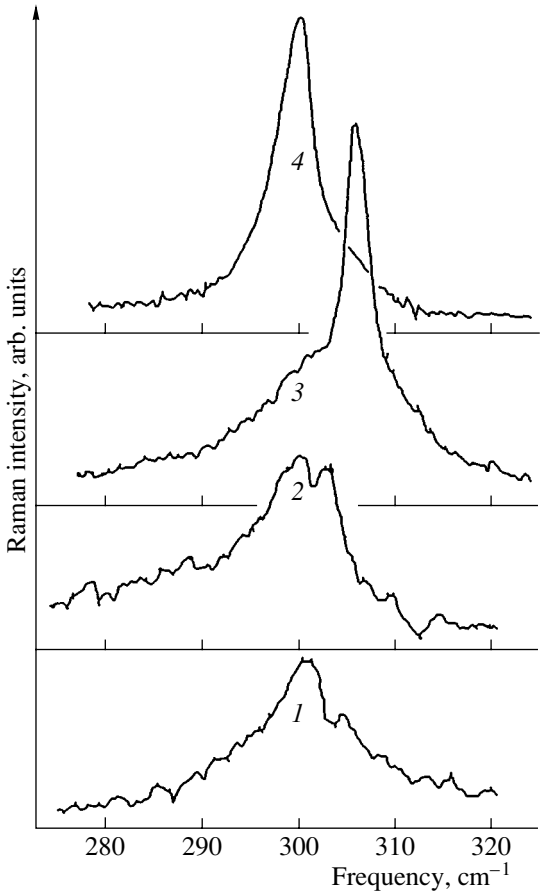

Fig. 2. Raman spectra of SiO_2 films that contained (*1*) 0.1, (*2*) 0.67, and (*3*, *4*) 3 at. % of Ge and were annealed at T_a = 1130°C under a pressure of (*1*–*3*) 12 kbar and (*4*) 1 bar. The excitation-radiation wavelength was 448 nm.

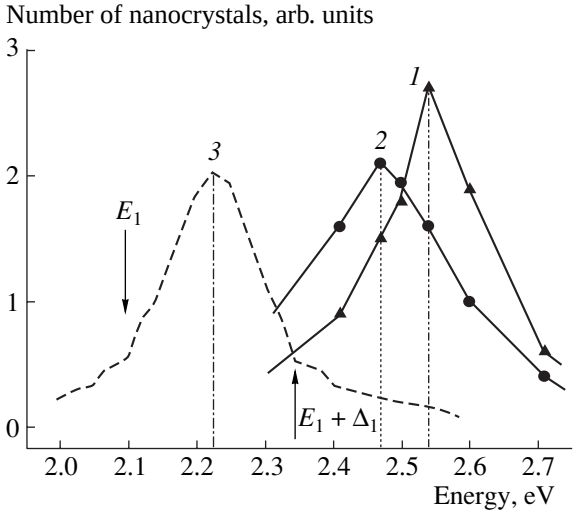

Fig. 3. Resonance dependences of Raman scattering by Ge–Ge optical phonons in nc-Ge formed as a result of annealing at P = (*1*) 1 bar and (*2*) 12 kbar; the films contained 3 at. % of Ge. Curve *3* corresponds to bulk Ge. Arrows indicate the exciton energies E_1 and $E_1 + \Delta_1$ in bulk Ge.

result, nc-Ge crystallites are compressed. These stresses are hydrostatic, since splitting of the phonon line into transverse and longitudinal modes is not observed. These stresses can be estimated from the frequency shift of the Ge–Ge mode in crystalline Ge; i.e., we used the formula

$$\gamma = (B/\omega_0)(d\omega_0/dP), \quad (1)$$

where γ is the Grüneisen constant, B is the bulk modulus of Ge (B = 750 kbar [13]), and $d\omega_0$ is the shift of the frequency $\omega_0 \approx 300$ cm^{-1} as the hydrostatic pressure varies by dP. The Grüneisen constant was found to be equal to 0.89 for Ge–Ge vibrations in bulk Ge [14]. Substituting the aforementioned numerical values into expression (1), we obtain the value of about 19.7 kbar for hydrostatic stresses of the Ge–Ge in nc-Ge. Data on the size of nc-Ge crystallites can be obtained from the resonance dependences of the Raman scattering by optical Ge–Ge phonons. Figure 3 shows these dependences for nc-Ge formed as a result of annealing (at P = 1 bar and 12 kbar) films containing 3 at. % of Ge and also for bulk Ge. Arrows indicate the energies E_1 and $E_1 + \Delta_1$ of an exciton in bulk Ge [15]. The shift of the energy (E_1, $E_1 + \Delta_1$) of the Raman resonance in nc-Ge to higher energies corresponds to quantization of the ground-state energy of a two-dimensional exciton at the critical point M_1 in germanium. It can be seen that the resonance width for nc-Ge formed at P = 12 kbar is larger than this width after annealing at P = 1 bar. This observation indicates that sizes of nc-Ge crystallites are distributed more nonuniformly in the former case. The smaller shift of transition E_1 to higher energies indicates that nc-Ge crystallites are, on the average, larger after annealing at P = 12 kbar. The effective masses of electrons and holes involved in the transition E_1 in Ge differ greatly for the directions which are perpendicular and parallel to the direction Λ. This means that exciton E_1 can be treated as a two-dimensionally confined quasiparticle. In order to calculate the sizes of nc-Ge crystallites, we used an expression derived in the effective-mass approximation for the energy of a two-dimensionally confined exciton E_1 [16]. For unstressed nc-Ge, the quantum-confinement energy was found to be equal to E_c = 0.3 eV, which, according to calculations, corresponded to an nc-Ge radius of about 3.5 ± 0.2 nm. When estimating the parameters of unstressed nc-Ge crystallites, we should take into account an increase in the exciton energy E_1 by the strain-induced shift of the levels $E_{stress} = \alpha P$, where $\alpha = 7.5 \times 10^{-3}$ eV/kbar [17] is the baric coefficient for (E_1, $E_1 + \Delta_1$) transitions, and P = 19.7 kbar. As a result, we obtain $E_{stress} \approx 0.15$ eV. Subtracting this energy from the value of the resonance shift, we find that E_c = 0.09 eV, which corresponds to an nc-Ge radius of about 5.7 ± 0.4 nm. In order to verify that our estimates of the nanocrystal parameters are realistic, we studied the properties of the structures SiO_2(:Ge) using the HRTEM. We observed no evidence

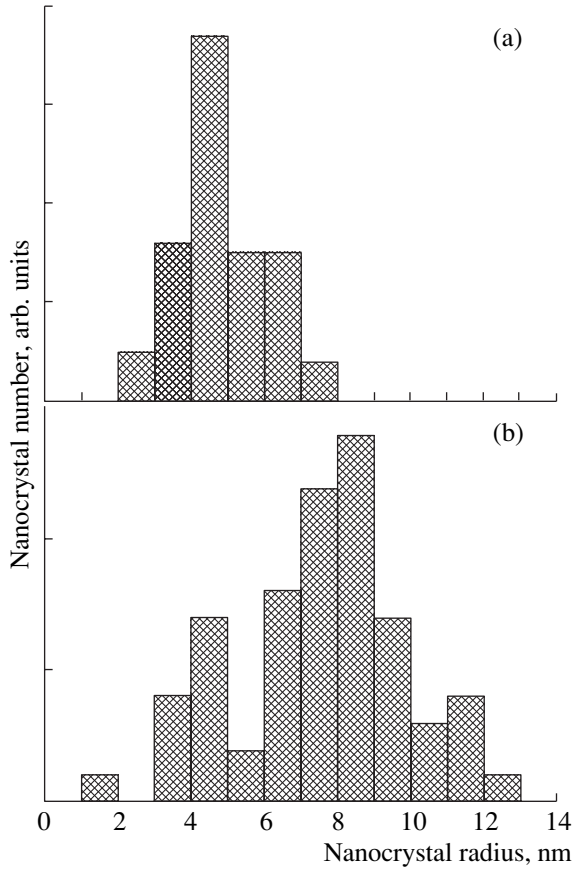

Fig. 4. Distributions of nanocrystal sizes obtained from statistical analysis of HRTEM data for SiO_2 films that contained 3 at. % of Ge and were annealed at T_a = 1130°C under pressure of (a) 1 bar and (b) 12 kbar.

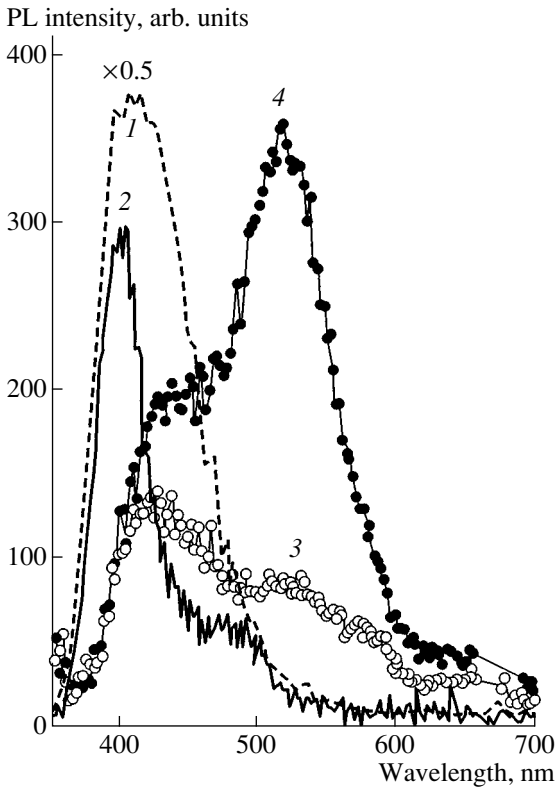

Fig. 5. Photoluminescence spectra of SiO_2 films that contained (*3*) 0.67 at. % and (*1*, *2*, *4*) 3 at. % of Ge and were annealed at T_a = (*1*) 600 and (*2*, *3*, *4*) 1130°C under a hydrostatic pressure of (*2*) 1 bar and (*1*, *3*, *4*) 12 kbar. The excitation-radiation wavelength was 337 nm.

for the formation of Ge nanoclusters or nanocrystals after annealing at T_a = 600°C. After the films containing 0.1 at. % of Ge were annealed at 1130°C, only noncrystalline nanoclusters were detected. The mean radius of these nanoclusters was about 2 nm. Germanium nanocrystals were formed only in the films that contained no less than 0.67 at. % of Ge. If the Ge atomic fraction was equal to 0.67 at. %, the mean radius of nanocrystals was about 6.2 nm. In Fig. 4, we show the size distributions for nanocrystals in the films which contained 3 at. % of Ge and were annealed at T_a = 1130°C at pressures P = 1 bar and 12 kbar. The mean radii of nanocrystals were found to be ~(4.5 ± 0.2) nm and ~(7.4 ± 0.4) nm, respectively. These radii differ by a mere 20–25% from the values obtained from the resonance dependences of Raman scattering. We believe that this agreement is quite satisfactory considering the measurement accuracy of our experiments. In the case of annealing at P = 1 bar, the size distribution of nc-Ge crystallites was much narrower than after annealing under hydrostatic pressure. The values of calculated interplanar spacings corresponded to these spacings in the diamond-like lattice of bulk Ge. It is noteworthy that nc-Ge crystallites were observed at a depth greater than 120 nm. Nanocrystals were not detected in the surface layer, which served as a sink for Ge in the course of annealing.

In Fig. 5, we show the PL spectra for the samples which contained 0.67 and 3 at. % of Ge and were annealed at T_a = 600 and 1130°C under pressures of 1 bar and 12 kbar. In the case of conventional annealing, a band peaked at 396 nm is dominant in the PL spectrum. A second (and less intense) peak is observed at about 460 nm. Rebohle *et al.* [18] attributed these peaks to recombination of electrons and holes at neutral oxygen vacancies in the ≡Ge–Si≡ and ≡Si–Si≡ centers, respectively. A broad high-intensity band in the violet–blue region of the spectrum is also formed as a result of annealing at T_a = 600°C and P = 12 kbar. The increase in T_a to 1130°C at P = 1130°C resulted in a shift of the PL spectrum to longer wavelengths. Notably, the concentration of implanted Ge was the determining factor in the formation of PL peaks. For the samples containing 0.1 at. % of Ge, we did not observe any PL in the visible region of the spectrum. A peak in the blue region of the spectrum (at about 427 nm) is dominant in the PL spectrum of the samples containing

0.67 at. % of Ge; at the same time, a shoulder with a lower intensity is formed in the green region of the spectrum (Fig. 5). A further increase in the Ge content to 3 at. % brings about an intensification of the PL peak in the green region of the spectrum (at about 520 nm) by approximately a factor of 4, whereas the intensity of the PL peak in the blue region of the spectrum increases insignificantly.

An analysis of the above data shows that hydrostatic compression, on the one hand, inhibits the drain of Ge to the surface and, on the other hand, is conducive to the formation of Ge nanocrystals with larger sizes and a wider distribution in sizes. It can be seen from comparison of spectra *3* and *4* in Fig. 2 that the amorphous Ge component is virtually absent in the Raman spectrum after conventional annealing; rather, only an intense peak corresponding to the crystalline Ge state is observed. This observation indicates that, in the case under consideration, the nc-Ge crystallites are formed owing to the agglomeration of germanium atoms into nanoclusters with their subsequent transformation into the crystalline state. The spectrum of the amorphous Ge phase is retained along with that of the stressed crystalline Ge phase after high-temperature annealing under hydrostatic pressure. This can be related, first of all, to a transition region between nc-Ge and the surrounding SiO_2 host. However, a decrease in the intensity of the peak at 300 cm^{-1} with increasing concentration of nanocrystals contradicts the above assumption. The second reason for the retention of the amorphous phase can be associated with the presence of noncrystalline Ge clusters. This means that the transition of Ge from the amorphous phase to the crystalline one is inhibited under hydrostatic pressure. A comparison of the data obtained by HRTEM, RBS, and Raman scattering indicates that nucleation of Ge crystalline phase is retarded if annealing is performed under hydrostatic pressure. This gives rise to a wide distribution in the size of nc-Ge crystallites. In addition, the difference between the elastic moduli of Ge and SiO_2 is conducive to rapid recovery (with lower activation energies) of the SiO_2 host matrix under conditions of compression. In this situation, excess Ge atoms can be pushed out of the host and rapidly segregate at nuclei of the crystalline Ge phase. Thus, growth of nc-Ge crystallites can proceed more rapidly in the course of annealing under hydrostatic pressure than in the course of conventional annealing. It is of interest that the properties of the Ge nanocrystals formed with stressed Ge–Ge bonds are described quite satisfactorily using the parameters of bulk Ge—the Grüneisen constant and the bulk modulus. It was found previously that Ge QDs formed by MBE in Si are described by smaller values of the aforementioned parameters than those characteristic of bulk Ge [13]. Differences between the values of γ and B obtained in this study and in [13] are most likely related to a difference between the elastic properties of host matrices which surround nc-Ge. For example, Si has larger values of the bulk modulus (970 kbar) than Ge (750 kbar). This means that the values of γ and B obtained by Quin *et al.* [13] are merely effective quantities characterizing an nc-Ge–Si system rather than parameters of nc-Ge. In our experiments, the SiO_2 host surrounding nc-Ge has a bulk modulus which is twice as small (370 kbar) as that in Ge. Thus, the host matrix does not exert a compressing effect on nc-Ge formed under hydrostatic pressure. Consequently, the constants γ and B obtained experimentally in this study are in fact characteristics of nc-Ge and do not differ from those of bulk material.

The PL band observed by us in the vicinity of 520 nm was detected previously in SiO_2 films with a high content of Ge (from 5 at. % [8] to 46 at. % [2]). As was mentioned in Section 1, the origin of this band is controversial. The band peaked at 520 nm is often related to radiative recombination of electrons and holes in nc-Ge with quantum-mechanical effects [2, 5, 6]. However, clear correlation between sizes of nanocrystals and the position of the PL peak under consideration has not been observed so far. This circumstance was the main reason for the search for alternative sources of the green-emission PL band. For example, recombination of electrons and holes in noncrystalline Ge nanoclusters with sizes no larger than about 2 nm has been considered [7]. The interface between the nc-Ge and SiO_2 host has also been mentioned as a plausible source of the PL band at $\lambda \approx 520$ nm [8]. However, this interface has also been thought of as a channel of nonradiative recombination for electrons and holes generated in nc-Si [2, 9]. In our experiments, we did not observe any PL from SiO_2 films that contained noncrystalline Ge nanoclusters with a size of $\leqslant 2$ nm. The appearance of a band peaked at about 520 nm correlated with the formation of stressed nc-Ge crystallites. Therefore, it is reasonable to assume that stressed nc-Ge crystallites represent the most likely source of the observed PL. However, we also failed to find any correlation between the sizes of the nc-Ge crystallites and the position of the green-emission PL band; this correlation can be expected when the Ge content increases from 0.67 to 3 at. %. The absence of this correlation can be caused by two factors. First, recombination of electrons and holes generated in extremely small nc-Ge crystallites can occur in the transition region between the nc-Ge and SiO_2 host [8] rather than within nc-Ge itself. Second, we should not completely rule out recombination of electrons and holes within an extremely small nc-Ge crystallite based only on the absence of a PL-peak shift as the sizes of nc-Ge crystallites increase. It should be taken into account that efficiency of radiative recombination is an inverse power-law function of nanocrystal size [19]. This means that the major contribution to the PL intensity is made by nanocrystals with small radii. The mechanism of the green-emission PL observed by us requires further investigation.

4. CONCLUSION

We studied the influence of hydrostatic compression on the implantation-induced synthesis of Ge nanocrystals (nc-Ge) in SiO_2. We ascertained that diffusion of Ge atoms in SiO_2 is retarded if high-temperature annealing is performed under hydrostatic pressure. It is shown that unstressed nc-Ge crystallites are formed as a result of conventional annealing. Annealing under pressure gives rise to hydrostatically stressed nc-Ge. The frequency shift of optical phonons was used to determine the stress in Ge nanocrystals. The shift of the resonance energy of Raman scattering (E_1, $E_1 + \Delta_1$) observed in nc-Ge corresponds to quantization of the ground-state energy for a two-dimensional exciton at the critical point M_1 of germanium. It is ascertained that the photoluminescence band peaked at 520 nm is observed only in the spectra of the films which contain stressed nc-Ge crystallites.

ACKNOWLEDGMENTS

We thank L. Rehbole for his help with the implantation of Ge ions, B.A. Kolesov for his help with studies of the Raman resonance spectra, and A.K. Gutakovskiĭ for his helpful participation in discussions concerning the HRTEM results.

REFERENCES

1. T. Takagahara and K. Takeda, Phys. Rev. B **46**, 15578 (1992).
2. Y. Maeda, Phys. Rev. B **51**, 1658 (1995).
3. Y.-W. Mo, D. E. Savage, B. S. Swartzentruber, and M. G. Lagally, Phys. Rev. Lett. **65**, 1020 (1990).
4. M. Grundman, O. Stier, and D. Bimberg, Phys. Rev. B **52**, 11969 (1995).
5. L. Yue and Y. He, J. Appl. Phys. **81**, 2910 (1997).
6. H. A. Atwater, K. V. Shcheglov, S. S. Wong, *et al.*, Mater. Res. Soc. Symp. Proc. **321**, 363 (1994).
7. S. Hayashi, J. Kanazawa, M. Takaoka, *et al.*, Z. Phys. D **26**, 144 (1993).
8. S. Y. Ma, Z. C. Ma, W. H. Zong, *et al.*, J. Appl. Phys. **84**, 559 (1998).
9. G. A. Kachurin, L. Rebol, I. E. Tyschenko, *et al.*, Fiz. Tekh. Poluprovodn. (St. Petersburg) **34**, 30 (2000) [Semiconductors **34**, 21 (2000)].
10. I. V. Antonova, A. Misiuk, V. P. Popov, *et al.*, Physica B (Amsterdam) **255**, 251 (1996).
11. I. E. Tyschenko, L. Rebohle, R. A. Yankov, *et al.*, Appl. Phys. Lett. **73**, 1418 (1998).
12. I. E. Tyschenko, K. S. Zhuravlev, E. N. Vandyshev, *et al.*, Opt. Mater. **17**, 99 (2001).
13. L. Quin, K. L. Teo, Z. X. Shen, *et al.*, Phys. Rev. B **64**, 075312 (2001).
14. F. Cerdeira, C. J. Buchenauer, F. H. Pollak, and M. Cardona, Phys. Rev. B **5**, 580 (1972).
15. M. A. Renucci, J. B. Renucci, R. Zeyher, and M. Cardona, Phys. Rev. B **10**, 4309 (1974).
16. K. L. Teo, S. N. Kwok, P. Y. Yu, and S. Guha, Phys. Rev. B **62**, 1584 (2000).
17. R. Zallen and W. Paul, Phys. Rev. **155**, 703 (1967).
18. L. Rebohle, J. von Borany, R. A. Yankov, *et al.*, Appl. Phys. Lett. **71**, 2809 (1997).
19. G. C. John and V. A. Singh, Phys. Rev. B **50**, 5329 (1994).

Translated by A. Spitsyn

Semiconductors, Vol. 37, No. 4, 2003, pp. 468–472. Translated from Fizika i Tekhnika Poluprovodnikov, Vol. 37, No. 4, 2003, pp. 485–489.

AMORPHOUS, VITREOUS, AND POROUS SEMICONDUCTORS

Laser Ultrasonic Study of Porous Silicon Layers

S. M. Zharkiĭ, A. A. Karabutov, I. M. Pelivanov, N. B. Podymova, and V. Yu. Timoshenko

International Laser Center, Faculty of Physics, Moscow State University, Vorob'evy gory, Moscow, 119899 Russia

Submitted June 25, 2002; accepted for publication July 22, 2002

Abstract—Propagation of ultrasonic signals induced by nanosecond laser pulses in porous silicon (*por*-Si) is considered from both the theoretical and the experimental viewpoints. The experimental samples are *por*-Si layers with 5- to 40-μm thickness and porosity of 50–75%; these layers were formed on a single-crystal silicon substrate by electrochemical etching. It is shown that the suggested ultrasonic laser method allows both the thickness and the porosity of a layer to be determined with the respective accuracies of no worse than 1 μm and 5%.

1. INTRODUCTION

First obtained as early as 1956 [1], porous silicon (*por*-Si) remains a subject of numerous studies due to its unique physicochemical properties (see reviews [2, 3]). Keen interest in this material is due to both the fundamental physical phenomena that take place in *por*-Si layers with sufficiently high porosity and the potential that it holds for electronics, optics, sensor science, and biomedical technologies (see, e. g., [4]).

To attain success in the practical and scientific use of *por*-Si layers, one has to know their basic microscopic characteristics (size and shape of pores and silicon residues) and the integral parameters (porosity, thickness). The latter can be measured by methods of laser optoacoustics (OA), which enable nondestructive rapid diagnostics of solids and fluids with high spatial resolution [5]. At the present time, detailed investigations of *por*-Si by OA methods are lacking. The aim of this study is to analyze the potentialities of laser optoacoustical methods for diagnostics of *por*-Si layers with various degrees of porosity.

2. EXPERIMENTAL

Samples of *por*-Si were obtained by conventional electrochemical etching [3] of single-crystal silicon substrates in the form of *p*-Si:B wafers with a resistivity of 1 Ω cm, (100) orientation of surface, and an initial thickness of 365 μm. The electrolyte was based on a mixture of hydrofluoric acid HF with ethanol. The volume fraction of HF varied in the range from 20 to 40%, which, at the used anodizing current density of 30 mA/cm^2, enabled modification of the porosity in the resulting layers [2].

Preliminary estimates of the layers' thickness h and porosity p were carried out during their fabrication. The thickness h was controlled by the rate and the time of etching and ranged from 10 to 40 μm. According to gravimetric measurements [2], the porosity of samples p varied from 50 to 80%.

Diagnostics of *por*-Si layers was carried out by means of OA spectroscopy with an ultrasonic wave laser source [6, 7]. The main idea of this method is the generation of broadband acoustic signals by pulsed laser radiation absorbed in the studied medium and the detection of these signals within a wide frequency range with a high time resolution. Laser-induced excitation offers an advantageous opportunity to generate short (~10 ns) intense probing acoustical pulses with a smooth envelope and broad frequency spectrum, whereas conventional ultrasonic sources are of little use for this purpose because of the low efficiency of piezoelectric excitation within a wide frequency range [6].

We realized the diagnostics of *por*-Si structural properties by employing the immersion measuring technique [8]. A pulse from an Nd^{3+} YAG laser (with a wavelength λ = 1.06 μm, a 1/*e*-level duration of about 10 ns, a pulse energy on the order of 10 mJ, and a repetition rate of 2 Hz) passed through a diffuser and was directed onto an ultrasonic optoacoustical generator *1* (ink in a quartz cell) (Fig. 1). The generator was coupled to a tank containing the studied sample *3* with *por*-Si layer *4* in between the immersion liquid layers *2*, *5*. Having passed through the sample, acoustic pulse entered a broadband piezoelectric detector *6*. The detected signal was transmitted to a Tektronix TDS-220 digital oscilloscope with a 100-MHz-wide analog band. Finally, the signals were processed using a personal computer.

Ethanol was chosen as the immersion liquid since it is well absorbed by *por*-Si and can be easily evaporated from it.

3. THEORETICAL BACKGROUND

3.1. Determination of a Porous Layer Thickness

Let us first consider the propagation of an OA signal in a silicon single crystal (*c*-Si). We assume an acoustic pulse with a plane wave front to be normally incident on an *c*-Si wafer of thickness *d*. When passing through the sample, the acoustic wave undergoes multiple reflections from its boundaries. Let *n* stand for the number of reflection events inside the sample; i. e. the sound wave makes *n* double travels across the wafer. Time delays between the first signal detected at the lower boundary and the first, second, …, and *n*th reflected signals are denoted by Δt_1, Δt_2, …, and Δt_n, respectively.

The velocity of sound in a single-crystal sample V_{Si} can be evidently expressed as

$$V_{\mathrm{Si}} = n\frac{2d}{\Delta t_1}. \quad (1)$$

We now assume that an acoustic pulse is incident on a silicon plate composed of two layers: a *por*-Si and an underlying *c*-Si substrate (Fig. 2). The total thickness of the wafer and the thickness of the *por*-Si layer are denoted by *d* and *h*, respectively. As a result of multiple reflections of the acoustic wave inside the sample, a pattern of multiple reverberations of the probing acoustic signal is observed at the output from the substrate [7].

The first signal to be detected at the exit from the substrate is the transmitted wave (shown by arrow *1* in Fig. 2). Since the *por*-Si layer is thinner than the *c*-Si layer, the second signal to come to the output is that reverberated in the upper layer (*2*). The third signal to come is that reflected within the sample substrate (*3*), the fourth signal is produced by reverberations in the wafer as a whole (*4*), and so on.

We designate the relevant delays between these signals by Δt_{12}, Δt_{13}, and Δt_{14}. Obviously, the porous layer thickness can be determined from one of the following formulas:

$$h = V_{por\text{-Si}}\frac{V_{\mathrm{Si}}\Delta t_{12}}{2V_{\mathrm{Si}} - V_{por\text{-Si}}}, \quad (2)$$

$$h = d - \frac{V_{\mathrm{Si}}\Delta t_{13}}{2}, \quad (3)$$

$$h = \frac{V_{por\text{-Si}}}{2}\frac{(V_{\mathrm{Si}}\Delta t_{14} - 2d)}{V_{\mathrm{Si}} - V_{por\text{-Si}}}, \quad (4)$$

where $V_{por\text{-Si}}$ is the velocity of sound in *por*-Si.

3.2. Determination of Porosity

Let us assume that the thickness of a *por*-Si layer is given. Then, it is possible to calculate the velocity of a longitudinal sound wave propagating in *por*-Si; as shown below, this is necessary for the calculation of the porosity of a layer.

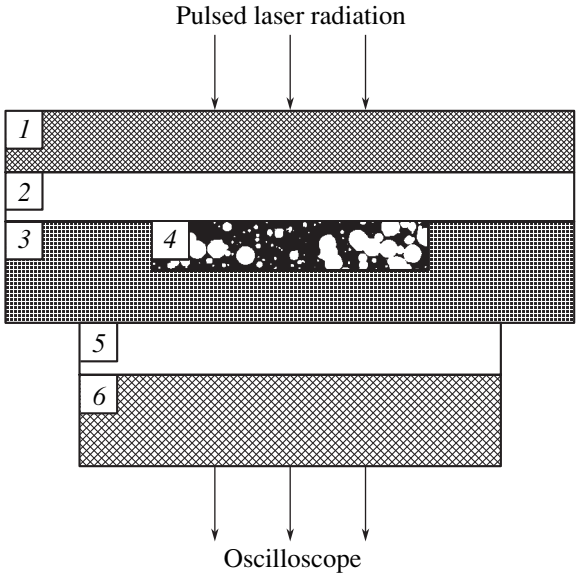

Fig. 1. Schematic representation of the immersion method with a laser ultrasonic source: (*1*) ultrasonic generator, (*2*) and (*5*) immersion liquid, (*3*) sample, (*4*) *por*-Si layer, and (*6*) piezoelectric detector.

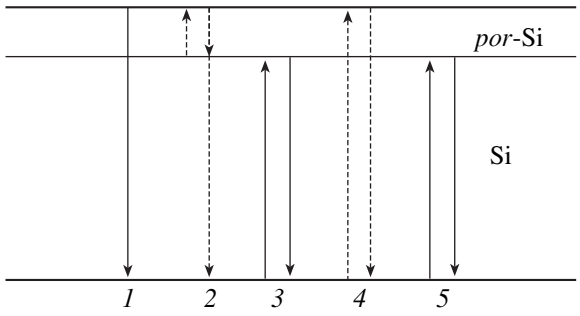

Fig. 2. Reverberation of probing ultrasonic pulse in a silicon sample with a porous layer (for details, see text).

Let an acoustic pulse be normally incident on the surface of the initial *c*-Si wafer at a time instant t_0 and detected at the other side of the wafer at the instant t_1. If the wave propagated through a silicon wafer of the same total thickness with a porous layer incorporated, this wave would be detected at the time instant t_2. The delay of the acoustic signal in a sample with a porous layer with respect to the reference signal (in a single-crystal layer) is equal to $\Delta t = t_2 - t_1$. This delay evidently stems from the different velocity of sound in *por*-Si and *c*-Si. Since the total sample thickness (the thickness of the *por*-Si layer plus that of the rest of the *c*-Si substrate) remains constant after the porous layer forma-

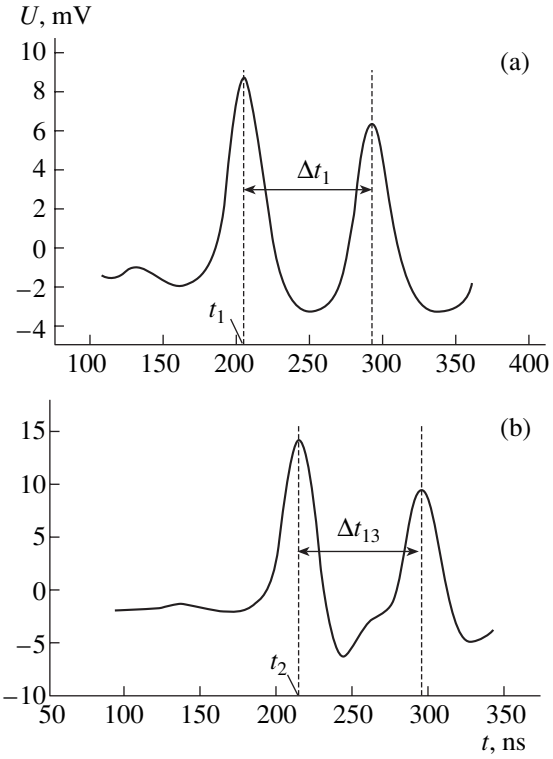

Fig. 3. Time shape of a probing acoustic pulse reverberated (a) in the single-crystal silicon sample and (b) in the sample with an incorporated *por*-Si layer ($h \approx 20$ μm, $p \approx 60\%$).

tion, the velocity of sound in it $V_{por\text{-}Si}$ can be determined from the expression

$$V_{por\text{-}Si} = \frac{hV_{Si}}{h + V_{Si}\Delta t}. \quad (5)$$

It is now necessary to relate the phase velocity of an ultrasound wave in *por*-Si to the value of its porosity. As mentioned above, ethanol was used as the immersion liquid. It was absorbed by the *por*-Si layer forming a combined silicon–ethanol medium. Since the size of pores and silicon residues in a *por*-Si layer is on the order of nanometers [2, 3], which is considerably smaller than the minimal wavelength $\lambda_{min} \approx 100$ μm of a probing OA pulse, calculations can be based on the two-phase mixture model [8].

Let us denote the volume content of silicon in a porous layer by η. Then, the volume content of ethanol is $1 - \eta$. The density of the porous layer (a combined medium) $\rho_{por\text{-}Si}$ is evidently related to the densities of silicon ρ_{Si} and ethanol ρ_{et} as

$$\rho_{por\text{-}Si} = \eta\rho_{Si} + (1 - \eta)\rho_{et}. \quad (6)$$

The velocity of a plane acoustic wave propagating in a porous layer can be expressed in terms of the increments of acoustic pressure and the density of material [9] as

$$\frac{\partial p}{\partial \rho_{por\text{-}Si}} \approx \frac{\Delta p}{\Delta \rho_{por\text{-}Si}} = V^2_{por\text{-}Si}. \quad (7)$$

An increment in the density of the combined porous layer is defined as [9, 10]

$$\frac{\Delta\rho_{por\text{-}Si}}{\rho_{por\text{-}Si}} = \eta\frac{\Delta\rho_{Si}}{\rho_{Si}} + (1 - \eta)\frac{\Delta\rho_{et}}{\rho_{et}}. \quad (8)$$

Therefore, the velocity of a sound wave in a porous layer can be written as

$$V^2_{por\text{-}Si} = \frac{1}{\rho_{por\text{-}Si}(\eta/\rho_{Si}V^2_{Si} + (1 - \eta)/\rho_{et}V^2_{et})}. \quad (9)$$

With a known value of $V_{por\text{-}Si}$, the volume content of silicon η in the porous layer can be derived from formula (9) in the form of quadratic-equation roots:

$$\eta_1 = \frac{-\beta + \sqrt{\beta^2 - 4\alpha\gamma}}{2\alpha}, \quad \eta_2 = \frac{-\beta - \sqrt{\beta^2 - 4\alpha\gamma}}{2\alpha}, \quad (10)$$

where

$$\alpha = \left(\frac{1}{V^2_{Si}} + \frac{1}{V^2_{et}} - \frac{\rho_{et}}{\rho_{Si}V^2_{Si}} - \frac{\rho_{Si}}{\rho_{Si}V^2_{et}}\right),$$

$$\beta = \left(\frac{\rho_{et}}{\rho_{Si}V^2_{Si}} + \frac{\rho_{Si}}{\rho_{Si}V^2_{et}} - \frac{2}{V^2_{et}}\right), \quad (11)$$

$$\gamma = \left(\frac{1}{V^2_{et}} - \frac{1}{V^2_{por\text{-}Si}}\right).$$

The values of ρ_{Si}, ρ_{et}, V_{Si}, and V_{et} are well known [11]: $\rho_{Si} = 2.33 \times 10^3$ kg/m^3, $\rho_{et} = 0.79 \times 10^3$ kg/m^3, $V_{Si} = 8.43 \times 10^3$ m/s, and $V_{et} = 1.17 \times 10^3$ m/s. This corresponds to $\alpha < 0$, $\beta > 0$. The velocity of sound in a combined porous layer $V_{por\text{-}Si}$ is evidently higher than that in ethanol V_{et} and becomes equal to it only at 100% porosity (the absence of a porous layer). Therefore, $\gamma \geq 0$. In these conditions, $\eta_1 \geq 0$ and $\eta_2 < 0$, which implies that only one root η_1 has physical meaning and $\eta = \eta_1$.

The porosity of the *por*-Si layer is related to the volume content of silicon by an obvious expression [3]

$$p = 1 - \eta, \quad (12)$$

where η is defined by (10).

Thus, measurement of the longitudinal velocity of sound in a combined porous layer is necessary and sufficient for the determination of *p*.

4. RESULTS AND DISCUSSION

Figure 3a shows the time shape of acoustic signals that passed through the initial *c*-Si plate (before the formation of a *por*-Si layer). The first peak corresponds to

Table

Sample no.	*por*-Si layer thickness h, μm	Etching-time estimate of h, μm	Ultrasound velocity in *por*-Si layer $V_{por\text{-}Si}$, 10^3 m/s	Porosity p, %	Gravimetrical estimate of p, %
1	8 ± 1	10	2.7 ± 0.2	56 ± 2	55
2	21 ± 1	20	2.0 ± 0.1	62 ± 3	60
3	24 ± 1	30	3.1 ± 0.4	54 ± 1	50
4	35 ± 1	40	1.51 ± 0.07	73 ± 3	75

the first transmitted signal; the second, to a double path (reverberation) of the signal in the sample. We calculate the longitudinal ultrasonic wave velocity in the single-crystal sample using formula (1), where Δt_1 stands for the time of delay between the first and the second signals. The resulting value $V_{Si} = 8.43 \times 10^3$ m/s is in good agreement with the known value of ultrasonic velocity in silicon [11].

Time shapes of the ultrasonic pulses that passed through the experimental samples with a porous layer are shown in Fig. 3b. The first detected signal corresponds to the first peak in the plots.

Figure 4 shows a typical spectrum of the first ultrasonic signal transmitted through a sample with a *por*-Si layer. It can be seen that the spectrum of the pulse generated by OAG drops to one-tenth of its peak value at $f_{max} \approx 35$ MHz. Accordingly, the shortest wavelength appearing in the pulse spectrum is $\lambda_{min} \approx 100$ μm. Since λ_{min} is more than twice the thickness of the porous layers ($\eta \approx 10$–40 μm), no resonance at $\lambda_{min}/2$ can be expected and, hence, no noticeable reverberation of the signal in *por*-Si is observed. The lack of reverberation of probing ultrasonic pulses in a porous layer indicates the proper choice of OAG. Indeed, in the case of double travel of the signal in *por*-Si, the reverberation pattern observed at the exit of the sample would be characterized by a period $g/V_{por\text{-}Si}$, which would complicate the interpretation of experimental data. Another condition to be met is that the duration of a probing pulse $\Delta\tau_{ref}$ must be shorter than the time of the double travel of the signal in the substrate $2(d-h)/V_{Si}$ in order to ensure the separation of reverberations in time. Thus, we have $\frac{2h}{V_{por\text{-}Si}} < \Delta\tau_{ref} < \frac{2(d-h)}{V_{Si}}$. Since the pulse duration $\Delta\tau_{ref} \approx 40$ ns (at the level of $1/e$) (Fig. 3), this condition is met for all of the samples studied.

Therefore, the second peak in Fig. 3b should be attributed to the reverberation of the signal in the single-crystal substrate, and the *por*-Si layer thickness can be calculated from formula (3). The accuracy of h determination is limited by the oscillograph rate of digital data acquisition $\delta t = 0.25$ ns. The calculated thicknesses of the layers are listed in the table. All values are accurate to within ±1 μm.

As was mentioned above, the velocity of an ultrasonic wave in a porous layer can be determined if one knows the difference Δt between the transit time of the signal in a sample with a porous layer and in a single-crystal sample of the same thickness. In our case, Δt was defined by the instants of time corresponding to the detection of signals transmitted through the porous samples (t_2 in Fig. 5) and through the uniform sample (t_1). The ultrasound velocity in the porous layers $V_{por\text{-}Si}$ was calculated from formula (5). Instability in the time

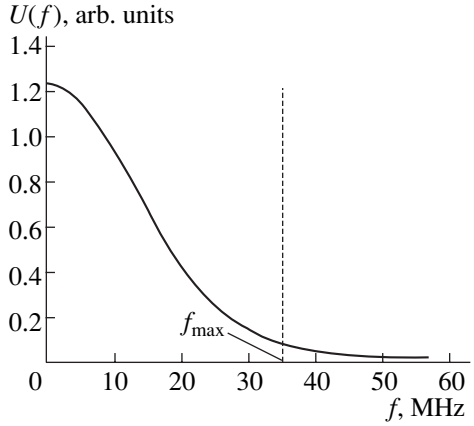

Fig. 4. Spectrum of ultrasonic signal transmitted through the sample with a *por*-Si layer.

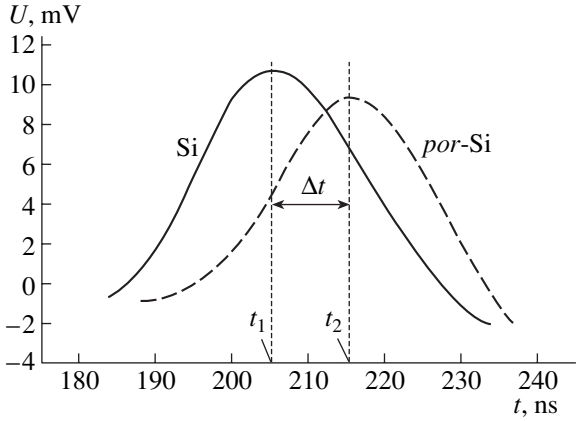

Fig. 5. Ultrasonic signals transmitted through the uniform *c*-Si layer (solid line) and the layer with a *por*-Si layer (dashed line).

of oscilloscope triggering accounts for the main experimental error and thus limits from below the thickness of a porous layer where the determination of porosity is possible: $h_{\min} = V_{por\text{-Si}}\sigma\tau \approx 2$ μm, where $\sigma\tau$ is the accuracy of time measurement ($\sigma\tau = 1$ ns) and $V_{por\text{-Si}}$ is the velocity of ultrasound in the porous layer. The results obtained are listed in the table.

It is important to note that the obtained velocities $V_{por\text{-Si}}$ are close to the velocity of ultrasound in ethanol ($V_{et} = 1.17 \times 10^3$ m/s). In view of the considerably high porosity of the samples (from 50 to 80%), the acoustic impedances of layers ($Z_{por\text{-Si}} = \rho_{por\text{-Si}} V_{por\text{-Si}}$) are close to those of ethanol. Therefore, most of the acoustic-pulse energy in a porous layer is reflected back from the *por*-Si/*c*-Si boundary and reverberations are no longer observed in the bulk of the crystal (Fig. 2, curve *4*). Subsequent reverberations take place only in the substrate.

The porosities of samples, calculated from formulas (10)–(12), are listed in the table, which also lists the relevant gravimetrical estimates. As can be seen from the table, all the values are determined with an accuracy no worse than 5%.

Another important point to be noted is that our method allows local determination of porosity, specifically, within the diameter of a laser beam spot on the sample surface. A thermooptically generated ultrasonic beam would have the same diameter with its size limited below only by the diffraction limit $a_0 = \sqrt{\frac{d\lambda_{\min}}{\pi}} \approx 100$ μm.

CONCLUSION

In this study, we developed an optoacoustical immersion method for the nondestructive diagnostics of *por*-Si layers. The method is based on the laser-induced generation of broadband acoustic pulses with their subsequent high-resolution detection after transmission through a studied sample. Both the porosity and the porous layer thickness were determined for a number of samples, the possibility of measuring the former locally was demonstrated. The porous layer thickness was estimated to better than 1 μm. The accuracy of the porosity calculation based on the two-phase mixture model appears to be no worse than 5%.

REFERENCES

1. A. Uhlir, Bell Syst. Tech. J. **35**, 333 (1956).
2. A. G. Cullis, L. T. Canham, and P. D. J. Calcott, J. Appl. Phys. **82**, 909 (1997).
3. O. Bisi, S. Ossicini, and L. Pavesi, Surf. Sci. Rep. **38**, 1 (2000).
4. *Proceedings of 2nd International Conference on Porous Semiconductors—Science and Technology*; Phys. Status Solidi A **182**, 7 (2000).
5. V. É. Gusev and A. A. Karabutov, *Laser Optical Acoustics* (Nauka, Moscow, 1991).
6. A. A. Karabutov, M. P. Matrosov, N. B. Podymova, and V. A. Pyzh, Akust. Zh. **37**, 311 (1991) [Sov. Phys. Acoust. **37**, 157 (1991)].
7. R. Truell, C. Elbaum, and B. B. Chick, *Ultrasonic Methods in Solid-State Physics* (Academic, New York, 1969; Mir, Moscow, 1972).
8. A. A. Karabutov, I. M. Kershteĭn, I. M. Pelivanov, and N. B. Podymova, Akust. Zh. **45**, 105 (1999) [Acoust. Phys. **45**, 94 (1999)].
9. L. F. Lependin, *Acoustics* (Vysshaya Shkola, Moscow, 1978).
10. V. V. Polyakov and A. V. Golovin, Pis'ma Zh. Tekh. Fiz. **20** (1), 54 (1994) [Tech. Phys. Lett. **20**, 452 (1994)].
11. *Physical Quantities. Handbook*, Ed. by I. S. Grigor'ev and E. Z. Meĭlikhov (Énergoatomizdat, Moscow, 1991).

Translated by A. Sidorova

Semiconductors, Vol. 37, No. 4, 2003, pp. 473–476. Translated from Fizika i Tekhnika Poluprovodnikov, Vol. 37, No. 4, 2003, pp. 490–493.

AMORPHOUS, VITREOUS, AND POROUS SEMICONDUCTORS

Raman Spectroscopy of Amorphous Carbon Modified with Iron

S. G. Yastrebov*^, V. I. Ivanov-Omskiĭ*, F. Dumitrache, and C. Morosanu*****

** Ioffe Physicotechnical Institute, Russian Academy of Sciences, St. Petersburg, 194021 Russia*
^e-mail: yastrebov@mail.ioffe.ru
*** National Institute for Lasers, Plasma, and Radiation Physics, Laser Department, P.O. Box MG-36, R-76900 Bucharest, Romania*
**** National Institute for Materials Physics, P.O. Box MG-7, R-76900 Magurele, Bucharest, Romania*
Submitted July 25, 2002; accepted for publication September 6, 2002

Abstract—Raman spectroscopy has been employed to study spectra of the vibrational frequencies of carbon in the range 1000–1800 cm^{-1} in amorphous carbon films modified with iron. The content of iron in a film has been set technologically by varying between the samples the area ratio of the graphite and iron parts of the target and monitored by Rutherford backscattering. Amorphous carbon layers containing 3, 26, 38, and 54 at. % iron have been obtained. The Raman spectra have the form of a broad band with features that are characteristic of amorphous carbon and lie at 1332 cm^{-1} (*D*-band) and 1552 cm^{-1} (*G*-band). At iron content of 38 and 54 at. %, the spectrum breaks up into a number of bands, which points to fragmentation of the matrix of amorphous carbon with increasing iron content. It is shown that the integral amplitude of scattering decreases nonlinearly with increasing iron content in a sample. The effect is analyzed in terms of a model that accounts for the linear dependence of the rate at which the number of atoms contributing to the scattering changes with the atomic fraction of carbon relative to the total number of carbon atoms in the film. *© 2003 MAIK "Nauka/Interperiodica".*

1. INTRODUCTION

Studies of the process of encapsulation of nanoclusters of ferromagnetic metals in thin films of amorphous carbon have gained momentum in recent years [1–5] in connection with the development of systems with an ultrahigh magnetic recording density. In this case, the unique ability of carbon atoms to form valence states with varied hybridization of atomic orbitals and, consequently, to create various configurations of atomic structures is employed. These properties impart to the structure of carbon a unique degree of adaptation and create prerequisites for the formation of various nanocomposites containing, in particular, metal nanoclusters. Here, encapsulation plays a double role: it protects nanoclusters from the corrosive action of the medium and weakens the exchange interaction between neighboring particles, which ensures ultrahigh density of magnetic recording. However, to optimize the process of synthesis and the magnetic properties of nanoclusters, it is important to know the nature of interaction between the nanoclusters and the carbon matrix. Raman spectroscopy of the vibrational modes of the carbon matrix is a valuable source of information of this kind.

2. SAMPLE PREPARATION

Experimental layers of amorphous carbon modified with iron, *a*-C:Fe, were grown using a magnetron whose cathode created a plasma ring 55 mm in diameter. As a target, we used a graphite disk 100 mm in diameter and covered with pieces of chemically pure iron (ARMCO). The content of iron in the films was varied by changing the ratio of the total area occupied by iron to the unoccupied area of the graphite target. We determined the elemental composition of the *a*-C:Fe films, i.e., the relative content of carbon and iron, by nuclear physical methods of elemental analysis: Rutherford backscattering and instantaneous nuclear reactions [5]. The table lists the compositions of films in relation to the surface area ratio of the iron (S_{Fe}) and graphite (S_C) targets. It can be seen that the films grown contain a minor amount of oxygen, which falls with decreasing relative surface area of the graphite target, and this suggests that graphite is the probable source of oxygen. The distance from the target to a substrate was 50 mm. Silicon wafers polished on both sides served as substrates. Before deposition, the reactor was evacuated to a pressure of 7×10^{-3} mTorr and then spectrally pure (99.999%) argon was fed into it through a needle

Table

Target area ratio S_{Fe}/S_C, %	Film thickness, μm	Elemental composition normalized to carbon content		
		C	Fe	O
0	0.5	1	0.03	0.11
3	0.96	1	0.35	0.18
10	1.16	1	0.62	0.05
30	1.78	1	1.2	0.06

1063-7826/03/3704-0473$24.00

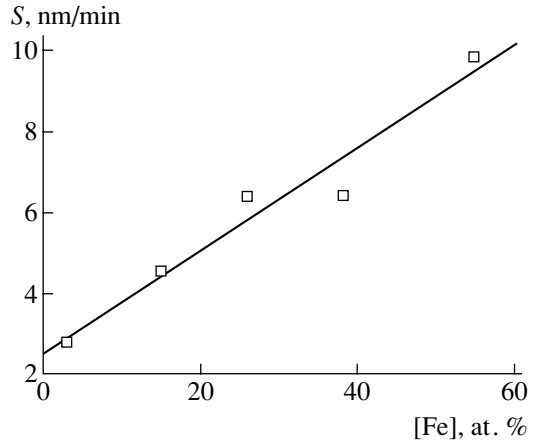

Fig. 1. Film growth rate *S* vs. iron content of a film. Straight line represents a linear approximation by means of the least-squares method.

leak valve. The rate of argon supply was measured with a rotameter and determined as 0.7 cm^3/s, and the argon pressure, with a Pirani vacuum gage, as about 40 mTorr. Prior to film deposition, the substrate was degassed at a temperature of 400°C for 20 min and then radiatively heated to 650°C. There was no additional heating in the deposition process, but the temperature of the substrate did not fall below 100°C due to its warming up in the course of film growth. The deposition was done at a constant power supply to the magnetron operating at a frequency of 1.78 MHz; the deposition time was varied between 2.5 and 3.5 h. The film thicknesses, which were measured with a Carl Zeiss interference microscope, are listed in the table. Under the conditions described, the growth rate *S* of a film depended on its composition and showed a substantial rise with increasing content of iron, according to Fig. 1. The straight line in the figure is a linear approximation by the least-squares method.

3. RESULTS AND DISCUSSION

We studied Raman spectra using an Ocean Optics R-2001 spectrometer with excitation by a laser with a wavelength of 785 nm and power of 500 mW. The light was led to and away from a sample with a fiber-optic waveguide. Figure 2 shows a Raman spectrum in the range of characteristic frequencies of vibrational modes in the carbon matrix of *a*-C:Fe. It can be seen that the spectrum has the form of a broad weakly structured band. The integral intensity of the band strongly depends on the content of iron introduced, which, by the way, would naturally be expected because of the decrease in the carbon fraction with increasing content of iron in the film. However, the manner in which the integral intensity depends on the content of iron is an important factor that furnishes information on the nature of interaction between iron and carbon. Attention should also be given to the change of the structural profile of the band with increasing iron content. These features are discussed below.

3.1. Structure of the Raman Band

Figure 3 shows, in linear coordinates, the Raman spectrum of a film with the lowest iron content (of those represented in Fig. 2). The spectral features are well seen in the figure. These features allow for the virtually ideal decomposition of the band into Gaussian components with frequencies of 1332 and 1548 cm^{-1}, which are characteristic of the *D*- and *G*-bands of amorphous carbon, respectively [6]. The decomposition yields a value of ~4.2 for the intensity ratio. According to the

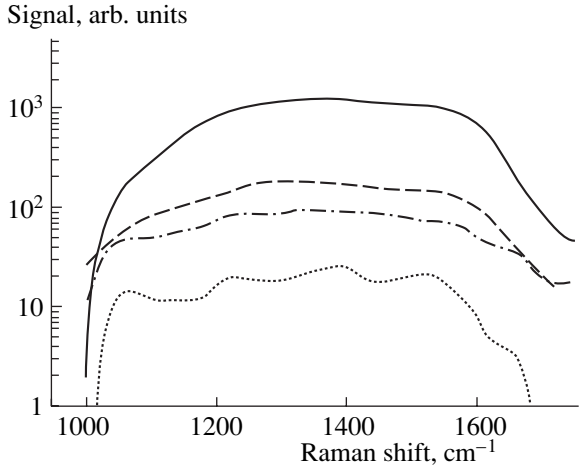

Fig. 2. Raman spectra at varied iron content in a film. Iron content [Fe]: solid line, 3; dashed line, 26; dot-dashed line, 38; dotted line, 54 at. %.

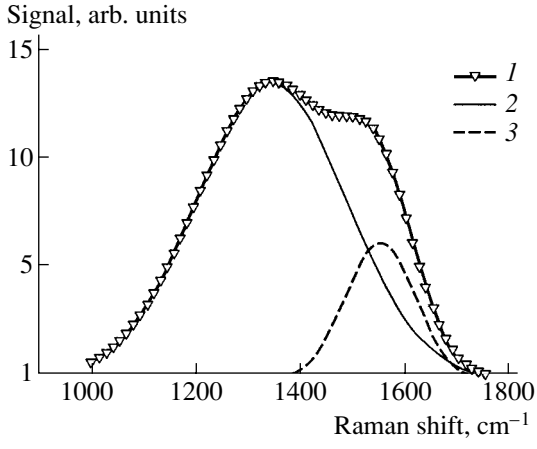

Fig. 3. Raman spectrum for a film with 3 at. % iron and its decomposition into Gaussian components: (*1*) experimental points and sum of the Gaussian components (solid line), (*2*) *D*-line, and (*3*) *G*-line.

known calibration [7], which enables evaluation of the linear dimensions of the sp^2 cluster, this value is 10 Å. Previously, we employed the approach [7] to evaluate the linear dimensions of sp^2 clusters in amorphous carbon modified with copper [8]. Analysis of the spectrum on the basis of decomposition into Gaussian components was only possible up to an Fe content of 25 at. % and yielded, at this Fe content, frequencies of 1344 and 1548 cm^{-1} for the *D*- and *G*-bands, respectively. With account taken of the FWHM of the Gaussian profile of the *D*-band, which is equal to ~200 cm^{-1}, the frequencies of the *G* and *D* bands can be considered virtually invariable at an iron content in the range of 0–25 at. %. The intensity ratio of the *D* and *G* bands also varies only slightly, by virtually no more than the evaluation error (it increases by ~15%). It may be assumed that, at these contents, iron introduced into the film does not exert any significant influence on the structure of chemical bonds of the carbon skeleton. Although the intensity of scattering falls dramatically with increasing iron content, as shown in Fig. 2, and smoothing should be done to improve the signal-to-noise ratio, it becomes clear how the scattering spectrum is changed on further raising the content of iron in the film, as shown in Fig. 4. It can be seen that the number of features grows with increasing iron content, which may be due to fragmentation of the amorphous carbon skeleton at high contents of iron.

3.2. Integrated Intensity of the Raman Band

Figure 5 shows the dependence of the integral intensity of the spectrum in Fig. 2 on the relative content of carbon x = [C]/[C+Fe]. The pronounced nonlinearity of this dependence suggests a certain interaction between iron and carbon atoms as opposed to a simple substitution, for which, naturally, a linear dependence would be expected. Let us consider a model that could account for the observed dependence. We assume that two types of carbon atoms exist: a carbon atom surrounded by other carbons, with which it can form chemical bonds (type I), and a carbon surrounded by iron atoms (type II). Only atoms of the first type contribute to the Raman signal at the given frequencies. Atoms of the second type either dissolve in iron, and make no contribution, or form chemical bonds with iron (iron carbides) and can contribute to scattering at a sufficient concentration, but in another frequency range. The variation of the number N of atoms of the first type with the total content x of carbon is proportional to the total number of carbon atoms in the film. For $N(x)$ at $x > 0$, we have the following differential equation:

$$\frac{dN(x)}{dx} = bN(x). \quad (1)$$

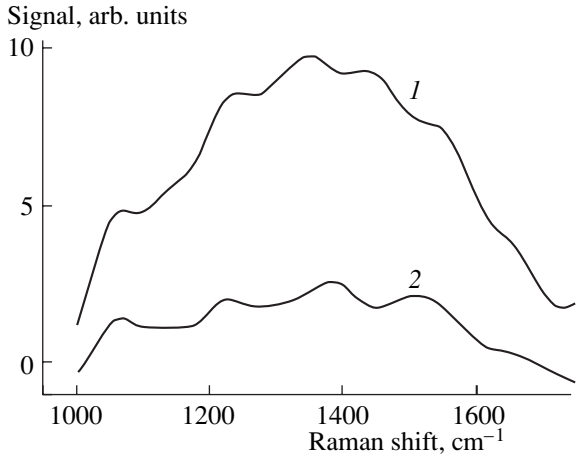

Fig. 4. Raman spectra of films of amorphous carbon modified with iron at an iron content of (*1*) 38 and (*2*) 54 at. %.

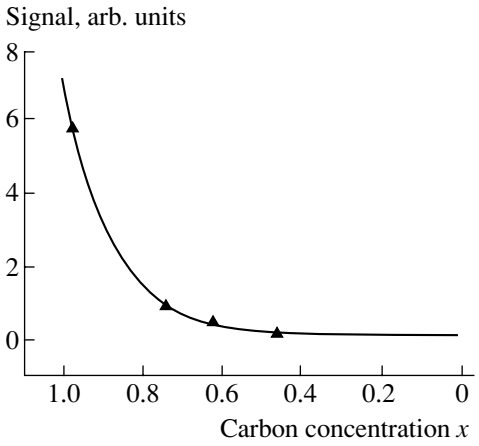

Fig. 5. Dependence of the integral signal of Raman scattering (points) on carbon content x and its approximation with Eq. (3) by means of the least-squares method (solid line).

Here, b is a proportionality factor that accounts for the interaction of carbon with iron. The solution to this differential equation can be represented as

$$N(x) = N_0 \exp(bx). \quad (2)$$

Above, we postulated a proportionality between the integral intensity of Raman scattering and the carbon content. With account of (2), this relation has the form

$$I(x) = BN(x). \quad (3)$$

Here, $I(x)$ is the integral intensity and B is the proportionality factor related to the scattering cross section of the carbon matrix. The results obtained in fitting the model to the experiment by means of the least-squares method are shown in Fig. 4; the following values of the parameters were obtained: $B = 290$, $b = 7.8$. However, the agreement between the model and the experiment leaves open the question of the state of carbon substituted by iron: whether carbon-dissolving iron clusters

or iron carbides are formed remains to be elucidated by further investigations.

4. CONCLUSION

The results obtained in studying the Raman spectra of amorphous carbon modified with iron allow the following conclusions.

At a low iron content (< 38 at. %), a band structure is discernible in Raman scattering curves, which enables an evaluation of the contribution to the overall scattering from the main bands characteristic of amorphous carbon (*D*- and *G*-bands). Such an evaluation was made and, in turn, made it possible to determine, using the known calibration, the average size of the graphite-like component of the skeleton of amorphous carbon, sp^2 clusters, as 1–2 nm. Analysis shows that, at low contents, iron does not significantly affect the average size of fragments.

With increasing iron content, the number of features distinguished in the spectra grows. This may be due to structural transformation of the carbon matrix, which leads to its fragmentation. It is shown that the integral amplitude of Raman scattering decreases exponentially as the iron content in a sample increases.

ACKNOWLEDGMENTS

This study was supported in part by the Russian Foundation for Basic Research, project no. 00-02-17004.

REFERENCES

1. T. Hayashi, S. Hirono, M. Tomita, and S. Umemura, Nature **381**, 772 (1996).
2. J. Jiao and S. Seraphin, J. Appl. Phys. **83**, 2442 (1998).
3. T. Cabioc'h, A. Naudon, M. Jaouen, *et al.*, Philos. Mag. B **79**, 501 (1999).
4. J.-J. Delaunay, T. Hayashi, M. Tomita, and S. Hirono, J. Appl. Phys. **82**, 2200 (1997).
5. T. K. Zvonareva, E. I. Ivanova, G. S. Frolova, *et al.*, Fiz. Tekh. Poluprovodn. (St. Petersburg) **36**, 734 (2002) [Semiconductors **36**, 695 (2002)].
6. C. Ferrari and J. Robertson, Phys. Rev. B **61**, 14095 (2000).
7. F. Tuinstra and J. L. Koenig, J. Chem. Phys. **53**, 1126 (1970).
8. V. I. Ivanov-Omskiĭ, T. K. Zvonareva, and G. S. Frolova, Fiz. Tekh. Poluprovodn. (St. Petersburg) **34**, 1450 (2000) [Semiconductors **34**, 1391 (2000)].

Translated by M. Tagirdzhanov

Semiconductors, Vol. 37, No. 4, 2003, pp. 477–481. Translated from Fizika i Tekhnika Poluprovodnikov, Vol. 37, No. 4, 2003, pp. 494–498.

AMORPHOUS, VITREOUS, AND POROUS SEMICONDUCTORS

Electrolytic Fabrication of Porous Silicon with the Use of Internal Current Source

D. N. Goryachev*, L. V. Belyakov, and O. M. Sreseli

Ioffe Physicotechnical Institute, Russian Academy of Sciences, St. Petersburg, 194021 Russia

** e-mail: dmitri.goryachev@mail.ioffe.ru*

Submitted October 9, 2002; accepted for publication October 11, 2002

Abstract—A new method of porous silicon fabrication is suggested which uses as a current source the potential difference arising between the silicon wafer and the platinum counter electrode immersed in an electrolyte solution. Addition of hydrogen peroxide to HF/ethanol electrolyte enables control over the current density in the process and fabrication of photoluminescent layers without an external current source. *© 2003 MAIK "Nauka/Interperiodica".*

1. INTRODUCTION

In recent years, porous silicon (*por*-Si) has found commercial applications in antireflection coatings of solar cells, sensor gas-analyzers, buffer layers in epitaxial technologies, etc. [1]. Therefore, the search for new simpler technologies for *por*-Si fabrication is a topical task.

The best-known and widespread process of *por*-Si fabrication is electrolysis [2]. A dense Si wafer is placed in an electrolytic bath with an aqueous solution of hydrofluoric acid HF, usually in mixture with ethyl or isopropyl alcohol. The counter electrode is a plate (grid, coil) of some metal that does not noninteract with hydrofluoric acid, most often platinum. An external bias (positive voltage at the Si wafer) between the wafer and the counter electrode is chosen so as to produce an appropriate current density, usually between 1–100 mA cm^{-2}, depending on the desired effect. In this process, silicon is dissolved (etched) with the formation of *por*-Si.

Another well-known process of *por*-Si formation is stain etching [1, 3]. This method is based on the spontaneous dissolution of an Si wafer submerged in the aforementioned solution, with certain oxidizing agents added, to give a *por*-Si film without an external bias.

Despite the apparent distinctions between these methods, they are based on the same physicochemical processes. In both cases, we are dealing with Si dissolution. In this process, initially neutral surface Si atoms pass into the solution in the form of positive ions

$$\mathrm{Si} + 2h^+ \longrightarrow \mathrm{Si}^{2+}$$

or, which is the same,

$$\mathrm{Si} - 2e^- \longrightarrow \mathrm{Si}^{2+}.$$

In this dissolution event, the electrical neutrality of Si is disturbed, a negative charge prohibiting further transport of Si ions to the solution appears on the wafer, and the dissolution ceases.

In the case of electrolysis with an external current source, the loss of positive charge from a crystal to the solution is compensated by the inflow of charge to the Si bulk from the contact on the rear side of the wafer. This ensures as long a silicon dissolution as is necessary. In the case of stain etching, the same result is achieved owing to the capture of electrons from a semiconductor by an oxidizing agent, which acts as the electron acceptor. However, this process can proceed only so long as open contact areas between the solution and solid Si are preserved. Further, with *por*-Si layer thickening, an alternative process becomes more probable, specifically, the extraction of electrons from the already formed *por*-Si layer, rather than from solid Si. In this case, *por*-Si dissolves, in the end, at the same rate as it is formed and further formation of *por*-Si ceases. Subsequent stages of Si dissolution (further oxidation of Si^{2+} ions to Si^{4+}, and binding of the formed Si ions by HF molecules into water-soluble H_2SiF_6 complexes and their diffusion into the solution bulk) totally coincide for both processes.

An alternative method of *por*-Si fabrication is possible in which the part of the current source is played by the potential difference which always appears between two dissimilar conductors immersed in an electrolyte solution, as occurs in a galvanic cell. This study is devoted to the implementation and analysis of this *por*-Si fabrication method using an internal current source without an external bias.

2. PRINCIPLES OF THE METHOD

If an Si sample, acting as an electrode, and some other metal—Pt, Ag, Cu—acting as a counterelectrode, are immersed in HF solution and the external electrical circuit is closed, an electric current starts to flow in the circuit and one of the electrodes dissolves. It is well

known that Si is a highly reactive element. Although its surface is always covered with passivating layers (oxide, hydroxides, hydrogen, etc.), nevertheless, in pair with a more electropositive material, the current arising in the short-circuit mode causes dissolution of silicon and *por*-Si formation must start at some definite current density.

The current density in the Si sample not only determines the rate of *por*-Si formation, but also exerts a strong influence on its structure and various physical properties. Therefore, the possibility of controlling the current density in the process is of crucial importance. In principle, the current density can be controlled by several methods. Evidently, the current in the circuit can be raised either by making the electromotive force greater (emf) or by reducing the circuit resistance. The potential of the Si electrode (and, correspondingly, the emf) can be raised by adding some oxidizing agent to the electrolyte. In this case, a "forced" extraction of electrons from the sample to ions (molecules) of the oxidizing agent occurs, with a corresponding increase of the Si potential with respect to the solution bulk. As concerns the short-circuit resistance, it includes nonlinear resistances of phase boundaries between Si and the electrolyte and between the electrolyte and the counter electrode, and also ohmic resistances of the sample and the electrolyte. In their turn, the resistances of phase boundaries are defined both by equilibrium interphase potential drops and by some additional overvoltages due to the limited rate of the electrode reactions. It is noteworthy that the necessary condition for current flow in an electrolyte cell is the occurrence of chemical reactions at both electrodes. An oxidation process of Si dissolution occurs at the anode, and the reduction of some components of the electrolyte, at the cathode (counter electrode). In the absence of oxidizing agents, only hydrogen ions can be reduced at the counter electrode, with the evolution of hydrogen gas. This process is highly power-consuming, so it can hinder the entire electrochemical process. At the same time, a variety of oxidizing agents are reduced much more easily than hydrogen ions. This is another argument in favor of adding various oxidizing agents to the electrolyte. It is worth noting that, in this case, the current increase in the short-circuit mode is due to the modification of the chemical reaction at the Si electrode, rather than that at the counter electrode.

3. EXPERIMENTAL

The source materials were (100) wafers of degenerate p^+-Si, 10 mΩ cm; *p*-Si:B, 12 Ω cm; and *n*-Si:P, 2 Ω cm. To fabricate an ohmic contact, a copper layer was chemically deposited onto the polished rear side of a wafer. Experiments were done with an Si sample with a working area of 0.45 cm^2 and a metallic (Pt, Cu, Ag) counter electrode placed into a Teflon electrolytic cell. The electrolyte was a 1 : 1 mixture of hydrofluoric acid (HF, 48%) with ethanol, with various oxidizing agents added. The light source was an incandescent lamp (W); the maximum sample illumination intensity was 0.1 W cm^{-2}. The rear side of the sample could be electrically connected with the counter electrode directly or via a milliammeter or an additional resistor reducing the current in the external circuit. In the experiment, the open-circuit voltage (emf) U_{oc} across the electrolytic cell, or the short-circuit current J_{sc} was measured. The photoluminescence (PL) spectra were recorded under excitation with a nitrogen laser in the pulse mode (wavelength 337.1 nm, pulse width 10 ns, repetition frequency 100 Hz) in a computerized setup including an MDR-2 monochromator and an FÉU-79 photomultiplier. The moment of measuring was delayed by about 3 μs with respect to the exciting pulse (a quasi-stationary mode).

4. RESULTS AND DISCUSSION

In the case of the initial electrolyte (without an oxidizing agent), the cell emf was $U_{oc} \approx 0.60$–0.68 V, varying slightly between p^+-, p^-, or *n*-Si. This result confirms the well-known assertion that the electrode potential of a semiconductor is virtually independent of the doping level [4]. The short-circuit current J_{sc} was 0.5–0.6 mA cm^{-2} for *p*- and *n*-type electrodes (in the latter case, under illumination) and up to 1.1 mA cm^{-2} for p^+-type. Such a low current density is insufficient for the formation of *por*-Si. As known, only etching of Si without *por*-Si formation proceeds at a low current density [5].

To raise the I_{sc}, we have studied the influence exerted on the electrolysis process by various oxidizing agents: nitric acid, potassium dichromate, iron(III) chloride, and hydrogen peroxide. It was established that all these oxidizing agents enhance the emf of the electrolytic cell nearly to the same degree. However, intensive formation of *por*-Si was observed only with hydrogen peroxide H_2O_2 and only with a Pt counter electrode. We attribute this to catalytic reactivity of Pt in the H_2O_2 reduction.

Figure 1 shows the emf of a cell with a p^+-Si electrode, U_{oc}, as a function of the H_2O_2 concentration expressed in moles per liter (M). As seen, the addition of an oxidant results in a significant rise of emf. In a wide range of oxidant concentrations *C*, a logarithmic growth of emf, typical for electrode potentials, is observed, in accordance with the Nernst equation

$$\varphi = \varphi_0 + kT/ne \ln C.$$

Here, φ and φ_0 are the actual and standard electrode potentials, respectively; *n* is the number of electrons involved in elementary chemical reactions at the electrodes.

Figure 2 shows the emf of a cell with nondegenerate Si as a function of the H_2O_2 concentration (curve *1* for *n*-Si, *3* for *p*-Si; both curves were recorded in the dark). As seen, U_{oc} also obeys the Nernst equation at a low

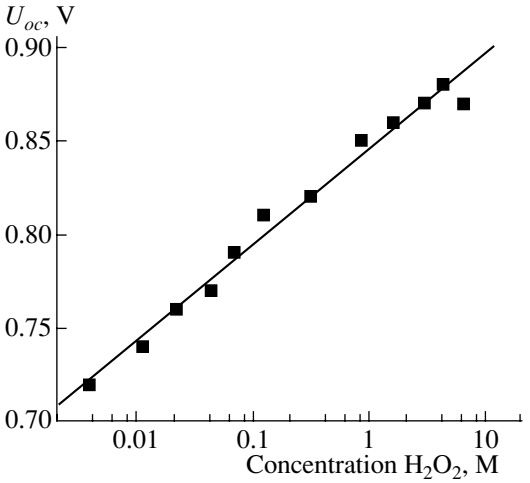

Fig. 1. The emf of the p^+-Si electrode U_{oc} vs. the H_2O_2 concentration C.

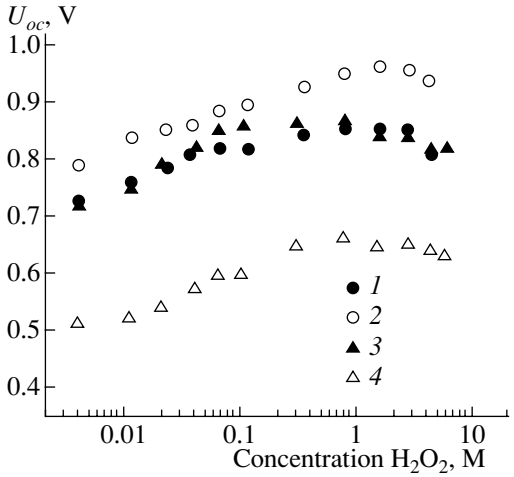

Fig. 2. The emf of silicon electrodes U_{oc} vs. the H_2O_2 concentration C: (*1*, *2*) *n*-type, (*3*, *4*) *p*-type; (*1*, *3*) in the dark, (*2*, *4*) under illumination.

concentration of H_2O_2. The rise of emf ceases as the concentration increases, and in several cases even its decrease is observed. We may assume that at high concentration of H_2O_2 the effective extraction of electrons from the semiconductor leads to self-dissolution of Si (i.e., to its stain etching, but without the formation of *por*-Si), and this impedes a further increase in emf. We believe that the absence of self-dissolution of p^+-Si in the studied range of H_2O_2 concentration is related to the fact that electrons are extracted from the Si conduction band.

In the case of nondegenerate Si, the illumination of a sample exerts a strong influence on the process. Curves *2* and *4* in Fig. 2 show emf as a function of the H_2O_2 concentration, recorded at an illumination intensity sufficient for photovoltage saturation. As seen, the curves largely reproduce the general run of curves *1* and *3*, but the emf for *p*-Si is about 80–140 mV lower, while for *n*-Si it is 60–100 mV higher. This behavior of nondegenerate Si seems quite natural, because blocking band bending always exists at the semiconductor–electrolyte interface and the photovoltage produced under illumination is added algebraically to the emf of the electrolytic cell. The photovoltage at the Si–electrolyte interface is noticeably smaller than that at the Si–air interface. This is due to the removal of oxides from the Si surface, with a corresponding modification of the nature of surface states in contact with the HF solution.

The dependence of the short-circuit current J_{sc} on the H_2O_2 concentration was measured by connecting a milliammeter to the electrodes for a short time (1–3 s). Figure 3 demonstrates that, simultaneously with the rise in emf, the increase in the concentration of H_2O_2 results in the current density in a p^+-sample increasing by a factor greater than 60 compared with the initial electrolyte. Linear dependences of $\ln J_{sc}$ vs. $\ln C$ were observed in all sample types. Since the current across barriers at phase boundaries depends exponentially on the potential drop

$$J_{sc} = J_0 \exp(-e\varphi/n_1 kT),$$

and the potential drop varies as a logarithm of concentration (see the Nernst equation above), the observed $J_{sc} \propto C^m$ dependence confirms our suggestion that the current is determined by the barriers at the electrodes, and its increase with increasing H_2O_2 concentration results from a lowering of the energy barriers at phase boundaries, rather than from a decrease in the ohmic resistance in the electrolyte.

On all three types of substrates, rather thick *por*-Si layers were successfully grown by electrolysis with an internal current source. For example, in one of the

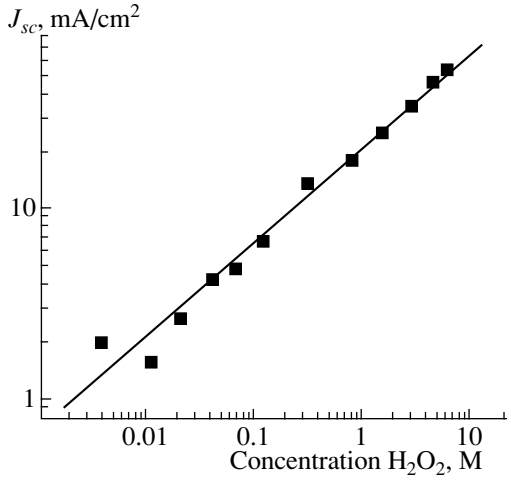

Fig. 3. Short-circuit current density J_{sc} vs. the H_2O_2 concentration C.

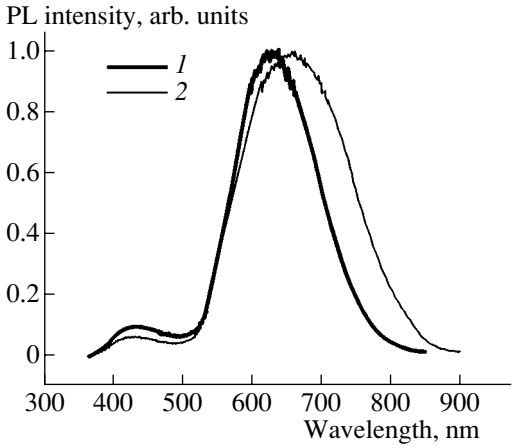

Fig. 4. Spectra of quasi-stationary photoluminescence of *por*-Si samples obtained with the same quantity of electricity passed through: (*1*) with internal, and (*2*) with external current source.

experiments with *p*-Si, the initial H_2O_2 concentration was 0.66 M and the process duration was 15 min. The layer thickness was about 5 μm.

The possibility of reducing the rate of *por*-Si formation by introducing additional resistance into the external circuit of the cell was confirmed. For example, in the case of p^+-Si at an H_2O_2 concentration of 6.15 M, the current density was reduced from 50.8 to 5 mA cm^{-2} by introducing additional resistance of about 650 Ω. An even *por*-Si layer about 30 μm thick was formed in 80 min. Similarly, the current density in *n*-Si was reduced from 13.5 to 5 mA cm^{-2} with an additional resistance of about 100 Ω. An even *por*-Si layer about 5 μm thick was formed in 15 min. In the case of *n*-Si, the rate of the process can also be reduced by reducing the illumination intensity of the sample.

Control experiments were performed to find out whether *por*-Si can be formed in the presence of H_2O_2 via stain etching, i.e., without closing the electric circuit. Si samples were immersed in electrolyte with an H_2O_2 concentration of 1.0 M and 6.16 M for 30 min. The formation of *por*-Si was not observed in these experiments.

The properties of *por*-Si samples fabricated by electrolysis without an external current source differ somewhat from the properties of samples produced by the standard method. At the same current density and time of etching, the former have a lower thickness (by 20–30%) but they exhibit much more intense (by a factor of ~2) photoluminescence.

The PL spectra of *por*-Si samples fabricated by electrolysis without an external current source also differ from the spectra of samples produced by the conventional method. Figure 4 shows typical PL spectra of two samples prepared by passing equal quantities of electricity through them: curves *1* and *2* refer to a sample fabricated with an internal current source and one formed with an external source in a standard electrolyte, respectively. As can be seen, the PL band in spectrum *1* is narrower (its FWHM is 140 nm against 190 nm in curve *2*) and the peak is shifted by 30 nm to shorter wavelengths. It is necessary to stress that the spectrum is narrowed on the long-wavelength side. In terms of the quantum-confinement model of *por*-Si formation, this indicates a decrease in the relative amount of larger crystallites.

We believe that the differences in the PL spectra stem from the presence in our electrolyte of an oxidizing agent, H_2O_2, which oxidizes and dissolves part of the *por*-Si crystallites being formed. This is indicated by the lower thickness of *por*-Si layers obtained in our electrolyte with the same quantity of electricity passing through. In this case, larger crystallites are primarily dissolved, which is in agreement with the assertions made in [6, 7]. The wider the band gap in a crystallite, the stronger the interatomic bonds within it, and the greater its chemical and corrosion resistance. Furthermore, the quantum-confinement broadening of the band gap of crystallites results in their electrical resistivity increasing as their size decreases. This causes the redistribution of short-circuit currents, preventing the dissolution of the smallest Si aggregates.

5. CONCLUSION

A new simplified electrochemical process has been developed for the fabrication of *por*-Si without an external current source, with only the electrode potential difference in an electrochemical cell employed. The specific features of *por*-Si formation by this procedure have been studied, and observed regular trends have been explained. The difference between the properties of *por*-Si produced by the new and standard methods have been revealed.

It is shown that introduction of hydrogen peroxide into a standard electrolyte does not lead to *por*-Si formation by the stain etching mechanism (without a current flow) but does allow for the production of a *por*-Si layer by electrolysis with an internal current source.

ACKNOWLEDGMENTS

This study was supported in part by the scientific programs “Physics of Solid-State Nanostructures” and “Low-Dimensional Quantum Structures” of the Presidium of the Russian Academy of Sciences, and by the Russian Foundation for Basic Research program, “Scientific Schools” (project no. 00-15-96750).

REFERENCES

1. G. Gullis, L. T. Canham, and P. D. J. Calcott, J. Appl. Phys. **82**, 909 (1997).

2. A. Uhlir, Bell Syst. Tech. J. **35**, 333 (1956); L. T. Canham, Appl. Phys. Lett. **57**, 1046 (1990); V. Lehmann and U. Goesele, Appl. Phys. Lett. **58**, 856 (1991).

3. R. M. Fathauer, T. George, A. Ksendzov, and R. P. Vasquez, Appl. Phys. Lett. **60**, 995 (1992); J. L. Coffer, in *Properties of Porous Silicon*, Ed. by L. T. Canham (INSPEC, London, 1997), Chap. 1.3.

4. V. A. Myamlin and Yu. V. Pleskov, *Electrochemistry of Semiconductors* (Nauka, Moscow, 1965; Plenum, New York, 1967).

5. D. Brumhead, L. T. Canham, D. M. Seekings, and P. J. Tufton, Electrochim. Acta **38**, 191 (1993).

6. D. N. Goryachev, L. V. Belyakov, and O. M. Sreseli, Fiz. Tekh. Poluprovodn. (St. Petersburg) **34**, 1130 (2000) [Semiconductors **34**, 1090 (2000)].

7. L. V. Belyakov, D. N. Goryachev, and O. M. Sreseli, Fiz. Tekh. Poluprovodn. (St. Petersburg) **34**, 1386 (2000) [Semiconductors **34**, 1334 (2000)].

Translated by D. Mashovets

Semiconductors, Vol. 37, No. 4, 2003, pp. 482–484. Translated from Fizika i Tekhnika Poluprovodnikov, Vol. 37, No. 4, 2003, pp. 499–501.

PHYSICS OF SEMICONDUCTOR DEVICES

3*C*-SiC *p–n* Structures Grown by Sublimation on 6*H*-SiC Substrates

A. A. Lebedev, A. M. Strel'chuk, D. V. Davydov, N. S. Savkina, A. S. Tregubova, A. N. Kuznetsov, V. A. Solov'ev, and N. K. Poletaev

Ioffe Physicotechnical Institute, Russian Academy of Sciences, St. Petersburg, 194021 Russia

Submitted September 3, 2002; accepted for publication September 6, 2002

Abstract—Sublimation epitaxy in a vacuum has been employed to grow *n*- and *p*-type 3*C*-SiC layers on 6*H*-SiC substrates. Diodes have been fabricated on the basis of the *p–n* structure obtained, and their parameters have been studied by measuring their current–voltage and capacitance–voltage characteristics and by applying the DLTS and electroluminescence methods. It is shown that the characteristics of the diodes studied are close to those of diodes based on bulk 3*C*-SiC. A conclusion is made that sublimation epitaxy can be used to fabricate 3*C*-SiC *p–n* structures on substrates of other silicon carbide polytypes. © *2003 MAIK "Nauka/Interperiodica".*

1. INTRODUCTION

Cubic silicon carbide is of particular interest from an application standpoint because of its highest, among SiC polytypes, carrier mobility, which is independent of the crystallographic direction. Furthermore, 3*C*-SiC inclusions are occasionally formed in epitaxial layers of hexagonal SiC polytypes having a wider energy gap. At the same time, fabrication of 3*C*-SiC-based devices is hindered by the lack of large-size substrates of this polytype. Therefore, obtaining 3*C*-SiC and studying its properties are topical research tasks.

In a previous communication of the same authors, growth of *n*-3*C*-SiC/*n*-6*H*-SiC heterostructures with a high quality of the 3*C*-SiC layer by sublimation epitaxy in a vacuum (SEV) was reported [1]. The aim of the present study was to obtain *p–n* 3*C*-SiC structures by means of SEV and to analyze their properties.

2. SAMPLES

It is known that varying the Si : C ratio in the growth zone strongly affects the heteropolytype epitaxy of silicon carbide. For example, the probability of 3*C*-SiC formation becomes higher with increasing Si concentration. Growth of 3*C*-SiC layers on 6*H*-SiC substrates is also possible in the case of sublimation epitaxy in an excess of silicon [2, 3].

The *p–n* structures studied were grown by sublimation epitaxy in a vacuum on 6*H*-SiC Lely substrates. First, an *n*-type epilayer was grown on the (0001)Si face of the substrate. An analysis of X-ray topographs demonstrated that the layer grown is mainly composed of a 3C modification of SiC. The area of the *n*-3*C*-SiC layer was about 25 mm^2; the *p–n* junction was formed by growing a p^+-3*C*-SiC layer doped with Al during the growth process. An analysis of X-ray topographs of a sample with a *p*-layer demonstrated that the 3*C*-SiC layer is formed over the entire epitaxy surface and has a finely twinned structure [4].

Ohmic contacts were fabricated by magnetron deposition of Al and Ti (contact to *n*-type layer) and Ni (contact to *n*-type layer), with subsequent vacuum annealing at 1100 and 900°C, respectively. Mesa structures with areas of 3×10^{-3}, 10^{-4}, and 8×10^{-5} cm^2 were fabricated by reactive plasma-ion etching through an Al mask.

3. EXPERIMENTAL RESULTS

To study the bulk and the boundaries of the epilayers, a sample was divided in two, so that the cross section passed through a row of diodes with the largest area. The cross sections of the diodes were studied by electron-beam-induced-current (EBIC) and secondary-electron (SE) methods on a JSM-50A scanning electron microscope. It is known that different secondary-electron yields are observed in regions with different types of conduction, which leads to the appearance of the so-called voltage contrast in the secondary-electron mode [5]. The magnitude of abrupt change in the SE signal, the midpoint of this change, and its half-width characterize, to a certain extent, the strength of the built-in electric field, the point of the highest field, and the width of the space charge region, respectively. Figure 1 shows the coordinate dependences of SE and EBIC signals, which were obtained in scanning the cross sections of the diodes studied. The SE curve is characterized by three regions with abrupt changes in the signal. The region with a maximum change in the SE signal corresponds to the *p–n* junction in 3*C*-SiC, which is also well seen in the EBIC mode. The remaining two regions correspond to isotype junctions, one formed by *n*-3*C*-SiC and *n*-6*H*-SiC, and the other, by *n*-6*H*-SiC

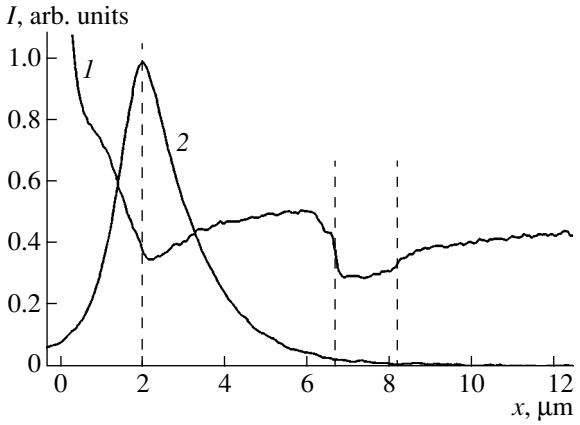

Fig. 1. (*1*) Secondary-electron and (*2*) EBIC signals from the *p–n* structures studied.

and n^+-6*H*-SiC substrate. Thus, a buffer *n*-6*H*-SiC layer ~1.5 mμ thick is formed on the 6*H*-SiC substrate in the initial stages of epitaxial growth. Then, polytype transformation occurs and an *n*-3*C*-SiC epilayer grows (~4.5 mμ thick). The considerable change in the SE signal at the interface of the 3*C*–6*H*-SiC isotype heterojunction points to a substantial potential drop across the boundary between the two semiconductors.

An estimate of the diffusion length of holes in the *n*-3*C*-SiC layer on the basis of the EBIC data yields a value of ~1.5 mμ. This indicates that holes injected from *p*-3*C*-SiC may diffuse across the *n*-3*C*-SiC layer as far as its interface with the 6*H*-SiC buffer layer.

The capacitance–voltage (*C–V*) characteristics of the structures were measured by the mercury probe technique, first on the surface of *n*- and *p*-type layers and then after the formation of diode mesa structures. The concentration $N_d - N_a$ was determined from the slope of the *C–V* characteristics to be $(1.7–2) \times 10^{17}$ cm^{-3} within the *n*-type layer and $N_a - N_d \approx 3 \times 10^{18}$ cm^{-3} on the surface of the *p*-type layer. The *C–V* characteristics of the diodes are linear in the C^{-2}–*V* coordinates, which means that the *p–n* junctions obtained are abrupt (Fig. 2). The capacitance cut-off voltage (V_c) is 2.05 ± 0.05 V, which is close to E_g for 3*C*-SiC (2.39 eV) and may be associated with a 3*C*-SiC-based homojunction.

A DLTS study revealed a center with a level at E_c – 0.63 eV, with parameters close to those of a structural defect in 3*C*-SiC epilayers grown by CVD [6, 7] and SEV [1] (Fig. 3). This observation substantiates the assumption that the base region of the structures studied is an *n*-type 3*C*-SiC layer.

A study of the current–voltage (*I–V*) characteristics of the diodes demonstrated that the voltage dependence of the current is exponential at small current densities: $J = J_0 \exp(qV/nkT)$, $n = 2.5–2.6$ (Fig. 4). The *I–V* characteristics of the diodes studied were close to those of *p–n* homostructures based on bulk 3*C*-SiC [8].

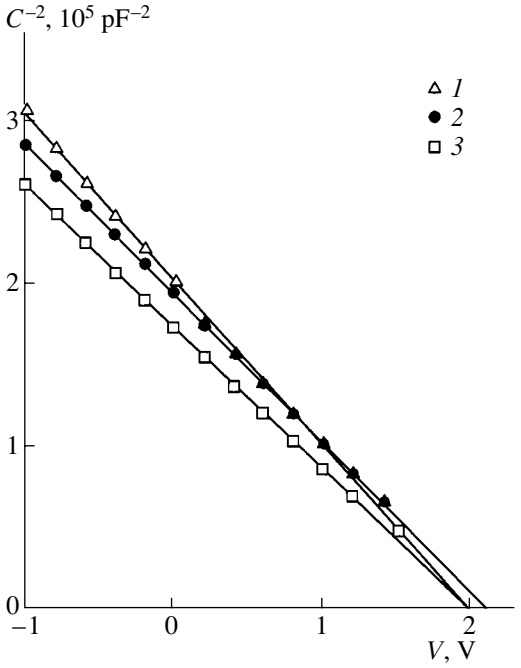

Fig. 2. Typical capacitance–voltage characteristics of the *p–n* structures studied, room temperature.

Electroluminescence (EL) spectra of the diodes are shown in Fig. 5. Bands peaked at $h\nu_{max} \approx 2.3$ eV ("green" band) and $h\nu_{max} \approx 2.9$ eV ("violet" band) can be distinguished in the EL spectra; the relative and absolute intensities of the bands grow with increasing forward current density *J* and temperature. The following spectral features should be noted: the positions of the EL bands peaked at $h\nu_{max} \approx 2.9$ eV and $h\nu_{max} \approx 2.3$ eV, which are close to the energy gaps of 6*H*-SiC and 3*C*-SiC; their narrow width at half maximum (in particular, compared with that of the so-called "green"

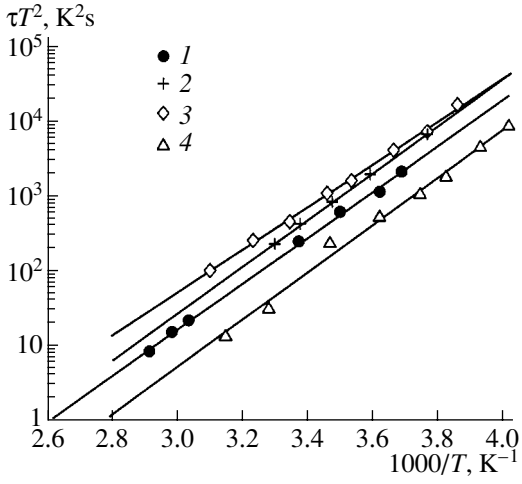

Fig. 3. Arrhenius plots for a center with an energy level E_c – 0.63 eV from (*1*) [1], (*2*) [6], (*3*) [7], and (*4*) present study.

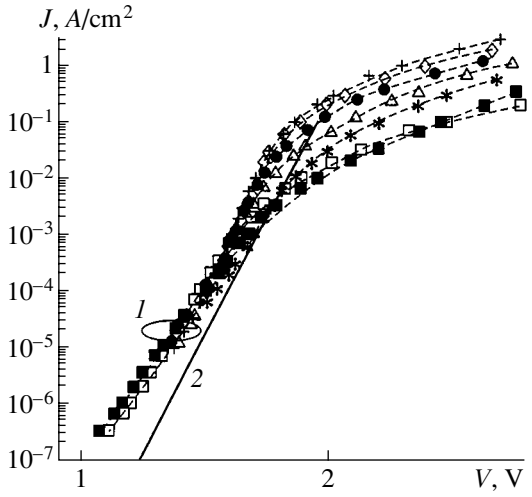

Fig. 4. Experimental (curves *1*, different symbols correspond to different diodes) and theoretical (curve *2*, for 3*C*-SiC *p–n* homojunction) forward current–voltage characteristics, room temperature.

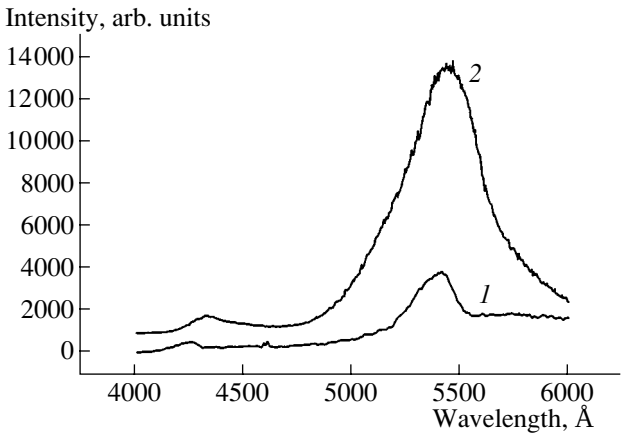

Fig. 5. EL spectra of the structures studied at a current I = 70 mA for temperatures T: (*1*) 300 and (*2*) 600 K.

band in SiC, which is due to defects); and the characteristic change in intensity on raising the current and upon heating. These observations make it possible to relate the two EL bands to annihilation of free excitons in 6*H*- and 3*C*-SiC.

Analysis of the data obtained shows that the characteristics of the structures in question correspond to those of 3*C*-SiC-based homojunctions. The emission band in the EL spectrum, which is related to recombination of free excitons in 6*H*-SiC, is due to diffusion of holes from p^+-3*C*-SiC across the 3*C*-SiC layer to the interface with the buffer 6*H*-SiC layer. The given emission appears within the base region, rather than at the metallurgical boundary of the *p–n* junction, which is well discernible under an optical microscope on the edge cross section of the sample.

4. CONCLUSION

The investigation performed has shown that good-quality 3*C*-SiC *p–n* structures can be fabricated by sublimation epitaxy in a vacuum on 6*H*-SiC substrates.

ACKNOWLEDGMENTS

This study was supported by the Russian Foundation for Basic Research (project nos. 00-02-16688 and 01-02-17657) and YEF (grant no. 2001/2-186).

REFERENCES

1. D. V. Davydov, A. A. Lebedev, A. S. Tregubova, *et al.*, Mater. Sci. Forum **338–342**, 221 (2000).
2. Yu. A. Vodakov, G. A. Lomakina, E. N. Mokhov, and V. G. Oding, Fiz. Tverd. Tela (Leningrad) **19**, 2812 (1977) [Sov. Phys. Solid State **19**, 1647 (1977)].
3. A. N. Andreev, A. S. Tregubova, M. P. Scheglov, *et al.*, Mater. Sci. Eng. B **46**, 141 (1997).
4. A. A. Lebedev, G. N. Mosina, I. P. Nikitina, *et al.*, Pis'ma Zh. Tekh. Fiz. **27** (24), 57 (2001) [Tech. Phys. Lett. **27**, 1052 (2001)].
5. J. I. Goldstein *et al.*, *Scanning Electron Microscopy and X-ray Microanalysis* (Plenum, New York, 1981; Mir, Moscow, 1984).
6. P. Zhou, M. G. Spenser, G. L. Harris, and K. Fekade, Appl. Phys. Lett. **50**, 1385 (1987).
7. K. Zekentes, M. Kayambaki, and G. Constantinidis, Appl. Phys. Lett. **66**, 3015 (1995).
8. A. M. Strel'chuk, V. S. Kiselev, and S. E. Avramenko, Mater. Sci. Eng. B **61–62**, 437 (1999).

Translated by M. Tagirdzhanov

Semiconductors, Vol. 37, No. 4, 2003, pp. 485–490. Translated from Fizika i Tekhnika Poluprovodnikov, Vol. 37, No. 4, 2003, pp. 502–507.

PHYSICS OF SEMICONDUCTOR DEVICES

Current and Temperature Tuning of Quantum-Well Lasers Operating in 2.0- to 2.4-μm Range

A. P. Astakhova*, A. N. Baranov, A. Viset**, A. N. Imenkov*, N. M. Kolchanova*, N. D. Stoyanov*, A. Chernyaev*, D. A. Yarekha**, and Yu. P. Yakovlev***

** Ioffe Physicotechnical Institute, Russian Academy of Sciences, Politekhnicheskaya ul. 26, St. Petersburg, 194021 Russia*

e-mail: Imenkov@iropt1.ioffe.ru

*** Université Monpellier II, France*

Submitted September 11, 2002; accepted for publication September 22, 2002

Abstract—Radiation spectra of GaInAsSb/GaAlAsSb-based quantum-well diode lasers in pulsed and quasi-continuous operation modes were studied in the temperatures range from –10 to +20°C with driving currents varying from 50 to 200 mA. For currents exceeding the threshold value by no more than 30%, a single-mode lasing was usually observed. A further increase in current leads, as a rule, to the appearance of 3–5 additional long-wavelength cavity modes, which suggests the growth of gain in this spectral range due to the interaction of modes. In single-mode conditions, the lasing wavelength is red-shifted with temperature at a rate of 2–3 Å/K because of the current-induced heating of the laser and the corresponding increase in the refractive index. The rate of this heating is estimated at 0.1 μs. *© 2003 MAIK "Nauka/Interperiodica".*

INTRODUCTION

Injection tunable GaInAsSb-based diode lasers operating in the range from 2.0 to 2.4 μm at room temperature hold much promise as sources of radiation for high-resolution spectroscopy. The overtones and Raman transitions of some gases fall between 2.0 and 2.4 μm. This is a range of strong absorption for many gases, a fact which has enabled the advent of portable gas analyzers capable of operating at comparatively high temperatures. According to [1], lasers on self-consistent quantum wells located at the GaSb/GaInAsSb interface are characterized not only by single-mode lasing and high efficiency, but also by a narrow emission line, which is narrower than a typical absorption line in molecular gases by one or two orders of magnitude. The operation temperature range of such lasers extends from 77 to 300 K [1–3]. By varying the temperature, the laser can be tuned to a prescribed range that includes the absorption lines of the gases to be studied. However, such lasers can operate when driven only by short pulses of current, and a change in the wavelength appears to be nonlinear, as follows from the nonlinear growth of temperature in the active region. To obtain undistorted recording of gas spectra requires that the temperature attain a steady-state value in a time period that is shorter than the current pulse duration and that the current increase during the pulse. In this case, a change in the lasing wavelength is a linear function of time through the pulse. Optimized quantum-well GaSb-based lasers have a low threshold current and may provide continuous (CW) lasing at room temperature and above [4]. This circumstance enables long pulses of current or even direct current to be used for the undistorted recording of spectra with a transient time of 0.1–1 μs. The total time of recording should be on the order of 1 ms, since the detection of several absorption lines is required to provide for their reliable recognition and identification.

In this study, we consider the performance of GaInAsSb-based quantum-well laser structures with three quantum wells in the active region in a wide range of currents and temperatures with the aim of elucidating the mechanisms behind tuning, estimating a possible operation rate, and clarifying the role of nonlinear optical effects in attaining single-mode lasing.

EXPERIMENTAL

We studied quantum-well structures based on GaInAsSb/GaAlAsSb heterojunctions with an active region ($Ga_{0.85}Al_{0.35}Sb_{0.97}As_{0.03}$) containing three 10-nm-thick GaInAsSb quantum wells spaced at 30 nm (Fig. 1). The wave functions of the carriers in the neighboring wells overlap only slightly, which results in the reduction of the width of the amplification spectrum. Layers composed of $Ga_{0.1}Al_{0.9}Sb_{0.93}As_{0.07}$ material with a thickness of up to 1.5 μm confine the 0.8-μm-thick active region. Two-groove mesachips with a stripe width of 18 μm and a step of 500 μm were formed by standard photolithography. The stripe width and the groove etching depth were chosen to provide the generation of only the fundamental spatial mode, thus improving the uniformity of amplification in the active region and favoring single-mode lasing (on a single longitudinal mode). Diode lasers with Fabry–Perot cavities 200–400 μm in

1063-7826/03/3704-0485$24.00 © 2003 MAIK "Nauka/Interperiodica"

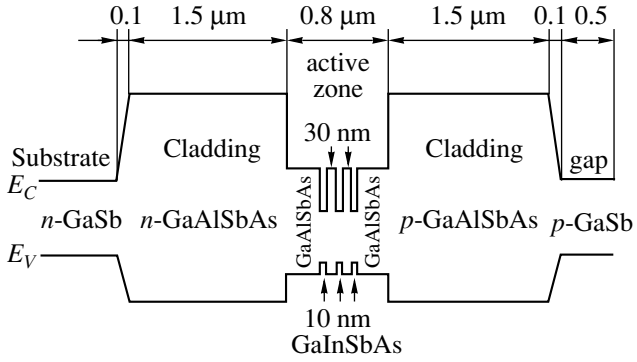

Fig. 1. Energy-band diagram of a frequency-modulated laser.

length were obtained by cleaving. Laser chip mounting on a special copper holder was done in two ways: (i) via an epitaxial layer (epilayer) adjacent to the surface, where a low thermal resistance of about 50 K/W should be ensured (for AV38-1K, AV43-1T chips), and (ii) with the chip substrate adjacent to the holder (for Bsp-T2-type chips). For measurements of the spectra of laser radiation, the copper holder with a chip were placed into a special HHL-type housing with a Peltier refrigerator installed, which enables variation in the chip temperature in the range from –20 to +40°C.

Radiation spectra of the diode lasers were measured at a fixed temperature and at currents varying from 50 to 200 mA. Lasers were driven by pulses of current with a duration of 1- to 1000-μs at a repetition rate of 512 Hz. In the latter case (the longest pulses), the off-duty ratio equaled 2; i. e., the quasi-CW mode of lasing was ensured. When recording the temperature dependences of spectra, the temperature was measured with an accuracy of 0.3°C.

RESULTS

When the current is only slightly higher than the threshold value and the lasing is single-frequency (Fig. 2), the wavelengths of lasers fabricated on different plates with quantum wells of various compositions fall in the range from 2.0 to 2.4 μm at room temperature. Due to the closeness of current to the threshold value, both generating and weak nongenerating modes are seen in the emission spectra, which are shown in Fig. 2. The radiation spectra of an AB38-1K laser pumped by pulses of current with different durations and magnitudes are plotted in Fig. 3. As long as the driving current exceeds the threshold value by no more than 30–50%, a single longitudinal mode is usually generated in both the pulsed and the quasi-CW operation modes. For example, it can be seen from the spectra of the same laser with a threshold value of 70 mA that quasi-CW single-mode lasing is observed up to a current of 90 mA. The intensity of this mode grows with current. A further increase in current leads to a decrease in this intensity and gives rise to adjacent long-wavelength modes, thus resulting in multimode lasing. The most intense mode appears to be that with the longest wavelength or the neighboring one spaced by 3–5 intermode intervals from the mode that is generated at small currents. For a small excess of current over the threshold (in quasi-CW regime), the lasing wavelength usually grows with current at a rate of 0.7 Å/mA and the total change may amount to 12–16 Å (Fig. 5). In quasi-CW conditions, the influence of the thermal resistance of the refrigerator is noticeable. For pulse durations of 1–100 μs and an off-duty ratio $Q >$

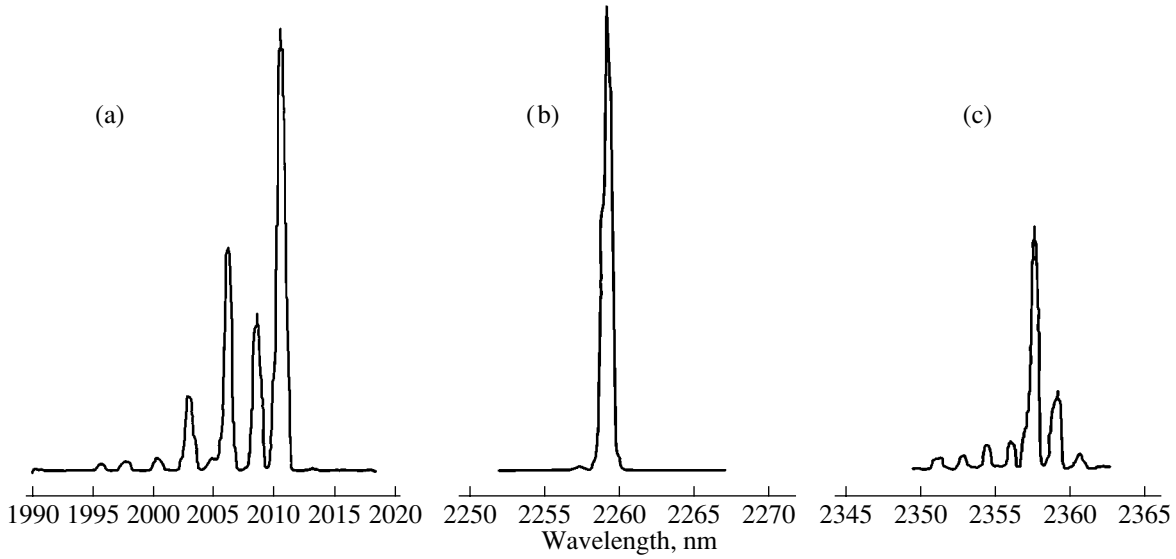

Fig. 2. Emission spectra measured at room temperature for different lasers and different pulse currents (a) AB43-1T, I = 80 mA, τ = 50 μs; (b) AB38-1K, I = 80 mA, τ = 10 μs; and (c) Bsp-T2, I = 155 mA, τ = 0.6 μs.

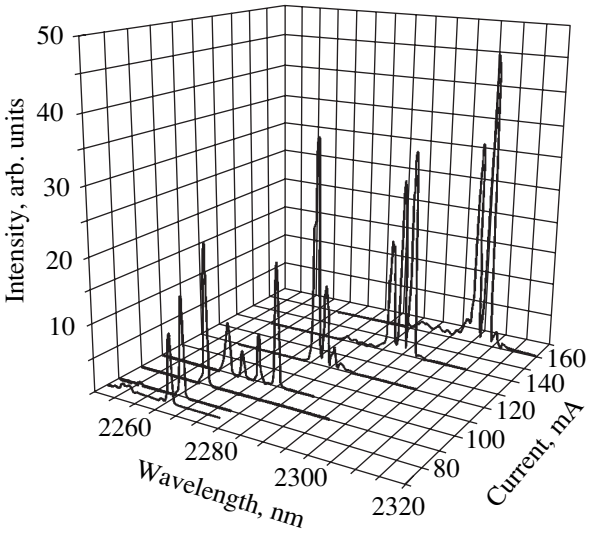

Fig. 3. Emission spectra of frequency-modulated AB38-1K laser at different currents in CW operation conditions; F = 512 Hz and T = 294 K.

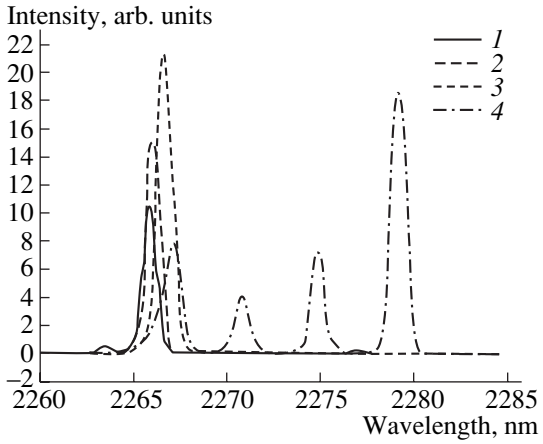

Fig. 4. Emission spectrum of AB38-1K laser in CW operation conditions as a function of current at a small excess over the threshold: I = (*1*) 75, (*2*) 80, (*3*) 90, and (*4*) 100 mA; F = 512 Hz, T = 294 K.

20, the change in the single-mode lasing wavelength is 2 to 10 times smaller than that observed in quasi-CW operation conditions (Fig. 6a). After the transition to multimode functioning occurs, the wavelengths of all the modes either remain nearly constant or decrease with current, as can be seen from Fig. 6a.

As soon as a twofold excess of current over the threshold is attained, the number of generated modes decreases and the lasing again comes close to single-mode operation. An increase in the wavelength with current is observed. Note that, during multimode operation, the intensity of dominant modes does not grow with current as it does during single-mode operation (Fig. 6b, curve *2*). Multimode operation is characterized by a summarized differential efficiency lower than that of single-mode operation (see Fig. 6b, curve *1*).

With an increase in temperature (Fig. 7) at a constant current, some cavity modes become red-shifted by 2–3 Å/K and additional long-wavelength modes appear, which causes an increase in the average lasing wavelength by 12 Å/K. The interval of a single-mode laser amounts to 4–12 Å.

DISCUSSION

Laser structures based on quantum-well material of the above composition provides for emission in the range from 2 to 2.4 μm. The structures under study had three potential quantum wells. At a given distance between wells, wave functions of electrons and holes in different wells practically do not overlap and no splitting of the quantum levels occurs. As a result, each quantum well operates individually, and the production of a large number of longitudinal waves (from 5 to 10) is not related to the amplification-spectrum inhomogeneity caused by quantum level splitting. At low currents, the radiation spectrum consists, as a rule, of a single mode that coincides with the peak of the undistorted gain spectrum, which accounts for the amplification from all three wells. An increase in the lasing wavelength can be attributed to the heating of the laser and the associated growth of the refractive index. Maximal change in the wavelength is observed when the period-to-pulse duration ratio equals 2. This fact can be easily understood from the following considerations.

As the pump current increases, new modes appear on the long-wavelength side of the spectrum, at first by one and then by several modes at a time. This increase in the number of modes can be associated with an enhanced amplification of long-wavelength modes due to nonlinear interaction between neighboring cavity modes [5]. The mode with the longest wavelength or

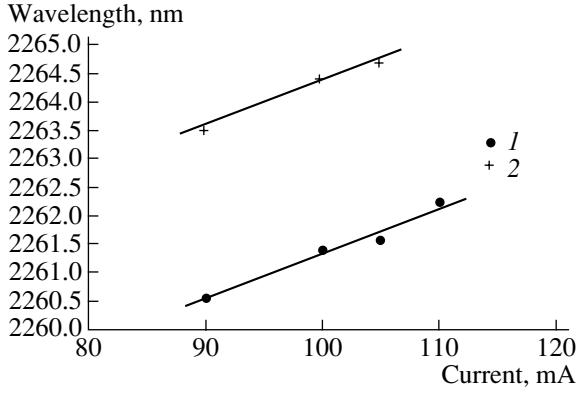

Fig. 5. Lasing wavelength as a function of current in AB43-1T laser at different temperatures T = (*1*) 278 and (*2*) 284 K.

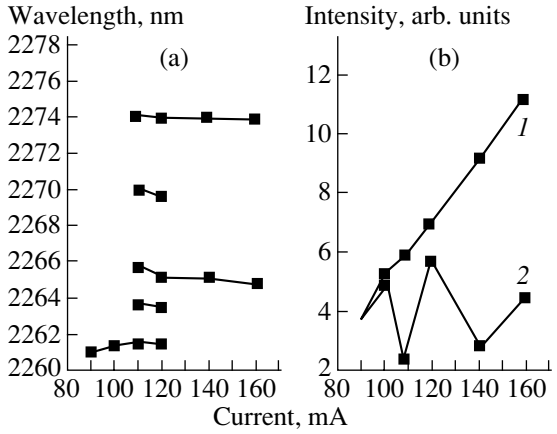

Fig. 6. (a) Cavity-mode wavelengths as functions of current for AB38-1K laser (τ = 100 μs, Q = 20, T = 300 K); (b) the intensity of radiation of (*1*) all modes and (*2*) the dominant mode as a function of current (τ = 100 μs, Q = 20, T = 300 K).

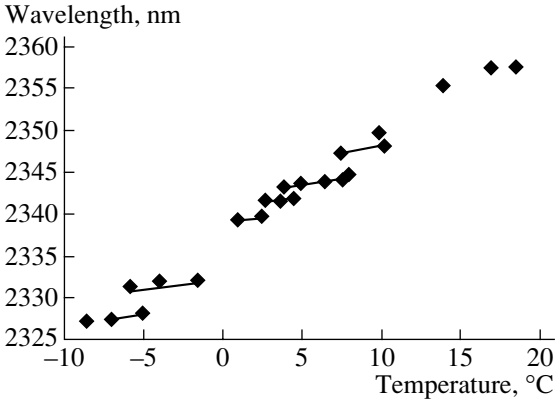

Fig. 7. Temperature dependence of the cavity-mode wavelengths for Bsp-T2 laser (τ = 0.6 μs, F = 512 Hz, I = 155 mA).

the neighboring one becomes the most intense since it is supported by shorter wavelength modes, which are quenched by the dominant mode but not entirely because the main mode owes its existence to them. The observed blue shift of the lasing frequency with current in a number of lasers or the pronounced retardation of the red shift in multimode operation can be related to a decrease in the refractive index due to an increase in the amplification of long-wavelength modes.

When the excess of current over the threshold is considerable, the radiation spectrum includes a smaller number of modes. This phenomenon was predicted in [6] from an analysis of two-mode interaction. In reality, several neighboring modes have comparable intensities and none of them can be considered weak, as was assumed in [6]. The new phenomenon of an increase in the lasing wavelength with current that considerably exceeds the threshold requires special explanation that takes comparable intensities of neighboring modes into account. Our data may be considered as the first experimental evidence of the influence that significant nonlinear optical effects have on both the mode composition of a quantum-well laser and the dependence of the lasing wavelength on current.

THERMAL RESISTANCE AND THERMAL INERTIA OF LASERS

The most efficient heat removal from a laser mounted with the epilayer in contact with the holder occurs via the epilayers located between the copper holder and the active region. The thickness of these layers h is about 2.5 μm. The heat-removal area equals the product of the cavity width w and the length L. In this case, the heat resistance can be expressed as

$$R_{T_1} = \frac{h}{Lw\chi} \quad (1)$$

and amounts to R_{T_1} = 50 K/W at L = 0.03 cm, w = 5 μm, h = 2.5 μm, and χ = 0.27 W/K cm. In the exponential approximation, the characteristic time constant for the establishment of a steady-state temperature is defined by the expression

$$\tau_1 = \frac{h^2 c_p \rho}{3\chi} \quad (2)$$

and equals τ_1 = 0.030 μs at a thermal conductivity χ = 0.08 cal/s cm K, heat capacity c_p = 0.02 cal/g K, and a specific weight of epilayers ρ = 5.65 g/cm^3. We also considered heat transfer through the above-lying epilayers and, then, through the substrate to the copper holder.

The conformal transformation method was applied to solve the problem of heat removal. The effective distance h^* of heat conduction in the bulk of a crystal may be introduced by the formula

$$h^* = \frac{w}{2}\left(\arcsin\frac{1}{\sqrt{1+\dfrac{\pi^2}{\ln^2\dfrac{D-w-\delta}{\delta}}-\ln^2\dfrac{w+\delta}{\delta}}}\right)^{-1}$$
$$\times \operatorname{arcsinh}\frac{\pi}{\ln\dfrac{w+\delta}{\delta}\sqrt{1+\dfrac{\pi^2}{\ln^2\dfrac{D-w-\delta}{\delta}}-\ln^2\dfrac{w+\delta}{\delta}}},$$

where δ is the width of the groove confining the active region and D is the total width of the laser. At $\delta = w$, we have h^* = 5.25 μm. Substitution of h* into (1) and (2) shows that the thermal resistance in the direction R_{T_2} is twice as high as that in the opposite (R_{T_1}) direction and

the inertia τ_2 is fourfold larger than τ_1. The resulting resistance and inertia can be calculated using the formulas

$$R_{T_\Sigma} = \frac{R_{T_1}R_{T_2}}{R_{T_1}+R_{T_2}}, \quad \tau_\Sigma = \tau_1\frac{R_{T_\Sigma}}{R_{T_1}} + \tau_2\frac{R_{T_\Sigma}}{R_{T_2}},$$

which yield $R_{T_\Sigma} = 34$ K/W and $\tau_\Sigma = 0.06$ μs.

For a laser chip mounted with its substrate on the copper holder, the conformal transformation yields the effective thickness of the heat conducting layer h_3^* in the form

$$h_3^* = \frac{w}{2}\left(\arcsin\frac{1}{\sqrt{1+\dfrac{4h^2}{D^2-w^2}}}\right)^{-1} \times \operatorname{arcsinh}\frac{2h}{w\sqrt{1+\dfrac{4h^2}{D^2-w^2}}}, \quad (4)$$

which yields $h_3^* = 9.0$ μm at the parameters specified above.

Substituting expression (4) for h_1 into formulas (1) and (2), we obtain the thermal resistance $R_{T_3} = 180$ K/W and the inertia $\tau_3 = 0.4$ μs. The above estimates suggest that mounting a laser chip with its epilayer in contact with the holder enables a fivefold decrease in the thermal conductivity and a sevenfold decrease in the inertia as compared to the case of mounting the chip with its substrate side on the holder. Even for 0.03-μs pulses of current, in the former case, the laser device approaches the steady-state temperature by one-half; i. e., its gain-frequency characteristic extends to the high-frequency region up to 5 MHz, which is an order of magnitude higher than in the latter case. The latter type of mounting, however, provides a larger (by a factor of 5) variation in frequency with current due to a greater thermal resistance and is preferable for lasers with a low operating current and for low-temperature operation.

TEMPERATURE-INDUCED MODE SHIFT

An amplification maximum in quantum-well structures $h\nu_{\max}$ is observed at a frequency corresponding to the difference in the energies of the quantum-confinement subbands for holes and electrons. A change in $h\nu_{\max}$ with temperature is governed mainly by the temperature dependence of the band-gap width of the narrow-gap layers $E_{g\min}$, since the other parameters of the quantum-well layers show only a slight temperature dependence. In the case studied, $P\dfrac{dh\nu_{\max}}{dT} \approx \dfrac{dE_{g\min}}{dt} \approx -0.27 \times 10^{-}$ eV/K. The corresponding change in the wavelength $\dfrac{d\lambda_{\max}}{dT}$ is given by

$$\frac{d\lambda_{\max}}{dT} \approx -\frac{dE_{g\min}\lambda}{dTh\nu_{\max}}. \quad (5)$$

We estimated this value from the data shown in Fig. 7 as 12 Å/K, which is close to the value of $\dfrac{d\lambda}{dT}$ calculated from formula (5) for the laser under consideration. For the other lasers, the calculated values of $\dfrac{d\lambda_{\max}}{dT}$ are in good agreement with the experimental data. The relative change in the refractive index with temperature is four times smaller than the corresponding change in the energy gap of the semiconductor where the radiation propagates. With this relationship taken into account, a change in the wavelength of each mode $\dfrac{d\lambda}{dT}$ is close to 2–3 Å/K, which correlates well with the experiment.

CURRENT-INDUCED MODE SHIFT

When the pump current exceeds the threshold but the intensity of lasing is insufficient for nonlinear effects to appear, a change in the wavelength with current should be governed by a change in the temperature in the active region. In order to obtain an undistorted spectrum of gases, it seems reasonable to operate at frequencies or pulse durations that ensure the establishment of a steady-state temperature in the active layer. In this case, the dependence of the wavelength of each mode on current is governed by the thermal resistance of the laser R_T which was calculated above for two different cases of laser chip mounting. Taking into account the inverse square-law dependence of semiconductor energy gaps on permittivity, we obtain a change in the wavelength with current in the following form:

$$\frac{d\lambda}{dI} = -0.25\frac{dE_{g\min}}{dT}\frac{\lambda}{E_{g\max}}R_T\left[(1-\eta_L)\frac{h\nu}{e} + 2IR_s + F\right], \quad (6)$$

where F is the excess of voltage in the active region over $h\nu/e$, e is the electron charge, R_s is a part of the series resistance arising in the region of laser layers and potential barriers, η_L is the differential quantum efficiency of lasing, and $E_{g\max}$ is the averaged energy gap in the waveguide layer.

With parameters typical of a laser mounted with its epilayer in contact with the holder ($F = 0.1$ V, $I = 0.1$ A, $R_s = 1$ Ω, $\eta_L = 0.5$ and $h\nu = 0.6$ eV, $\lambda = 2$ μm, $E_{g\max} = 1$ eV, $E_{g\max}/dT = -0.4 \times 10^{-3}$ eV/K, and $R_T = 34$ K/W),

we have $d\lambda/dI = 40$ Å/A. The increase in temperature in the active layer can be calculated from the expression

$$\Delta T = \Delta I R_T \left[(1 - \eta_L) \frac{h\nu}{e} + 2IR_s + F \right]. \quad (7)$$

According to (7), the increase in temperature during the growth of current from 80 to 130 mA is $\Delta T = 1$ K.

The above estimates suggest that a change in the temperature in the active region and a corresponding change in the lasing wavelength are moderate. This behavior is especially typical of high-efficiency lasers. In such lasers, it is possible to raise the value of F. To this end, one should reduce the cavity length L, thus enhancing the active-region voltage and increasing the thermal resistance due to a reduction of the active-region area. This would entail a rise in the threshold current and a corresponding increase in the variation of current during single-mode operation. In spite of the fact that η_L tends to unity and R_s tends to 0, there is no obstacle to obtaining an appreciable variation of λ with current.

No noticeable contribution to the heating of the laser is made by the radiation absorbed in the substrate because of the heat-removal area is large.

CONCLUSION

It is shown that GaInAsSb/GaAlAsSb-based quantum-well structures can be used in the design of temperature- or current-tunable lasers operating in the range from 2 to 2.4 μm at room temperature. The tuning range of the lasing mode extends from 4 to 16 Å. The maximal frequency of wavelength modulation with current ranges from 0.35 to 2 MHz for different methods of chip mounting on the holder. The thermal resistance of lasers falls between 40 and 250 K/W, which allows one to vary the steepness of the dependence of wavelength on current.

The temperature dependence of the refractive index is believed to be the main mechanism of tuning.

At currents exceeding the threshold by more than 50%, the lasing becomes multimode due to nonlinear optical interaction between the cavity modes. Eventually, this interaction may enable the substantial expansion of the frequency range of tuning.

REFERENCES

1. V. G. Avetisov, A. N. Baranov, A. N. Imenkov, *et al.*, Pis'ma Zh. Tekh. Fiz. **16** (14), 66 (1990) [Sov. Tech. Phys. Lett. **16**, 549 (1990)].
2. A. N. Imenkov, A. A. Popov, and Yu. P. Yakovlev, Pis'ma Zh. Tekh. Fiz. **21** (12), 59 (1995) [Tech. Phys. Lett. **21**, 470 (1995)].
3. T. N. Danilova, A. N. Imenkov, N. M. Kolchanova, *et al.*, Fiz. Tekh. Poluprovodn. (St. Petersburg) **30** (7), 1244 (1996) [Semiconductors **30**, 656 (1996)].
4. D. A. Yarekha, G. Glastre, A. Perona, *et al.*, Electron. Lett. **36**, 537 (2000).
5. P. G. Eliseev and A. P. Bogatov, Tr. Fiz. Inst. im. P. N. Lebedeva, Akad. Nauk SSSR **166**, 15 (1986).
6. A. P. Bogatov, P. G. Eliseev, O. G. Okhotnikov, *et al.*, Kvantovaya Élektron. (Moscow) **10**, 1857 (1983).

Translated by A. Sidorova

Semiconductors, Vol. 37, No. 4, 2003, pp. 491–492. Translated from Fizika i Tekhnika Poluprovodnikov, Vol. 37, No. 4, 2003, pp. 508–509.

PERSONALIA

Vladimir Ivanovich Ivanov-Omskiĭ (dedicated to his 70th birthday)

Professor Vladimir Ivanovich Ivanov-Omskiĭ recently celebrated his 70th birthday. He is a prominent scientist in the field of semiconductor physics and materials science of semiconductors and the head of a laboratory at the Ioffe Physicotechnical Institute of the Russian Academy of Sciences. After graduating with distinction from the department of chemistry at Leningrad State University in 1955 with a major in physical chemistry, V.I. Ivanov-Omskiĭ was assigned to the Ioffe Physicotechnical Institute of the USSR Academy of Sciences for postgraduate studies; under the supervision of B.T. Kolomiets and N.A. Goryunova, he started studying new semiconducting materials.

That was a time when the very possibility of controlling the properties of III–V semiconductors by growing a continuous sequence of their solid solutions was under discussion; moreover, it was not clear whether it was possible to preserve reasonably high electron mobility (characteristic of initial binary compounds) in the resulting ternary compounds. Ivanov-Omskiĭ developed a method for ultraslow zone equalization for the growth of equilibrium solid solutions in an InSb–GaSb system, grew the corresponding single crystals, and was first in the world to show that high electron mobility was in fact retained in the ternary compounds. By developing the methods for controlling the properties of semiconductors (in particular, using modulation of the band gap), he grew a single crystal composed of two compounds, InSb and GaSb, with an abrupt interface between them. Later on, such crystals became referred to as heterostructures. From his first independent steps in research, Ivanov-Omskiĭ took an active interest in narrow-gap semiconductors. The search for unconventional methods for controlling the electrical properties of these semiconductors led to studies of the phenomenon of magnetic injection of nonequilibrium charge carriers. In the course of these studies, Ivanov-Omskiĭ was involved in observations of a basically new phenomenon, i.e., negative luminescence; later on, this phenomenon was used with good results in infrared technique.

Ivanov-Omskiĭ became internationally renowned for a series of studies performed under his guidance and devoted to the technology of growth of narrow-gap $Hg_{1-x}Cd_xTe$ solid solutions and their derivatives; and for investigations of the electrical, optical, photoelectric properties of these materials and corresponding device structures. With the aim of gaining deeper insight into special features of electronic phenomena in narrow-gap semiconductors, Ivanov-Omskiĭ, in collaboration with his colleagues, studied a typical zero-gap semiconductor, HgTe, which later became a classical example of the realization of a zero-gap electron energy spectrum. The team headed by Ivanov-Omskiĭ was awarded the State Prize of the USSR for this series of studies.

For many years, Ivanov-Omskiĭ retained his interest in magnetooptical phenomena in semiconductors in the infrared region of the spectrum; this interest resulted in the development of a long-wavelength laser magnetospectrometer that had high stability and was based on molecular lasers with optical pumping provided by a tuned CO_2 laser. Observation of a fine structure in the GaAs electron spectrum may be considered as one of the outstanding physical results achieved using this spectrometer.

Ivanov-Omskiĭ contributed to the physics of semimagnetic semiconductors; using long-wavelength mag-

1063-7826/03/3704-0491$24.00

netospectroscopy, he directly determined the exchange-coupling constant in HgMnTe crystals from the measured splitting of spectral lines for the intracenter excitation of acceptors. Ivanov-Omskiĭ was first to observe electron spin resonance in the far infrared region of the spectrum for Mn atoms subjected to exchange interaction with neighboring atoms in the lattice of a semimagnetic semiconductor.

Ivanov-Omskiĭ has recently devoted his attention to studies of the structure of nanocomposites based on amorphous carbon and to the investigation of special features of electronic and optical phenomena in these composites. Notably, the most important results of these studies are related to the discovery of the activation of Raman frequencies in the optical-absorption spectra of the nanocomposite's carbon matrix when metals are introduced into the amorphous carbon structure and to the observation of resonance Raman scattering by hydrogen molecules adsorbed by carbon-containing centers in the structure of the matrix. In addition, the distortion of a hydrogen molecule caused by the interaction of this molecule with adsorbent was measured for the first time.

Professor Ivanov-Omskiĭ gives much time and effort to training young scientists. Under his supervision, 42 candidate theses and 11 doctoral theses were defended. Ivanov-Omskiĭ published more than 300 papers in Soviet, Russian, and foreign journals. For a long time, he has been a member of the Editorial Board of the journal "Fizika i tekhnika poluprovodnikov."

Ivanov-Omskiĭ celebrates his 70th birthday tirelessly continuing his scientific and pedagogical activity. We wish him good health and further achievements in the creative endeavors.

Colleagues and friends,
Editorial Board of the journal
Fizika i tekhnika poluprovodnikov.

Translated by A. Spitsyn